

# **Corrosion inhibition: a spectroscopic study**

A thesis submitted to The University of Manchester for the degree of

**Doctor of Philosophy**

in the Faculty of Science and Engineering

**2016**

**Maria Torres-Molina**

School of Chemistry



# Contents

|                       |    |
|-----------------------|----|
| List of Abbreviations | 9  |
| List of Figures       | 13 |
| List of Tables        | 23 |
| Abstract              | 25 |
| Declaration           | 27 |
| Copyright statement   | 29 |
| Acknowledgements      | 31 |

## Chapter 1. Introduction

|  |    |
|--|----|
| 1.1. Corrosion in the oil and gas industry   | 37 |
| 1.2. Corrosion inhibitors                    | 39 |
| 1.3. Model compounds approach                | 44 |
| 1.4. ATR-FTIR and Raman Spectroscopy         | 46 |
| 1.5. Vibrational Sum Frequency Generation    | 48 |
| 1.6. X-ray Photoelectron Spectroscopy        | 50 |
| 1.7. Near Edge X-ray Absorption Spectroscopy | 55 |
| 1.8. Density Functional Theory               | 57 |
| 1.9. Aims                                    | 59 |
| 1.10. References                             | 61 |

## **Chapter 2. Imidazole based corrosion inhibitors**

|   |    |
|---|----|
| 2.1. Introduction                         | 73 |
| 2.2. Model compounds                      | 75 |
| 2.2.1. Experimental                       | 75 |
| 2.2.2. Imidazoline compounds              | 78 |
| 2.2.3. 2-Mercaptobenzimidazole            | 81 |
| 2.3. Vibrational Sum Frequency Generation | 87 |
| 2.4. Density Functional Theory            | 89 |
| 2.4.1. Experimental                       | 89 |
| 2.4.2. Results and discussion             | 90 |
| 2.5. Conclusions                          | 96 |
| 2.6. References                           | 98 |

## **Chapter 3. Benzotriazole for protection of Fe**

|                                       |     |
|---------------------------------------|-----|
| 3.1. Introduction                     | 105 |
| 3.2. Model compounds                  | 107 |
| 3.2.1. Experimental                   | 107 |
| 3.2.2. Results and discussion         | 108 |
| 3.3. X-ray Photoelectron Spectroscopy | 111 |
| 3.3.1. Experimental                   | 111 |
| 3.3.2. Results and discussion         | 112 |
| 3.4. Conclusions                      | 118 |

|                 |     |
|-----------------|-----|
| 3.5. References | 119 |
|-----------------|-----|

## **Chapter 4. Phosphate esters for the protection of Fe**

|   |     |
|---|-----|
| 4.1. Introduction   | 125 |
| 4.2. Experimental   | 128 |
| 4.3. Results and discussion   | 129 |
| 4.3.1. Control experiment of H <sub>2</sub> O on Fe (110)                   | 129 |
| 4.3.2. Control experiment of CO <sub>2</sub> + H <sub>2</sub> O on Fe (110) | 132 |
| 4.3.3. Dibutyl phosphate ester on Fe (110)                                  | 137 |
| 4.3.3.1. XPS study in UHV   | 137 |
| 4.3.3.2. XPS study under NAP conditions                                     | 142 |
| 4.3.4. PAE 136 on Fe (110)  | 147 |
| 4.3.4.1. XPS study in UHV   | 148 |
| 4.3.4.2. XPS study under NAP conditions                                     | 152 |
| 4.4. Conclusions  | 156 |
| 4.5. References   | 157 |

## **Chapter 5. Phosphonic acids for the protection of Fe**

|                                       |     |
|---------------------------------------|-----|
| 5.1. Introduction                     | 163 |
| 5.2. Model compounds                  | 167 |
| 5.2.1. Experimental                   | 167 |
| 5.2.2. Results and discussion         | 173 |
| 5.3. X-ray Photoelectron Spectroscopy | 181 |

|   |     |
|---|-----|
| 5.3.1. Phenylphosphonic acid on Fe (110)    | 181 |
| 5.3.1.1. Experimental                       | 181 |
| 5.3.1.2. Results and discussion             | 182 |
| 5.3.2. Benzylphosphonic acid on Fe (110)    | 190 |
| 5.3.2.1. Experimental                       | 190 |
| 5.3.2.2. Results and discussion             | 190 |
| 5.3.3. Hexadecylphosphonic acid on Fe (110) | 197 |
| 5.3.3.1. Experimental                       | 197 |
| 5.3.3.2. Results and discussion             | 198 |
| 5.3.3.2.1. XPS study in UHV                 | 198 |
| 5.3.3.2.2. XPS study under NAP conditions   | 201 |
| 5.4. Conclusions                            | 208 |
| 5.5. References                             | 210 |

## **Chapter 6. Protecting steel from corrosion**

|                             |     |
|-----------------------------|-----|
| 6.1. Introduction           | 217 |
| 6.2. Experimental           | 218 |
| 6.3. Results and discussion | 220 |
| 6.4. Conclusions            | 232 |
| 6.5. References             | 233 |

## **Chapter 7. Conclusions and further work**

|                  |     |
|------------------|-----|
| 7.1. Conclusions | 237 |
|------------------|-----|

|                   |     |
|-------------------|-----|
| 7.2. Further work | 240 |
|-------------------|-----|

## Appendices

|   |     |
|---|-----|
| Appendix 1: structural data for $[\text{Fe}(\text{IMH})_4\text{Cl}_2]\text{Cl}$   | 245 |
| Appendix 2: structural data for $[\text{Fe}_3\text{O}(\text{HCO}_2)_6(\text{BIH})_3]\text{Cl} \cdot 2(\text{C}_2\text{H}_3\text{N})$ (2)        | 249 |
| Appendix 3: structural data for $[\text{Cu}(\text{MBIH}_2)(\text{dppp})\text{Cl}]$ (3)  | 253 |
| Appendix 4: IR and Raman spectra for MeBTAH and $[\text{Fe}_{14}\text{O}_6(\text{MeBTA})_6(\text{MeO})_{18}\text{Cl}_6]$                        | 257 |
| Appendix 5: IR and Raman spectra for Me <sub>2</sub> BTAH and $[\text{Fe}_{14}\text{O}_6(\text{Me}_2\text{BTA})_6(\text{MeO})_{18}\text{Cl}_6]$ | 258 |
| Appendix 6: IR and Raman spectra for ClBTAH and $[\text{Fe}_{14}\text{O}_6(\text{ClBTA})_6(\text{MeO})_{18}\text{Cl}_6]$                        | 259 |
| Appendix 7: IR spectra for TZAH and $[\text{Fe}_{14}\text{O}_6(\text{TZA})_6(\text{MeO})_{18}\text{Cl}_6]$                                      | 260 |
| Appendix 8: DFTP calculations   | 261 |
| Appendix 9: Publication from this thesis  | 265 |

**Word count: 51500**



## List of Abbreviations

|                                  |  |
|----------------------------------|--|
| AATP                             | 3-Anisalidene-amino-1,2,4-triazole phosphonate                       |
| AATP                             | 3-Anisalidene-amino-1,2,4-triazole phosphonate                       |
| AMP                              | Amino-tris(methylene- phosphonic acid)                               |
| AMP                              | Amino-tris(methylene- phosphonic acid)                               |
| ATR-FTIR                         | Attenuated Total Reflectance Fourier Transform Infrared Spectroscopy |
| bcc                              | body centered cubic system   |
| BE                               | Binding Energy   |
| BIH                              | Benzimidazole  |
| BP                               | British Petroleum  |
| BP-ICAM                          | British Petroleum International Centre for Advanced Materials        |
| BTAH                             | Benzotriazole  |
| BzPO <sub>3</sub> H <sub>2</sub> | Benzylphosphonic acid  |
| CASA                             | Common Astronomy Software Applications package                       |
| CASTEP                           | Cambridge Serial Total Energy Package                                |
| CIBTAH                           | 5-Chlorobenzotriazole  |
| DbPO <sub>2</sub> H              | Dibutyl phosphate ester  |
| DC                               | Direct Current   |
| DFPT                             | Density Functional Perturbation Theory                               |
| DFT                              | Density Functional Theory  |
| DpPO <sub>2</sub> H              | Diphenyl phosphate ester   |

|                                  |   |
|----------------------------------|---|
| dppp                             | 1,3-Bis(diphenylphosphino)propane   |
| <b>E</b>                         | Electric vector   |
| EDTMP                            | Ethylenediamine- tetrakis(methylenephosphonic acid)                         |
| EDTMP                            | Ethylenediamine-tetrakis(methylenephosphonic acid)                          |
| fcc                              | face-centered cubic system  |
| FTIR                             | Fourier Transform Infrared Spectroscopy                                     |
| GE                               | Grazing Emission  |
| GGA                              | Generalized Gradient Approximations   |
| GS                               | Gupta and Sen   |
| H2phpzH                          | 3(5)-(2-Hydroxyphenyl)pyrazole  |
| Hchp                             | 6-Chloro-2-hydroxypyridine  |
| HdPO <sub>3</sub> H <sub>2</sub> | Hexadecylphosphonic acid  |
| Hdpzpy                           | 2,6-Bis(pyrazol-3-yl)pyridine   |
| HEDP                             | 1-Hydroxyethylidene-bisphosphonic acid                                      |
| HEDP                             | 1-Hydroxyethylidene-bisphosphonic acid                                      |
| HL1                              | 3-(4-Methylbenzoyl)-propionic acid  |
| HL2                              | 4-Oxo-4phenylbutanoic acid  |
| HL3                              | 4-(4-Methylphenyl)botanoic acid   |
| HO <sub>3</sub> NP <sub>2</sub>  | N,N-tetramethyl-bis(phosphor-nate)-3-hydroxylpropyl<br>bis(methylene)amine, |
| HOC <sub>3</sub> NP <sub>2</sub> | N,N-tetramethyl-bis(phosphor- nate)-3-hydroxylpropyl-                       |

|                      |  |
|----------------------|--|
|                      | bis(methylene)amine                                      |
| HPAA                 | Hydroxyphosphonoacetic acid                              |
| HPAA                 | Hydroxyphosphonoacetic acid                              |
| HSalH                | Salicylaldoxime  |
| ICP-OES              | Inductively Coupled Plasma Optical Emission Spectroscopy |
| IMH                  | Imidazole  |
| IR                   | Infrared Spectroscopy                                    |
| ISO                  | International Standards Organization                     |
| KE                   | Kinetic Energy   |
| LDA                  | Local Density Approximation                              |
| LEED                 | Low-Energy Electron Diffraction                          |
| MBIH <sub>2</sub>    | 2-Mercaptobenzimidazole                                  |
| Me <sub>2</sub> BTAH | 5,6-Dimethyl-1H-benzotriazole                            |
| MeBTAH               | 5-Methyl-1H-benzotriazole                                |
| NACE                 | National Association of Corrosion Engineers              |
| NAP                  | Near Ambient Pressure                                    |
| NE                   | Normal Emission  |
| NEXAFS               | Near Edge X-ray Absorption Fine Structure                |
| pH                   | Minus log of activity of [H <sup>+</sup> ]               |
| phen                 | Phenanthroline   |

|   |   |
|---|---|
| PhPO <sub>3</sub> H <sub>2</sub>          | Phenylphosphonic acid                       |
| pKa                                       | Minus log of the acid dissociation constant |
| PSI                                       | Photon Science institute                    |
| py  | Pyridine                                    |
| RGA                                       | Residual Gas Analyzer                       |
| SFG                                       | Sum Frequency Generation                    |
| <i>t</i> BuPO <sub>3</sub> H <sub>2</sub> | <i>Tert</i> -butylphosphonic acid           |
| TZAH                                      | 1H-1,2,3-Triazole                           |
| UHV                                       | Ultra High Vacuum                           |
| VB  | Valence Band                                |
| VSFS                                      | Vibrational Sum Frequency Generation        |
| XPS                                       | X-ray Photoelectron Spectroscopy            |
| XRD                                       | X-ray Diffraction                           |

## List of Figures

- Figure 1.1. Photograph of pipelines covered by snow and workers fixing the leakage of the Prudhoe Bay oil spill.<sup>6</sup> 38
- Figure 1.2. Chemical structure of some of the compounds presented in this Thesis. 43
- Figure 1.3. Model of the corrosion inhibitor Acorga P5000 studied by Tasker *et al.*<sup>70</sup> (top left) and organic active compounds studied by Winpenny *et al.*<sup>71,72</sup> (top right and bottom). 45
- Figure 1.4. Schematic representation of an energy level diagram showing the processes involved in IR and Raman spectroscopy. 47
- Figure 1.5. Diagram showing the sum frequency generation process. 49
- Figure 1.6. Energy level diagram showing the SFG process. 49
- Figure 1.7. Schematic illustration of the dipole selection rule. 50
- Figure 1.8. Schematic representation of the electronic process that takes place in XPS. 51
- Figure 1.9. Photograph of the lab source NAPXPS at Photon Science Institute in the University of Manchester. 52
- Figure 1.10. Schematic representation of the main chambers and features of the NAP XPS kit at The University of Manchester. 53
- Figure 1.11. Schematic representation showing the way the electrons escape the surface in all directions (left) and the differential pumping system in the XPS kit (right, image courtesy of Dr Alex Walton from The University of Manchester). 55
- Figure 1.12. Illustration of the unit cell for a bcc system with a (110) plane. 55
- Figure 1.13. Schematic representation of the NEXAFS process for the C 1s edge. 56
- Figure 1.14. Schematic representation of the interaction of NEXAFS radiation with a molecule containing an aromatic ring deposited on a surface. 57

|   |    |
|---|----|
| Figure 2.1. Possible electronic configurations of MBIH <sub>2</sub> , thiol (left) and thione (right).  | 73 |
| Figure 2.2. Some of the possible binding modes for partially deprotonated MBIH <sub>2</sub> (top) and completely deprotonated MBIH <sub>2</sub> (bottom) labelled according to ‘Harris notation.’ <sup>21</sup>   | 74 |
| Figure 2.3. Single crystal X-ray structure for compounds <b>1</b> (left) and <b>2</b> (right). Colours: C, grey; N, blue; O, red; Cl, green and Fe, yellow. Hydrogen atoms omitted for clarity.   | 78 |
| Figure 2.4. ATR-FTIR spectra for IMH (a), compound <b>1</b> (b), BIH (c) and compound <b>2</b> (d).   | 79 |
| Figure 2.5. Suggested mechanism for the hydrogenation of CO <sub>2</sub> .  | 80 |
| Figure 2.6. Raman spectra for BIH (a), compound <b>1</b> (b), IMH (c) and <b>2</b> (d).   | 80 |
| Figure 2.7. Single crystal X-ray structure for compound <b>3</b> . Colours: C, grey; N, dark blue; S, yellow; Cu, light blue; P, orange and Cl, green. Hydrogen atoms omitted for clarity.  | 81 |
| Figure 2.8. Single crystal X-ray structure for compounds <b>5</b> (left) and <b>6</b> (right). Colours: C, grey; N, blue; O, red; S, yellow; P, orange; Au, cream and Zn, pink. Hydrogen atoms and CF <sub>3</sub> CO <sub>2</sub> anion omitted for clarity. | 82 |
| Figure 2.9. ATR-FTIR spectra of MBIH <sub>2</sub> (a), compound <b>3</b> (b), <b>5</b> (c) and <b>6</b> (d).  | 84 |
| Figure 2.10. Single crystal X-ray structures for compounds <b>11</b> (left) and <b>12</b> (right). Colours: C, grey; N, blue; S, yellow; Cu and light blue. Hydrogen atoms omitted for clarity.   | 85 |
| Figure 2.11. Single crystal X-ray structure for compounds <b>13</b> (left) and <b>14</b> (right). Colours: C, grey; N, blue; O, red; S, yellow; Fe, brown and Ni, green. Hydrogen atoms omitted for clarity.  | 85 |
| Figure 2.12. SFG spectra of MBIH <sub>2</sub> 10 mM, 25 mM in ethanol and pure ethanol acquired with $t \approx 0.33$ ps (left) and $t \approx 1$ ps (right).   | 86 |

|   |     |
|---|-----|
| Figure 2.13. SFG in situ and ex situ spectra of MBIH <sub>2</sub> 25 mM in ethanol acquired with $t \approx 0.33$ ps (left) and SFG ex situ spectra of clean steel and exposed to 0.01 M HCl/2 mM MBIH <sub>2</sub> acquired with $t \approx 0.8$ ps (right). | 88  |
| Figure 2.14. Optimised geometry calculated for MBIH <sub>2</sub> . Colours: C, grey; N, blue; S, yellow.  | 90  |
| Figure 2.15. Experimental (black) and simulated (red) IR spectra for MBIH <sub>2</sub> .  | 88  |
| Figure 2.16. Experimental vs. simulated IR frequencies for MBIH <sub>2</sub> .  | 91  |
| Figure 2.17. Experimental (black) and simulated (red) IR spectra for MBID <sub>2</sub> .  | 92  |
| Figure 2.18. Experimental vs. simulated IR frequencies for MBID <sub>2</sub> .  | 94  |
| Figure 3.1. Schematic representation of Cu-BTA complex suggested by Cotton and co-workers. <sup>7</sup>   | 106 |
| Figure 3.2. Single crystal X-ray structure for compound <b>16</b> (left) and a simplified top view (right) to show the binding mode. Colours: C, grey; N, blue; Fe, yellow; Cl, green. Hydrogen atoms omitted for clarity.                                    | 109 |
| Figure 3.3. Raman spectra for BTAH (a) and compound <b>16</b> (b).  | 109 |
| Figure 3.4. IR spectra for BTAH (a) and compound <b>16</b> (b).   | 110 |
| Figure 3.5. UHV XPS survey spectrum recorded for a powder sample of compound <b>16</b> .  | 112 |
| Figure 3.6. UHV XPS core level spectra for C 1s (a), O 1s (b) and N 1s (c) recorded for compound <b>16</b> as a powder on tantalum at $h\nu = 1400$ eV.   | 113 |
| Figure 3.7. UHV narrow spectra of the core level $2p_{3/2}$ for iron recorded at $h\nu = 1400$ eV, see text for binding energy of the peaks.  | 115 |
| Figure 3.8. Valence band spectra for the compound <b>16</b> as a powder on tantalum foil at $h\nu = 50$ (black) and 60 eV (red). The arrows show an increase in intensity of features in the valence band at the iron 3p-3d resonance.                        | 118 |

- Figure 4.1. Low pressure pure iron phase transition diagram showing the different allotropes of Fe for different temperatures and pressures.<sup>1</sup> 125
- Figure 4.2. Chemical structure of the general form of a phosphate triester (a), phosphate diester (b), phosphonic acid (c) and phosphonate ion (d). 127
- Figure 4.3 NAP XPS C 1s core level spectra for a clean Fe (110) surface (top left), O 1s (top right) and C 1s (middle left) core level spectra recorded at 373 K, O 1s core level spectra recorded at 423 K (middle right) and C 1s and O 1s core level spectra recorded at 473 K (bottom). 130
- Figure 4.4 NAP XPS Fe 2p core level spectra recorded in the presence of 8 mbar of H<sub>2</sub>O at 373 (top left), 423 (top right) and 473 K (bottom). 132
- Figure 4.5. NAP XPS O 1s core level spectra recorded in the presence of 2 mbar of CO<sub>2</sub> (top left) with 0.2 (top right), 0.7 (bottom left) and 2 mbar (bottom right) of H<sub>2</sub>O on an Fe (110) surface. 133
- Figure 4.6. NAP XPS C 1s core level spectra recorded in the presence of 2 mbar of CO<sub>2</sub> (top left) with 0.2 (top right), 0.7 (bottom left) and 2 mbar (bottom right) of H<sub>2</sub>O on an Fe (110) surface. 135
- Figure 4.7. NAP XPS Fe 2p core level spectra recorded in the presence of 2 mbar of CO<sub>2</sub> (top left) with 0.2 (top right), 0.7 (bottom left) and 2 mbar (bottom right) of H<sub>2</sub>O on an Fe (110) surface. 136
- Figure 4.8. UHV XPS survey scan (top left), core level for C 1s (top right), O 1s (bottom left) and P 2p (bottom right) for deposited DbPO<sub>2</sub>H on an Fe (110) surface recorded at room temperature. 137
- Figure 4.9. Schematic representation of the binding modes that DbPO<sub>2</sub>H shows on the Fe surface. 138
- Figure 4.10. UHV XPS core level for C 1s (left) and O 1s (right) for DbPO<sub>2</sub>H on an Fe (110) surface recorded at 373 (top), 423 (middle) and 473 K (bottom). 139
- Figure 4.11. UHV XPS core level for C 1s (left) and O 1s (right) for DbPO<sub>2</sub>H on an Fe (110) surface recorded at 523 (top) and 573 K (bottom). 141

Figure 4.12. NAP XPS core level for C 1s (top left), O 1s (top right) and P 2p (bottom) for DbPO<sub>2</sub>H on an Fe (110) surface recorded in the presence of 10 mbar of H<sub>2</sub>O at room temperature. 142

Figure 4.13. NAP XPS core level for C 1s (left) and O 1s (right) for DbPO<sub>2</sub>H on an Fe (110) surface recorded in the presence of 8 mbar of H<sub>2</sub>O at 373 (top), 423 (middle) and 473 K (bottom). 143

Figure 4.14. NAP XPS core level for O 1s (top left), C 1s (top right) and P 2p (bottom) for DbPO<sub>2</sub>H on an Fe (110) surface recorded in the presence of 2 mbar of CO<sub>2</sub>. 145

Figure 4.15. NAP XPS core level for O 1s for DbPO<sub>2</sub>H on an Fe (110) surface recorded in the presence of 2 mbar of CO<sub>2</sub> (top left) and with 0.7 (top right) and 2 mbar (bottom) of H<sub>2</sub>O. 146

Figure 4.16. Chemical structure of the composition of the commercial corrosion inhibitor PAE 136 where n= 13-15. 148

Figure 4.17. UHV XPS core level for C 1s (top left) and O 1s (top right) and P 2p (bottom) PAE 136 on an Fe (110) surface recorded at room temperature. 149

Figure 4.18. UHV XPS core level for C 1s (left) and O 1s (right) PAE 136 on an Fe (110) surface recorded at 370, 470, 520 and 573 K. 151

Fi Figure 4.19. NAP XPS core level for C 1s (top left) and O 1s (top right) and P 2p (bottom) for PAE 136 on an Fe (110) surface recorded under a H<sub>2</sub>O pressure of 0.3 mbar. 152

Figure 4.20. NAP XPS core level for C 1s (top left) and O 1s (top right) and P 2p (bottom) for PAE 136 on an Fe (110) surface recorded under a H<sub>2</sub>O pressure of 3 mbar. 154

Figure 4.21. NAP XPS core level for C 1s (top left) and O 1s at 373 K (top right), P 2p (middle) and O 1s (bottom) at 423 K measured with 4 h of difference for PAE 136 on an Fe (110) surface recorded under a H<sub>2</sub>O pressure of 3 mbar. 155

Figure 5.1. Some organic phosphonic acids and esters used as corrosion inhibitors. Abbreviations: AMP = amino-tris(methylene- phosphonic acid), HEDP = 1-hydroxyethylidene-bisphosphonic acid, HO<sub>3</sub>NP<sub>2</sub> = N,N-tetramethyl-bis(phosphor-

nate)-3-hydroxypropyl-bis(methylene)amine, AATP = 3-anisalidene-amino-1,2,4-triazole phosphonate, HPAA = hydroxyphosphonoacetic acid, EDTMP = ethylenediamine-tetrakis(methylenephosphonic acid).<sup>2</sup> 164

Figure 5.2. An illustration of a number of possible binding modes for doubly deprotonated phosphonate ligands labelled using Harris notation.<sup>6</sup> 165

Figure 5.3. Illustration representing the suggested binding modes for phenylphosphonic acid on an anatase TiO<sub>2</sub> (101) surface.<sup>13</sup> 166

Figure 5.4. Single crystal X-ray structure for compounds **22** (top), **24** (bottom left) and **28** (bottom right). Colours: C, grey; O, red; P, orange; Cl, green; Fe, yellow. Hydrogen atoms omitted for clarity. 173

Figure 5.5. Single crystal X-ray structure for compounds **25** and **29**. Colours: C, grey; O, red; P, orange; Fe, yellow. Hydrogen atoms omitted for clarity. 174

Figure 5.6. Single crystal X-ray structure for compounds **27** and **30**. Colours: C, grey; O, red; P, orange; Fe, yellow. Hydrogen atoms omitted for clarity. 174

Figure 5.7. Single crystal X-ray structure of PhPO<sub>3</sub>H<sub>2</sub> (left) and <sup>t</sup>BuPO<sub>3</sub>H<sub>2</sub> (right). Colours: C, grey; O, red; P, orange; Fe; H, white. 177

Figure 5.8. Selected region of the IR spectra for compounds **28**, **23**, **22** (left) and **29**, **25** and **24** (right). 178

Figure 5.9. Selected region of the IR spectra for compounds **27**, **31** (left), **30** and **32** (right). 179

Figure 5.10. UHV XPS survey (top left), C 1s (top right), O 1s (bottom left), N 1s (bottom middle) and P 2p (bottom right) spectra recorded from the sputtered and annealed Fe (110) single crystal. 182

Figure 5.11. UHV XPS core level O 1s (left) and P 2p (right) spectra recorded after a first deposition of PhPO<sub>3</sub>H<sub>2</sub> on an Fe (110) surface. 184

Figure 5.12. UHV XPS core level for O 1s (left) and P 2p (right) spectra recorded after a second deposition of PhPO<sub>3</sub>H<sub>2</sub> on an Fe (110) surface. 185

- Figure 5.13. UHV XPS O 1s (left) and P 2p (right) core level spectra of  $\text{PhPO}_3\text{H}_2$  on an Fe (110) surface recorded after heating the sample to 423 K. 186
- Figure 5.14. NEXAFS spectra recorded of  $\text{PhPO}_3\text{H}_2$  on an Fe (110) surface along the [001] (left) and [1-10] (right) crystal directions. 187
- Figure 5.15. Plot of intensity of C 1s to  $p^*$  transitions versus incident angle of photons fitted with Stöhr equations for the [001] (red) and [1-10] (black) crystal directions. 188
- Figure 5.16. Schematic representation of the suggested interaction of  $\text{PhPO}_3\text{H}_2$  with the given Fe (110) surface when forming a monolayer at 423 K. 189
- Figure 5.17. Schematic representation of the suggested interaction of  $\text{PhPO}_3\text{H}_2$  with the given Fe (110) surface when there is a thick layer. 189
- Figure 5.18. UHV XPS survey (left) and C 1s (right) spectra recorded from the sputtered and annealed Fe (110) single crystal. 191
- Figure 5.19. UHV XPS core level spectra for C 1s (top left), O 1s (top right) and P 2p (bottom) recorded after a 3 minute deposition of  $\text{BzPO}_3\text{H}_2$  on an Fe (110) surface, the p- $p^*$  shake up process marked with a dot on the C 1s spectrum. 193
- Figure 5.20. UHV XPS core level of  $\text{BzPO}_3\text{H}_2$  spectra recorded for C 1s (top), O 1s (middle) and P 2p (bottom) at 350 (left) and 400 K (right). 194
- Figure 5.21. UHV XPS core level spectra of  $\text{BzPO}_3\text{H}_2$  on an Fe (110) surface for C 1s (top left), O 1s (top right) and P 2p (bottom) recorded at 550 K. 195
- Figure 5.22. UHV XPS core level spectra of  $\text{BzPO}_3\text{H}_2$  on an Fe (110) surface recorded at GE for C 1s (top), O 1s (middle) and P 2p (bottom); at 400 and 550 K. 196
- Figure 5.23. UHV XPS core level spectra of  $\text{HdPO}_3\text{H}_2$  on an Fe (110) surface recorded at room temperature wide scan (top left), C 1s (top right), O 1s (bottom left) and P 2p (bottom right). 198
- Figure 5.24 UHV XPS core level spectra of  $\text{HdPO}_3\text{H}_2$  on an Fe (110) surface recorded at 373 (top), 423 (middle) and 473 K (bottom). 200

|  |     |
|--|-----|
| Figure 5.25. NAP XPS C 1s (right) and O 1s (left) core level spectra of $\text{HdPO}_3\text{H}_2$ on an Fe (110) surface in the presence of 2.5 mbar of $\text{H}_2\text{O}$ recorded at room temperature.   | 201 |
| Figure 5.26. NAP XPS core level spectra of $\text{HdPO}_3\text{H}_2$ on an Fe (110) surface in the presence of 2.5 mbar of $\text{H}_2\text{O}$ recorded at 373 (top) and 423 K (bottom).  | 202 |
| Figure 5.27. NAP XPS Fe 2p core level spectra of $\text{HdPO}_3\text{H}_2$ on an Fe (110) surface in the presence of 2.5 mbar of $\text{H}_2\text{O}$ recorded at room temperature (top left), 373 (top right) and 423 K (bottom).   | 203 |
| Figure 5.28. NAP XPS C 1s (left) and O 1s (right) core level spectra of $\text{HdPO}_3\text{H}_2$ on an Fe (110) surface recorded in the presence of 2 mbar of $\text{CO}_2$ .   | 204 |
| Figure 5.29. NAP XPS core level spectra of $\text{HdPO}_3\text{H}_2$ on an Fe (110) surface recorded in the presence of 2 mbar of $\text{CO}_2$ with 0.3 (top), 1 (middle) and 2 mbar of $\text{H}_2\text{O}$ (bottom).  | 205 |
| Figure 5.30. Schematic representation of the swelling process $\text{HdPO}_3\text{H}_2$ suffers following the addition of $\text{H}_2\text{O}$ .   | 206 |
| Figure 5.31. NAP XPS Fe 2p core level spectra of $\text{HdPO}_3\text{H}_2$ on an Fe (110) surface recorded in the presence of 2 mbar of $\text{CO}_2$ (top left) with 0.3 (top left), 1 (bottom left) and 2 mbar of $\text{H}_2\text{O}$ (bottom right).   | 207 |
| Figure 6.1. Cartoon illustrating steel termination as a function of environment. <sup>6</sup>  | 218 |
| Figure 6.2. Schematic representation of the steel plates submerged in the acidic solutions and sealed with parafilm.   | 219 |
| Figure 6.3. Photograph of the steel plates before introducing them in the UHV system of the XPS instrument. Plate 1 control experiment. Plates 2-5 are labelled according to the inhibitor used: 2 $\text{PhPO}_3\text{H}_2$ , 3 $\text{BzPO}_3\text{H}_2$ , 4 PAE 136 and 5 $\text{DbPO}_2\text{H}$ . | 220 |
| Figure 6.4. UHV XPS survey scan of a steel plate submerged for 20 h in 1 M HCl.  | 221 |
| Figure 6.5. UHV XPS spectra recorded for Fe 2p, O 1s, C 1s and Cl 2p for a steel plate submerged in 1 M HCl for 20 h.  | 222 |

- Figure 6.6. UHV XPS spectra recorded for Fe  $2p_{3/2}$  for a steel plate submerged in 1 M HCl for 20 h fitted for FeCl<sub>3</sub> (top left), FeCl<sub>2</sub> (top right) and FeO (bottom). 223
- Figure 6.7. UHV XPS spectra recorded for Fe  $2p_{3/2}$ , O 1s, C 1s and Cl 2p for a steel plate submerged in 1 M HCl and BzPO<sub>3</sub>H<sub>2</sub> for 20 h. 224
- Figure 6.8. UHV XPS spectra recorded for Fe  $2p_{3/2}$ , O 1s, C 1s and Cl 2p for a steel plate submerged in 1 M HCl and PAE 136 for 20 h. 226
- Figure 6.9. UHV XPS spectra recorded for Fe  $2p_{3/2}$ , O 1s, C 1s and Cl 2p for a steel plate submerged in 1 M HCl and DbPO<sub>2</sub>H for 20 h. 227
- Figure 6.10. UHV XPS spectra recorded for P 2p for a steel plate submerged in 1 M HCl (top left), BzPO<sub>3</sub>H<sub>2</sub> (top right), PAE 136 (bottom left) and DbPO<sub>2</sub>H (bottom right) for 20 h. 230
- Figure 6.11. Schematic representation of the possible binding modes for DbPO<sub>2</sub>H on a steel surface in an acidic media. 231
- Figure 7.1. Schematic representation of the proposed binding modes for MBIH<sub>2</sub>, PhPO<sub>3</sub>H<sub>2</sub>, BzPO<sub>3</sub>H<sub>2</sub> and HdPO<sub>3</sub>H<sub>2</sub> on a single crystal Fe (110) surface. 238
- Figure 7.2. Schematic representation of the proposed binding modes for DbPO<sub>2</sub>H on a single crystal Fe (110) surface (a and b) and on a steel surface (a, b and c). 239
- Figure 7.3. Chemical structure of compounds that would be of interest to study: *tert*-butylphosphonic acid (*t*BuPO<sub>3</sub>H<sub>2</sub>, left), *n*-butyl phosphate ester (*n*(BuO)PO<sub>3</sub>H<sub>2</sub>, centre), diphenyl phosphate ester (DpPO<sub>2</sub>H, right). 241



## List of Tables

|  |     |
|--|-----|
| Table 1.1. Different possible ranges of pressures with nomenclature and mean free path that the electron will traverse before being scattered or losing energy.  | 53  |
| Table 2.1. Thioamide bands for MBIH <sub>2</sub> and compounds <b>3</b> , <b>5</b> and <b>6</b> .  | 83  |
| Table 2.2. Assignment of thioamide bands for compounds found in the literature.  | 86  |
| Table 2.3. Experimental and calculated vibrational frequencies and assignment from calculations for MBIH <sub>2</sub> . Symbols: $\nu$ stretching, $\delta$ bending, $\beta$ in plane bending and $\gamma$ out of plane bending.                               | 93  |
| Table 2.4. Experimental and calculated vibrational frequencies and assignment for MBID <sub>2</sub> . Symbols: $\nu$ stretching, $\delta$ bending, $\beta$ in plane bending and $\gamma$ out of plane bending.   | 95  |
| Table 3.1. Energy and percentage contribution of multiplet split peaks to Fe 2p spectra. FWHM are slightly larger than reported in the work of Grosvenor <i>et al.</i> , <sup>32</sup> which is attributed to a slightly lower resolution in the present work. | 116 |
| Table 3.2. Comparison of binding energies of the main Fe 2p <sub>3/2</sub> photoelectron peak and energy difference between the photoelectron peak and the satellite for selected Fe <sup>3+</sup> compounds and compound <b>16</b> . <sup>32</sup>            | 117 |
| Table 4.1. Peak assignments and their respective binding energies (eV) for the spectra of Fe (110) single crystal in the presence of 8 mbar of H <sub>2</sub> O at different temperatures.   | 131 |
| Table 4.2. Peak assignments and their respective binding energies (eV) for Fe (110) surface exposed to 2 mbar of CO <sub>2</sub> with ratios of H <sub>2</sub> O (in mbar) in Figures 4.6 and 4.7.   | 134 |
| Table 4.3. Peak assignments and their respective binding energies (eV) for the spectra of DbPO <sub>2</sub> H on Fe (110) single crystal in Figures 4.8, 4.10 and 4.11.  | 140 |
| Table 4.4. Peak assignments and their respective binding energies (eV) for the spectra of DbPO <sub>2</sub> H on Fe (110) single crystal in Figures 4.12 and 4.13.   | 144 |

|  |     |
|--|-----|
| Table 4.5. Peak assignments and their respective binding energies (eV) for the spectra of DbPO <sub>2</sub> H on Fe (110) single crystal in figures 4.14 and 4.15.   | 147 |
| Table 4.6. Peak assignments and their respective binding energies (eV) for the spectra of PAE 136 on Fe (110) single crystal in Figures 4.17 and 4.18 in UHV.  | 150 |
| Table 4.7. Peak assignments and their respective binding energies (eV) for the spectra of PAE 136 on Fe (110) single crystal in Figures 4.19, 4.20 and 4.21 under H <sub>2</sub> O pressure (mbar) and at different temperatures (K).                | 153 |
| Table 5.1. IR frequencies, binding mode and assignment of the bands of the PO <sub>3</sub> group for compounds <b>22-32</b> .  | 176 |
| Table 5.2. IR frequencies and assignment for compounds found in the literature.  | 180 |
| Table 5.3. Peak assignments for O 1s and P 2p peaks and their respective binding energies (eV) for the recorded spectra of PhPO <sub>3</sub> H <sub>2</sub> on an Fe (110) surface.  | 183 |
| Table 5.4. Absolute areas for the P 2p and Fe 3p peaks corresponding to the experiments of PhPO <sub>3</sub> H <sub>2</sub> on a Fe(110) surface.  | 186 |
| Table 5.5. Peak assignments for O 1s and P 2p spectra and their respective binding energies (eV) for the spectra of BzPO <sub>3</sub> H <sub>2</sub> in Figures 5.19, 5.20, 5.21 and 5.22, NE = normal emission and GE = grazing emission.           | 192 |
| Table 5.6. Peak assignments and their respective binding energies (eV) for the spectra of HdPO <sub>3</sub> H <sub>2</sub> in Figures 5.23 and 5.24.   | 199 |
| Table 5.7. Peak assignments and their respective binding energies (eV) for the spectra of HdPO <sub>3</sub> H <sub>2</sub> in the presence of 2.5 mbar of H <sub>2</sub> O shown in Figures 5.25 and 5.26.   | 202 |
| Table 5.8. Peak assignments and their respective binding energies (eV) for the spectra of HdPO <sub>3</sub> H <sub>2</sub> in the presence of 2 mbar of CO <sub>2</sub> and different ratios of H <sub>2</sub> O (in mbar) in Figures 5.29 and 5.31. | 207 |
| Table 6.1. Peak assignments and their respective binding energies (eV) for the O 1s core level spectra for samples 1, 3, 4 and 5.  | 222 |
| Table 6.2. Peak assignments and their respective binding energies (eV) for the Fe 2p <sub>3/2</sub> , C 1s, and Cl 2p core level spectra for samples 1, 3, 4 and 5.  | 223 |

# Abstract

## Corrosion inhibition: a spectroscopic study

A thesis submitted to The University of Manchester for the degree of Doctor of Philosophy in the Faculty of Science and Engineering

2016

**Maria Torres-Molina**

Although many organic compounds are known to inhibit corrosion, in most cases it remains unknown how they specifically interact with a surface and how they decrease the corrosion rate. This lack of mechanistic knowledge currently makes the design and choice of new active compounds a case of trial and error. Understanding these organic molecule-metal surface interactions could lead to the design of new corrosion inhibitors for the oil and gas industry.

In this project it is intended to move the understanding of corrosion inhibition and other surface phenomena from empirical observation towards a mechanistic understanding. Using a combination of surface sensitive techniques such as vibrational sum frequency generation and X-ray photoelectron spectroscopy, and theoretical modelling through the preparation of model complexes of relevant corrosion inhibitors.

Two families of corrosion inhibitors have been studied and are presented here. For nitrogen based corrosion inhibitors a combination of theoretical calculations and experimental analysis of vibrational modes of model compounds have proved to be a good method to assist in understanding of surface phenomena.

For phosphorus based corrosion inhibitors an extensive study of model compounds has been done. In addition to this, different phosphonic acids and phosphate esters have been studied on a Fe (110) and steel surfaces in ultra high vacuum and in more realistic conditions using near ambient pressures in order to investigate if changes in the environmental conditions lead to a different behaviour. These have been compared to the study of PAE 136, a commercial corrosion inhibitor composed by a mixture of phosphate esters used in the extraction of oil, proving that one of the selected model compounds has a better inhibitive activity in both an ideal and a more realistic system.

The results presented in this thesis demonstrate that every corrosion inhibitor needs to be tested in the conditions in which it is going to be used as it is not possible to predict if a given active compound is going to have the same behaviour for different environments.



## **Declaration**

No portion of the work referred to in the thesis has been submitted in support of an application for another degree or qualification of this or any other university or other institute of learning.

**Maria Torres-Molina**



## Copyright statement

**i.** The author of this thesis (including any appendices and/or schedules to this thesis) owns certain copyright or related rights in it (the “Copyright”) and s/he has given The University of Manchester certain rights to use such Copyright, including for administrative purposes.

**ii.** Copies of this thesis, either in full or in extracts and whether in hard or electronic copy, may be made **only** in accordance with the Copyright, Designs and Patents Act 1988 (as amended) and regulations issued under it or, where appropriate, in accordance with licensing agreements which the University has from time to time. This page must form part of any such copies made.

**iii.** The ownership of certain Copyright, patents, designs, trade marks and other intellectual property (the “Intellectual Property”) and any reproductions of copyright works in the thesis, for example graphs and tables (“Reproductions”), which may be described in this thesis, may not be owned by the author and may be owned by third parties. Such Intellectual Property and Reproductions cannot and must not be made available for use without the prior written permission of the owner(s) of the relevant Intellectual Property and/or Reproductions.

**iv.** Further information on the conditions under which disclosure, publication and commercialisation of this thesis, the Copyright and any Intellectual Property and/or Reproductions described in it may take place is available in the University IP Policy (see <http://documents.manchester.ac.uk/DocuInfo.aspx?DocID=487>), in any relevant Thesis restriction declarations deposited in the University Library, The University Library’s regulations (see <http://www.manchester.ac.uk/library/aboutus/regulations>), and in The University’s policy on Presentation of Theses.



## Acknowledgements

This thesis would not have been possible without the help of DC and Tom. Thank you both for adopting me as your student and for being there every time I needed you. Thanks Tom for introducing me to the surface science world and for teaching me almost everything I know about it. David it has been a pleasure demonstrating your course, it has made me realise how much I like teaching! Hopefully I have not let you down. Thanks Rob for co-supervising me and for always providing a different point of view to my project.

Most of all I would like to thank Richard for choosing me for this particular project. It has not been what I expected but it has both challenged and enriched me in so many ways. I hope I have lived up to your expectations. Manchester has definitely exceeded mine.

I would also like to thank present and former members of the Magnets group for suffering my noisiness and annoying happiness. All Liddle's, Schröder's, Mills', Natrajan's, Leigh's and POB's groups for being part of such a great department. Mike, Claire, Tom, Titch, James, Fleur, Martyn, Sav, Lydia, Hannah, Chris, Anton, Rico, Guillem for making this last year the best out of my four years in ugly, rainy Manchester, I am going to miss you loads.

Thanks to BP-ICAM for the economic support and for making this project possible. Aleks, Dr Dave, Matt, Hadeel, Michelle, Tracey, Rob, Phil and Sheetal, thanks for making the BP-ICAM feel like a family.

Special thanks to Gavin for encouraging me to come to the UK and helping me through the application process, I would not have come to Manchester if it weren't for you!

Finally, I would like to thank my family for always believing in me and for their support, especially during the last months of my PhD in which I am afraid I have been quite irritable and annoying. I am sorry if I have been rude or sharp to you due to the stress but you know I love you loads. Nixon, Ranchito, Dalí and Gari, you've been the best pets a girl could wish for.

And of course, the most important person in my world, my mum. For always supporting me even though I know it is very hard for her to be so far away from me.



*Curiosity killed the cat,  
satisfaction brought him back*



# Chapter 1. Introduction



## 1.1. Corrosion in the oil and gas industry

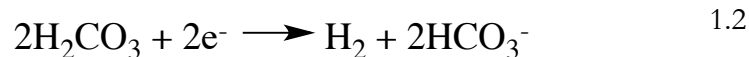
Corrosion is a naturally occurring phenomenon commonly defined as the deterioration of a metal that results from a chemical or electrochemical reaction with its environment, according to the National Association of Corrosion Engineers (NACE).<sup>1</sup> A more specific definition is given by ISO 8044:2015,<sup>2</sup> which defines corrosion as a physicochemical interaction – often of an electrochemical nature – between a metal and its environment that results in changes in the properties of the metal, and which may lead to significant impairment of the function of the metal, the environment, or the technical system of which these form a part. These definitions differentiate corrosion from other deterioration processes such as erosion, galling or wear. Corrosion causes a reduction in the thickness of a metallic surface which can lead to the contamination or loss of goods – in such different cases as oil pipelines or beer vessels. It can also lead to scale formation, if the corrosion products are not soluble, narrowing the bore of a pipeline and reducing the flow. Economic loss via replacement and repair of equipment; and most importantly, hazards or injury to people from failure of infrastructure or machinery. For all these reasons corrosion is an important problem that needs to be addressed. In particular, in the case of BP, internal corrosion of a pipeline (Figure 1.1) led to the biggest oil spill of Alaska's North Slope, known as the Prudhoe Bay oil spill. On the 2<sup>nd</sup> March 2006 it was discovered that a pipeline had been leaking for 5 days, spilling a total of 212,252 gallons of crude oil (almost one million litres) through a 0.64 cm hole on a 86 cm diameter pipeline.<sup>3</sup> In this case the corrosion was caused by bacterial contamination which, in the presence of hydrocarbons or  $H_2$ , reduces the sulfate anions present in the seawater to sulfide. Oil companies use biocide in order to fight against bacteria, but when the oil flow is too low it causes sediment and sludge to sit on the bottom of the pipeline, hindering the interaction and protecting the bacteria.<sup>4</sup> As a result of the great economic and environmental impact of this accident, the company committed to update their corrosion detection program by maintenance pigs, which allow to perform maintenance operations without stopping the flow, through

their pipelines at more regular intervals.<sup>5</sup> This is only a small example of how a failure caused by corrosion can be catastrophic.



Figure 1.1. Photograph of pipelines covered by snow and workers fixing the leakage of the Prudhoe Bay oil spill.<sup>6</sup>

For a corrosion process to take place there must be the oxidation of a metal – a reaction that takes place at the anode – and the reduction of the corrosive agent at the cathode.  $O_2$  reduction is the most common cathodic reaction, because it is the cause of atmospheric corrosion. However in the oil extraction process there is a different type of corrosion, known as sweet and sour corrosion, caused by  $CO_2$  and  $H_2S$  respectively, which take place in the absence of  $O_2$ .



Sweet corrosion is caused by the  $CO_2$  injected into wells to enhance oil recovery.<sup>7</sup> It firstly dissolves in water forming carbonic acid, which dissociates into bicarbonate ions and protons. These ions diffuse to iron surfaces where a redox reaction takes place to form  $FeCO_3$ , thus corroding the metal. Sour corrosion is caused by  $H_2S$  which can be produced from chemical reactions during the extraction process or exist naturally within

the oil itself. The  $\text{H}_2\text{S}$  dissociates in water to give bisulfide ions and protons, which again cause the corrosion of the metal and forms  $\text{FeS}$ . Both of these corrosion products are insoluble and precipitate on the surface, creating a passivation layer that stops or slows down further corrosion, this is known as anodic protection. The kinetics of layer formation depend on several factors including flow rates, oil and brine composition and partial pressure of the acidic gases. The formation of  $\text{FeS}$  is faster than of  $\text{FeCO}_3$ .<sup>8</sup> Although this provides an initial protection, these layers are highly unstable and can easily fracture, exposing the bare steel to the corroding agents and leading to pitting corrosion.

The oil and gas industry is commonly divided into three sectors:

- Upstream, which involves the exploration and production of oil;
- Midstream, which includes any transportation of both crude and refined oil;
- Downstream, which refers to refinement of the petroleum crude oil.

The downstream conditions are more severe as refinement of the crude oil requires high pressures and temperatures, whilst for the extraction of oil the temperatures do not exceed 200 °C. Corrosion processes in upstream and downstream sectors are different and have to be addressed individually. The purpose of this project was initially to study corrosion inhibition for both upstream and downstream, but as the research developed it was decided to focus on studying the prevention of corrosion for upstream processes specifically.

## 1.2. Corrosion inhibitors

Corrosion is the cause of financial and environmental losses and so understanding the chemistry involved, with a view to prevention, is an important area of research. There are four main methods to protect metals against corrosion: providing physical protection by using coatings or paints, designing more suitable materials, what is known as cathodic protection and with the use of corrosion inhibitors.

Coatings are a hard layer of material that provide a physical barrier to a metallic surface against corroding agents. There are many ways to apply the coatings such as electrolytic deposition, physical vapour deposition, chemical vapour deposition, spraying, plating and painting amongst others. Coatings can be divided into two main groups: inorganic coatings and organic coatings which have recently gained a lot of attention, as they are more environmentally friendly.<sup>9</sup> Chromate compounds have been used to inhibit corrosion for many surfaces including aluminium, zinc and steel, because they are very effective and remarkably cheap.<sup>10-12</sup> They contain  $\text{Na}_2\text{CrO}_4$  or  $\text{Na}_2\text{Cr}_2\text{O}_7$  and they form a very stable passivation layer when reducing to  $\text{Cr}^{3+}$ . However they are also an extreme irritant and highly toxic and for this reason several environmental laws were passed in 2006 to limit the use of  $\text{Cr}^{6+}$  based corrosion inhibitors in the European Union and, although they are still in use, they will be completely forbidden by 2017.<sup>12</sup> The use of W and Mo based corrosion inhibitors has also been limited as they are harmful and toxic for the environment.<sup>13</sup> There are also ceramic coatings of alumina and silicate.<sup>14</sup>

Conducting polymer coatings have gained a lot of interest recently as they are not toxic or harmful to the environment and they provide good physical and anodic protection.<sup>9</sup> There is a such a great variety of coatings that even the thinnest material discovered up to date, graphene, has proven to be a good coating for copper and nickel surfaces<sup>15</sup> claiming to be the 'thinnest known corrosion-protection coating'.<sup>16</sup>

Carbon steel is an inexpensive material and it is easy to fabricate and for these reasons it has found widespread use in the oil and gas industry. However it does not exhibit high resistance to corrosion. Changing the composition of the material used and adding non-metallic components can help promote corrosion protection although achieving this without compromising their mechanical properties can be a real challenge. For example, the addition of copper and chromium to steel leads to a more compact rust layer promoting passivation.<sup>17</sup> Nickel is also added as an alloying element to help reduce corrosion of steel. Designing smoother surfaces with fewer angles and sharp features in which moisture can be trapped can help to reduce corrosion.<sup>18</sup>

The principle of cathodic protection is to make the metal the cathode. This can be done by coupling the metallic surface with a less noble – more easily oxidised – material that becomes the anode of the reaction. With this method it is the sacrificial anode that oxidises instead of the steel and by doing so discharges an electric current to the pipeline, lowering the potential of steel. The most commonly used sacrificial anodes for steel are magnesium<sup>19,20,21</sup> and zinc<sup>21–23</sup> although aluminium<sup>21,24,25</sup> is a cheaper alternative.<sup>26</sup> This is a good protective method as it does not require an external power source, but it is not ideal for treating large areas.

When it is not possible to use a sacrificial anode, cathodic protection can be achieved by applying an external DC current. This method allows for the protection of a large surface area with one single installation and is commonly used in the oil and gas industry,<sup>27</sup> an example of an anode for pipelines is made of iron with silicon, carbon and graphite.<sup>26</sup>

Corrosion inhibitors are chemical substances which, when added in a small concentration into a corrosive environment, reduce or minimise the corrosion rate without changing the concentration of corrosive species.<sup>28</sup> Corrosion inhibitors can be inorganic or organic compounds and they inhibit corrosion by either adsorbing on the surface through a functional group – chemisorption – or by reacting with the metallic surface and forming insoluble compounds that precipitate on the surface. Organic corrosion inhibitors can also provide protection by forming hydrogen bonds with hydroxyl groups on the oxidised metallic surfaces. Although there are many effective corrosion inhibitors in use, in most cases it is still unknown how the molecules interact with the metallic surface, because of the difficulty of proving the nature of the inhibitor-metal interaction as multiple processes might take place. This lack of mechanistic knowledge makes the choice and discovery of new active compounds a case of trial and error. Thus, a deeper understanding of the surface chemistry of inhibitors is essential for the development of new and more effective corrosion inhibitors.

Organic corrosion inhibitors are usually compounds with electron-donating heteroatoms such as sulfur, nitrogen, phosphorus or oxygen and with delocalised

electrons such as in an aromatic ring. Sometimes they include a hydrocarbon chain, which makes the molecule partially soluble in oil.<sup>29</sup>

Heterocyclic compounds containing nitrogen atoms like benzotriazole<sup>30-34</sup> (BTAH), and imidazole derivatives;<sup>35-41</sup> and containing sulfur<sup>39,40,42-45</sup> like 2-mercaptobenzimidazole<sup>46,47</sup> (MBIH<sub>2</sub>) have shown inhibitive properties for different metallic surfaces. The lone pair electrons of the electron-donating atoms favours the interaction with the vacant orbitals on the metallic surfaces, while the aromatic functionality gives extra electronic density and surface coverage.

Phosphorus based corrosion inhibitors are commonly used in industry. Organic phosphonic acids are used as inhibitors in water cooling systems<sup>48,49,50</sup> because they are environmentally friendly.<sup>51</sup> It is thought that they inhibit corrosion by capturing the metallic cations that are in solution because of corrosion and forming insoluble compounds that precipitate on the surface and stop further corrosion.<sup>52,53</sup>

Phosphate esters are used to assist in the protection of pipes against corrosion in the extraction of oil.<sup>54,55</sup> In particular ethoxylated tridecylalcohol phosphate esters are used to stop Ca<sup>2+</sup> from precipitating inside the pipes as it forms a soluble compound with the phosphate.<sup>56</sup> Phosphate esters react with metallic cations in the same way as phosphonic acids and provide a physical barrier against corroding agents for steel.<sup>57</sup> A more detailed introduction for each type of corrosion inhibitor studied in this project will be provided at the beginning of each chapter.

An important fact to take into account when choosing corrosion inhibitors is their environmental impact. There is a special interest in trying to use more environmentally friendly corrosion inhibitors. Some non-toxic, biodegradable natural products that are available in the nature have been shown to have inhibitive properties.<sup>58</sup> Some examples are the extracts of natural products such as banana peel,<sup>59</sup> garlic peel,<sup>60</sup> rosemary,<sup>61</sup> curry leaves,<sup>62</sup> pomegranate<sup>63</sup> and caffeic acid<sup>64</sup> amongst others. In 2015 Almufarij *et al.* found that green leafy vegetables such as parsley inhibited the corrosion of carbon steel in 1 M HCl.<sup>58</sup> Several studies have proven the inhibitive activity of lawsone – henna extract on steel in the presence of HCl<sup>65-67</sup> and in seawater in the presence of Zn<sup>2+</sup>.<sup>68</sup> The

mechanism of action is still unknown, but has been reported to be via chemisorption on the active sites of the surface<sup>66</sup> and also by complexation to produce a compound that precipitates on the surface creating a passivation layer.<sup>67,68</sup>

Figure 1.2 shows the chemical structure of some of the organic compounds under study in this Thesis. BTAH, imidazole (IMH), benzimidazole (BIH) and MBIH<sub>2</sub> are known to have inhibitive properties and the results obtained from these are presented in Chapters 2 and 3. For the study of phosphorus based corrosion inhibitors it was decided to use small molecules to study the fundamentals of the organic-metal interaction in order to compare it with the corrosion inhibitors used in industry.

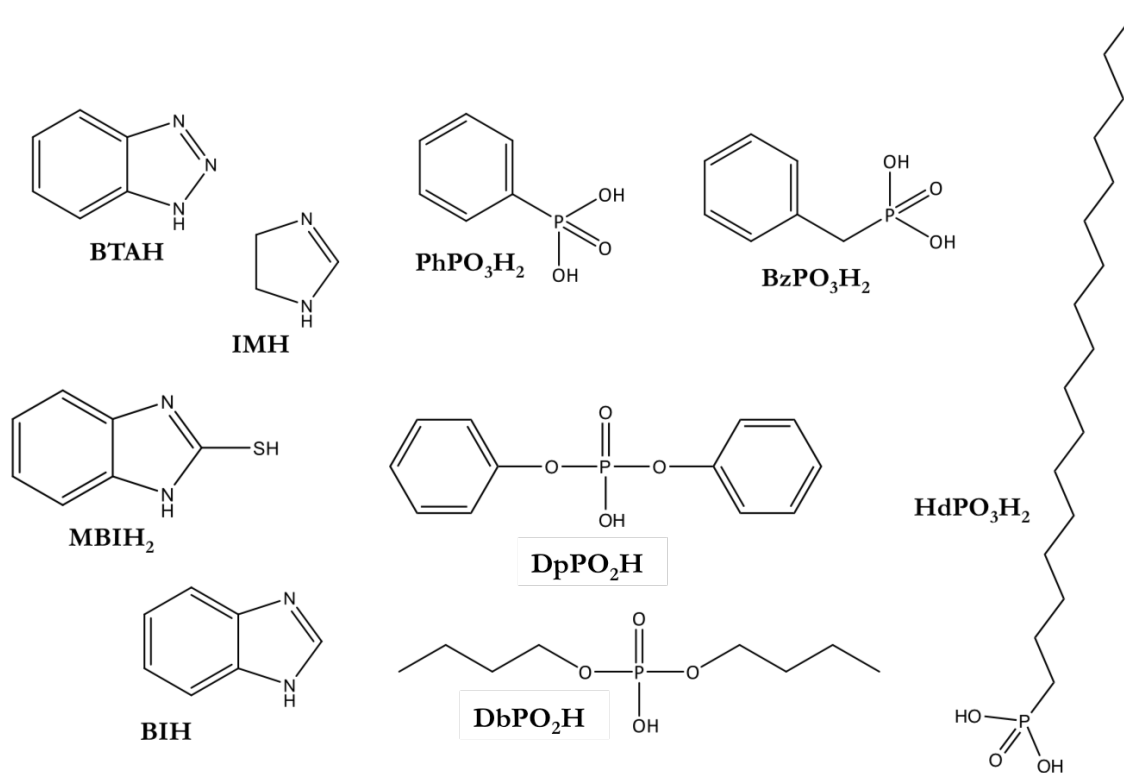


Figure 1.2. Chemical structure of some of the compounds presented in this Thesis.

From left to right and top to bottom: benzotriazole (BTAH), imidazole (IMH), phenylphosphonic acid (PhO<sub>3</sub>H<sub>2</sub>), benzylphosphonic acid (BzPO<sub>3</sub>H<sub>2</sub>), 2-mercaptobenzimidazole (MBIH<sub>2</sub>), diphenyl phosphate ester (DpPO<sub>2</sub>H), benzimidazole (BIH), dibutyl phosphate ester (DbPO<sub>2</sub>H) and hezadecylphosphonic acid (HdPO<sub>3</sub>H<sub>2</sub>).

### 1.3. Model compounds approach

A fundamental way to study corrosion inhibitors to get a better understanding of their interaction with a metallic surface is treating them as ligands and synthesising model complexes. The structure of the compounds obtained from single crystal X-ray diffraction provides information on the interaction of the ligand with the metallic cation at an atomic level and shows the preferred binding modes of interaction for a given corrosion inhibitor. Infrared and Raman spectroscopy of the compounds link the specific binding modes with specific bands that can assist identification. This information combined with theoretical modelling and surface measurements can help to elucidate the mechanism of action of the corrosion inhibitors and aid the design of new compounds.

The idea of using model complexes of corrosion inhibitors to understand their mechanism of action has previously been reported. In 1999 Tasker *et al.* investigated Acorga P5000, a mixture of 5-nonylsalicylaldoxime of different chain lengths known to inhibit corrosion.<sup>69</sup> Although this corrosion inhibitor was known to inhibit corrosion for iron there was no information on its binding and mechanism of action apart from the experimental evidence of the formation of a purple passivation layer on steel when treated with the active compound.

They reported the synthesis and characterization of purple tetrametallic iron model compounds with a salicylaldoxime ( $H_2SalH$ ) and other derivatives (Figure 1.3) with similar structures to Acorga P5000. The comparison of the X-ray photoelectron spectroscopy (XPS) spectra of the isolated compound and of a steel plate treated with salicylaldoxime under acidic conditions led to the conclusion that the corrosion inhibition of these active compounds is due to the formation of a tetrametallic cluster complex, which creates a purple layer on the surface protecting it against the corroding agents.<sup>69</sup>

Another example using this methodology for the design of new active compounds was published by Winpenny *et al.*<sup>70,71</sup> who studied a known corrosion inhibitor provided by

CIBA Speciality Chemicals and two similar compounds by synthesising model complexes with these and obtaining additional information from theoretical modelling and Raman spectroscopy. Figure 1.3 shows 3-(4-methylbenzoyl)-propionic acid (HL1), a corrosion inhibitor produced by Ciba Speciality Chemicals as a water-borne coating.

They synthesised an  $\{\text{Fe}_{10}\}^{3+}$  molecular wheel and a  $\{\text{Fe}_{11}\}^{3+}$  cluster with HL1, both previously reported.<sup>72,73</sup> The corrosion inhibitor shows two different binding modes in the compounds, as in the undecametallic cluster the 3-keto function is involved in a hydrogen bond with a bridging hydroxide that is not present in the wheel. This is supported by the shift in the carbonyl and in the Raman spectrum.

Solution adsorption isotherm experiments of HL1, 4-oxo-4-phenylbutanoic acid (HL2) and 4-(4-methylphenyl)butanoic acid (HL3), shown in Figure 1.3, on an oxide surface show that HL3 does not adsorb as well as HL1 and HL2 because of the lack of the 3-keto function that provides the extra hydrogen bonding. The extra methyl group in HL1 compared to HL2 gives more surface coverage, providing a better protection to the surface.<sup>70,71</sup>

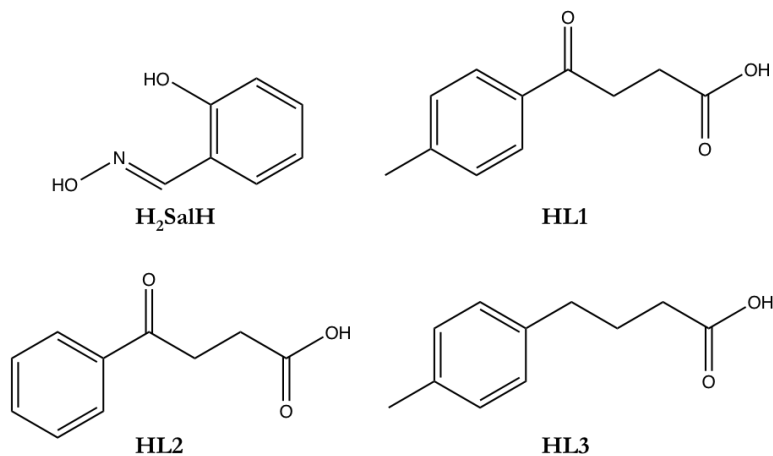


Figure 1.3. Model of the corrosion inhibitor Acorga P5000 studied by Tasker *et al.*<sup>69</sup> (top left) and organic active compounds studied by Winpenny *et al.*<sup>70,71</sup> (top right and bottom).

From this work they learned that this organic inhibitor interacts with the surface via the oxygen atoms at one end of the molecule whilst the other end participates in an intermolecular interaction with the molecules nearby creating a protective layer on the

surface. Based on the results obtained they designed a new corrosion inhibitor that showed better activity. This work shows the great importance of the model compounds approach as it led to finding a new and cheaper corrosion inhibitor that was patented by the company.<sup>74</sup>

## 1.4. ATR-FTIR and Raman spectroscopy

When electromagnetic radiation interacts with matter it can be reflected, transmitted, scattered or absorbed. Spectroscopy is the study of these processes. Infrared radiation does not have enough energy to cause electronic transitions, but it induces vibrational and rotational transitions when interacting with a molecule.

A vibration is IR active if it causes a change in the molecular dipole moment. Technically, a vibration is any change of shape of the molecule and these can be stretching, bending or rotation of bonds. These vibrations can be symmetrical – without changing the molecular dipole – or antisymmetrical – with change in the molecular dipole and hence IR active.

FTIR spectroscopy is based on the absorption of radiation. When the energy of the incident IR radiation matches the energy of a specific vibrational mode, so that the change in intensity of the IR light can be detected. Raman spectroscopy (Figure 1.4) is also based on the existence of vibrational modes but it measures scattered radiation instead. In this case when a beam of light is applied to a molecule most of it is elastically scattered (Rayleigh scattering) meaning that the excitation of the electron density of the molecule by absorption of the photon returns a photon of the same energy on relaxation from the virtual state. A photon may also be emitted when the molecule relaxes to an excited vibrational state instead of the ground state (Stokes scattering) or excitation can be from an excited vibrational state and return to the ground state (anti-Stokes scattering). In both cases the scattered light has a different energy than the incident light, Raman shift can be used to identify the vibrational modes of a molecule.

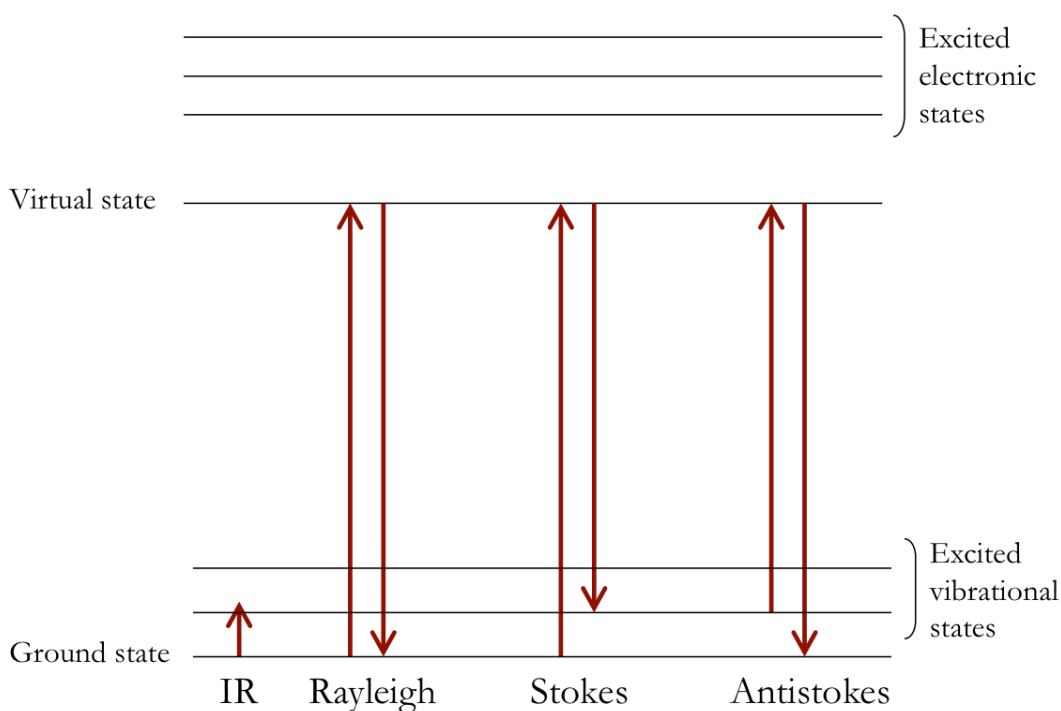


Figure 1.4. Schematic representation of an energy level diagram showing the processes involved in IR and Raman spectroscopy.

As the basis of these two techniques are different there can be vibrational modes active in one and not in the other. For a vibrational mode to be IR active the vibration taking place has to cause a change in the molecular dipole of the molecule. A vibrational mode will be Raman active if it causes a change in the polarisability of the molecule, which physically translates into a distortion of the electronic cloud of the molecule when interacting with an electromagnetic field. For this reason IR and Raman provide complementary information.

It is important to know that the frequency of vibration between two atoms in a bond depends on the mass of the atoms and the strength of the bond. The frequency between two bonded atoms with mass  $m_1$  and  $m_2$  would be:

$$v = \frac{1}{2\pi c} \sqrt{\frac{k}{\mu}} \quad 1.4$$

Where  $k$  is the molecular force constant,  $c$  is speed of light and  $m$  is the reduced mass given by the following equation:

1.5

$$\mu = \frac{m_1 m_2}{m_1 + m_2}$$

The strength of a chemical bond is proportional to the bond order, i.e. a double bond is stronger than a single bond and a triple bond is stronger still. Deuteration of a bond causes a change in the reduced mass which leads to an energy shift in a bond when deuterating a compound, a method that can facilitate the assignment of bands and that has been used in this project.

The equipment used in this project is an attenuated total reflectance infrared spectrometer (ATR-FTIR), which is a variation of FTIR. In this technique the IR beam is applied at an angle of 45 ° instead of going directly through the sample and it is totally reflected. It has the advantage of not requiring sample preparation, resulting in reproducible spectra.<sup>29</sup>

## 1.5. Vibrational Sum Frequency Spectroscopy

Vibrational sum frequency spectroscopy is a non-linear optical spectroscopy technique that provides a vibrational spectrum of the molecules present at an interface, for example between liquid and solid. This is a two-step process that combines infrared absorption and Raman scattering. For this reason a vibrational mode has to fulfil both IR and Raman selection rules to be active, thus there must be a change in the molecular dipole and in the polarisability of the molecule.

In a VSFS experiment (Figure 1.5) two photons  $\omega_1$  (infrared) and  $\omega_2$  (visible) impinge upon a surface, coincident in time generating a third photon  $\omega_3$  (sum frequency signal). Because the frequency of the photon is conserved, the energy is also conserved and it is equal to the sum of the two incident photons.<sup>30</sup>

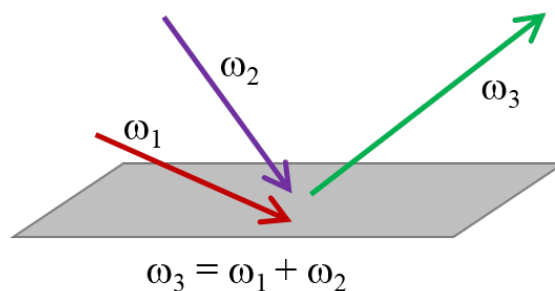


Figure 1.5. Diagram showing the sum frequency generation process.

This is known as a three-wave mixing process (meaning two waves in, one out), which, by definition, can only occur at interfaces, where there is a discontinuity in the local optical environment. In Figure 1.6 the electronic process for this transition is shown.

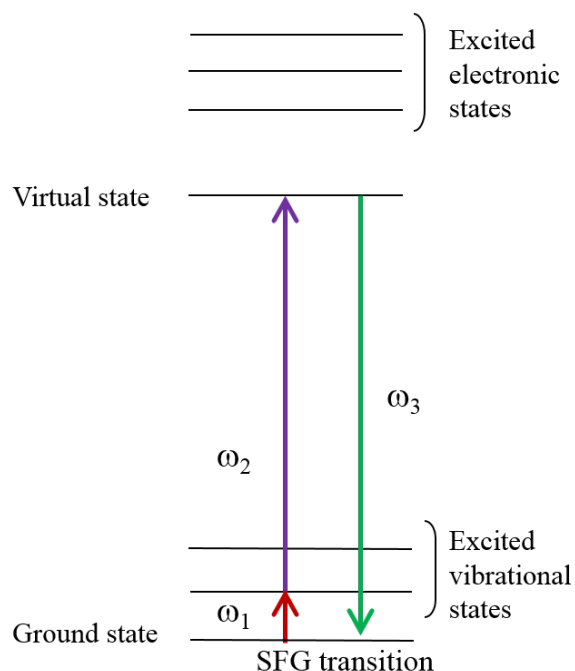


Figure 1.6. Energy level diagram showing the SFG process.

When the IR beam hits the surface, an electron is excited from the ground state to the first vibrational state, the second excitation is then caused by the visible beam that causes an anti-Stokes excitation. The electron then ‘falls’ either from a virtual or real electronic state, generating an SFG photon. To obtain a signal it is necessary that the beams of light are coincident in space and time. This is accomplished by a system of mirrors and pinholes in order to make the path of the two beams the same.

For adsorbed species on a surface, VSFS provides information about the interaction between the molecule and the surface and also about their orientation, whilst ignoring bulk contributions. This means that the VSFS technique can be used to probe surface and interfacial chemistry and processes at the solid-gas, solid-liquid, liquid-liquid and liquid-gas interfaces as long as one of the materials is transparent to visible IR radiation.

In this context, it is important take into account that the spectra in solution and solid phase might differ. In solution samples the molecules are randomly orientated and all vibrations causing a change in de dipole are active. However, when the sample is measured on a surface, according to the dipole selection rule, the image dipole of some vibrations cancels out the total change in de dipole and so are not active.

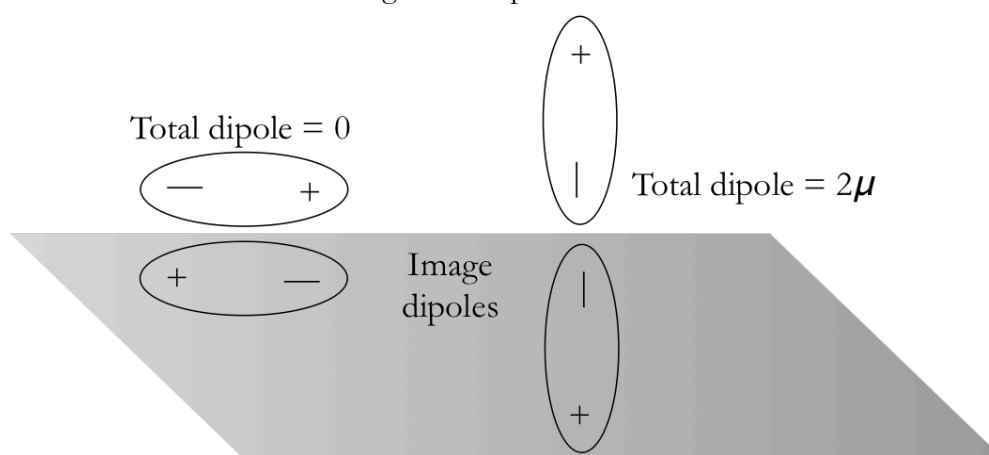


Figure 1.7. Schematic illustration of the dipole selection rule.

## 1.6. X-ray Photoelectron Spectroscopy

X-ray photoelectron spectroscopy (XPS) is a surface analytical technique that is usually carried out at very low pressures ( $<10^{-9}$  mbar). It is surface sensitive and the electrons are extracted from about 10 nm into the surface.<sup>75</sup> As an atom's bonding environment affects its binding energy (BE), XPS provides information on the chemical elemental composition present on the surface. The sample is often placed in an ultra high vacuum (UHV) environment. This serves two purposes: to increase the path length of the electron as it travels from the sample to the electron analyser; and to reduce the

contamination of the surface. The latter is particularly important in the study of model systems where the goal is to understand the interaction of a single type of molecule with a well characterised surface. The surface is irradiated with X-rays of energy  $h\nu$ , which are absorbed by atoms at the surface, resulting in the removal of an electron. XPS measures the kinetic energy (KE) of the electrons that escape the surface (see figure 1.8), allowing the binding energy of the electron to be deduced from the following equation:

$$BE = h\nu - (KE + \phi) \quad 1.6$$

where  $\phi$  is an instrument work function.

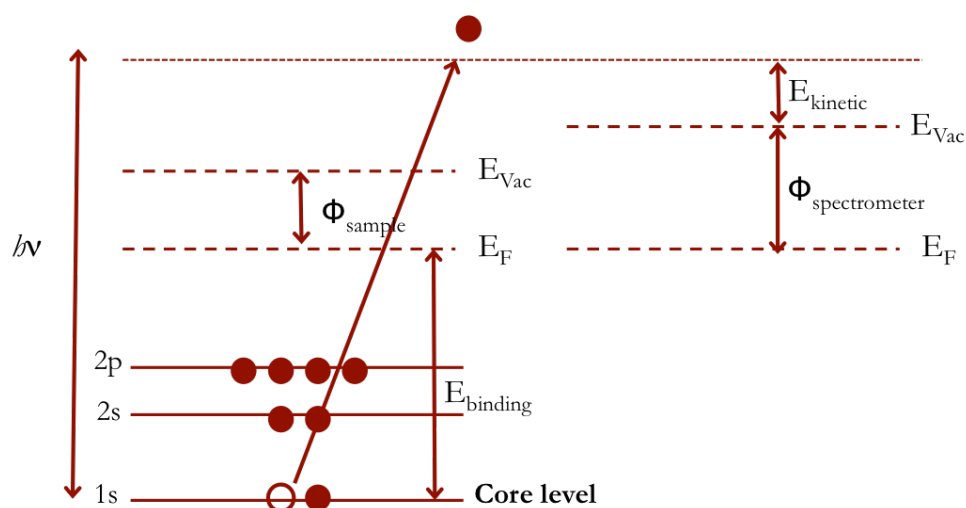


Figure 1.8. Schematic representation of the electronic process that takes place in XPS.

XPS is employed in different research fields like heterogeneous catalysis, corrosion and electrochemistry, but the necessity to work at extremely low pressures makes it difficult to investigate in a more realistic environment. This limitation is no longer an issue thanks to the development of a new variety of XPS done in low vacuum or what it is also known as near ambient pressure (NAP).<sup>76-78</sup>

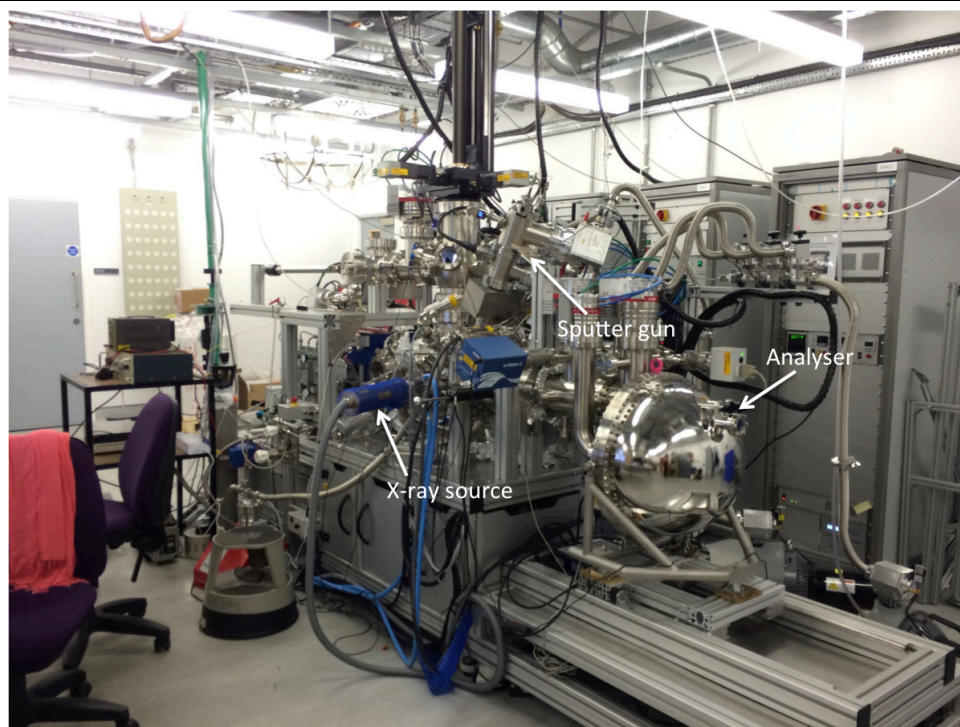


Figure 1.9. Photograph of the laboratory source NAPXPS at Photon Science Institute in the University of Manchester.

Even though this is a very new field of surface science that is still developing it has already been reported in the study of catalysis,<sup>77,79–90</sup> electrochemistry,<sup>91</sup> adsorption of CO<sup>92</sup> and capture of CO<sub>2</sub><sup>93</sup> but has not been used to study corrosion to any great extent.<sup>94,95</sup> NAP XPS can be done at different synchrotrons around the world such as MAXlab, Diamond, Bessy, Alba and Soleil, but there are not many laboratory based sources. Only two exist in the UK – in Manchester and Imperial College – and a handful of others in Synfuels in China, ISAS in Berlin, Notre Dame in Indiana, KBSI in Korea and the Paul Scherrer Institute in Switzerland. Figure 1.9 shows a photograph of the equipment at the Photon Science Institute in The University of Manchester.

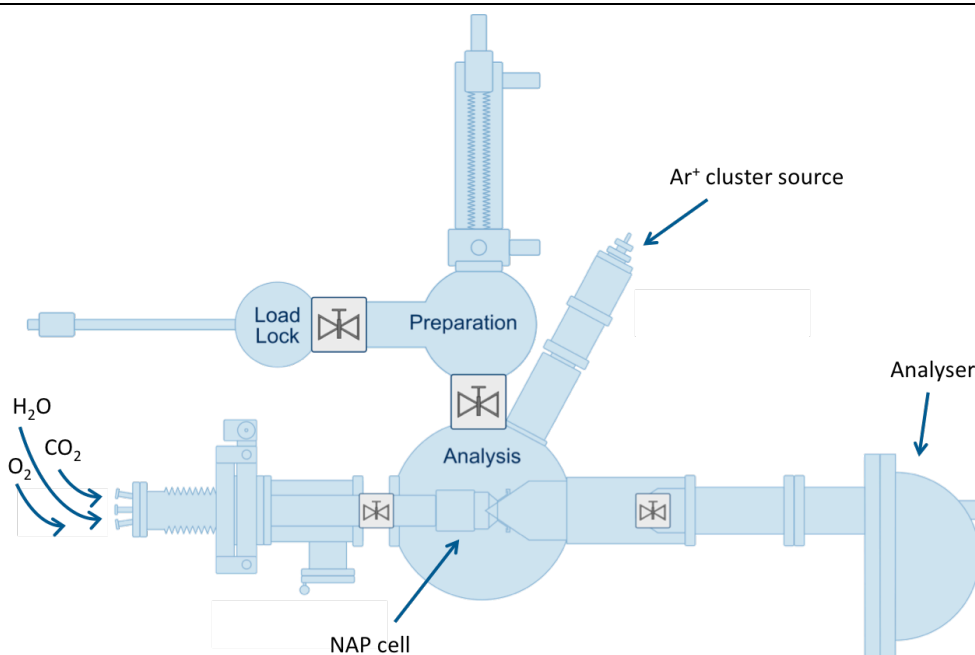


Figure 1.10. Schematic representation of the main chambers and features of the NAP XPS instrument at The University of Manchester.

Figure 1.10 shows a schematic diagram of the main chambers of the NAP XPS equipment. The instrument has a load lock to introduce the samples and to evaporate organic compounds in situ, a preparation chamber in which the preparation and cleaning of the samples can be done and the main analysis chamber. The main chamber is at UHV and the spectra can be collected whilst heating and Ar<sup>+</sup> ion sputtering allowing the study of real life changes on systems that are temperature dependent. The NAP cell is situated in a different chamber and has to be introduced when NAP measurements are required. This is perfectly sealed with Si<sub>3</sub>N<sub>4</sub> windows allowing measurements to be carried out at higher pressures without compromising the pressure of the other chambers. The temperature in this chamber reaches 700 °C. Currently the gases available are O<sub>2</sub>, H<sub>2</sub>O, CO<sub>2</sub> and CO but in the near future there will also be H<sub>2</sub> and NH<sub>3</sub>.

This instrument can reach up to 30 mbar although the measurements are usually taken at lower pressures. The electrons have to travel all the way to the analyser in order to be detected. The higher the pressure, the longer the path the electrons must travel, which results in fewer electrons reaching the detector, Table 1.1 shows the electron mean free

path calculated in air and room temperature. This translates to a loss of intensity and an increase of the acquisition time.

In order to solve this issue there is a differential pumping system to reduce the pressure in the analyser lens system. This increases the mean free path of the electrons so that more electrons will reach the detector. Figure 1.11 shows a schematic representation of the process. Both UHV and NAP experiments have positive and negative aspects. In UHV there is no loss of electrons and it is easier to keep the surfaces clean and flat allowing very precise information to be gathered on close to ideal systems.

Table 1.1. Different possible ranges of pressures with nomenclature and mean free path that the electron will traverse before being scattered or losing energy in air and at room temperature.

| <b>Vacuum range</b> | <b>Pressure (mbar)</b> | <b>Mean free path</b> |
|---------------------|------------------------|-----------------------|
| Ambient Pressure    | 1013                   | 68 nm                 |
| Low Vacuum          | 300 – 1                | 0.1 – 100 mm          |
| Medium Vacuum       | 1 – $10^{-3}$          | 0.1 – 100 mm          |
| High Vacuum         | $10^{-3}$ – $10^{-7}$  | 10 cm – 1 km          |
| Ultra High Vacuum   | $10^{-7}$ – $10^{-12}$ | 1 km – $10^5$ km      |

However UHV can change the composition of the samples in case of hydration or volatile components on the surface, meaning that the system under study is sometimes different to that which entered the XPS equipment. NAP experiments allow for the study of more realistic systems with higher pressures and in the presence of different gasses that mimic real life situations.

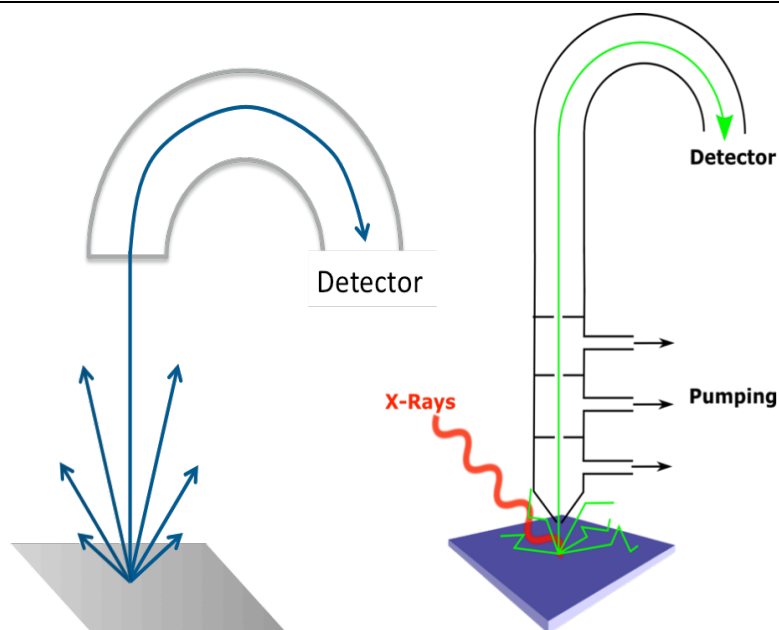


Figure 1.11. Schematic representation showing the way the electrons escape the surface in all directions (left) and the differential pumping system in the XPS instrument (right, image courtesy of Dr Alex Walton from The University of Manchester).

The XPS experiments presented in Chapters 3, 4 and 5 have been done on an Fe(110) single crystal surface, results presented in Chapter 6 have been done on AISI 1010 carbon steel. Metallic iron crystallises in a body-centred cubic structure (bcc). Figure 1.12 shows the unit cell in which the metallic atoms are represented as solid grey spheres, where a central atom is surrounded by eight other metallic atoms situated on the vertices of the unit cell. The single crystal used for these experiments has been cut in the (110) plane as shown below. The resulting surface is very compact.

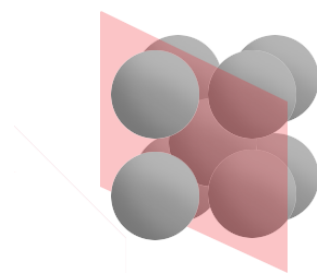


Figure 1.12. Illustration of the unit cell for a bcc system with a (110) plane.

Iron undergoes a phase transition from bcc to a face-centred cubic system at *ca.* 1394 °C<sup>96</sup> meaning the crystal cannot be heated above that temperature, which complicates the process of cleaning the crystal.<sup>97</sup>

## 1.7. Near Edge X-ray Absorption Fine Structure

Near Edge X-ray Absorption Fine Structure (NEXAFS) is a synchrotron-based technique developed in the 1980s to study the structure of molecules bound to surfaces that provides information about the electronic structure and orientation of small molecules on surfaces.<sup>98</sup> In this technique, the sample is irradiated with monochromatic X-rays and the energy is varied around an ionisation edge, in the case of the experiments presented in this thesis around the C 1s ionisation edge, which has an energy of 285 eV. The electromagnetic radiation generated at a synchrotron covers a wide range of the electromagnetic spectrum and is highly polarisable. With the help of a monochromator it is possible to select a single wavelength providing a bright, tuneable, polarised light for experiments. The reason NEXAFS cannot be done in laboratory based sources is because of the need of tuneable photon energy over a range of energies that can only be achieved from synchrotron sources. When the sample is irradiated the targeted atom absorbs the energy, gets excited to a higher energy level creating a core hole. An electron from a higher electronic level fills the core hole and the remaining energy is released in form of an Auger electron or fluorescence photon. This makes the technique both surface sensitive if an Auger electron is released or bulk sensitive if fluorescence photons are emitted, the Auger electron emission or fluorescence yield is measured as a function of the incident energy.

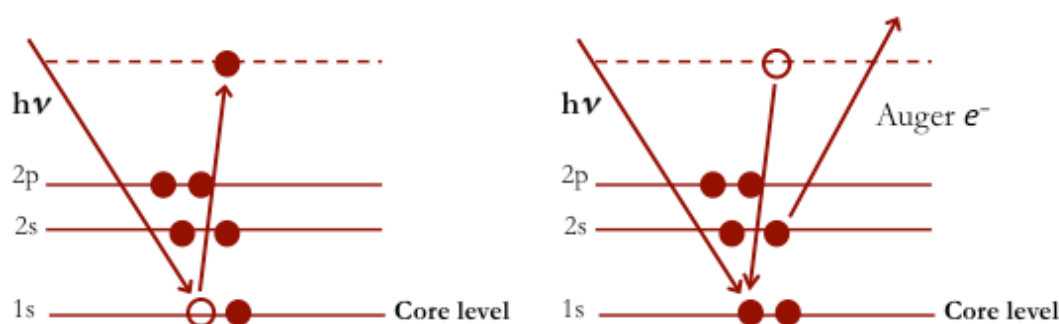


Figure 1.13. Schematic representation of the NEXAFS process for the C 1s edge.

One of the most important features of NEXAFS is that it can identify different bonding environments when the molecules are ordered on the surface. For example, for a molecule with an aromatic system like a benzene ring the  $\pi^*$  orbitals are orientated

perpendicular to the plane of the ring whilst the  $\sigma^*$  orbitals are in plane with the ring. Because the radiation in NEXAFS is polarised it interacts with the sample at a certain angle. As there is a maximum in intensity of the resonance process when the  $\mathbf{E}$  vector is parallel to the  $\pi^*$  orbitals, the orientation in which molecules are bound to the surface can be determined simply by changing the incident angle. For aromatic molecules, the height or the intensity of the peak is calculated for each angle and the data fitted to the Stöhr equations for two-fold symmetry,<sup>99</sup>

$$I_V^{par} = \cos^2 \theta \cos^2 \alpha + \sin^2 \theta \cos^2 \alpha \cos^2 \varphi \quad 1.7$$

$$I_V^{perp} = \sin^2 \alpha \sin^2 \varphi \quad 1.8$$

$$I_V = A [P I_V^{par} + (1 - P) I_V^{perp}] \quad 1.9$$

Figure 1.14 shows a schematic representation of how the  $\mathbf{E}$  vector and X-ray radiation interacts with the  $\pi^*$  system at different angles.

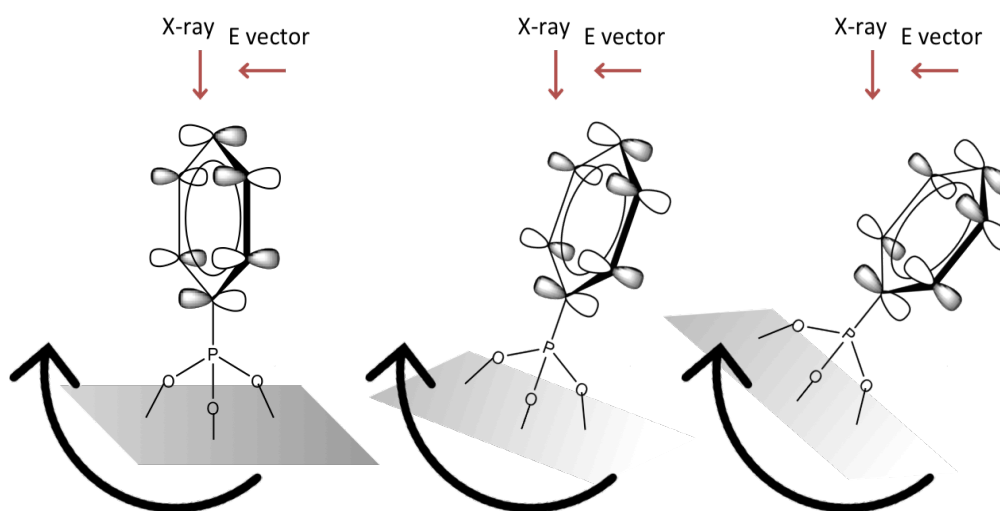


Figure 1.14. Schematic representation of the interaction of NEXAFS radiation with a molecule containing an aromatic ring deposited on a surface.

## 1.8. Density Functional Theory

Density Functional Theory (DFT) is a powerful tool for calculating properties of different systems. It is widely used in different fields and most commonly used to calculate binding energies of molecules in Chemistry and band gaps in Physics. It uses several approximations in order to make the systems as simple as possible to facilitate the calculations. The aim of this methodology is to predict the behaviour of electrons from first principles. That is achieved by solving the time-dependent Schrödinger equation,

$$E\Psi = \hat{H}\Psi \quad 1.10$$

which takes into account the positions of all particles at all times. As nuclei are much bigger and slower than electrons it can be assumed that the nuclei are static, thus the electronic wavefunction depends on the nuclear positions, but not their velocities. This assumption is known as the Born-Oppenheimer approximation.<sup>100</sup>

$$(\Psi_{molecules} = \Psi_{electrons}(\vec{r}_i + \vec{R}_j) + \Psi_{nucleus}(\vec{r}_i + \vec{R}_j)) \quad 1.11$$

$$(\Psi_{molecules} = \Psi_{electrons}(\vec{r}_i + \vec{R}_j) + \Psi_{nucleus}(\vec{R}_j)) \quad 1.12$$

The Schrödinger equation is simplified by this assumption, as it only applies quantum mechanics to electrons but it is still very complicated to solve. The Kohn-Sham approximation postulates that a given system of non-interacting electrons would generate the same density as a system in which the electrons interact with each other.<sup>101</sup>

Therefore the electronic energy of the system can now be described by:

$$E_{kin} + E_{e-e} = E_{kin}^{non-int} + E_{e-e}^{non-int}[\rho] + E_{XC}[\rho] \quad 1.13$$

where  $E_{XC}[\rho]$  is the exchange-correlation function. After these approximations the Schrödinger equation is:

$$\hat{H}[\rho]\Psi_m(r) = E_m\Psi_m(r) \quad 1.14$$

$$\hat{H}[\rho] = -\frac{\hbar^2}{2m}\nabla^2 + \hat{V}_{e-e}^{non-int}[\rho] + \hat{V}_{e-n}[\rho] + \hat{V}_{XC}[\rho] \quad 1.15$$

The only unknown variable in this equation is the exchange correlation,  $\hat{V}_{XC}[\rho]$ , which is only 10% of the total energy of the system proving that these approximations are accurate enough.

The Local Density Approximation (LDA) assumes that the exchange energy depends only on the local electronic density at each point in space.<sup>100</sup> This approximation is fairly simple and very accurate, but it fails when there are rapid changes in the electronic density, which usually happens with molecules. An alternative to this approximation is the Generalized Gradient Approximation (GGA),<sup>102</sup> which considers a gradient of the electron density. This approximation leads to an improvement in the typical chemistry calculations like atomization energies,<sup>103</sup> energy barriers<sup>103–105</sup> and structural energy differences.<sup>106–109</sup> There are different parameterisations of the GGA to choose from depending on the calculation, one of the most accurate is from Perdew, Burke and Ernzerhof (PBE).<sup>110</sup>

The CASTEP code<sup>111,112</sup> was developed in 1992 by Payne *et al.*<sup>113</sup> using a plane wave pseudopotential method for solid state materials. The code follows Bloch's theorem that stipulates that if the nuclei are arranged periodically in a solid, the potential is also periodic and the electronic density has the same periodicity, this makes the possible wave functions semiperiodic.<sup>114</sup>

CASTEP is user friendly as all input variables have default sets for basis set size, plane wave cut off energy, k-point sets and Fourier transform.<sup>112</sup> It can either be used in parallel or serial depending on the k-points and the processors used. It can be used to calculate total energies, electronic structures, to do geometric optimisations, molecular dynamics, transition states, phonons, electric field response and exchange and correlation energies.<sup>112</sup>

The characteristic of CASTEP that it is going to be explored in this thesis is the ability to predict IR and Raman spectra for the solid state, not only the energies of the bands, but also their relative intensities, when used correctly. The way to do this is by first

carrying out a geometric optimisation to eliminate stress forces in the solid. Density functional perturbation theory (DFPT) is used to calculate the response of a system when exposed to an electric field, which allows for a simulation of the bands and intensities in the IR and Raman spectra.

## 1.9. Aims

The major goal of this project is to gain a better understanding of how corrosion inhibitors interact with metallic surfaces to facilitate the selection and design of new corrosion inhibitors. This project is divided into two parts: synthesis and characterisation of metal compounds using corrosion inhibitors as ligands and investigation of the interaction of corrosion inhibitors with a metallic surface.

The first part of the project is focused on the synthesis of iron compounds with both nitrogen and phosphorus based corrosion inhibitors and similar ligands. The purpose of this is to gain an understanding of how the organic compound binds to a metallic cation at an atomic level using single crystal X-ray diffraction (XRD). Additionally a spectroscopic study of the vibrational modes is undertaken (ATR-FTIR and Raman spectroscopy) to find fingerprints for the binding modes present in the compounds. The idea of this is to have a library of binding modes and spectroscopic bands to allow identification by spectroscopic methods without the need for XRD. Theoretical calculations of the vibrational modes of the corrosion inhibitors in the solid state were used to assist with the assignment and understanding of the bands in the spectra.

For the study of the corrosion inhibitors on a surface it was first decided to do vibrational sum frequency spectroscopy (VSFS), a novel surface and interface-specific optical technique. However, this has proven to be less useful than anticipated due to significant noise in the fingerprint regions of the corrosion inhibitors under study.

For this reason it was decided to move on to other surface sensitive techniques. X-ray photoelectron spectroscopy (XPS) can give fast and accurate information about the

binding energy of the molecules and the state of the surface. This can be done in ultra high vacuum (UHV) and at near ambient pressure (NAP) or low vacuum. This technique was previously UHV exclusive, but it can now be performed at higher pressures using different gases. For this project H<sub>2</sub>O and CO<sub>2</sub> have been used in order to mimic sweet corrosion. Near edge X-ray absorption fine structure (NEXAFS) investigates the orientation of the molecules when there is an ordered  $\pi$  system on the surface and can therefore be used to determine the angle of molecules with aromatic functionality. However this can only be done using synchrotron radiation, as it needs monochromatic X-rays with a high degree of polarisation and so its use is limited.

Initially, this project was focused on nitrogen based corrosion inhibitors such as benzotriazole and some sulfur containing compounds like 2-mercaptobenzimidazole; Chapters 2 and 3 are centred on these and in the investigation of them using the model compounds method. As the project developed, and following the suggestions of the industrial sponsors, it was decided to focus on the study of phosphonic acids and phosphate esters, which are more relevant to the extraction of oil; Chapters 4, 5 and 6 show the results obtained for phosphorus based corrosion inhibitors.

## 1.10. References

- 1 NACE, *Corrosion basics, an introduction*, Houston, TX, 1984.
- 2 ISO 8044:2015, *Corros. Met. Alloy. - Basic terms Defm.*, 2015.
- 3 Unified Command Joint Information Center, *GC-2 Oil Transit Line Situation Report*, March 2008.
- 4 E. Schulze and H. A. Mooney, *Biodiversity and ecosystem function*, Springer-Verlag, 1993.
- 5 A. Bailey, *Provid. Cover. Alaska North. Canada's oil gas Ind.*, 2006, **11**.
- 6 The Associated Press, *The Seattle Times*, 2006.

- 7 R. P. Roberge, *Handbook of Corrosion Engineering*, McGraw-Hill, New York, USA, 2000.
- 8 S. Papavinasam, A. Doiron, J. Li, D. Park and P. Liu, *NACE Int. Corros. Conf. Expo 2010*, 2010, **8843**, 1–23.
- 9 M. Ates, *J. Adhes. Sci. Technol.*, 2016, **4243**, 1–27.
- 10 B. R. W. Hinton, *J. Alloys Compd.*, 1992, **180**, 15–25.
- 11 S. H. Zaferani, M. Peikari, D. Zaarei, I. Danaee, J. M. Fakhraei and M. Mohammadi, *Corrosion*, 2013, **69**, 372–387.
- 12 S. Pommiers, J. Frayret, A. Castetbon and M. Potin-Gautier, *Corros. Sci.*, 2014, **84**, 135–146.
- 13 E. Almeida, T. . Diamantino, M. . Figueiredo and C. Sá, *Surf. Coatings Technol.*, 1998, **106**, 8–17.
- 14 W. Ma and H. Dong, *Therm. Barrier Coatings*, 2011, 25–52.
- 15 R. K. Singh Raman and A. Tiwari, *JOM*, 2014, **66**, 637–642.
- 16 D. Prasai, J. C. Tuberquia, R. R. Harl, G. K. Jennings and K. I. Bolotin, *ACS Nano*, 2012, **6**, 1102–1108.
- 17 Y. Y. Chen, H. J. Tzeng, L. I. Wei, L. H. Wang, J. C. Oung and H. C. Shih, *Corros. Sci.*, 2005, **47**, 1001–1021.
- 18 E. E. White, *Corros. Conf. Olympia*, 1964, 11–14.
- 19 P. F. George, J. J. Newport and J. L. Nichols, *Corrosion*, 1956, 51–57.
- 20 J. G. Kim, J. H. Joo and S. J. Koo, *J. Mater. Sci. Lett.*, 2000, **19**, 477–479.
- 21 M. Andrei, F. Di Gabriele, P. L. Bonora and D. Scantlebury, *Mater. Corros.*, 2003, **54**, 5–11.
- 22 A. A. Sagüés and R. G. Powers, *Corrosion*, 1996, **52**, 508–522.

- 
- 23 C. Rousseau, F. Baraud, L. Leleyter and O. Gil, *J. Hazard. Mater.*, 2009, **167**, 953–958.
- 24 T.-M. Tsai, *J. Mar. Sci. Technol.*, 1996, **4**, 17–21.
- 25 S. M. A. Shibli, B. Jabeera and R. Manu, *Mater. Lett.*, 2007, **61**, 3000–3004.
- 26 M. Kutz, in *Handbook of Environmental Degradation of Materials*, ed. E. Inc., William Andrew, 2n Edition., 2012, pp. 771–798.
- 27 M. Karami, *J. Press. Vessel Technol.*, 2012, **134**, 054501.
- 28 Wranglén, *An Introduction to the Corrosion and protection of Metals*, Chapman and Hall, London, 1985.
- 29 J. W. Palmer, W. Hedges and J. L. Dawson, *The Use of Corrosion Inhibitors in Oil and Gas Production*, Maney Publishing, Leeds, 2004.
- 30 L. Procter and Gamble, 1947, **652339**, British Patent.
- 31 I. Dugdale and J. B. Cotton, *Corros. Sci.*, 1963, **3**, 69–74.
- 32 J. B. Cotton and I. R. Scholes, *Brit. Corros. J.*, 1967, **2**, 1–5.
- 33 B. Sathianandhan, K. Balakrishnan and N. Subramanyan, *Brit. Corros. J.*, 1970, **5**, 270–273.
- 34 R. J. Chin, D. Altura and K. Nobe, *Corrosion*, 1973, **29**, 185–187.
- 35 E. Stupnišek-Lisac, A. Gazivoda and M. Madžarac, *Electrochim. Acta*, 2002, **47**, 4189–4194.
- 36 D. Q. Zhang, L. X. Gao and G. D. Zhou, *Corros. Sci.*, 2004, **46**, 3031–3040.
- 37 M. Christov and A. Popova, *Corros. Sci.*, 2004, **46**, 1613–1620.
- 38 K. F. Khaled and M. A. Amin, *J. Appl. Electrochem.*, 2009, **39**, 2553–2568.
- 39 J. Aljourani, M. A. Golozar and K. Raeissi, *Mater. Chem. Phys.*, 2010, **121**, 320–

- 325.
- 40 M. Benabdellah, A. Tounsi, K. F. Khaled and B. Hammouti, *Arab. J. Chem.*, 2011, **4**, 17–24.
- 41 M. Yadav, P. N. Yadav and U. Sharma, *Indian J. Chem. Technol.*, 2013, **20**, 363–370.
- 42 M. M. Musiani and G. Mengoli, *J. Electroanal. Chem.*, 1987, **217**, 187–202.
- 43 T. Shahrabi, H. Tavakholi and M. G. Hosseini, *Anti-Corrosion Methods Mater.*, 2007, **54**, 308–313.
- 44 A. Popova, M. Christov, S. Raicheva and E. Sokolova, *Corros. Sci.*, 2004, **46**, 1333–1350.
- 45 J. Aljourani, K. Raeissi and M. A. Golozar, *Corros. Sci.*, 2009, **51**, 1836–1843.
- 46 M. Mahdavian and S. Ashhari, *Electrochim. Acta*, 2010, **55**, 1720–1724.
- 47 P. Morales-Gil, M. S. Walczak, C. R. Camargo, R. A. Cottis, J. M. Romero and R. Lindsay, *Corros. Sci.*, 2015, **101**, 47–55.
- 48 I. Sekine and Y. Hirakawa, 1986, 272–277.
- 49 Y. Gonzalez, M. C. Lafont, N. Pebere, G. Chatainier, J. Roy and T. Bouissou, *Corros. Sci.*, 1995, **37**, 1823–1837.
- 50 G. Gunasekaran, R. Natarajan, V. S. Muralidharan, N. Palaniswamy and B. V. A. Rao, *Anti-Corrosion Methods Mater.*, 1997, **44**, 248–259.
- 51 B. Balanaga Karthik, P. Selvakumar and C. Thangavelu, *Asian J. Chem.*, 2012, **24**, 3303–3308.
- 52 K. D. Demadis, C. Mantzaridis and P. Lykoudis, *Ind. Eng. Chem. Res.*, 2006, **45**, 7795–7800.
- 53 M. Papadaki and K. D. Demadis, *Comments Inorg. Chem.*, 2009, **30**, 89–118.

- 54 B. Alink, S. A. Ramachandran, S. A. Campbell, B. A. Outlaw and V. A. Jovancicevic, *Corros.* **99**, 1999, **37**.
- 55 S. Whitfield, *Sci. Technol. Concr. Admixtures*, 2015, 471–479.
- 56 J. F. Tate, 1973, **3720265**, U.S. Patent.
- 57 E. Babaian-Kibala, *Oil Gas J.*, 1994, 31.
- 58 G. M. Al-senani, S. I. Al-saeedi and R. Almufarij, *Orient. J. Chem.*, 2015, **31**, 2077–2086.
- 59 M. Sangeetha, S. Rajendran, J. Sathiyabama and P. Prabhakar, *J. Nat. Prod. Plant. Resour.*, 2012, **2**, 601–610.
- 60 S. S. de Assunção Araújo Pereira, M. M. Pêgas, T. L. Fernández, M. Magalhães, T. G. Schöntag, D. C. Lago, L. F. de Senna and E. D’Elia, *Corros. Sci.*, 2012, **65**, 360–366.
- 61 S. Hassan and S. Edrah, *J. Ind. Res. Technol.*, 2011, 1–9.
- 62 A. Sharmila, A. A. Prema and P. A. Sahayaraj, *Rasayan J. Chem.*, 2010, **3**, 74–81.
- 63 M. A. Chidiebere, C. E. Ogukwe, K. L. Oguzie, C. N. Eneh and E. E. Oguzie, *Ind. Eng. Chem. Res.*, 2012, **51**, 668–677.
- 64 F. S. de Souza and A. Spinelli, *Corros. Sci.*, 2009, **51**, 642–649.
- 65 H. Al-Schaibani, *Maternwiss. Werksttech.*, 2000, **31**, 1060–1063.
- 66 A. Ostovari, S. M. Hoseinieh, M. Peikari, S. R. Shadizadeh and S. J. Hashemi, *Corros. Sci.*, 2009, **51**, 1935–1949.
- 67 M. Edussuriya, A. S. Dissanayake and S. Lanka, *Online J. Sci. Technol.*, 2012, **2**, 32–36.
- 68 V. Johnsirani, J. Sathiyabama, S. Rajendran and A. S. Prabha, *Int. Sch. Res. Netw.*, 2012, **2012**, 1–9.

- 69 J. M. Thorpe, R. L. Beddoes, D. Collison, C. D. Garner, M. Helliwell, J. M. Holmes and P. A. Tasker, *Angew. Chemie Int. Ed.*, 1999, **38**, 1119–1121.
- 70 M. Frey, S. G. Harris, J. M. Holmes, D. A. Nation, S. Parsons, P. A. Tasker, S. J. Teat and R. E. P. Winpenny, *Angew. Chemie Int. Ed.*, 1998, 3245–3248.
- 71 M. Frey, S. Harris, J. Holmes, D. Nation, S. Parsons, P. Tasker and R. Winpenny, *Chem. Eur. J.*, 2000, **6**, 1407–15.
- 72 S. M. Gorun, G. C. Papaefthymiou, R. B. Frankel and S. J. L. Ia, *J. Am. Chem. Soc.*, 1987, 3337–3348.
- 73 K. L. Taft, C. D. Delfs, G. C. Papaefthymiou, S. Foner, D. Gatteschi and S. J. Lippard, *J. Am. Chem. Soc.*, 1994, **116**, 823–832.
- 74 P. A. Tasker, D. A. Nation, A. Braig and M. Frey, *Ciba Spec. Chem. Hold. Inc.*, 2000, **WO20000434**, British Patent.
- 75 M. P. Seah, *Surf. Interface Anal.*, 2012, **44**, 497–503.
- 76 M. Salmeron and R. Schlögl, *Surf. Sci. Rep.*, 2008, **63**, 169–199.
- 77 F. Tao, M. E. Grass, Y. Zhang, D. R. Butcher, J. R. Renzas, Z. Liu, J. Y. Chung, B. S. Mun, M. Salmeron and G. A. Somorjai, *Science (80-. )*, 2008, 932–934.
- 78 D. Frank Ogletree, H. Bluhm, E. D. Hebenstreit and M. Salmeron, *Nucl. Instruments Methods Phys. Res. Sect. A Accel. Spectrometers, Detect. Assoc. Equip.*, 2009, **601**, 151–160.
- 79 R. Toyoshima, M. Yoshida, Y. Monya, K. Suzuki, B. S. Mun, K. Amemiya, K. Mase and H. Kondoh, *J. Phys. Chem. Lett.*, 2012, **3**, 3182–3187.
- 80 R. Toyoshima and M. Yoshida, *J. Phys. Chem. C*, 2012, 18691–18697.
- 81 T. C. R. Rocha, A. Oestereich, D. V Demidov, M. Havecker, S. Zafeiratos, G. Weinberg, V. I. Bukhtiyarov, A. Knop-Gericke and R. Schlögl, *Phys. Chem. Chem. Phys.*, 2012, **14**, 4554–4564.

- 82 R. Toyoshima, M. Yoshida, Y. Monya, K. Suzuki, K. Amemiya, K. Mase, B. S. Mun and H. Kondoh, *J. Phys. Chem. C*, 2013, **117**, 20617–20624.
- 83 R. Toyoshima, M. Shimura, M. Yoshida, Y. Monya, K. Suzuki, K. Amemiya, K. Mase, B. S. Mun and H. Kondoh, *Surf. Sci.*, 2014, **621**, 128–132.
- 84 N. J. Divins, I. Angurell, C. Escudero, V. Pérez-Dieste and J. Llorca, *Science (80-. .)*, 2014, **346**, 620–623.
- 85 M. Eichelbaum, M. Hävecker, C. Heine, A. M. Wernbacher, F. Rosowski, A. Trunschke and R. Schlögl, *Angew. Chemie Int. Ed.*, 2015, **54**, 2922–2926.
- 86 D. D. Falcone, J. H. Hack, A. Y. Klyushin, A. Knop-Gericke, R. Schlögl and R. J. Davis, *ACS Catal.*, 2015, **5**, 5679–5695.
- 87 A. Y. Klyushin, R. Arrigo, Y. Youngmi, Z. Xie, M. Hävecker, A. V. Bukhtiyarov, I. P. Prosvirin, V. I. Bukhtiyarov, A. Knop-Gericke and R. Schlögl, *Top. Catal.*, 2016, **59**, 469–477.
- 88 W. T. Hong, K. A. Stoerzinger, E. J. Crumlin, E. Mutoro, H. Jeon, H. N. Lee and Y. Shao-Horn, *Top. Catal.*, 2016, **59**, 574–582.
- 89 S. Krick Calderón, M. Grabau, L. Óvári, B. Kress, H. P. Steinrück and C. Papp, *J. Chem. Phys.*, 2016, **144**.
- 90 K. Yuan, J.-Q. Zhong, X. Zhou, L. Xu, S. L. Bergman, K. Wu, G. Q. Xu, S. L. Bernasek, H. X. Li and W. Chen, *ACS Catal.*, 2016, **6**, 4330–4339.
- 91 B. Bozzini, M. Amati, P. Bocchetta, S. Dal Zilio, A. Knop-Gericke, E. Vesselli and M. Kiskinova, *Electrochim. Acta*, 2015, **174**, 532–541.
- 92 R. Toyoshima, M. Yoshida, Y. Monya, K. Suzuki, K. Amemiya, K. Mase, B. S. Mun and H. Kondoh, *Phys. Chem. Chem. Phys.*, 2014, **16**, 23564–23567.
- 93 I. Niedermaier, M. Bahlmann, C. Papp, C. Kolbeck, W. Wei, S. Krick Calderón, M. Grabau, P. S. Schulz, P. Wasserscheid, H. P. Steinrück and F. Maier, *J. Am. Chem. Soc.*, 2014, **136**, 436–441.

- 94 V. A. Saveleva, V. Papaefthimiou, M. K. Daletou, W. H. Doh, C. Ulhaq-Bouillet, M. Diebold, S. Zafeiratos and E. R. Savinova, *J. Phys. Chem. C*, 2016, **120**, 15930–15940.
- 95 A. Y. Klyushin, T. C. R. Rocha, M. Hävecker, A. Knop-Gericke and R. Schlögl, *Phys. Chem. Chem. Phys.*, 2014, **16**, 7881–6.
- 96 E. J. Mittemeijer, *Fundamentals of Materials Science: The Microstructure-Property Relationship*, Springer, Berlin, 2010.
- 97 M. Grunze, *J. Vac. Sci. Technol. A Vacuum, Surfaces, Film.*, 1986, **4**, 2396.
- 98 G. Hähner, *Chem. Soc. Rev.*, 2006, **35**, 1244–1255.
- 99 J. Stöhr, *NEXAFS Spectroscopy*, Springer Science & Business Media, Berlin, Illustrate., 2003.
- 100 M. Born and R. Oppenheimer, *Ann. Phys.*, 1927, **20**, 457–484.
- 101 W. Kohn and L. J. Sham, *Phys. Rev.*, 1965, **140**, A1133–A1138.
- 102 J. P. Perdew, *Phys. Rev. B*, 1986, **33**, 8822–8824.
- 103 J. Perdew, J. Chevary, S. Vosko, K. Jackson, M. Pederson, D. Singh and C. Fiolhais, *Phys. Rev. B*, 1993, **48**, 4978–4978.
- 104 A. D. Becke, *J. Chem. Phys.*, 1992, **96**, 2155–2160.
- 105 E. I. Proynov, E. Ruiz, A. Vela and S. D. R., *Int. J. Quantum Chem.*, 1995, **56**, 61–78.
- 106 B. Hammer, K. W. Jacobsen and J. K. Nørskov, *Phys. Rev. Lett.*, 1993, **70**, 3971–3974.
- 107 P. H. T. Philipsen, G. te Velde and E. J. Baerends, *Chem. Phys. Lett.*, 1994, **226**, 583–588.
- 108 B. Hammer and M. Scheffler, *Phys. Rev. Lett.*, 1995, **74**, 3487–3490.

- 109 D. R. Hamann, *Phys. Rev. Lett.*, 1996, **76**, 660.
- 110 J. P. Perdew, K. Burke and M. Ernzerhof, *Phys. Rev. Lett.*, 1996, **77**, 3865–3868.
- 111 M. D. Segall, P. J. D. Lindan, M. J. Probert, C. J. Pickard, P. J. Hasnip, S. J. Clark and M. C. Payne, *J. Phys. Condens. Matter*, 2002, **14**, 2717–2744.
- 112 S. J. Clark, M. D. Segall, C. J. Pickard, P. J. Hasnip, M. I. J. Probert, K. Refson and M. C. Payne, *Z. Krist.*, 2005, **220**, 567–570.
- 113 M. C. Payne, M. P. Teter, D. C. Allan, T. A. Arias and J. D. Joannopoulos, *Rev. Mod. Phys.*, 1992, **64**, 1045–1097.
- 114 N. W. Ashcroft and N. D. Mermin, *Solid State Physics*, Holt Saunders, Philadelphia, 1976.



## Chapter 2. Imidazole based corrosion inhibitors



## 2.1. Introduction

As explained in Chapter 1, nitrogenated heterocyclic organic compounds like imidazole (IMH) and benzimidazole (BIH) are good corrosion inhibitors.<sup>1-7</sup> It is known that compounds containing both sulfur and nitrogen atoms have greater inhibitive properties,<sup>5,8,9</sup> in particular 2-mercaptobenzimidazole (MBIH<sub>2</sub>), which is a nitrogen and sulfur based compound known to be a corrosion inhibitor for copper<sup>10,11</sup> and steel.<sup>5,6,12-16</sup> Even though it was thought that sulfur containing corrosion inhibitors acted by forming an insoluble compound on the surface,<sup>17,18</sup> more recent work suggests that the compound is chemisorbed on the surface through the sulfur atom.<sup>13,15,16,19</sup>

The aim of this chapter is to get a better understanding about the metal-inhibitor interaction for this type of corrosion inhibitor in order to understand its inhibitive mechanism. To do this, the model compounds approach (Chapter 1) has been applied to the ligands MBIH<sub>2</sub>, IMH and BIH and their binding modes have been studied. In addition, theoretical calculations of the binding modes of MBIH<sub>2</sub> have been done to allow a better assignment of the bands in the spectra.

MBIH<sub>2</sub> can adopt two different electronic configurations according to the stabilising effect of a surrounding medium. The sulfur atom is bound to the carbon atom through a single bond in the thiol form and through a double bond in the thione; this affects the hybridisation of the nitrogen atoms. In the thione configuration both nitrogen atoms are equivalent and have a sp<sup>3</sup> hybridisation while in the thiol they have a different electronic configuration.

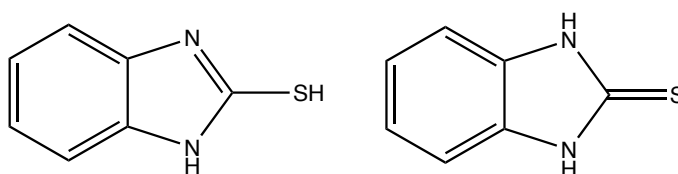


Figure 2.1. Possible electronic configurations of MBIH<sub>2</sub>, thiol (left) and thione (right).

When MBIH<sub>2</sub> acts as a ligand in a coordination compound it has a great variety of possible binding modes as it can bind to metal atoms only through the sulfur, only through the nitrogen or through both, depending on the nature of the metallic atom.

According to Pearson and Songstad's theory<sup>20</sup> a hard base like nitrogen will have more affinity to bind to different metallic atoms than sulfur that is considered a soft base and so the binding mode is expected to be different for different transition metals.

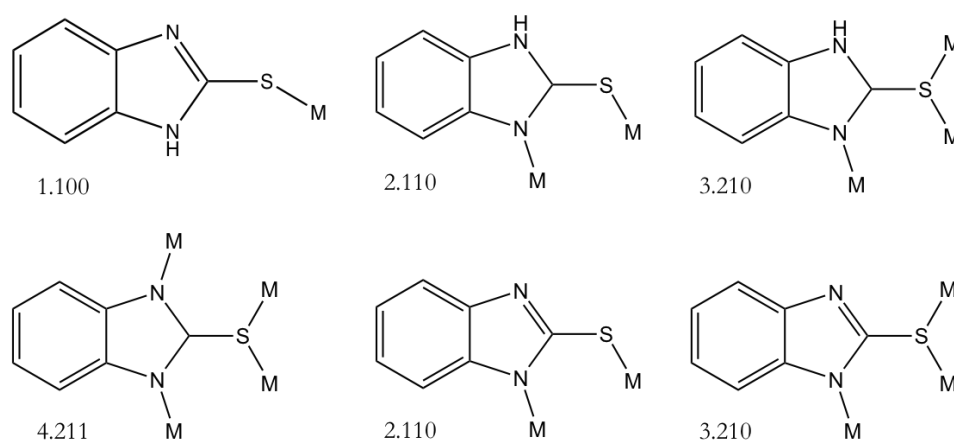


Figure 2.2. Some of the possible binding modes for partially deprotonated MBIH<sub>2</sub> (top) and completely deprotonated MBIH<sub>2</sub> (bottom) labelled according to Harris notation.<sup>21</sup>

It is intended to create a model to easily predict and identify the binding modes of MBIH<sub>2</sub> without the need to determine the X-ray structure of the compounds. For this reason some novel compounds have been synthesised as well as some taken from the literature to study their infrared spectra. In addition to that the IR data available for all the published compounds containing this ligand have been compiled and studied.

To try to understand how MBIH<sub>2</sub> inhibits corrosion it is important to know how it binds to metallic surfaces and, even though it is not expected to bind only through the nitrogen atoms, it is not easy to predict if it will bind only through the sulfur or if it would have a more complicated binding mode. For this reason sum frequency generation (SFG) of MBIH<sub>2</sub> has been performed, firstly on a gold surface as it is inert to atmospheric oxidation and makes the study and understanding of the system easier, and then on steel. Density functional theory (DFT) calculations in the solid state have been carried out to allow a better assignment of the vibrational modes.

## 2.2. Model compounds

Two novel iron compounds have been synthesised with BIH and IMH as well as a novel copper compound with MBIH<sub>2</sub>. Here the synthesis of previously reported MBIH<sub>2</sub> compounds is also presented, to study their infrared spectra. The experimental details are shown below.

### 2.2.1. Experimental

Reagents were purchased from Aldrich and used without further purification. All solvents were from Fisher Scientific and Sigma Aldrich and were used without further purification.

Analytical data were obtained by the Microanalytical Service at the University of Manchester. Carbon, nitrogen, phosphorus and hydrogen analysis was performed using a Flas 200 elemental analyser. Metal analysis was performed by Thermo iCap 6300 Inductively Coupled Plasma Optical Emission Spectroscopy (ICP-OES).

Raman spectra were recorded with a HORIBA T64000 Raman Spectrometer in the Photon Science Institute at the University of Manchester.

IR spectra of neat powders were recorded using a Thermo Scientific Nicolet iS5 FTIR spectrometer equipped with an iD5 ATR. The penetration depth of the beam is directly proportional to the wavelength of the incident beam, which means that photons with higher wavenumbers penetrate the sample less than photons with lower wavenumbers. This causes attenuation on the intensity of the peaks on the left hand side of the spectra.

X-ray data were collected in-house on a SuperNova, single source at offset Atlas diffractometer. Using Olex2,<sup>22</sup> the structure was solved with the Superflip<sup>23</sup> structure solution program using Charge Flipping and refined with the ShelXL<sup>24</sup> refinement package using Least Squares minimisation.

**[Fe(IMH)<sub>4</sub>Cl<sub>2</sub>]Cl (1):** A solution of FeCl<sub>3</sub> (0.30 g, 1.85 mmol), NaOMe (0.10 g, 1.85 mmol) and IMH (0.13 g, 1.85 mmol) in MeCN (9 mL) was heated in a Teflon-lined autoclave at 100 °C for 12 h under autogenous pressure. Cooling to room temperature at a rate of 0.05 °C/min gave a yellow solution and a brown precipitate and small red crystals. The crystals were separated from the precipitate by repeated washing and decanting with cold MeCN. Elemental analysis, calculated (%) for C<sub>12</sub>H<sub>16</sub>Cl<sub>3</sub>FeN<sub>8</sub>: C 33.17, H 3.71, Cl 24.48, N 25.79; found: C 33.02, H 3.83, Cl 25.37, N 26.25. ATR-FTIR  $\nu/\text{cm}^{-1}$ : 3129 (m), 3065 (m), 2950 (m), 2825 (m), 2624 (m), 1576 (m), 1535 (m), 1484 (m), 1406 (m), 1323 (m), 1244 (m), 1159 (m), 1103 (m), 1057 (s), 943 (m), 842 (m, br), 753 (s, br), 631 (s) 613 (s).

**[Fe<sub>3</sub>O(HCO<sub>2</sub>)<sub>6</sub>(BIH)<sub>3</sub>]Cl (2):** A solution of FeCl<sub>3</sub> (0.30 g, 1.85 mmol), NaOMe (0.10 g, 1.85 mmol) and BIH (0.22 g, 1.85 mmol) in MeCN (9 mL) was heated in a Teflon-lined autoclave at 100 °C for 12 h under autogenous pressure. Cooling to room temperature at a rate of 0.05 °C/min gave a brown powder, which was dissolved in DMF. MeCN was allowed to diffuse into the orange filtrate at room temperature for a week giving red crystals. Elemental analysis calculated (%) for C<sub>27</sub>H<sub>24</sub>ClFe<sub>3</sub>N<sub>6</sub>O<sub>13</sub>: C 38.45, H 2.87, Cl 4.20, N 9.96; found: C 38.23, H 2.94, Cl 4.35, N 10.02. ATR-FTIR  $\nu/\text{cm}^{-1}$ : 3067(br, w), 2976 (br, w), 2826 (br, w), 1607 (s), 1491 (m), 1446 (w), 1423 (w), 1367 (s), 1303 (m), 1268 (m), 1250 (m), 1155 (w), 1132 (w), 1111 (w), 1007 (w), 967 (m), 934 (w), 886 (w), 827 (br, w), 746 (s), 573 (br, m). Raman  $\nu/\text{cm}^{-1}$ : 441 (m), 562 (br, m), 634 (m), 765 (m), 778 (m), 888 (m), 973 (w), 1011 (s), 1116 (m), 1160 (br, m), 1255 (s), 1272 (m), 1307 (m), 1353 (s), 1426 (br, w), 1502 (s).

**[Cu(MBIH<sub>2</sub>)(dppp)]Cl (3):** A mixture of CuCl (0.049 g, 0.5 mmol) and 1,3-bis(diphenylphosphino)propane (dppp) (0.206 g, 0.5 mmol) were stirred in MeCN (20 mL) for 30 min. To this was added a solution of MBIH<sub>2</sub> (0.075 g, 0.5 mmol) in MeOH (15 mL) and stirred for 2 h. The resulting clear solution was filtered and left undisturbed, after 2 d clear crystals suitable for X-ray diffraction were collected. Elemental analysis calculated (%) for C<sub>34</sub>H<sub>32</sub>ClCuN<sub>2</sub>P<sub>2</sub>S: C 61.72, H 4.87, Cl 5.36, N 4.23, P 9.36; found: C 60.94, H 4.79, Cl 5.56, N 4.35, P 9.47. ATR-FTIR  $\nu/\text{cm}^{-1}$ : 3064 (w, br),

2964 (w, br), 2857 (w, br), 1619 (m), 1505 (m), 1456 (s), 1407 (w), 1361 (w), 1345 (w), 1259 (m), 1218 (w), 1182 (m), 1090 (w, br), 1011 (w, br), 896 (w), 797 (m), 731 (s), 618 (m), 596 (m).

**[Au<sub>2</sub>(dppp)Cl<sub>2</sub>] (4):** A solution of dppp (0.089 g, 0.215 mmol) in acetone (15 mL) was added to a suspension of [AuCl(SMe)<sub>2</sub>] (0.127 g, 0.430 mmol) in acetone (15 mL). After stirring the resulting mixture for 2 h a white precipitate was filtered, washed with acetone, diethyl ether and dried under vacuum.<sup>25,26</sup> Elemental analysis calculated (%) for C<sub>27</sub>H<sub>26</sub>Au<sub>2</sub>Cl<sub>2</sub>P<sub>2</sub>: C 36.97, H 2.99, Cl 8.08, P 7.06; found: C 37.42, H 2.98, Cl 8.42, P 6.85. ATR-FTIR  $\nu/\text{cm}^{-1}$ : 3050 (w), 1709 (w), 1482 (m), 1434 (s), 1405 (w), 1384 (w), 1184 (w), 1158 (w), 1128 (w), 1104 (s), 998 (w), 983 (m), 940 (m), 837 (m), 742 (s), 690 (s), 669 (m).

**[Au<sub>2</sub>(dppp)(MBIH)<sub>2</sub>] · 2CF<sub>3</sub>CO<sub>2</sub>H (5):** To a solution of **4** (310 mg, 0.35 mmol) in CH<sub>2</sub>Cl<sub>2</sub> (15 mL) was added AgCF<sub>3</sub>CO<sub>2</sub> (156 mg, 0.71 mmol), and the reaction mixture was stirred at room temperature for 30 min. The suspension was filtered through celite to remove the AgCl precipitate, and added into a suspension of 2-mercaptobenzimidazole (MBIH<sub>2</sub>) (160 mg, 0.71 mmol) in CH<sub>2</sub>Cl<sub>2</sub> (15 mL). The reaction mixture was stirred for 2 h at room temperature. The resulting solution was concentrated to 5 mL, and the addition of Et<sub>2</sub>O (75 mL) gave an off-white precipitate that was collected by filtration and washed with Et<sub>2</sub>O.<sup>26</sup> Elemental analysis, calculated (%) for C<sub>41</sub>H<sub>36</sub>N<sub>4</sub>P<sub>2</sub>S<sub>2</sub>Au<sub>2</sub> · 2CF<sub>3</sub>CO<sub>2</sub>H: C 40.55, H 2.87, N 4.20, S 4.81; found: C 40.52, H 2.90, N 4.13, S 4.87. ATR-FTIR  $\nu/\text{cm}^{-1}$ : 3055 (w, br), 2820 (w, br), 1662 (s, br), 1515 (m, br), 1459 (m), 1436 (m), 1414 (m), 1350 (w), 1278 (w), 1177 (s, br), 1127 (s), 1104 (s), 1027 (w), 999 (w), 968 (w), 827 (m), 797 (m), 741 (s), 717 (m), 690 (s), 618 (m), 599 (m).

**[Zn<sub>4</sub>O<sub>4</sub>(MBIH)<sub>6</sub>] · 3MeOH (6):** A mixture of Zn(MeCO<sub>2</sub>)<sub>2</sub> · 2H<sub>2</sub>O (0.0385 g, 0.175 mmol) and MBIH<sub>2</sub> (0.0392 g, 0.26 mmol) in water (3.5 mL) and methanol (3.5 mL) was sealed in a Teflon-lined stainless steel reactor and heated for three days at 120 °C. After slowly cooling the sample to room temperature at a rate of 0.05 °C/min yellow crystals were collected after 2 days.<sup>27</sup> Elemental analysis, calculated (%) for

$C_{45}H_{42}N_{12}O_4S_6Zn_4$ : C 42.60, H 3.34, N 13.25, S 15.26; found: C 43.07, H 3.27, N 13.20, S 15.23. ATR-FTIR  $\nu/cm^{-1}$ : 3392 (w), 1490 (w), 1412 (s), 1376 (s), 1348 (s), 1296 (m), 1272 (m), 1223 (m), 1168 (m), 1168 (w), 1147 (w), 1017 (w), 1000 (m), 932 (w), 903 (w), 815 (w), 739 (s), 696 (w), 606 (m).

Compounds  $[SbBr_2(MBIH_2)_4]Br \cdot H_2O^{28}$  (7),  $[SbCl_2(MBIH_2)_4]Cl \cdot 2H_2O \cdot MeOH^{29}$  (8),  $[SbCl_2(MBIH_2)_4]Cl \cdot 3H_2O \cdot MeCN^{29}$  (9),  $[SbCl_3(MBIH_2)_2]^{29}$  (10),  $[N(CH_2CH_3)_4][Cu_3(MBI)_2]^{27}$  (11),  $[N(CH_3)(CH_2CH_3)_3][Cu_6(MBIH)_6]Cl_2^{27}$  (12),  $[Fe_2(MBIH)_2(NO)_4]^{30}$  (13) and  $[Ni_2(MBIH)_4]_2[NiCl_2(MBIH_2)_2(MeCN)_2]^{31}$  (14) were not synthesised but, their IR data that was previously reported is reviewed.

### 2.2.2. Imidazoline compounds

Compounds **1** and **2** were easily synthesised under solvothermal conditions, Figure 2.3 shows their single crystal X-ray structure. Compound **1** is a monometallic compound that crystallizes in an orthorhombic system in which the iron atom has a slightly distorted octahedral geometry. There are four monodentate imidazole ligands bound to the metallic atom, chlorine atoms occupy the two remaining trans coordination positions.

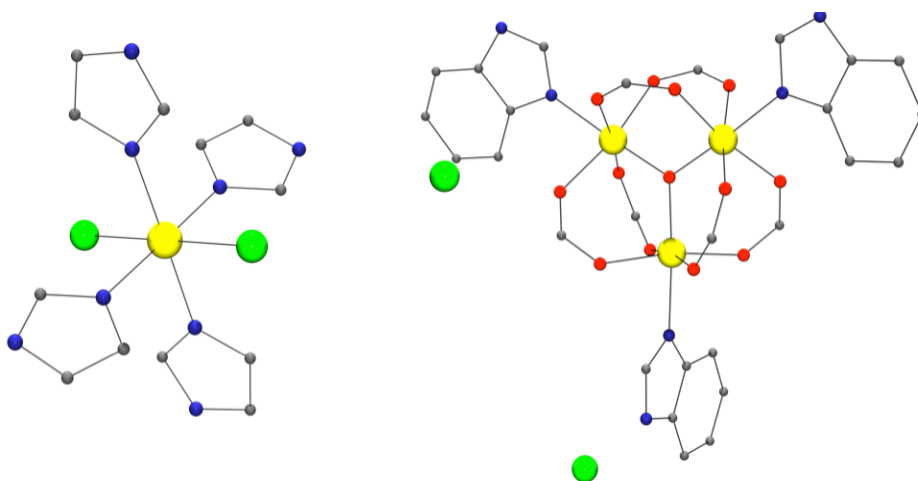


Figure 2.3. Single crystal X-ray structure for compounds **1** (left) and **2** (right). Colours: C, grey; N, blue; O, red; Cl, green and Fe, yellow. Hydrogen atoms omitted for clarity.

Figure 2.4 shows the IR spectra for compounds **1** and **2** (black) and their pure ligands (red). The single crystal X-ray data suggests that the imidazole ligands are protonated, this is supported by the presence of the broad band at high frequency in the infrared spectra due to the N-H bond vibration, that would not be present in case the ligand was completely deprotonated.

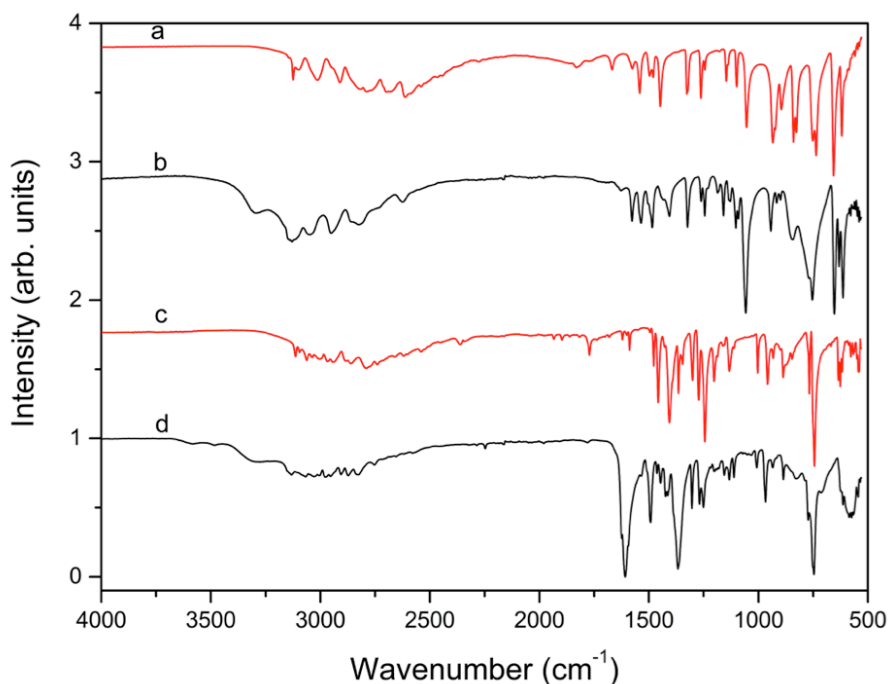


Figure 2.4. ATR-FTIR spectra for IMH (a), compound **1** (b), BIH (c) and compound **2** (d).

Compound **2** has a similar structure to the mixed-valent iron triangle compounds previously reported by Timco *et al.*<sup>32,33</sup> The novel compound reported here consists in a planar oxocentred iron triangle with six formate groups bridging the metallic atoms. Each iron atom is hexacoordinated and bound to four oxygen atoms from the formate groups, one  $\mu_3$ -O atom and one nitrogen atom from the benzimidazole. The later ligand is acting as monodentate and, even though the reaction was carried out under basic conditions, it remains protonated (see high frequency region in the IR spectrum in Figure 2.4). It is believed that traces of formate anions were formed in situ by hydrogenation of CO<sub>2</sub> present in the air catalysed by iron following the mechanism suggested in Figure 2.5. Even though most catalysts for this hydrogenation are

expensive compounds of noble metals such as ruthenium and iridium,<sup>34</sup> some  $\text{Fe}^{2+}$  based catalysts have been recently reported.<sup>35-41</sup>

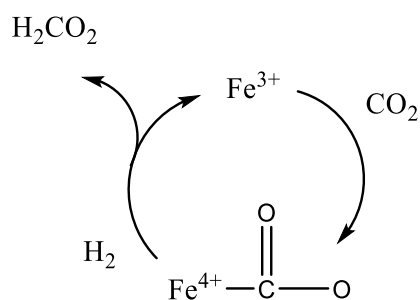


Figure 2.5. Suggested mechanism for the hydrogenation of  $\text{CO}_2$ .

Raman spectra of the crystalline powders have been recorded. Figure 2.6 shows the Raman spectra for compounds **1** and **2** (black) and the pure ligands (red). Compound **2** shows the appearance of the Fe-N bond stretching band at low frequencies ( $560\text{ cm}^{-1}$ ). The bands corresponding to the N-H bond bending ( $619$  and  $1412\text{ cm}^{-1}$ ) are still present in the compound spectrum it remains protonated.

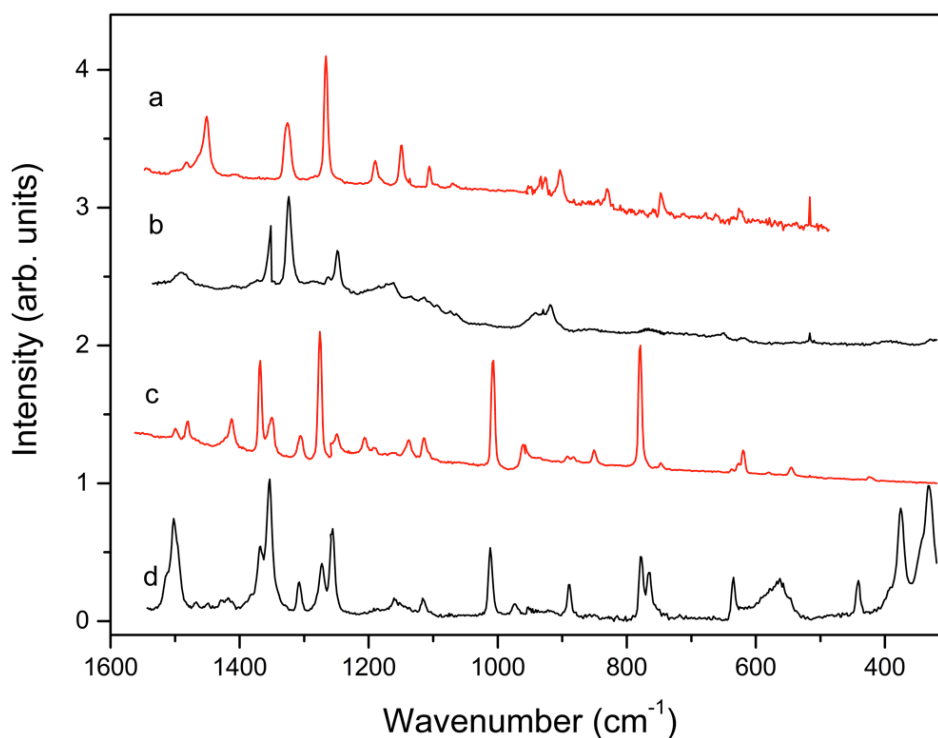


Figure 2.6. Raman spectra for BIH (a), compound **1** (b), IMH (c) and **2** (d).

### 2.2.3. 2-Mercaptobenzimidazole

The same reaction followed to synthesise compounds **1** and **2** was carried out with  $\text{MBIH}_2$  but no compound could be isolated suggesting that this ligand needs different conditions to react with a metallic cation and form a compound. The sulfur atom has an ideal position in the ligand for coordination creating steric impediment to the nitrogen atoms making it less favourable for them to coordinate. According to Pearson and Songstad's theory a soft electron-efficient like sulfur does not have much affinity to bind to a hard electron-deficient metal like iron.<sup>20</sup> Aldoshin *et al.* succeeded in synthesising a dimetallic  $\text{Fe}^{2+}$  compound with  $\text{MBIH}_2$  by reacting it with  $\text{Fe}^{2+}$  in presence of nitrogen monoxide.<sup>30</sup> In the compound both iron atoms are held together by bridging  $\text{MBIH}$  (partially deprotonated) with a binding mode 2.110 (Figure 2.2). Compound **3** crystallises in a monoclinic system and it is a novel compound. In this monometallic compound the copper atom has a distorted tetrahedral geometry and it is bound to two phosphorus atoms from the phosphine, a sulfur atom from the imidazoline ligand and a chlorine atom.  $\text{MBIH}_2$  is fully protonated and displays a 1.100 binding mode.

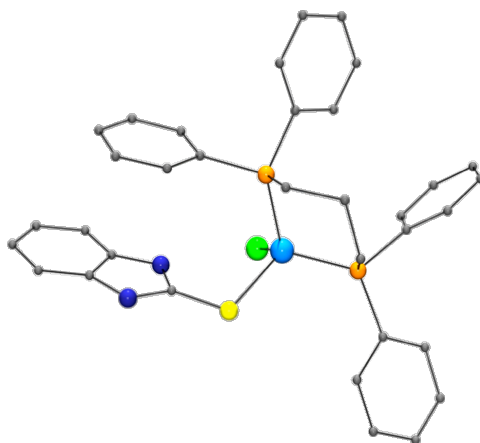


Figure 2.7. Single crystal X-ray structure for compound **3**. Colours: C, grey; N, dark blue; S, yellow; Cu, light blue; P, orange and Cl, green. Hydrogen atoms omitted for clarity.

Compounds **5** and **6** were synthesised as previously reported<sup>26,27</sup> to study the vibrational spectra and identifying fingerprints for the different binding modes. Their single crystal X-ray structures weren't determined, but their purity was checked by elemental analysis

and infrared spectroscopy. In compound **5** (Figure 2.8) both gold atoms have a linear coordination and are held together by the bridging bis(phenylphosphino)propane (dppp). The imidazoline ligand is partially deprotonated and bound to the gold atom through the sulphur with a 1.100 binding mode. The nitrogen atom is still protonated and it participates in an hydrogen bond with the  $\text{CF}_3\text{CO}_2$  anion with a separation distance between the nitrogen and the oxygen atoms of 2.761(7) Å.

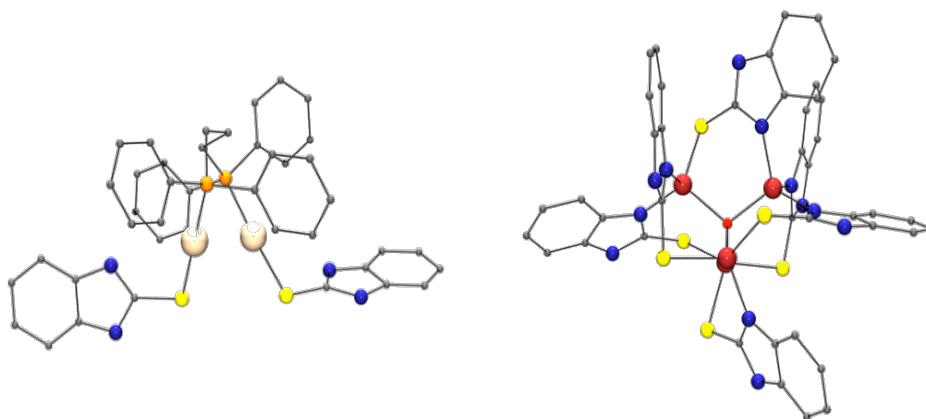


Figure 2.8. Single crystal X-ray structure for compounds **5** (left) and **6** (right). Colours: C, grey; N, blue; O, red; S, yellow; P, orange; Au, cream and Zn, pink. Hydrogen atoms and  $\text{CF}_3\text{CO}_2$  anion omitted for clarity.

Compound **6** consists in four zinc atoms (one of the zinc atom is eclipse by another one in figure 2.8) held together by a central oxygen atom forming a distorted tetrahedron. All imidazoline ligands are partially deprotonated and have the binding mode 2.110. All zinc atoms have a tetrahedral coordination, all presenting different coordination environments. One is coordinated to three sulfur atoms from different ligands and the centred oxo anion; another one is bound to two sulfur atoms, one nitrogen atom all different ligands and the oxo; the third zinc is bound to one sulfur and two nitrogen from different ligands and the oxo and the fourth zinc is bound to three nitrogen from different ligands and the oxo.

Table 2.1. Thioamide bands for MBIH<sub>2</sub> and compounds **3**, **5** and **6**.

|                   |              | Thioamide bands (cm <sup>-1</sup> ) |      |      |      |     |
|-------------------|--------------|-------------------------------------|------|------|------|-----|
|                   | Binding mode | N-H                                 | I    | II   | III  | IV  |
| MBIH <sub>2</sub> | -            | 3148, 3111                          | 1509 | 1339 | 1016 | 735 |
| <b>3</b>          | <b>1.100</b> | 3064                                | 1505 | 1345 | 1011 | 731 |
| <b>5</b>          | <b>1.100</b> | 3055                                | 1515 | 1350 | 1027 | 741 |
| <b>6</b>          | <b>2.110</b> | 3392                                | 1490 | 1348 | 1017 | 739 |

MBIH<sub>2</sub> has two possible electronic configurations (see Section 2.1), thione and thiol, the former being the most stable in the solid state. For this reason, in the ATR-FTIR of the pure ligand the S-H bond stretch (expected at *ca.* 2500 cm<sup>-1</sup>) is not present. This band is not going to appear in the compound spectra either as in all the cases the sulfur atom is deprotonated and bound to a metallic atom. A more detailed study of the pure ligand can be found in Section 2.4 where some DFPT calculations are presented. It is well known that thioamide ligands have four characteristic bands known as ‘thioamide bands’ at ~1500, 1300, 1000 and 800 cm<sup>-1</sup>, which have previously been assigned.<sup>42,43</sup> Band I has contributions of  $\delta$ N-H,  $\delta$ C-H and  $\nu$ C=N; band II is a mixed band with contributions from  $\nu$ C-N,  $\delta$ N-H,  $\delta$ C-H and  $\nu$ C=S; band III has contributions from  $\nu$ C-N and  $\nu$ C-S and band IV is mainly from the C-S bond. The behaviour and changes these bands suffer when forming a coordination compound can be used to determine the nature of bonding in the metal complexes.<sup>42,43</sup>

Figure 2.9 shows the IR spectra for compounds **3**, **5** and **6** as well as for the pure ligand, the assignments of the bands are presented in Table 2.1. In the spectra of all the compounds as well as in the pure ligand the N-H stretching band is present as in all cases there is, at least, one nitrogen atom protonated. When the binding is only through the sulfur this band shifts to lower frequencies whilst when the ligand is partially deprotonated it suffers a big blue shift. This indicates that the N-H band could have important information about the binding mode of the ligand.

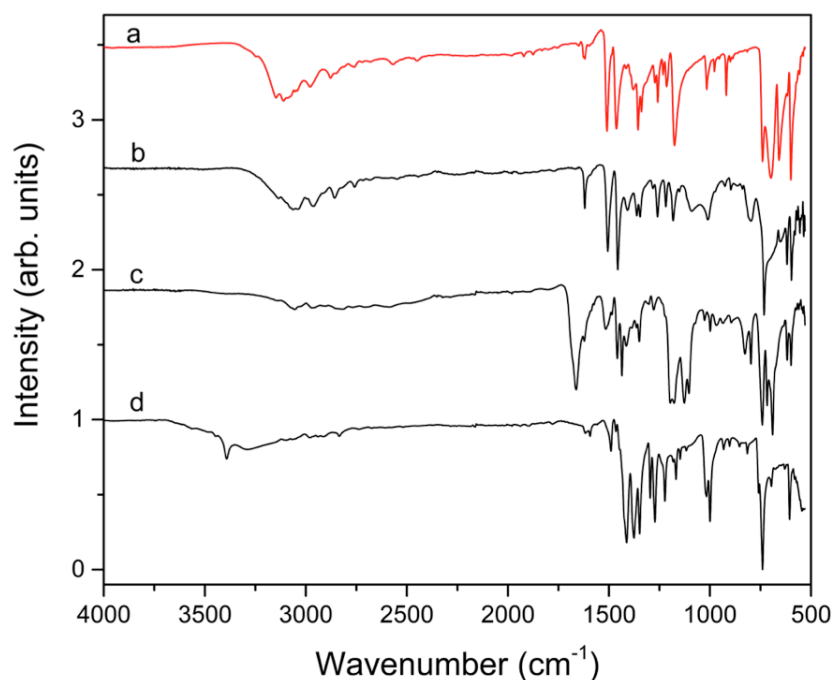


Figure 2.9. ATR-FTIR spectra of MBIH<sub>2</sub> (a), compound **3** (b), **5** (c) and **6** (d).

The IR data for all the compounds with MBIH<sub>2</sub> that have their spectroscopic data published have been studied and the assignment of the bands done, see Table 2.2. In compounds **7**,<sup>28</sup> **8**, **9** and **10**<sup>29</sup> the ligand is fully protonated and bound to the antimony atoms only through the sulfur, binding mode 1.100.

Compound **11** consists on a 2-D network where trimetallic units are repeated. There are two equivalent coppers with two different coordination environments. The imidazoline ligand is fully deprotonated and it shows the 4.211 binding mode. In compound **12** all copper atoms are equivalent, bound to one nitrogen atom and two sulfur atoms from three ligands with distorted trigonal planar coordination geometry. The ligand in this compound is partially deprotonated and shows a 3.210 binding mode.

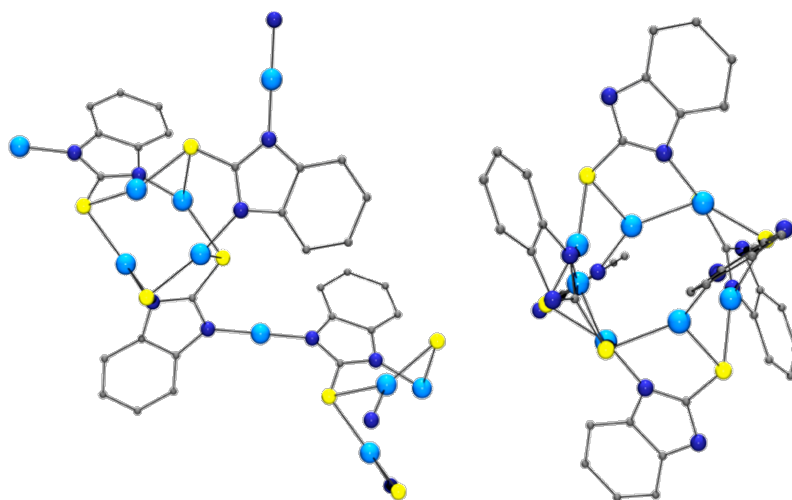


Figure 2.10. Single crystal X-ray structures for compounds **11** (left) and **12** (right). Colours: C, grey; N, blue; S, yellow; Cu and light blue. Hydrogen atoms omitted for clarity.

Compound **13** is dimetallic, the iron atoms are held together by two bridging MBIH with a 2.110 binding mode. The metal atoms have a distorted tetrahedral geometry and two coordinated nitrogen monoxide molecules complete the coordination sphere. Compound **14** is formed exclusively by two nickel atoms and four MBIH ligands with a 2.110 binding mode.

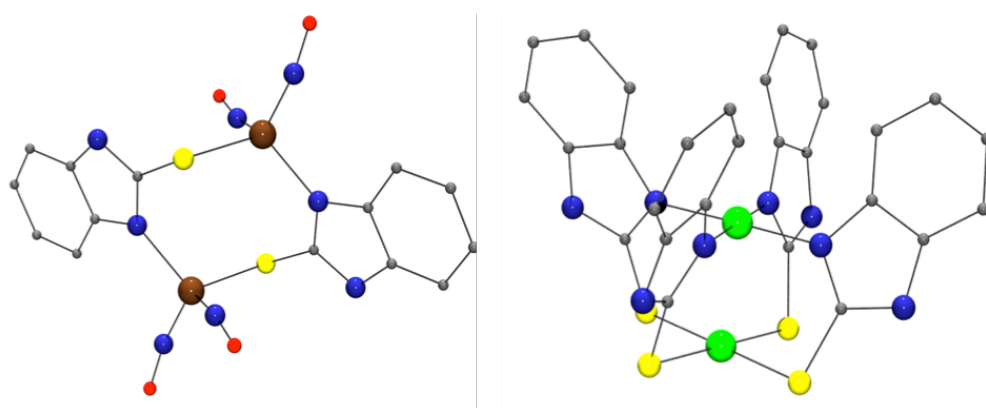


Figure 2.11. Single crystal X-ray structure for compounds **13** (left) and **14** (right). Colours: C, grey; N, blue; O, red; S, yellow; Fe, brown and Ni, green. Hydrogen atoms omitted for clarity.

From the spectroscopic data of these compounds it can be seen how the frequency of certain vibrational modes shifts depending on the binding mode. Band I does not

depend on any vibrational mode involving sulfur and so when the binding is just through sulfur this band does not have a significant change compared to the free ligand. However when the binding is through both nitrogen and sulfur there is a red shift of about 30-70  $\text{cm}^{-1}$  due to the coordination of the nitrogen to the metallic atom; this change can be seen in compounds **11**, **12**, **13** and **14**. Band II is a combination of C-N and C=S stretches and N-H and C-H bending modes. As this band is more complicated and it has different contributions it is not easy to predict and to understand its behaviour. Experimental data suggest that for all binding modes it suffers a small blue shift in comparison to the free ligand. However, this band, like band I, does not provide any information about the binding mode. The biggest change in this band can be seen for compounds **11** and **12**, in which the sulfur is bound to two metallic atoms and for which there is a bigger shift of the band.

Table 2.2. Assignment of thioamide bands for compounds found in the literature.

|                         |              | Thioamide bands ( $\text{cm}^{-1}$ ) |      |      |      |     |
|-------------------------|--------------|--------------------------------------|------|------|------|-----|
|                         | Binding mode | N-H                                  | I    | II   | III  | IV  |
| <b>MBIH<sub>2</sub></b> | -            | 3148, 3111                           | 1509 | 1339 | 1016 | 735 |
| <b>7<sup>28</sup></b>   | <b>1.100</b> | 3069                                 | 1491 | 1347 | 1007 | 751 |
| <b>8<sup>29</sup></b>   | <b>1.100</b> | 3064                                 | 1492 | 1348 | 1011 | 753 |
| <b>9<sup>29</sup></b>   | <b>1.100</b> | 3069                                 | 1498 | 1349 | 1007 | 746 |
| <b>10<sup>29</sup></b>  | <b>1.100</b> | 3098                                 | 1508 | 1346 | 1013 | 739 |
| <b>11<sup>27</sup></b>  | <b>4.211</b> | -                                    | 1455 | 1370 | 1002 | 742 |
| <b>12<sup>27</sup></b>  | <b>3.210</b> | 3445                                 | 1424 | 1350 | 1007 | 755 |
| <b>13<sup>30</sup></b>  | <b>2.110</b> | 3207                                 | 1467 | 1384 | 1002 | 742 |
| <b>14<sup>31</sup></b>  | <b>2.110</b> | 3244                                 | 1492 | 1348 | 1004 | 756 |

Band III has dependence on both nitrogen and sulfur and it suffers, in both cases, a small red shift that it is slight bigger when the ligand is bound through sulfur and nitrogen.

The biggest change is seen in the N-H bond stretching, which when the binding is through sulfur has a red shift of about  $100\text{ cm}^{-1}$  and, when the binding is also through the nitrogen, there is a blue shift of about  $250\text{ cm}^{-1}$ . The band is not present when there is not a protonated nitrogen atom like in the binding mode 4.211. This band depends on the mode and it is present in the region used in SFG so it can be used as a diagnosed agent for the binding mode of  $\text{MBIH}_2$  on a surface.

## 2.3. Vibrational Sum Frequency Generation

As explained in Chapter 1, SFG is a technique that allows the study of molecules at an interface. In this section solid-gas and solid-liquid interfaces have been explored. The collection, fitting and interpretation of the data was done in collaboration with Dr Dimitri Chekulaev as part of the BP-ICAM project. A first experiment was carried out using a gold surface because it does not corrode in air and it makes the system more simple and easier to understand. The gold surface was cleaned under sonication and was dipped into solutions of  $\text{MBIH}_2$  in ethanol of different concentrations (10 mM and 25 mM) and dried under a  $\text{N}_2$  flow. The ex situ spectrum was collected at both  $t \approx 0.33$  and 1 ps in the region where the  $\text{Csp}^2\text{-H}$  stretches are expected to appear (between  $2800$  and  $3200\text{ cm}^{-1}$ ). A delay in the visible pulse is applied in order to eliminate the non-resonant background in the spectra. In the spectra (Figure 2.12) there is a clear peak that appears at  $3070\text{ cm}^{-1}$  assigned to the  $\text{Csp}^2\text{-H}$  bond vibration. An inconvenience of looking at such a narrow region is that N-H and C-H bond vibrations cannot be studied at the same time, which might lead to a wrong assignment of the peak. In order to confirm the assignment of the peak theoretical calculations (Section 2.4) of the IR active vibrational modes for both  $\text{MBIH}_2$  and  $\text{MBID}_2$  have been done and will be in more detail in Section 2.4. The signal at  $2970\text{ cm}^{-1}$  is assigned to the  $\text{Csp}^3\text{-H}$  vibration of the adsorbed ethanol on the surface.

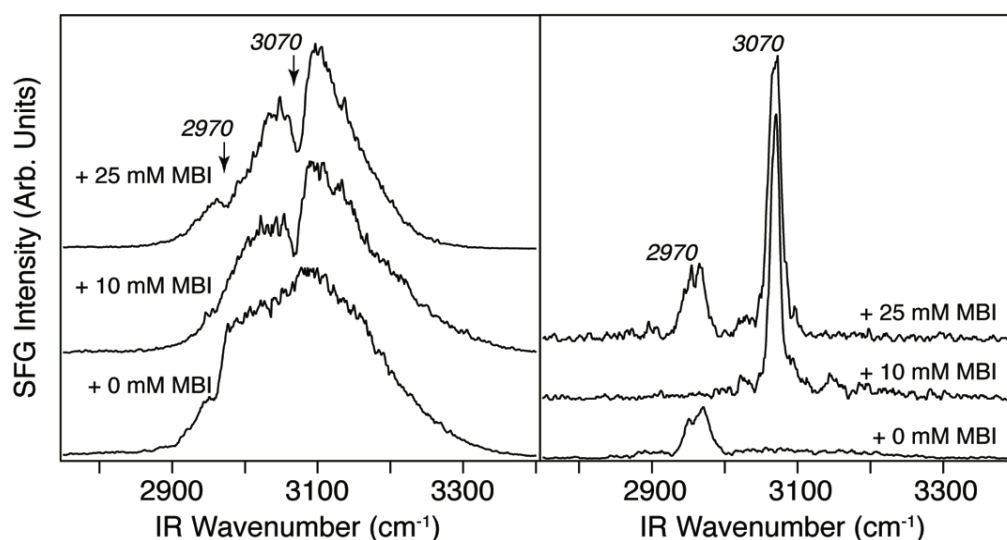


Figure 2.12. SFG spectra of MBIH<sub>2</sub> 10 mM, 25 mM in ethanol and pure ethanol acquired with  $t \approx 0.33$  ps (left) and  $t \approx 1$  ps (right).

SFG data were also collected for a solid-liquid interface using a liquid cell for a 25 mM solution of MBIH<sub>2</sub> in ethanol at  $t \approx 0.33$  ps. Figure 2.13 compares the in situ spectrum with the equivalent ex situ spectrum. Besides a decrease in the signal to noise there is no major change and both Csp<sup>2</sup>-H from MBIH<sub>2</sub> and Csp<sup>3</sup>-H from the ethanol can be observed suggesting that the compound interacts with the gold surface in the same way in the solid state and in solution.

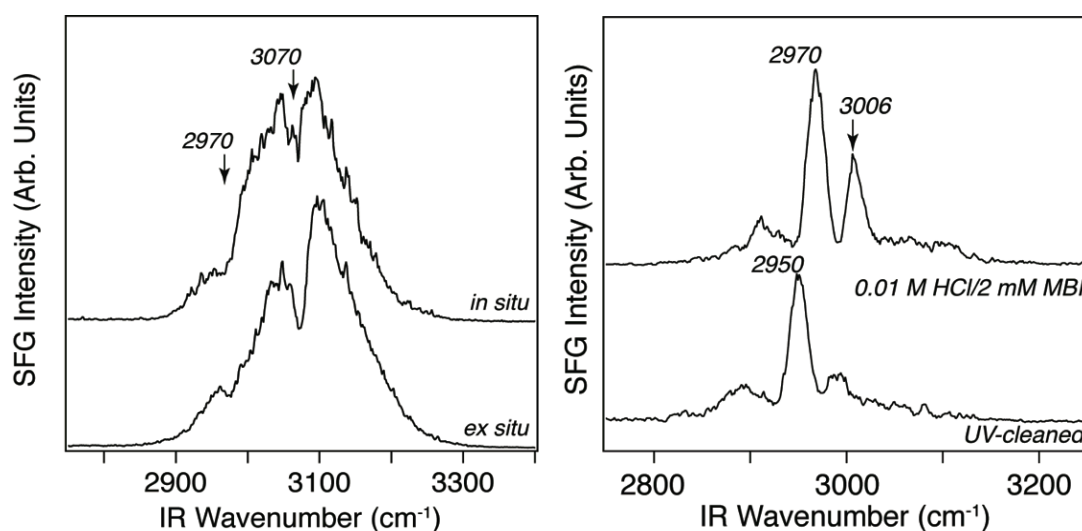


Figure 2.13. SFG in situ and ex situ spectra of MBIH<sub>2</sub> 25 mM in ethanol acquired with  $t \approx 0.33$  ps (left) and SFG ex situ spectra of clean steel and exposed to 0.01 M HCl/2 mM MBIH<sub>2</sub> acquired with  $t \approx 0.8$  ps (right).

Following the measurements on the Au surface, similar work was done on an X65 steel substrate. In this case, MBIH<sub>2</sub> was added to a 0.01 M HCl aqueous solution to address the issue of corrosion inhibition in acidic solution. It has been previously reported that a 2 mM solution of MBIH<sub>2</sub> in 0.01 M HCl inhibits the corrosion of carbon steel in a 93%.<sup>16</sup> The metallic surface was polished and cleaned with UV light, immersed in a 0.01 M HCl/2 mM MBIH<sub>2</sub> aqueous solution for 4 h and then dried under a N<sub>2</sub> flow. Figure 2.13 shows the recorded spectra at  $t \approx 0.8$  ps for the clean steel surface and the one exposed to the inhibitor. The resonances at 2950 and 2970 cm<sup>-1</sup> are assigned to adventitious carbon from atmospheric contamination and the one at 3006 cm<sup>-1</sup> to the Csp<sup>2</sup>-H vibration from MBIH<sub>2</sub>. There is a significant shift of the peak from the gold surface to the steel surface, which might indicate a change in the local binding environment. SFG spectra for two different surfaces show a small red shift for the N-H bond stretching suggesting that the MBIH<sub>2</sub> binds to the metallic surface only through the sulfur atom.

Unfortunately the experimental set up does not allow study of the low frequency region of the spectrum, so there is no possibility to study the thioamide bands or the S-H bond-stretching region.

## 2.4. Density functional theory

### 2.4.1. Experimental

Calculation of the vibrational modes was first attempted using the Gaussian package,<sup>44</sup> which calculates the vibrational modes of isolated molecules in the gas phase and so the assignments at high wavenumbers are not reliable. Subsequently calculations were performed using the CASTEP<sup>45,46</sup> code, which allows to calculate properties of solids using a plane-wave pseudopotential method. Calculations were done with exchange and correlation effects described by the generalized gradient approximation (GGA) of Perdew-Burke-Ernzerhof<sup>47</sup> (PBE) and a cut off energy of 600 eV.

A geometry optimisation is needed in order to eliminate stress forces in the solid state before the calculation of the vibrational modes can be done, Figure 2.14 shows the packing on the solid state for this compound. The calculation was performed using the experimental X-ray structure coordinates of  $\text{MBIH}_2$ ,<sup>48</sup> which in the solid state is in the thione tautomeric form, as a starting structure.

For the deuteration experiment,  $\text{MBIH}_2$  was deuterated by stirring the compound in deuterated ethanol with 2 drops of DCl for 5 days and then crystallised by slow evaporation of the solvent in air. The calculation was done using the same X-ray structure of  $\text{MBIH}_2$ ,<sup>48</sup> but this time exchanging the hydrogen atoms for deuterium and using the same calculation setup and parameters used for the previous experiment.

## 2.4.2. Results and discussion

In order to better understand the behaviour of  $\text{MBIH}_2$  and to facilitate the assignment of the bands on the SFG experiment, theoretical calculations of the vibrational modes have been done to simulate the solid state IR spectrum.

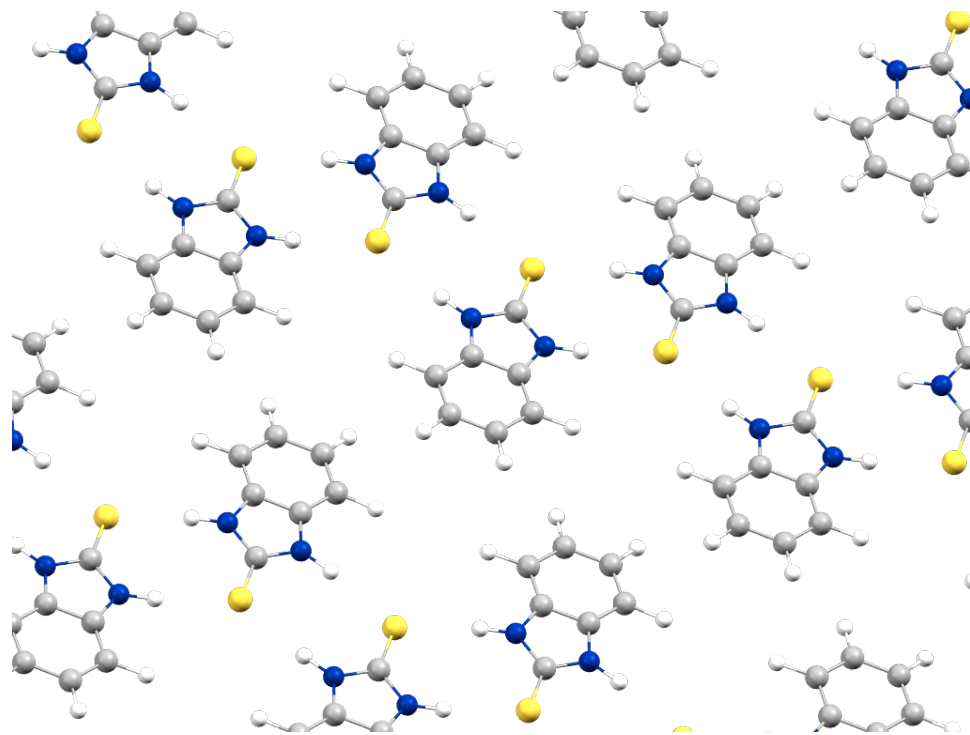


Figure 2.14. Optimised geometry calculated for  $\text{MBIH}_2$ . Colours: C, grey; N, blue; S, yellow.

Figure 2.16 shows the experimental (black) and simulated (red) IR spectra for MBIH<sub>2</sub> showing a very good agreement between the calculated and experimental spectra. The CASTEP code is very accurate calculating the intensity of the peaks, but it calculates them as a single point, meaning that the spectrum has to be manually broadened in order for it to have a more realistic appearance. Plotting the experimental versus the calculated vibrational frequencies is a good way to check the agreement between the calculated and experimental vibrational frequencies. Figure 2.16 confirms the calculation method used is very accurate and reliable.

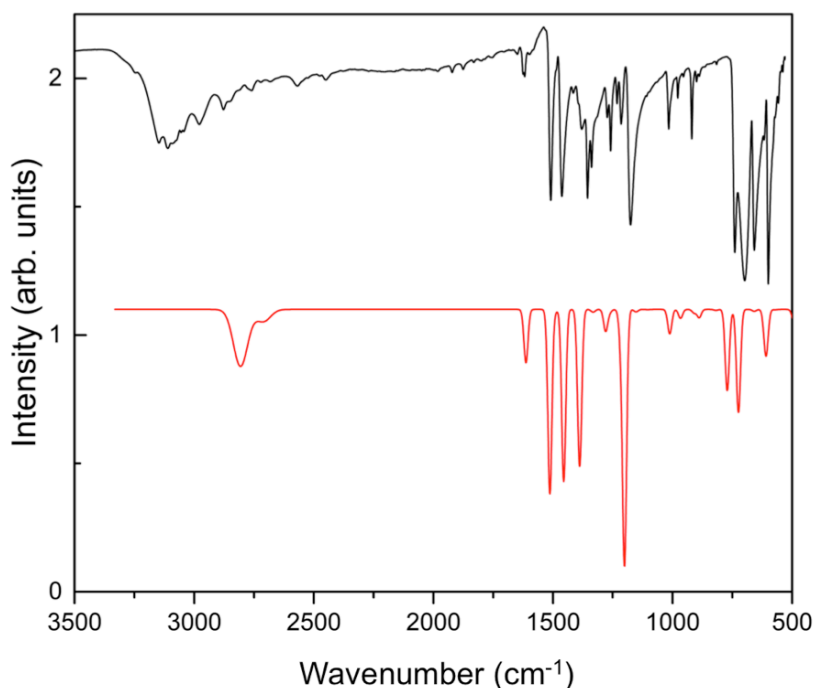


Figure 2.16. Experimental (black) and simulated (red) IR spectra for MBIH<sub>2</sub>.

Table 2.3 shows the calculated and experimental vibrational frequencies and the assignment of the bands. There are some discrepancies between the assignments from these calculations and the empirical assignments from the literature.

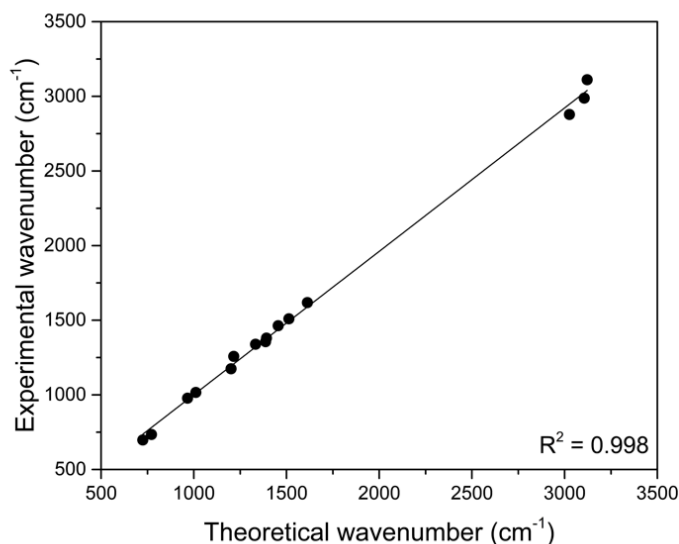


Figure 2.17. Experimental vs. simulated IR frequencies for MBIH<sub>2</sub>.

According to these the C-C stretch also contributes to the thioamide band I, but this does not change the model compounds assignment. Band II has mainly contribution of the N-H bond stretch and the calculations do not show the C-S bond stretch contribution, anyway this band does not have much information of the binding mode of the ligand in the model compounds. The biggest discrepancy is on band IV as according to the calculations it is due to the ring bending and not to a combination to the C-N and C-S bond stretches which might explain why this band does not change following the coordination of the ligand, as would be expected from the reported data found in the literature.

It can be noticed that the agreement between the experimental and the simulated vibrational frequencies is not as good at high frequencies where the C-H and N-H bond vibrations happen. This might be because in the experimental spectra these bands are usually broad due to hydrogen bonding and humidity effects, which are not taken into account in the calculation.

Table 2.3. Experimental and calculated vibrational frequencies and assignment from calculations for MBIH<sub>2</sub>. Symbols:  $\nu$  stretching,  $\delta$  bending,  $\beta$  in plane bending and  $\gamma$  out of plane bending.

| Experimental cm <sup>-1</sup> | Theoretical cm <sup>-1</sup> | Assignment                  |
|-------------------------------|------------------------------|-----------------------------|
| 3111                          | 3122                         | $\nu$ N-H                   |
| 2988                          | 3106                         | $\nu$ C-H                   |
| 2878                          | 3026                         | $\nu$ N-H                   |
| 2568                          | -                            | -                           |
| 1618                          | 1613                         | $\nu$ C-C + $\nu$ C-N       |
| 1509                          | 1513                         | <b>Band I</b>               |
| 1463                          | 1455                         | $\nu$ C-C                   |
| 1380                          | 1392                         | $\delta$ C-H + $\delta$ N-H |
| 1356                          | 1387                         | $\nu$ C-C                   |
| 1339                          | 1333                         | <b>Band II</b>              |
| 1258                          | 1215                         | $\delta$ C-H + $\nu$ C-N    |
| 1215                          | -                            | -                           |
| 1175                          | 1201                         | $\delta$ N-H                |
| 1016                          | 1011                         | <b>Band III</b>             |
| 978                           | 966                          | $\beta$ ring                |
| 735                           | 772                          | <b>Band IV</b>              |
| 698                           | 725                          | $\gamma$ C-H                |

The C-H and N-H bonds vibrate at a similar frequency and for this reason sometimes it can be difficult to assign them. This becomes a bigger problem in the SFG spectra where only a very narrow region of the spectrum is collected. Deuterating the labile hydrogen atoms of organic compounds can assist on the assignment of C-H and N-H bands. For very polar bonds such as N-H or COOH groups the hydrogen atom is easily exchanged by simply stirring the solution in a deuterated solvent for as long as necessary. To get the same exchange for more stable bonds such as C-H it is necessary

to synthesise the compounds from scratch with simpler deuterated compounds. For compounds like  $\text{MBIH}_2$  that have both C-H and N-H bonds deuteration experiments are extremely useful as this will affect to the vibrations involving nitrogen atoms but not carbon.<sup>49</sup> The energy of the vibrations of a bond depends both on the strength of the bond and the molar mass of the atoms and so a shift to lower frequency is to be expected following deuteration.

Figure 2.18 shows the experimental and simulated IR spectra for deuterated  $\text{MBIH}_2$  ( $\text{MBID}_2$ ) and calculated the theoretical vibrational modes (Figure 2.17).

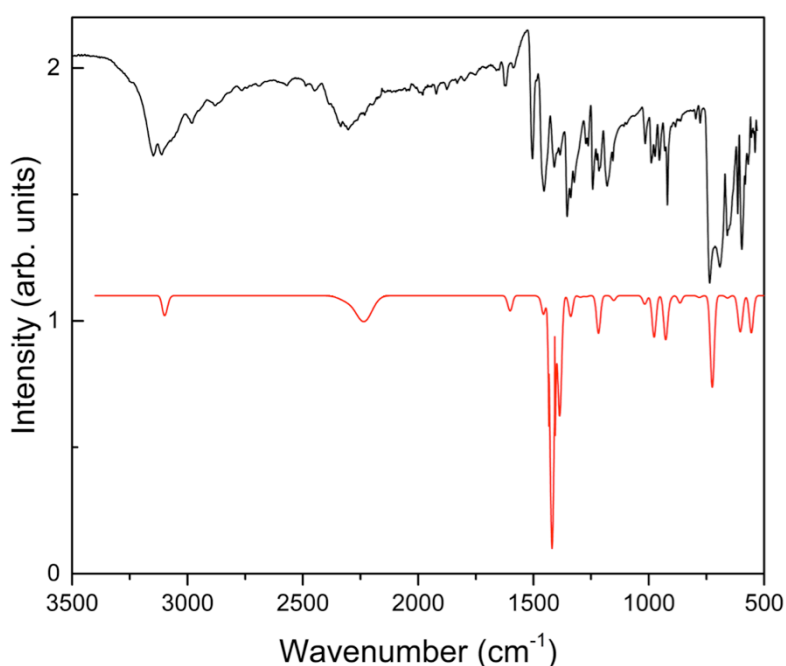


Figure 2.18. Experimental (black) and simulated (red) IR spectra for  $\text{MBID}_2$ .

Again there is good agreement between the experimental and the calculated frequencies for the vibrational modes (Figure 2.18). The assignment of the bands in this case is more complicated as the calculation was done for 100% deuterated  $\text{MBID}_2$  while in the experiment there is non-deuterated compound left causing some discrepancies on the agreement.

Table 2.4. Experimental and calculated vibrational frequencies and assignment for MBID<sub>2</sub>. Symbols:  $\nu$  stretching,  $\delta$  bending,  $\beta$  in plane bending and  $\gamma$  out of plane bending.

| Experimental cm <sup>-1</sup> | Theoretical cm <sup>-1</sup> | Assignment  |
|-------------------------------|------------------------------|---|
| 3148                          | 3106                         | $\nu$ C-H   |
| 3111                          | 3102                         | $\nu$ C-H   |
| 2981                          | 3091                         | $\nu$ C-H   |
| 2336                          | 2309                         | $\nu$ N-D <sub>sym</sub>                            |
| 2303                          | 2235                         | $\nu$ N-D <sub>asym</sub>                           |
| 1620                          | 1609                         | $\nu$ C-C + $\nu$ C-N                               |
| -                             | 1599                         | $\nu$ C-C   |
| 1505                          | 1475                         | $\nu$ C-C + $\delta$ C-H + $\nu$ C-N                |
| 1454                          | 1457                         | $\nu$ C-C + $\delta$ C-H + $\nu$ C-N                |
| 1410                          | 1420                         | $\nu$ C-N   |
| 1354                          | 1387                         | $\beta$ ring  |
| 1338                          | 1339                         | $\beta$ ring  |
| 1215                          | 1218                         | $\beta$ ring  |
| 1180                          | 1152                         | $\delta$ C-H  |
| 1015                          | 1014                         | $\nu$ C-C + $\delta$ C-H + $\delta$ N-H + $\nu$ C-N |
| 989                           | 977                          | $\beta$ ring  |
| 919                           | 927                          | $\delta$ C-N  |

The experimental IR spectrum (black) shows the expected shift of the N-D stretch band, which is also reflected in the simulated (red) spectrum. The experimental N-D vibrations (2236 and 2303 cm<sup>-1</sup>) are comparable with the calculated ones (2309 and 2235 cm<sup>-1</sup>), again proving the reliability of the calculation method used.

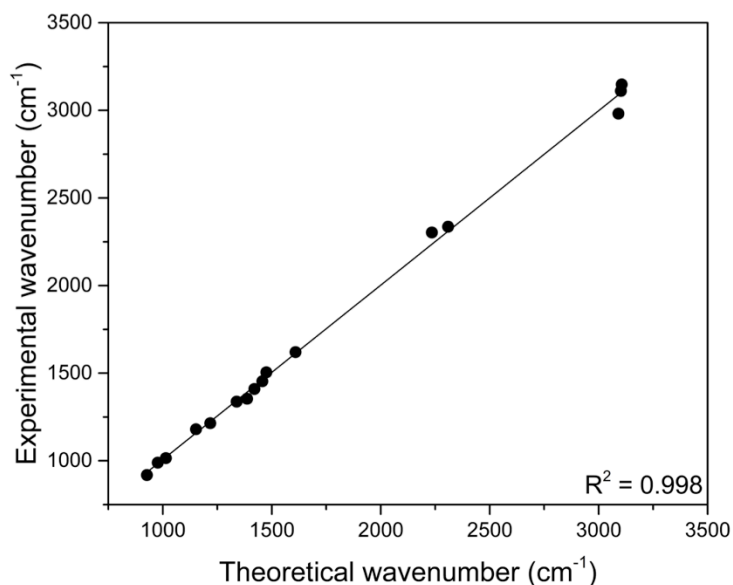


Figure 2.18. Experimental vs. simulated IR frequencies for MBID<sub>2</sub>.

There are other changes in the spectra following deuteration in the C-N stretch region, as the vibrational modes involving the nitrogen atom will also be affected for the isotopic mass of deuterium.

As a following experiment, the intention was to perform SFG on the prepared deuterated sample of MBID<sub>2</sub> used to do the ATR-FTIR. A preliminary study in which the data were very noisy showed no change in the resonance of the peak. Even though this was not further studied, the lack of a change in the spectra suggested that the assignment was done correctly in the first place and the peak seen at 3070 cm<sup>-1</sup> is caused by the Csp<sup>2</sup>-H bond vibration.

## 2.5. Conclusions

Three novel compounds have been synthesised with IMH, BIH and MBIH<sub>2</sub> and have been characterised by X-ray crystallography and IR and Raman spectroscopies. The model compounds synthesised with IMH and BIH show a preference of these ligands to remain protonated and act as a monodentate ligand in a coordination compound. Even though no fingertips have been found for their binding modes the presence of the N-H bond stretch on the IR and Raman spectra has confirmed the monodentate binding mode.

The assignment for the established thioamide bands has been done for a group of compounds with the corrosion inhibitor MBIH<sub>2</sub> in which it shows different binding modes. Even though bands II, III and IV do not provide much information on the binding mode of the ligand, band I shows a red shift when the binding is through both the nitrogen and sulfur atoms. The band that provides more information of the binding mode is the N-H bond stretching, which suffers a small red shift when the binding is only through sulfur and a big blue shift when the binding is through nitrogen and sulfur.

The SFG spectra on the N-H bond stretching region proves that MBIH<sub>2</sub> binds to gold and steel surfaces. According to what it has been seen from the model compounds' infrared spectra the vibration frequency of the band suggests a bond through the sulfur atom for both surfaces.

However, there is some variation on the vibration frequency suggesting that the binding is different for the different surfaces, which is not that surprising as the metallic surfaces have very different properties and so a given compound is expected to interact with it in a different way.

Theoretical calculations have been successfully performed in the solid state in order to facilitate the assignments of the IR frequencies, showing a very good agreement with the experimental data and facilitating the assignment of the peaks in the narrow region

on the SFG spectra. The calculation method has been proven to be very reliable even when making changes in the molecule, i.e. deuteration.

## 2.6. References

- 1 E. Stupnišek-Lisac, A. Gazivoda and M. Madžarac, *Electrochim. Acta*, 2002, **47**, 4189–4194.
- 2 D. Q. Zhang, L. X. Gao and G. D. Zhou, *Corros. Sci.*, 2004, **46**, 3031–3040.
- 3 M. Christov and A. Popova, *Corros. Sci.*, 2004, **46**, 1613–1620.
- 4 K. F. Khaled and M. A. Amin, *J. Appl. Electrochem.*, 2009, **39**, 2553–2568.
- 5 J. Aljourani, M. A. Golozar and K. Raeissi, *Mater. Chem. Phys.*, 2010, **121**, 320–325.
- 6 M. Benabdellah, A. Tounsi, K. F. Khaled and B. Hammouti, *Arab. J. Chem.*, 2011, **4**, 17–24.
- 7 M. Yadav, P. N. Yadav and U. Sharma, *Indian J. Chem. Technol.*, 2013, **20**, 363–370.
- 8 O. Benali, L. Larabi, M. Traisnel, L. Gengembre and Y. Harek, *Appl. Surf. Sci.*, 2007, **253**, 6130–6139.
- 9 Y. Abboud, A. Abourriche, T. Saffaj, M. Berrada, M. Charrouf, A. Bennamara, N. Al Himidi and H. Hannache, *Mater. Chem. Phys.*, 2007, **105**, 1–5.
- 10 M. M. Musiani and G. Mengoli, *J. Electroanal. Chem.*, 1987, **217**, 187–202.
- 11 T. Shahrabi, H. Tavakholi and M. G. Hosseini, *Anti-Corrosion Methods Mater.*, 2007, **54**, 308–313.
- 12 A. Popova, M. Christov, S. Raicheva and E. Sokolova, *Corros. Sci.*, 2004, **46**, 1333–1350.

- 13 J. Aljourani, K. Raeissi and M. A. Golozar, *Corros. Sci.*, 2009, **51**, 1836–1843.
- 14 M. Mahdavian and S. Ashhari, *Electrochim. Acta*, 2010, **55**, 1720–1724.
- 15 P. Morales-Gil, M. S. Walczak, R. A. Cottis, J. M. Romero and R. Lindsay, *Corros. Sci.*, 2014, **85**, 109–114.
- 16 P. Morales-Gil, M. S. Walczak, C. R. Camargo, R. A. Cottis, J. M. Romero and R. Lindsay, *Corros. Sci.*, 2015, **101**, 47–55.
- 17 M. Ohsawa and I. Science, *Corros. Sci.*, 1979, **19**, 709–722.
- 18 C. W. Yan, H. C. Lin and C. N. Cao, *Electrochim. Acta*, 2000, **45**, 2815–2821.
- 19 R. Tremont, H. De Jesús-Cardona, J. García-Orozco, R. J. Castro and C. R. Cabrera, *J. Appl. Electrochem.*, 2000, **30**, 737–743.
- 20 R. G. Pearson and J. Songstad, *J. Am. Chem. Soc.*, 1967, **89**, 1827–1836.
- 21 R. A. Coxall, S. G. Harris, D. K. Henderson, S. Parsons, P. A. Tasker and R. E. P. Winpenny, *J. Chem. Soc. Dalt. Trans.*, 2000, 2349–2356.
- 22 O. V. Dolomanov, L. J. Bourhis, R. J. Gildea, J. A. K. Howard and H. Puschmann, *J. Appl. Crystallogr.*, 2009, **42**, 339–341.
- 23 L. Palatinus and G. Chapuis, *J. Appl. Crystallogr.*, 2007, **40**, 786–790.
- 24 G. M. Sheldrick, *Acta Crystallogr. Sect. A, Found. Crystallogr.*, 2008, **64**, 112–122.
- 25 H. Schmidbaur, A. Wohlleben, F. Wagner, O. Orama and G. Huttner, *Chem. Ber.*, 1977, **110**, 1748–1754.
- 26 M.-C. Brandys, M. C. Jennings and R. J. Puddephatt, *J. Chem. Soc., Dalt. Trans.*, 2000, 4601–4606.
- 27 S. C. Chen, R. M. Yu, Z. G. Zhao, S. M. Chen, Q. S. Zhang, X. Y. Wu, F. Wang and C. Z. Lu, *Cryst. Growth Des.*, 2010, **10**, 1155–1160.
- 28 I. I. Ozturk, S. K. Hadjidakou, N. Hadjiliadis, N. Kourkoumelis, M. Kubicki, A.

- J. Tasiopoulos, H. Scliman, M. M. Barsan, I. S. Butler and J. Balzarini, *Inorg. Chem.*, 2009, **48**, 2233–2245.
- 29 I. I. Ozturk, S. K. Hadjikakou, N. Hadjiliadis, N. Kourkoumelis, M. Kubicki, M. Baril, I. S. Butler and J. Baizarini, *Inorg. Chem.*, 2007, **46**, 8652–8661.
- 30 N. Sanina, T. Roudneva, G. Shilov, R. Morgunov, N. Ovanesyanyan and S. Aldoshin, *Dalton Trans.*, 2009, 1703–1706.
- 31 M. E. Nikiforova, M. O. Talismanova, G. G. Aleksandrov, S. K. Kotovskaya, A. Sidorov, V. M. Novotortsev, V. N. Ikorskii, V. N. Charushin, I. L. Eremenko and I. I. Moiseev, *Russ. Chem. Bull., Int. Ed.*, 2006, **55**, 2181–2186.
- 32 J. Overgård, E. Rentschler, G. A. Timco, N. V. Gerbeleu, V. Arion, A. Bousseksou, J. P. Tuchagues and F. K. Larsen, *J. Chem. Soc. Dalton Trans.*, 2002, 2981–2986.
- 33 J. Overgård, E. Rentschler, G. A. Timco and F. K. Larsen, *ChemPhysChem*, 2004, **10**, 1755 – 1761.
- 34 W. H. Wang, Y. Himeda, J. T. Muckerman, G. F. Manbeck and E. Fujita, *Chem. Rev.*, 2015, **115**, 12936–12973.
- 35 C. Federsel, A. Boddien, R. Jackstell, R. Jennerjahn, P. J. Dyson, R. Scopelliti, G. Laurenczy and M. Beller, *Angew. Chemie Int. Ed.*, 2010, **49**, 9777–9780.
- 36 R. Langer, Y. Diskin-Posner, G. Leitus, L. J. W. Shimon, Y. Ben-David and D. Milstein, *Angew. Chemie Int. Ed.*, 2011, **50**, 9948–9952.
- 37 C. Ziebart, C. Federsel, P. Anbarasan, W. Baumann, A. Spannenberg, M. Beller and R. Jackstell, *J. Am. Chem. Soc.*, 2012, 20701–20704.
- 38 Y. Zhang, A. D. MacIntosh, J. L. Wong, E. A. Bielinski, P. G. Williard, B. Q. Mercado, N. Hazari and W. H. Bernskoetter, *Chem. Sci.*, 2015, **6**, 4291–4299.
- 39 O. Rivada-Wheelaghan, A. Dauth, G. Leitus, Y. Diskin-Posner and D. Milstein, *Inorg. Chem.*, 2015, **54**, 4526–4538.

- 40 F. Bertini, I. Mellone, A. Ienco, M. Peruzzini and L. Gonsalvi, *ACS Catal.*, 2015, **5**, 1254–1265.
- 41 F. Bertini, N. Gorgas, B. Stöger, M. Peruzzini, L. F. Veiros, K. Kirchner and L. Gonsalvi, *ACS Catal.*, 2016, 2889–2893.
- 42 B. Singht and K. P. Thakur, *J. Inorg. Nucl. Chem.*, 1974, **36**, 1735–1737.
- 43 B. Singh, M. M. P. Rukhaiyar and R. J. Sinha, *J. Inorg. Nucl. Chem.*, 1977, **39**, 29–32.
- 44 M. J. Frisch, G. W. Trucks, H. B. Schlegel, G. E. Scuseria, M. A. Robb, J. R. Cheeseman, G. Scalmani, V. Barone, B. Mennucci, G. A. Petersson, H. Nakatsuji, M. Caricato, X. Li, H. P. Hratchian, A. F. Izmaylov, J. Bloino, G. Zheng, J. L. Sonnenberg, M. Hada, M. Ehara, K. Toyota, R. Fukuda, J. Hasegawa, M. Ishida, T. Nakajima, Y. Honda, O. Kitao, H. Nakai, T. Vreven, J. J. A. Montgomery, J. E. Peralta, F. Ogliaro, M. Bearpark, J. J. Heyd, E. Brothers, K. N. Kudin, V. N. Staroverov, R. Kobayashi, J. Normand, K. Raghavachari, A. Rendell, J. C. Burant, S. S. Iyengar, J. Tomasi, M. Cossi, N. Rega, J. M. Millam, M. Klene, J. E. Knox, J. B. Cross, V. Bakken, C. Adamo, J. Jaramillo, R. Gomperts, R. E. Stratmann, O. Yazyev, A. J. Austin, R. Cammi, C. Pomelli, J. W. Ochterski, R. L. Martin, K. Morokuma, V. G. Zakrzewski, G. A. Voth, P. Salvador, J. J. Dannenberg, S. Dapprich, A. D. Daniels, Ö. Farkas, J. B. Foresman, J. V. Ortiz, J. Cioslowski and D. J. Fox, 2009, Inc. Gaussian, Wallingford, CT.
- 45 M. D. Segall, P. J. D. Lindan, M. J. Probert, C. J. Pickard, P. J. Hasnip, S. J. Clark and M. C. Payne, *J. Phys. Condens. Matter*, 2002, **14**, 2717–2744.
- 46 S. J. Clark, M. D. Segall, C. J. Pickard, P. J. Hasnip, M. I. J. Probert, K. Refson and M. C. Payne, *Z. Krist.*, 2005, **220**, 567–570.
- 47 J. P. Perdew, K. Burke and M. Ernzerhof, *Phys. Rev. Lett.*, 1996, **77**, 3865–3868.
- 48 G. R. Form, E. S. Raper and T. C. Downie, *Acta Crystallogr. Sect. B Struct.*

*Crystallogr. Cryst. Chem.*, 1976, **32**, 345–348.

49 F. Billes, H. Endrédi and B. Várady, *Technology*, 2001, 136–144.

# Chapter 3. Benzotriazole for the protection of Fe



### 3.1. Introduction

Organic compounds containing donor atoms and delocalised electrons provide proven examples of organic corrosion inhibitors, see Chapter 1. For these reasons heterocyclic compounds are good candidates as they fulfil both requirements. Benzotriazole (BTAH) and derivatives thereof are well established corrosion inhibitors for copper alloys,<sup>1,2,3</sup> steel<sup>4</sup> and iron surfaces.<sup>5</sup> They have at least three donor atoms and an aromatic ring, which gives the delocalisation of electrons and also surface coverage; for these reasons it was decided to apply the model compound approach to this family of organic molecules.

Copper surfaces are quite stable under atmospheric conditions. But they get corroded in aggressive environments such as the presence of acids or gasses (for example HCl, CO<sub>2</sub>, H<sub>2</sub>S), which happens in industry. Under these conditions alloy surfaces need to be protected to avoid economic loss and possible accidents. BTAH has shown to be an excellent inhibitor under these conditions and so a lot of interest on its mechanism has arisen, although there is controversy about how this organic compound acts.<sup>6</sup> Its mechanism is still not well understood because a large number of processes might take place.

It is well known that BTAH inhibits corrosion by creating a physical barrier.<sup>2</sup> BTAH reacts with the cuprous and cupric ions found in solution as a result of the corrosion forming an insoluble compound in water that precipitates onto the surface providing what is known as passivation in situ.<sup>3</sup> The suggested structure is a Cu<sup>+</sup> polymeric linear compound as shown in Figure 3.1. The structure suggested by Cotton was later confirmed by Poling *et al.*,<sup>7</sup> who also proposed the formation of a thick layer that does not stop at a monolayer level as Cotton suggested.

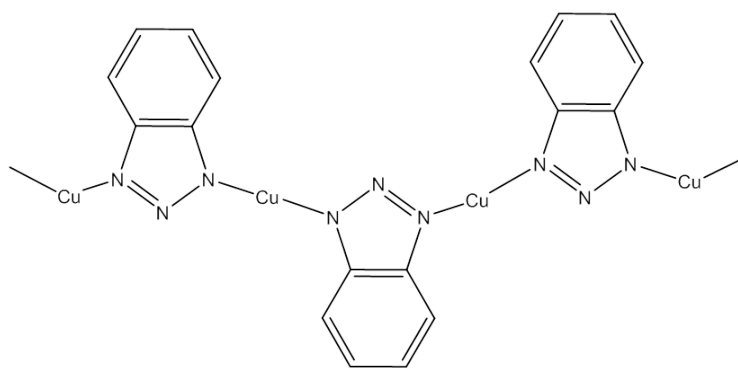


Figure 3.1. Schematic representation of Cu-BTA complex suggested by Cotton and co-workers.<sup>7</sup>

Even though there still is controversy about the exact interaction and thickness of the passivation layer as well as if there are both  $\text{Cu}^+$  and  $\text{Cu}^{2+}$  present, what it is clear is that BTAH reacts with a layer of oxide on the surface and stops further corrosion.<sup>6</sup>

To better understand the chemistry of BTAH and its interaction with copper and other metals several coordination compounds have been synthesised with different metallic cations, such as  $\text{Cu}^{2+}$ ,<sup>8,9,10,11</sup>  $\text{Ni}^{2+}$ ,<sup>12,13</sup>  $\text{Zn}^{2+}$ ,<sup>11,13</sup>  $\text{Hg}^{2+}$ ,<sup>14</sup>  $\text{Re}^{5+}$ ,<sup>15</sup>  $\text{Ag}^+$ ,<sup>16</sup>  $\text{Fe}^{3+}$ ,<sup>17</sup>  $\text{Cr}^{3+}$  and  $\text{V}^{3+}$ .<sup>18</sup>

A lot of work has been done in order to understand the interaction of BTAH with copper, but not much has been reported on iron.<sup>19,20</sup> Tian and co-workers reported a study in which they compared the surface enhanced Raman scattering spectra of iron electrodes submerged in a solution of BTAH and of a pure Fe-BTA complex.<sup>20</sup> From their results they suggested that BTAH binds to the iron surface through two of the N atoms in a similar way that it does with copper, forming an insoluble polymeric complex that protects the surface.

Thus a deeper understanding of the surface chemistry of current inhibitors is essential for the development of new corrosion inhibitors. The focus of this chapter is to understand how BTAH interacts with metals at a molecular scale, by performing a vibrational study of model compounds; and by doing X-ray photoelectron spectroscopy (XPS) of the compound on a single crystal iron surface.

## 3.2. Model compounds

### 3.2.1. Experimental

Reagents were purchased from Aldrich and used without further purification. All solvents were from Fisher Scientific and Sigma Aldrich and were used without further purification.

Analytical data were obtained by the Microanalytical Service at The University of Manchester. Carbon, nitrogen, phosphorus and hydrogen analysis was performed using a Flas 200 elemental analyser. Metal analysis was performed by Thermo iCap 6300 Inductively Coupled Plasma Optical Emission Spectroscopy (ICP-OES).

Raman spectra were recorded with a HORIBA T64000 Raman Spectrometer in the Photon Science Institute at The University of Manchester.

IR spectra of neat powders were recorded using a Thermo Scientific Nicolet iS5 FTIR spectrometer equipped with an iD5 ATR. The penetration depth of the beam is directly proportional to the wavelength of the incident beam, which means that photons with higher wavenumbers penetrate the sample less than photons with lower wavenumbers. This causes attenuation on the intensity of the peaks on the left hand side of the spectra.

**[Fe<sub>3</sub>O(MeCO<sub>2</sub>)<sub>6</sub>(H<sub>2</sub>O)<sub>3</sub>]Cl (15):** FeCl<sub>3</sub> · 6H<sub>2</sub>O (3.24 g, 12 mmol) was dissolved in H<sub>2</sub>O (40 mL), to the brown reaction mixture was added of MeCO<sub>2</sub>Na · 3H<sub>2</sub>O (3.27 g, 24 mmol). The mixture were stirred for *ca.* 30 min and then filtered to leave a dark red solution. Big dark red crystals appeared in a few days.<sup>21</sup>

**[Fe<sub>14</sub>O<sub>6</sub>(BTA)<sub>6</sub>(MeO)<sub>18</sub>Cl<sub>6</sub>] (16):** A solution of **15** (0.30 g, 0.48 mmol) and BTAH (0.17 g, 1.43 mmol) in MeOH (9 mL) was heated in a 15 mL Teflon-lined autoclave at 100 ° C for 12 h under autogenous pressure. Cooling to room temperature at a rate of 0.05 ° C/min gave red crystals and an orange precipitate. The precipitate was separated and discarded. The red crystals were purified by repeated washing and decanting.<sup>17,18</sup>

Elemental analysis calculated (%) for  $\text{Fe}_{14}\text{C}_{54}\text{H}_{78}\text{O}_{24}\text{N}_{18}\text{Cl}_6$ : C 27.51, H 3.3, N 10.69, Fe 33.16, Cl 9.02; found: C 24.48, H 3.16, N 10.09, Fe 33.27, Cl 11.86. ATR-FTIR  $\nu/\text{cm}^{-1}$ : 2923 (br,m), 2820 (m), 1574 (w), 1491 (w), 1443 (m), 1292 (w), 1273 (m), 1221 (s), 1146(w), 1046 (s), 994(m), 926 (w), 786 (s), 755 (s), 642 (m), 586 (br, s). Raman  $\nu/\text{cm}^{-1}$ : 1577 (m), 1496 (w), 1444 (m), 1397 (s), 1381 (s), 1296 (m), 1206 (m), 1150 (m), 1130 (m), 1051 (s), 994 (w), 791 (w), 641 (w), 610 (br, w), 436 (br, m), 396 (br, m), 330 (w).

The same compound was synthesized with the ligands 5-methyl-1*H*-benzotriazole (MeBTAH), 5,6-dimethyl-1*H*-benzotriazole (Me<sub>2</sub>BTAH), 5-chlorobenzotriazole (ClBTAH) and 1*H*-1,2,3-triazole (TZAH) but the results are not described in this section as the spectroscopic data didn't provide any different information.<sup>18</sup> Infrared and Raman spectra can be found in the Appendices.

### 3.2.2. Results and discussion

Benzotriazole has three nitrogen atoms that can bind to metal atoms forming a transition metal compound. Figure 3.2 shows the structure of  $[\text{Fe}_{14}\text{O}_6(\text{BTA})_6(\text{MeO})_{18}\text{Cl}_6]$  derived from single crystal X-ray diffraction and a simplified structure to give a better understanding of the coordination mode. There are fourteen iron atoms and six deprotonated BTAH ligands. The ligand is a mono-anion and all nitrogen atoms are coordinated to metal atoms. The coordination mode of the ligand is 3.111 according to Harris notation.<sup>22</sup> Every nitrogen atom in the ligand binds to one  $\text{Fe}^{3+}$ , which presents a distorted octahedral geometry. Two  $\mu_2$ -methoxides, a  $\mu_4$ -oxide and a chloride complete the coordination spheres.<sup>17,18</sup>

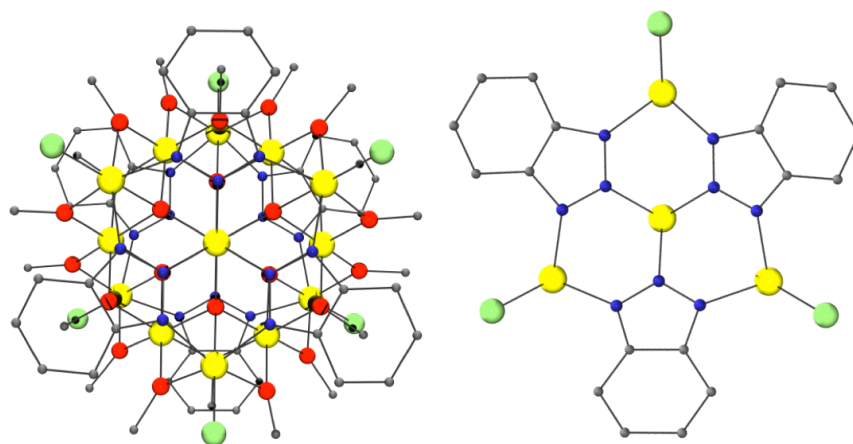


Figure 3.2. Single crystal X-ray structure for compound **16** (left) and a simplified top view (right) to show the binding mode. Colours: C, grey; N, blue; Fe, yellow; Cl, green.

Hydrogen atoms omitted for clarity.

Figure 3.3 shows the Raman spectra of BTAH and  $[\text{Fe}_{14}\text{O}_6(\text{BTA})_6(\text{MeO})_{18}\text{Cl}_6]$ . The first hint that the ligand has bound to the metal is the appearance of bands belonging to the Fe-N bond stretching at *ca.*  $400\text{ cm}^{-1}$ . Surprisingly, the band corresponding to the C-N stretch at  $1390\text{ cm}^{-1}$  for BTAH undergoes a very small shift in the compound due to the bonding ( $1395\text{ cm}^{-1}$ ).

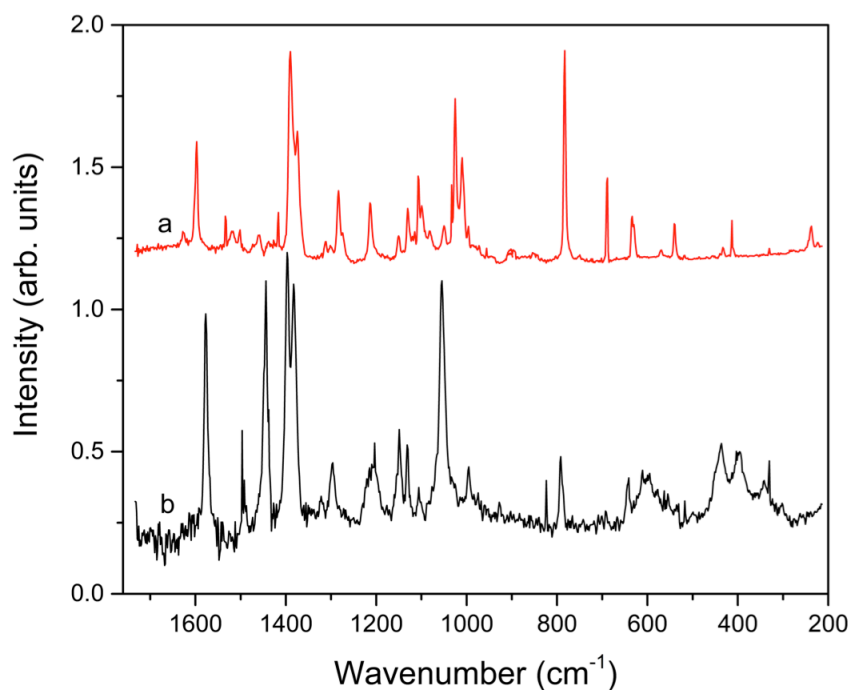


Figure 3.3. Raman spectra for BTAH (a) and compound **16** (b).

The IR spectra for compound **16** and the pure ligand are shown in Figure 3.4. The broad band corresponding to N-H bond stretching at *ca.* 3300  $\text{cm}^{-1}$  for the ligand disappears in the compound showing that the ligand is deprotonated and bound to the metallic centre. The bands at 2924 and 2820  $\text{cm}^{-1}$  in the spectra of compound **16** correspond to the  $\text{Csp}^2\text{-H}$  and  $\text{Csp}^3\text{-H}$  stretches respectively and the broad band at *ca.* 3300  $\text{cm}^{-1}$  is due to the N-H stretching. It can be seen that following coordination this band disappears as the ligands deprotonate (Figure 3.4 b). The bands at 1221.7 and 1046.9  $\text{cm}^{-1}$  in the free ligand spectrum are assigned to N=N and N-N stretches respectively. These bands undergo a shift to higher frequencies following coordination being 1268.4  $\text{cm}^{-1}$  for N=N and 1077.6  $\text{cm}^{-1}$  for the N-H stretch. This behavior is in good agreement with similar compounds reported by Perlepes *et al.* with MeBTAH and  $\text{Ni}^{2+}$ <sup>23</sup> and  $\text{Co}^{2+}$ <sup>24</sup>.

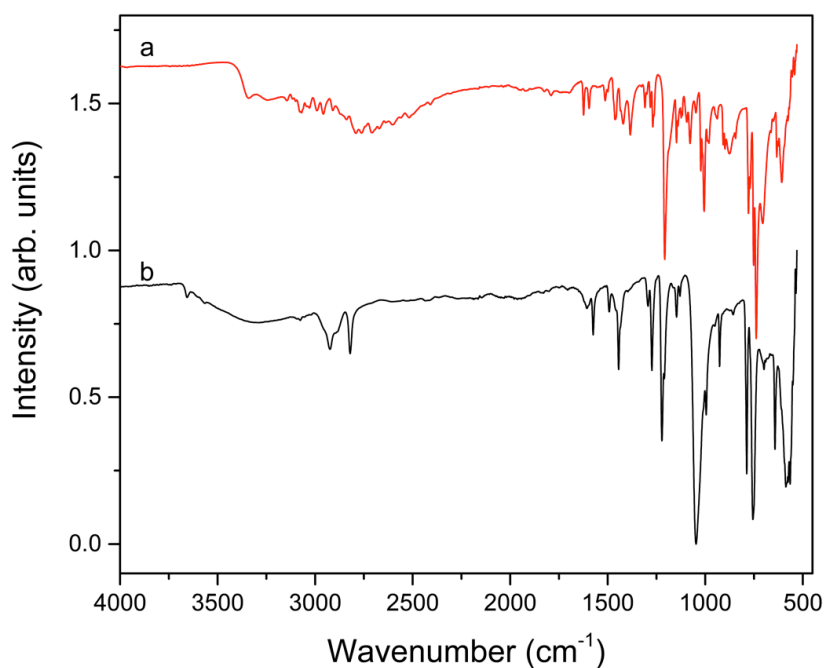


Figure 3.4. IR spectra for BTAH (a) and compound **16** (b).

## 3.3. X-ray Photoelectron Spectroscopy

### 3.3.1. Experimental

Photoelectron spectra were recorded on beamline D1011 of the MAX-Lab synchrotron in Lund University in Sweden. The beamline uses a bending magnet radiation in the range of 30-1600 eV from the 1.5 GeV (200mA) 3<sup>rd</sup> generation MAX II storage ring of 90 m of circumference. The beamline is equipped with a SX-700 monochromator with a plane-elliptical focussing mirror. The spot size is about 1 mm vertically and 2 mm horizontally. Preparation and analysis chambers are separated by a gate valve. The latter is equipped with a SCIENTA SES200 hemispherical electron analyser and a MCP.<sup>25</sup>

Compound **16** was mounted on a sample manipulator, firstly by sticking a small amount of powder to a double-sided conducting tape attached to a tantalum sample holder. However, spectra recorded in this arrangement were found to charge and spectra were of a poor quality. As a result a small amount of powder was mixed with a drop of ethanol to make a thick paste. This was then smeared directly onto the tantalum plate and the ethanol allowed to evaporate in the vacuum load lock at a pressure of  $1 \times 10^{-6}$  mbar. The complex is rather labile and there is the possibility that some of the chloride could be replaced by ethanol. Once all of the ethanol had evaporated the samples were introduced into the analysis chamber at a base pressure of  $2 \times 10^{-10}$  mbar, where they were analysed using synchrotron radiation of a photon energy ( $h\nu$ ) of 1400 eV for core level scans, and 50 and 60 eV for valence scans. Spectra were continuously monitored for changes, particularly in the C 1s and O 1s regions, during exposure to the synchrotron radiation beam, in order to ensure that no beam damage occurred. Spectra are aligned on the binding energy scale to the C 1s peak at an energy of 284.8 eV<sup>26</sup> and fitted using CASA XPS software.<sup>27</sup> 70 % Gaussian: 30 % Lorentzian curves were used for all fitting. The Fe 2p<sub>3/2</sub> spin orbit split spectrum is fitted according to the multiplet structure described by Gupta and Sen (GS)<sup>26,28,29</sup> associated with Fe<sup>3+</sup> species. The binding energy of the Fe 2p<sub>3/2</sub> spectrum and energy difference between the 2p<sub>3/2</sub> photoelectron peak and the satellite is consistent with Fe<sup>3+</sup> as the predominant

oxidation state. This work was carried out in collaboration with Dr Andrew Thomas and PhD student Mark Jackman.

### 3.3.2. Results and discussion

An XPS survey scan of the powder of compound **16** is shown in Figure 3.5. The peaks present are consistent with the molecule under investigation, with C 1s, N 1s, Fe 2p, O 1s and Cl 2p and 2s features clearly visible in the spectrum. The peaks at around 230 and 240 eV correspond to the tantalum, suggesting that the evaporation of the compounds on the surface at UHV does not give a full coverage of the surface.

The spectra were not found to change significantly over time and appeared to be homogenous at different points on the sample confirming that beam damage was minimal over the timescales employed in these measurements.

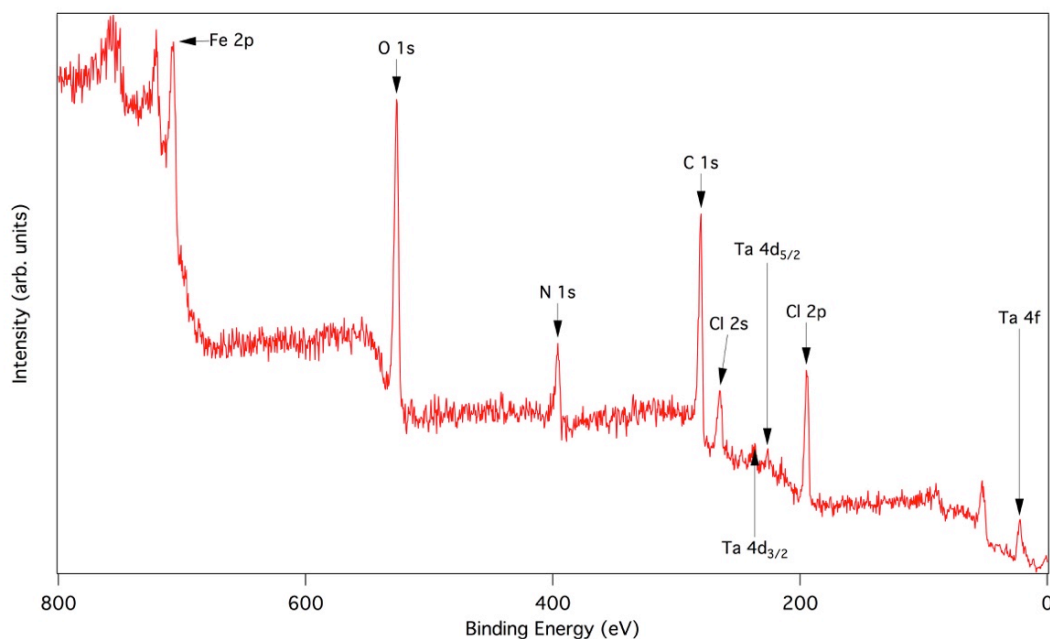


Figure 3.5. UHV XPS survey spectrum recorded for a powder sample of compound **16**.

Figure 3.6 shows the detailed photoelectron spectra for the core level of the atoms present; C 1s, O 1s and N 1s regions. The C 1s spectrum can be fitted with two peaks at binding energies of 284.8 eV (85 %) and 287.5 eV (15 %). The lower energy peak is

associated with C-C, C-H and methoxy species<sup>30</sup> and that at higher energies with bonding to N or carbonyl groups.<sup>30</sup> Here it is expected only C-N bonding and for compound **16** there should be a 7:2 ratio of peak intensities for (C-H,C-C,C-O):C-N,C-OH. What is measured here it is a peak area ratio in the C 1s spectrum is 5.7:1, which is attributed to contamination of the powder with atmospheric hydrocarbon and possibly residual ethanol from the sample mounting process, because ethanol can replace chloride in the molecule.<sup>31,32</sup>

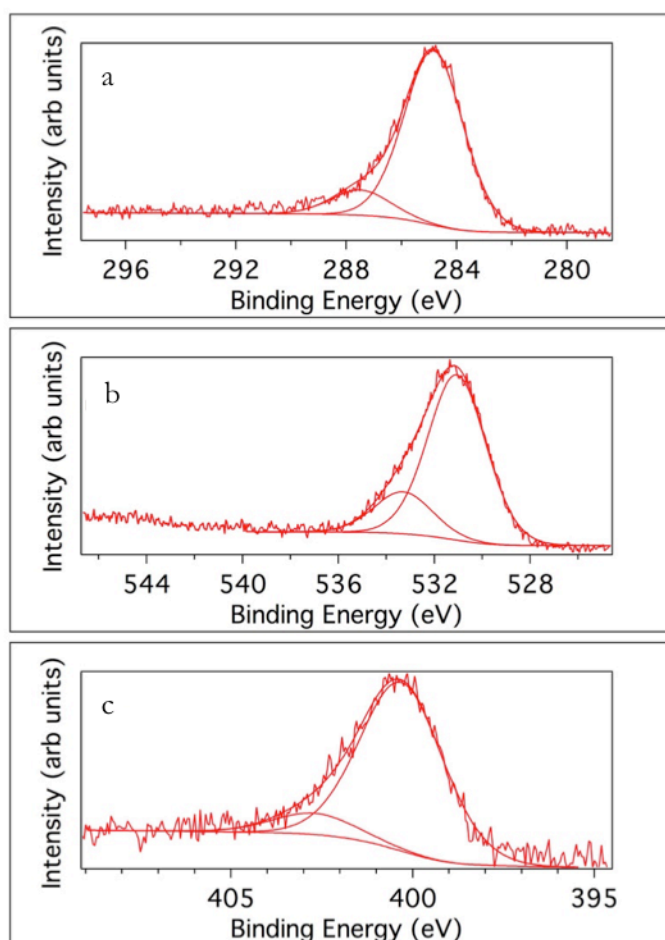


Figure 3.6. UHV XPS core level spectra for C 1s (a), O 1s (b) and N 1s (c) recorded for compound **16** as a powder on tantalum at  $h\nu = 1400$  eV.

The oxygen spectrum in Figure 3.6 (b) can also be fitted with two peaks. A large peak at a binding energy of 531.0 eV (80 %) and a smaller one at 533.3 eV (20 %). The lower energy peak is at an energy commonly associated with metal oxides<sup>26</sup> and it is assumed that at least a portion of the peak is derived from the Fe-O species present in the complex with the remainder from the methoxy oxygen. The small peak is at an energy

associated with hydroxides and presumably arises from contamination, again possibly linked to the ethanol used to prepare the sample. Some portion of the hydroxide signal is also likely to arise from exposure to water in the atmosphere during sample preparation.

The N 1s spectrum in Figure 3.6 (c) can also be fitted with two peaks at binding energies of 400.4 eV (89 %) and 402.8 eV (11 %). The main peak here is attributed to N-Fe bonding and no evidence of protonated nitrogen is observed in agreement with the IR spectrum in Figure 3.4. The peak at an energy of 402.8 eV could be associated with the Ta substrate, but it is most likely to be due to a N with a different chemical environment.

Figure 3.7 shows the Fe 2p spectrum fitted with the multiplet peaks suggested by Gupta and Sen (GS) for Fe<sup>3+</sup> species.<sup>26,28,29</sup> This splitting arises through a combination of electrostatic effects, the interaction of the spin-orbit split Fe 2p core hole and the five partially occupied 3d orbitals, each containing an unpaired electron, and crystal field effects.<sup>28,29</sup> The binding energy of centre of gravity of the Fe 2p<sub>3/2</sub> peak (from the raw data) is 712.1 eV, and that of the satellite is 719.0 eV both of which are consistent with Fe in a +3 oxidation state.<sup>26</sup> Fe<sup>2+</sup> with a ligand of similar electronegativity to BTAH would give rise to a satellite of greater than 5.2 eV above the centre of gravity of the main Fe 2p<sub>3/2</sub> peak, clearly there is no peak in this region so the presence of Fe<sup>2+</sup> can be ruled out. The multiplet peak binding energies, relative areas and energy splittings are given in Table 3.1. Strictly speaking since there are three different Fe<sup>3+</sup> environments (6 x N<sub>2</sub>O<sub>3</sub>Cl, 6 x O<sub>6</sub> and 2 x N<sub>3</sub>O<sub>3</sub>), three sets of multiplets should be fitted. However, because it is difficult to predict the precise binding energy shifts associated with the different ligands, any attempt to do this would involve over-analysing the data. The important finding is that the multiplet structure associated with Fe<sup>3+</sup> gives a good fit to the data thus confirming the oxidation state.<sup>26</sup>

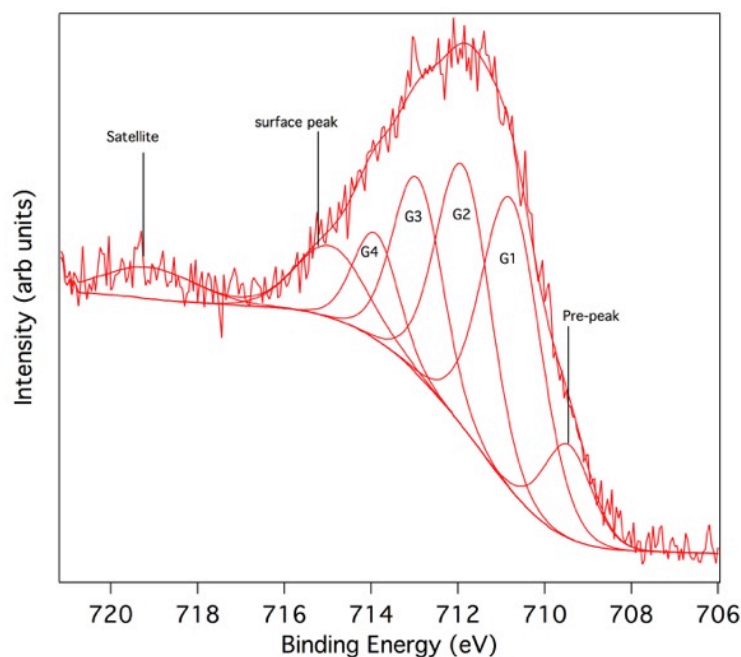


Figure 3.7. UHV narrow spectra of the core level  $2p_{3/2}$  for iron recorded at  $h\nu = 1400$  eV, see text for binding energy of the peaks.

Grosvenor *et al.*<sup>26</sup> also studied the Fe  $2p_{3/2}$  multiplet splitting and binding energies for a number of high spin Fe<sup>2+</sup> and Fe<sup>3+</sup> compounds and found that the ionic bonding character (due to the electronegativity of the ligand) of the materials led to an increase in both the binding energy of the Fe  $2p_{3/2}$  peak and the energy difference  $DE_{pk-sat}$  between the photoelectron peak and the shake-up satellite. A selection of binding energies of the Fe  $2p_{3/2}$  photoelectron and  $DE_{pk-sat}$  values from Grosvenor *et al.*<sup>26</sup> are shown in Table 3.2, along with data from this work for comparison. The value of the energy splitting,  $DE_{pk-sat}$ , for compound **16** lies slightly closer to that for Fe-O than Fe-Cl. If one takes the Pauling values of electronegativity and takes the mean values of these for the three ligands values of 3.44 (O), 3.26 (N<sub>2</sub>O<sub>3</sub>Cl) and 3.24 (N<sub>3</sub>O<sub>3</sub>) are obtained. The electronegativity on the Pauling scale lies at 3.16 thus the splitting lying closer to that observed for O containing compounds is not surprising. This splitting suggests a reasonable degree of ionicity in the ligand-Fe bonds. The molecule to surface bonding strength of azoles on copper has been shown to be related to the electronegativity and hardness of the azole, with larger molecules of lower electronegativity thought to bond more strongly. The effect of the electronegativity is

attributed to the electronegativity of the smallest molecule studied, triazole, being similar to the work function of copper. As the electronegativity of the ligand decreases, charge transfer can occur from the molecule to the metal to provide stronger bonding<sup>5</sup>. The work function of iron is lower than that of copper, and as one may expect larger azoles to form more stable bonds to Fe.

Table 3.1. Energy and percentage contribution of multiplet split peaks to Fe 2p spectra.

FWHM are slightly larger than reported in the work of Grosvenor *et al.*,<sup>26</sup> which is attributed to a slightly lower resolution in the present work.

| Peak      | Binding energy (eV) | Area (%) | FWHM |                                     |
|-----------|---------------------|----------|------|-------------------------------------|
| <b>G1</b> | 710.9               | 37.3     | 1.6  |                                     |
| <b>G2</b> | 712.0               | 31       | 1.5  | $\Delta E_{G1-G2} = 1.1 \text{ eV}$ |
| <b>G3</b> | 713.1               | 21.4     | 1.4  | $\Delta E_{G2-G3} = 1.1 \text{ eV}$ |
| <b>G4</b> | 714.1               | 10.3     | 1.2  | $\Delta E_{G3-G4} = 1.0 \text{ eV}$ |

In the peak fitting of the Fe spectrum shown in Figure 3.7, it was necessary to include a surface peak and a pre-peak in order to obtain a satisfactory fit. The origin of the surface peak has been explained both by a reduction in co-ordination of the surface Fe ions<sup>33</sup> and also as due to a reduction in crystal field splitting energy of Fe<sup>3+</sup> ions at the surface.<sup>34</sup> The origin of the pre-peak has been assigned to Fe in lower oxidation states sitting near defect sites in samples, thought to be produced in preparation of the samples. In the present case it is possible that it arises due to the different chemical environments of Fe ions in the complex as discussed above. The relative intensities of the GS split peaks match quite well with those predicted by Gupta and Sen. This may suggest that the crystal field splitting by the BTAH ligands is less than found in Fe-oxides. However, again the interpretation is somewhat complicated by the fact there are three different ligands, all of different electronegativity which may skew the weighting of the individual peaks from those fitted in this work.

Valence band (VB) spectra recorded at photon energies of 50 and 60 eV are shown in Figure 3.8. The main valence band lies between 5 and 12 eV binding energy. There is some structure present at a binding energy of 15 – 18 eV, which is attributed to N and C 2ps bonding orbitals in the ligands.<sup>35,36</sup> In addition, it is well known that contamination from water and carbonaceous species results in features in this binding energy region.<sup>37</sup> The photon energies of 50 and 60 eV at which the valence band spectra are recorded were chosen to be below and close to the Fe 3p to 3d photoemission resonance energies, respectively.<sup>38</sup> Any enhancement in the intensity in the resonant spectrum is associated with the presence of Fe 3d density of states, and therefore acts as a fingerprint for Fe. The spectra are normalized to the background at around 22 eV. As can be seen the spectrum recorded on-resonance shows an enhancement in intensity in the low binding energy part of the valence band, (marked with arrows) suggesting the Fe 3d derived states are mainly located here.<sup>39</sup> There also appears to be a slight resonance enhancement of the background between 10 and 20 eV. This may be due to resonance of a satellite feature associated with metal-ligand interactions.<sup>39</sup> However the satellite is not well resolved because it will lie below the C 2s and ps-derived states of the ligands, and they may be contaminant species present on the surface of the material.

Table 3.2. Comparison of binding energies of the main Fe 2p<sub>3/2</sub> photoelectron peak and energy difference between the photoelectron peak and the satellite for selected Fe<sup>3+</sup> compounds and compound **16**.<sup>26</sup>

| Compound   | Binding energy (eV) | $\Delta E$ (eV) |
|--|---------------------|-----------------|
| <b>16</b>  | 712.1               | 6.9             |
| <b><math>\alpha</math>-Fe<sub>2</sub>O<sub>3</sub></b> | 710.8               | 8.5             |
| <b><math>\gamma</math>-Fe<sub>2</sub>O<sub>3</sub></b> | 711.0               | 8.3             |
| <b><math>\gamma</math>-FeOOH</b>                       | 711.5               | 8               |
| <b>FeF<sub>3</sub></b>                                 | 715.1               | 8.7             |
| <b>FeCl<sub>3</sub></b>                                | 711.5               | 5.7             |
| <b>FeBr<sub>3</sub></b>                                | 710.3               | 4.9             |

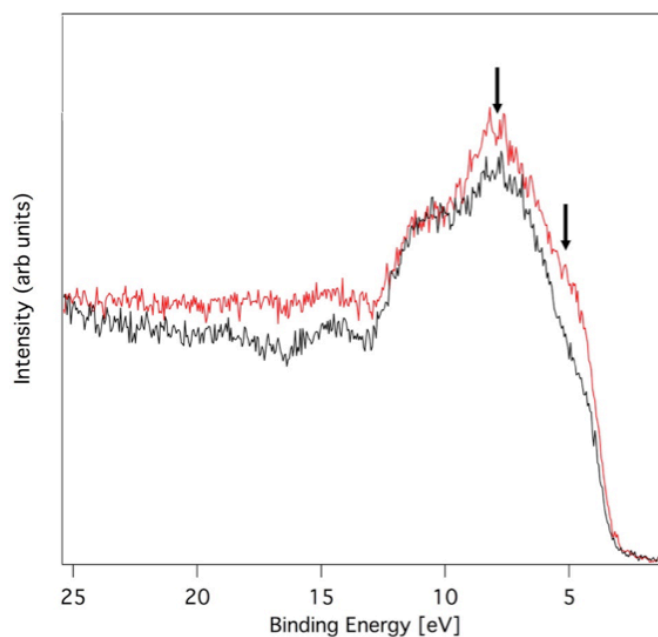


Figure 3.8. Valence band spectra for the compound **16** as a powder on tantalum foil at  $h\nu = 50$  (black) and  $60$  eV (red). The arrows show an increase in intensity of features in the valence band at the iron 3p-3d resonance.

### 3.4. Conclusions

It has been proven that both IR and Raman spectroscopies contain information of the binding mode of the ligands on a compound and so they can be used in the identification and differentiation of binding modes. This is only possible if, previously to the acquisition of the data, the finger prints of the ligand have been identified and their behaviour is perfectly understood depending on the atomic environment. For azole compounds the band that contains the most information about the binding of the ligand to a metallic atom in a compound is the N-H bond vibration.

This allows the identification of the binding mode without the need of resolving the single crystal X-ray structure, which, in some cases is not possible if the compound does not form stable crystals or these are difficult to obtain. This information can also be used to assist in the assignment of the bands when doing surface measurements such as VSFS.

Synchrotron XPS of compound **16** shows the Fe to be primarily in the +3 oxidation state with the main contribution of the Fe 3d states to the low binding energy part of the VB. The majority of the N is assumed to be bonded to the Fe centres. Bonding appears to be predominantly ionic and the average electronegativity of the ligands is between that of O and Cl. Synchrotron XPS on a bending magnet beamline appears to be a suitable method for analysis of these compounds, with no evidence of beam induced damage to the molecules; and hence also likely to be applicable studies of beam reactive corrosion inhibitors on a metal surface.

### 3.5. References

- 1 L. Procter and Gamble, 1947, **652339**, British Patent.
- 2 I. Dugdale and J. B. Cotton, *Corros. Sci.*, 1963, **3**, 69–74.
- 3 J. B. Cotton and I. R. Scholes, *Brit. Corros. J.*, 1967, **2**, 1–5.
- 4 B. Sathianandhan, K. Balakrishnan and N. Subramanyan, *Brit. Corros. J.*, 1970, **5**, 270–273.
- 5 R. J. Chin, D. Altura and K. Nobe, *Corrosion*, 1973, **29**, 185–187.
- 6 M. Finšgar and I. Milošev, *Corros. Sci.*, 2010, **52**, 2737–2749.
- 7 G. W. Poling, *Corros. Sci.*, 1970, **10**, 359–370.
- 8 J. H. Marshall, *Inorg. Chem.*, 1978, **17**, 3711–3713.
- 9 K. Nielsen and I. Soetofte, *Acta Chem. Scand. A*, 1984, **38**, 253–263.
- 10 J. Handley, D. Collison, C. D. Garner, M. Helliwell, R. Docherty, J. R. Lawson and P. A. Tasker, *Angew. Chemie Int. Ed.*, 1993, **105**, 1085–1087.
- 11 M. Murrie, C. D. Garner, P. A. Tasker and S. S. Turner, *Polyhedron*, 1998, **17**, 3031–3143.

- 12 E. G. Bakalbassis, E. Diamantopoulou, S. P. Perlepes, C. P. Raptopoulou, V. Tangoulis and T. F. Zafiroopoulos, *J. Chem. Soc., Chem. Commun.*, 1995, 1347–1348.
- 13 V. Tangoulis, C. P. Raptopoulou, A. Terzis, E. G. Bakalbassis, E. Diamantopoulou and S. P. Perlepes, *Inorg. Chem.*, 1998, **37**, 3142–3153.
- 14 A. L. Spek, A. R. Siedle and J. Reedijk, *Inorganica Chim. Acta*, 1985, **100**, L15–L19.
- 15 B. Machura, J. O. Dziegielewski, R. Kruszynski and T. J. Bartczak, *Polyhedron*, 2003, **22**, 2869–2875.
- 16 I. Ino, J. C. Zhong, M. Munakata, T. Kuroda-Sowa, M. Maekawa, Y. Suenaga and Y. Kitamori, *Inorg. Chem.*, 2000, **39**, 4273–9.
- 17 D. M. Low, L. F. Jones, A. Bell, E. K. Brechin, T. Mallah, E. Rivière, S. J. Teat and E. J. L. McInnes, *Angew. Chemie Int. Ed.*, 2003, **42**, 3781–3784.
- 18 R. Shaw, R. H. Laye, L. F. Jones, D. M. Low, C. Talbot-Eeckelaers, Q. Wei, C. J. Milios, S. Teat, M. Helliwell, J. Raftery, M. Evangelisti, M. Affronte, D. Collison, E. K. Brechin and E. J. L. McInnes, *Inorg. Chem.*, 2007, **46**, 4968–4978.
- 19 S. Asakura, C. C. Lu and K. Nobe, *J. Electrochem. Soc.*, 1974, **121**, 605–609.
- 20 J. L. Yao, B. Ren, Z. F. Huang, P. G. Cao, R. A. Gu and Z.-Q. Tian, *Electrochim. Acta*, 2003, **48**, 1263–1271.
- 21 M. K. Johnson, D. B. Powell and R. D. Cannon, *Spectrochim. Acta Part A Mol. Spectrosc.*, 1981, **37**, 995–1006.
- 22 R. A. Coxall, S. G. Harris, D. K. Henderson, S. Parsons, P. A. Tasker and R. E. P. Winpenny, *J. Chem. Soc. Dalton Trans.*, 2000, 2349–2356.
- 23 E. Diamantopoulou, T. F. Zafiroopoulos, S. P. Perlepes, C. P. Raptopoulou and A. Terzis, *Polyhedron*, 1994, **13**, 1593–1608.
- 24 J. C. Plakatouras, S. P. Perlepes, D. Mentzafos, A. Terzis, T. Bakas and V. Papaefthymiou, *Polyhedron*, 1992, **11**, 2657–2672.

- 25 A. MAX-lab Preobrajenski, *D1011 Website: <https://www.maxlab.lu.se/node/38>*.
- 26 A. P. Grosvenor, B. A. Kobe, M. C. Biesinger and N. S. McIntyre, *Surf. Interface Anal.*, 2004, **36**, 1564–1574.
- 27 Casa Software Ltd., *CasaXPS Version 2.3.16 PR 1.6*.
- 28 R. P. Gupta and S. K. Sen, *Phys. Rev. B*, 1974, **10**, 71–77.
- 29 R. P. Gupta and S. K. Sen, *Phys. Rev. B*, 1975, **12**, 15–19.
- 30 S. Günther, L. Zhou, M. Hävecker, A. Knop-Gericke, E. Kleimenov, R. Schlögl and R. Imbihl, *J. Chem. Phys.*, 2006, **125**, 114709.
- 31 F. Basolo and R. G. Pearson, *Mechanisms of Inorganic Reactions*, John Wiley, New York, USA, 1967.
- 32 R. G. Wilkins, *Kinetics and Mechanism of Reactions of Transition Metal Complexes*, VCH, Weinheim, 2nd Editio., 1991.
- 33 M. Bronold, Y. Tomm and W. Jaegermann, *Surf. Sci.*, 1994, **314**, L931–L936.
- 34 T. Droubay and S. A. Chambers, *Phys. Rev. B*, 2001, **64**, 205414.
- 35 E. Soria, E. Román, E. M. Williams and J. L. De Segovia, *Surf. Sci.*, 1999, **433**, 543–548.
- 36 E. Soria and S. S. Centre, *Surf. Sci.*, 2000, **451**, 188–196.
- 37 A. G. Thomas, M. J. Jackman, M. Wagstaffe, H. Radtke, K. Syres, J. Adell, A. Lévy and N. Martsinovich, *Langmuir*, 2014, **30**, 12306–14.
- 38 W. R. Flavell, J. Hollingworth, J. F. Howlett, A. G. Thomas, M. M. Sarker, S. Squire, Z. Hashim, M. Mian, P. L. Wincott and D. Teehan, *J. Synchrotron Radiat.*, 1995, **2**, 264–271.
- 39 R. J. Lad and V. E. Henrich, *Phys. Rev. B*, 1989, **39**, 13478–13485.



## Chapter 4. Phosphate esters for the protection of Fe



## 4.1. Introduction

Iron is the main component of steel, which is widely used because it is fairly cheap and easy to fabricate. Steel is the main material used in the oil and gas industry so understanding the oxidation processes of iron is very important. Iron has three allotropic forms:  $\delta$ -iron with a body centred cubic (bcc) crystal structure, which forms at the solidification temperature (1538 °C). When it reaches 1394 °C the metallic solid undergoes a phase transition (Figure 4.1) to  $\gamma$ -iron, also known as austenite, that has a face centred cubic system (fcc) and is stable until 912 °C, at which point it becomes  $\alpha$ -iron, also known as ferrite. Ferrite, which has a bcc crystal structure, is paramagnetic above its Curie temperature of 770 °C and ferromagnetic below.<sup>1</sup> This change is not considered a phase transition, because there is only change in the electronic structure of the material and not in its crystal structure. Ferromagnetic ferrite is the basis of steel materials and for this reason it was decided to study the corrosion inhibitors on this surface. All the results presented in Chapters 4 and 5 have been performed using a Fe(110) single crystal of the ferrite phase.

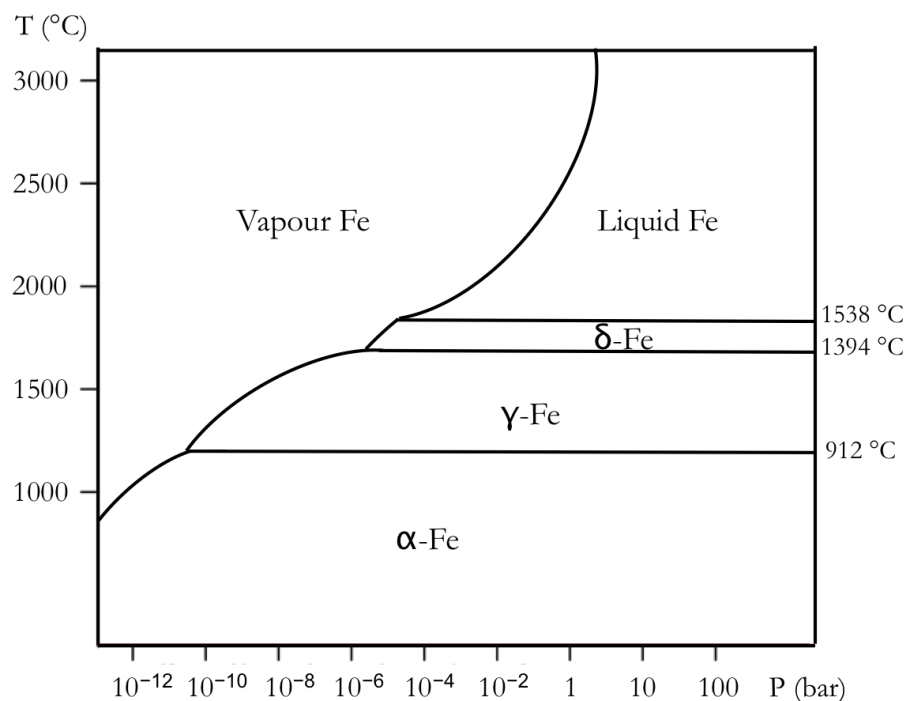


Figure 4.1. Low pressure pure iron phase transition diagram showing the different allotropes of Fe for different temperatures and pressures.<sup>1</sup>

Carbon atoms dissolve in iron, occupying the interstitial sites of the metallic structure. This happens during the formation process and for this reason Fe single crystals are known to have a very long cleaning process to prepare the surface as every time the surface is annealed C segregates to the surface. C has a high solubility in the fcc Fe and when this is cooled to the bcc form, cementite ( $\text{Fe}_3\text{C}$ ) forms.<sup>2</sup> The Fe crystal has two types of C contamination as judged as; contamination due to the carbide at 283 eV,<sup>3,4</sup> and contamination by the adsorption of hydrocarbon compounds from the air, or graphite like carbon with a peak at 284.4 eV.<sup>5</sup> The latter one could be completely removed from the surface, by repeated  $\text{Ar}^+$  sputtering/annealing processes because it is a superficial contamination from exposure with air. However the peak at lower binding energy cannot be removed as it comes from within the crystal itself.

Annealing the crystal also gets rid of oxide contamination, but at the same time brings to the surface other contaminants like sulfur, nitrogen and the already mentioned carbide.<sup>6</sup> For practical purposes in this work it was decided to work with small amounts of C contamination on the surface because the cleaning process of the Fe(110) single crystal could take up to 3 or 4 days and the carbide was never completely removed from the surface.

Phosphate esters are anionic surfactants that have good lubricant properties, they are stable in a wide range of pH and they are soluble in oily and organic solvents. The esterification process can take place by reacting an alcohol with a phosphating agent such as polyphosphoric acid or phosphorus pentoxide,<sup>7-9</sup> the alkyl substituent comes from the alcohol and it can have different degrees of ethoxylation. Phosphate esters have the general form shown in Figure 4.2 (a and b) and are formed when the hydrogen atoms on a phosphonic acid (c) are replaced by a hydrocarbon radical. Some confusion in the literature comes from the fact that the totally deprotonated species derived from a phosphonic acid is known as phosphonate (d), and sometimes the terms phosphate and phosphonate are used interchangeably in the oil industry.

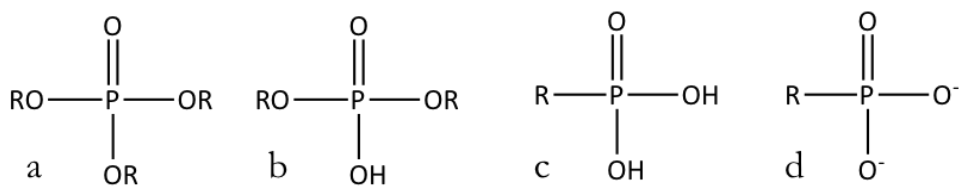


Figure 4.2. Chemical structure of the general form of a phosphate triester (a), phosphate diester (b), phosphonic acid (c) and phosphonate ion (d).

As it has been explained in Chapter 1, phosphate esters are used in the extraction of oil to protect the pipes against corrosive acids present in the oil crude.<sup>10,11</sup>

Phosphate esters are used in the protection of Al<sup>12-14</sup> and steel in the presence of O<sub>2</sub>,<sup>15-17</sup> H<sub>2</sub>,<sup>18</sup> and in aqueous<sup>19</sup> and oil environment.<sup>10,11,16,18,20-23</sup> These compounds are thought to react with the oxidised metallic surface, capturing the metallic cations to form a coordination complex that precipitates on the surface and creates a protective film.<sup>15,16,20,21</sup>

In some cases phosphate esters are used in the presence of other elements that improve protection. Ethoxylated phosphate esters are used to stop the precipitation of Ca<sup>2+</sup> on the surface, which could lead to pitting, inside the pipes in the extraction of oil.<sup>10</sup> These esters usually contain N atoms to improve interaction with the surface.<sup>18,21</sup>

A recent study on phosphate esters of different chain length showed that compounds with longer aliphatic chains adsorb better on the surface and have a higher protective activity.<sup>19</sup> However this study was performed on phosphate esters of chains of 4, 6 and 8 C atoms, whereas commercial corrosion inhibitors have longer lengths (10 to 20 C atoms). It is not yet known if chains longer than 20 provide a higher protection.

The main goal of this chapter is to get a better understanding on how PAE 136, a commercial corrosion inhibitor used in the extraction of oil by BP binds to a metallic surface and how it inhibits corrosion. Dibutyl phosphate ester (DbPO<sub>2</sub>H) has also been studied as a model and simpler compound of PAE 136 in order to facilitate the understanding of the chemisorption of PAE 136. These have firstly been studied in UHV and later at low pressures of H<sub>2</sub>O, CO<sub>2</sub> and a mixture of both to investigate the

possibility of a different behaviour under different conditions and to mimic sweet corrosion.

In order to understand the interaction of the different phosphate esters and phosphonic acids (Chapter 5) with the Fe(110) single crystal surface in a corrosive environment it is important to have a good understanding of the behaviour of the clean surface under the same conditions.

## 4.2. Experimental

The experiments were first carried out on a clean Fe(110) single crystal. The Fe(110) surface was cleaned by repeated 1 keV Ar<sup>+</sup> ion bombardment and annealing to 873 K in vacuum. In all the experiments there was some residual carbide that could not be completely removed at 283 eV.

The work presented here was carried out in the Photon Science Institute in Manchester in a near ambient pressure (NAP) XPS equipped with a SPECS Focus 500 monochromated Al K $\alpha$  source (photon energy 1486.6 eV), focused to a size of 300  $\mu$ m. The analyser is a SPECS 150 mm Phoibos 150 NAP. The analysis chamber is separated from the sample preparation chamber by means of a gate valve. The Fe(110) crystal was held in place by a tantalum wire. A thermocouple was attached to the sample plate allowing monitoring of the sample temperature. The pressure in the analysis chamber was about  $1.5 \times 10^{-10}$  mbar during measurements prior water exposure. Photoemission spectra were collected at normal emission.

Dibutyl phosphate ester (DbPO<sub>2</sub>H) 96% was purchased from Sigma Aldrich and CO<sub>2</sub> 99.995% used in the NAP XPS experiments was purchased from CK Special Gases Limited and used without further purification. Commercial corrosion inhibitor PAE 136 was provided by Lakeland Laboratories. The H<sub>2</sub>O used in the NAP experiments is deionised, which was purified to remove dissolved gasses by repeated freeze-thaw cycles.

The fitting of the data has been done using CASA XPS software<sup>24</sup> using a 70 % Gaussian : 30 % Lorentzian curves. Atoms which core level is a p, d or f orbital give rise to a doublet due to the spin-orbit splitting. The P 2p core level exhibits spin-orbit splitting with a separation of 0.9 eV thus two peaks are fitted.<sup>25,26</sup> The area ratio depends on the degeneracy of each spin state, for a 2p orbital the ratio of  $2p_{1/2}$  and  $2p_{3/2}$  will be 1:2.

In the control experiments the signal of the  $\text{OH}^-$  in the O 1s core level spectra has been fitted with two components, assigned to adsorbed  $\text{OH}^-$  and lattice  $\text{OH}^-$  with a full width at half maximum (FWHM) constrained to be the same for all the O 1s peaks.<sup>27-30</sup> However in the study of the corrosion inhibitor and the model compound, the  $\text{OH}^-$  signal has been fitted using only one component with a bigger FWHM in order to facilitate the fittings, as using two components does not provide more information about the binding.

## 4.3. Results and discussion

### 4.3.1. Control experiment of $\text{H}_2\text{O}$ on Fe(110)

Once the carbide C signal reached a stationary level the clean sample was transferred to the NAP cell where it was exposed to a water pressure of 8 mbar at 373 K. The spectra were recorded at different temperatures on the same day without further preparation. The acquisition of one set of data, i.e. recording spectra for Fe 2p, O 1s, C 1s and P 2p for a given temperature, takes up to 4 h. This is because at higher pressures the electrons have a smaller mean path length which reduces the number of electrons reaching the analyser as has been explained in Chapter 1. In addition the high intensity of the  $\text{H}_2\text{O}$  peak attenuates the corrosion inhibitor signal. For this reason the range of temperatures at which the spectra were measured is determined by the amount of time allotted on the instrument.

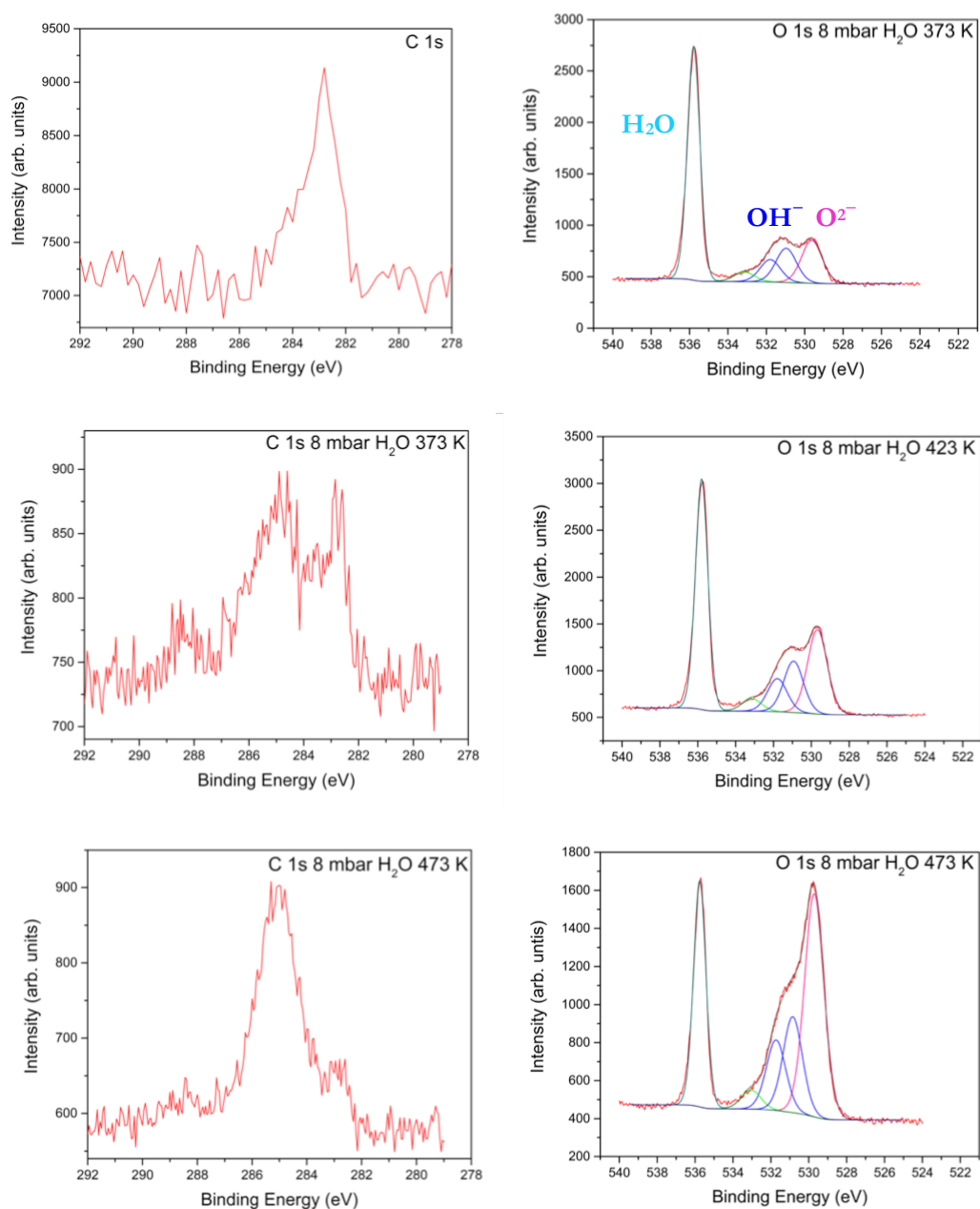


Figure 4.3 NAP XPS C 1s core level spectra for a clean Fe(110) surface (top left), O 1s (top right) and C 1s (middle left) core level spectra recorded at 373 K, O 1s core level spectra recorded at 423 K (middle right) and C 1s and O 1s core level spectra recorded at 473 K (bottom).

Figure 4.3 shows the carbide C present on the clean surface and the C 1s spectrum recorded in the presence of 8 mbar of H<sub>2</sub>O at different temperatures. Here it can be seen that, in addition to the carbide C peak at 283 eV, another peak at higher binding

energy 285 eV arises suggesting the H<sub>2</sub>O displaces C containing species from the walls of the NAP cell depositing residues on the surface.

Figure 4.3 shows the O 1s core level spectra recorded in the presence of 8 mbar of H<sub>2</sub>O and at different temperatures. The intense peak at high binding energy (535.9 eV) in the O 1s spectrum is due to the gas phase water in the NAP cell. The O 1s peak can be fitted with 4 components. An oxide peak at 529.6 eV (pink); two hydroxide components: the lattice OH<sup>-</sup> at 530.9 eV and an adsorbed OH<sup>-</sup> at 531.8 eV (both blue).<sup>27-30</sup> There is another peak at 533.1 eV (green) which has been assigned to carbonate in the walls of the NAP cell that has been deposited on the surface. From these spectra it can be seen that the surface becomes more oxidised with temperature as would be expected. The oxide peak becomes more intense at 423 K and it is as high as the vapour H<sub>2</sub>O peak at 473 K. The hydroxide peaks also increase their intensity. The assignments and binding energies of these peaks are in Table 4.1.

Table 4.1. Peak assignments and their respective binding energies (eV) for the spectra of Fe(110) single crystal in the presence of 8 mbar of H<sub>2</sub>O at different temperatures.

|                                | <b>Binding Energy (eV)</b> |              |              |
|--------------------------------|----------------------------|--------------|--------------|
|                                | <b>O 1s</b>                |              |              |
|                                | <b>373 K</b>               | <b>423 K</b> | <b>473 K</b> |
| <b>O<sup>2-</sup></b>          | 529.6                      | 529.7        | 529.7        |
| <b>Lattice OH<sup>-</sup></b>  | 531.0                      | 530.9        | 530.9        |
| <b>Adsorbed OH<sup>-</sup></b> | 531.8                      | 531.8        | 531.7        |
| <b>Other</b>                   | 533.2                      | 533.2        | 533.1        |
| <b>H<sub>2</sub>O</b>          | 535.8                      | 535.8        | 535.8        |

The Fe 2p core level spectra (Figure 4.4) also show evidence of oxidation, which increases as the temperature is raised. For the surface at 373 K there is only a Doniach-Šunjić line shape characteristic of metallic Fe.<sup>30</sup> Following exposure to water at elevated temperature there is an increase in intensity to the high binding energy side of the Fe

$2p_{3/2}$  peak characteristic of higher oxidation states of Fe.<sup>29</sup> Fitting of Fe 2p to identify the oxide/hydroxide/carbonate formed requires P/O complex multiplet structure, which for the mixed metal/oxidised material would be meaningless due to the number of peaks required.

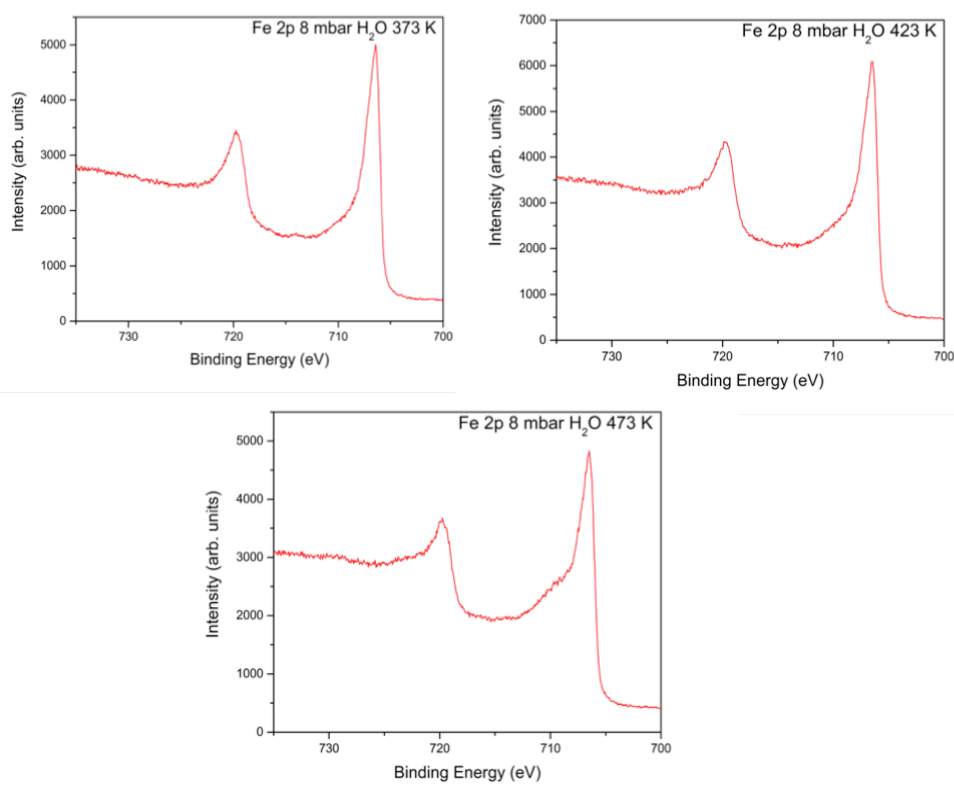


Figure 4.4 NAP XPS Fe 2p core level spectra recorded in the presence of 8 mbar of H<sub>2</sub>O at 373 (top left), 423 (top right) and 473 K (bottom).

### 4.3.2. Control experiment of CO<sub>2</sub> + H<sub>2</sub>O on Fe(110)

The Fe(110) single crystal was cleaned until the point where the carbide C contamination reached a stationary state and all the oxide formed in the previous experiment was removed from the surface. The sample was then exposed to 2 mbar of CO<sub>2</sub> and the core level spectra were recorded. In order to mimic the sweet corrosion found in the extraction of oil in which CO<sub>2</sub> is naturally present and there is also water,

the sample was exposed to different H<sub>2</sub>O pressures. The spectra were recorded for 10:1, 3:1 and 1:1 P(CO<sub>2</sub>):P(H<sub>2</sub>O) ratios.

Figure 4.5 shows the O 1s core level spectra for all the experiments performed. The presence of CO<sub>2</sub> oxidises the surface as it causes the appearance of the hydroxide peaks (blue) and oxide (pink).<sup>31</sup> The peak at 533 eV is assigned to adsorbed CO on the surface according to the literature,<sup>31</sup> suggesting that the CO<sub>2</sub> gas used in the experiment is not of high purity. There is also evidence of the oxidation from the O<sup>2-</sup> peak (pink) and the OH<sup>-</sup> peaks (blue),<sup>27-30</sup> all the assigned binding energies for these spectra are shown in table 4.2.

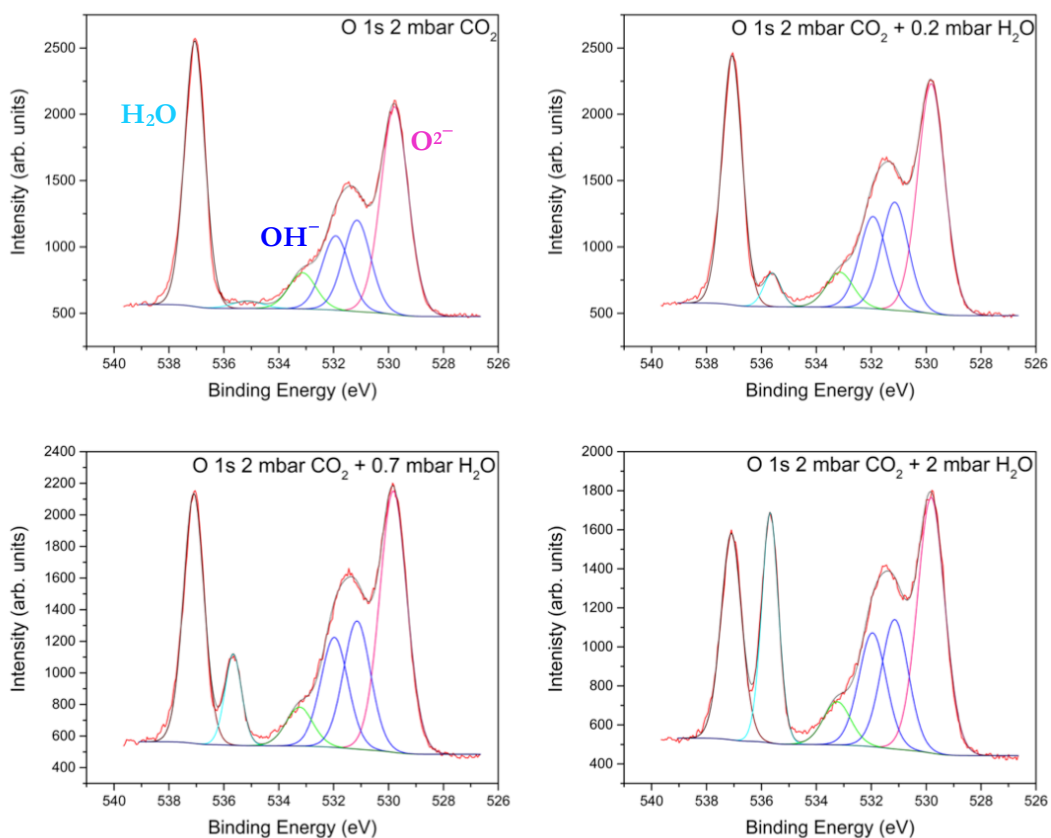


Figure 4.5. NAP XPS O 1s core level spectra recorded in the presence of 2 mbar of CO<sub>2</sub> (top left) with 0.2 (top right), 0.7 (bottom left) and 2 mbar (bottom right) of H<sub>2</sub>O on an Fe(110) surface.

When adding the water it can be observed that the intensity of the oxide and hydroxide peaks increases slightly, but it seems that what is causing the oxidation of the surface is mainly the presence of the  $\text{CO}_2$ . Reaction of  $\text{CO}_2$  in the presence of  $\text{H}_2\text{O}$  to produce  $\text{H}_2\text{CO}_3$  allows Fe to be oxidised in analogy to the sweet corrosion process (see equation 1.2). This is consistent with the observation of C-O and C=O in the O 1s XPS spectra. In Table 4.2 the assignment of all peaks for the different relative pressures is shown for O 1s and C 1s.

Table 4.2. Peak assignments and their respective binding energies (eV) for Fe(110) surface exposed to 2 mbar of  $\text{CO}_2$  with ratios of  $\text{H}_2\text{O}$  (in mbar) in Figures 4.6 and 4.7.

|                                | <b>Binding Energy (eV)</b> |  |  |  |
|--------------------------------|----------------------------|--|--|--|
|                                | <b>O 1s</b>                |  |  |  |
|                                | <b>2 CO<sub>2</sub></b>    | <b>2 CO<sub>2</sub> + 0.2 H<sub>2</sub>O</b> | <b>2 CO<sub>2</sub> + 0.7 H<sub>2</sub>O</b> | <b>2 CO<sub>2</sub> + 2 H<sub>2</sub>O</b> |
| <b>O<sup>2-</sup></b>          | 529.6                      | 529.7  | 529.7  | 529.7                                      |
| <b>Lattice OH<sup>-</sup></b>  | 531.1                      | 531.1  | 531.1  | 531.1                                      |
| <b>Adsorbed OH<sup>-</sup></b> | 531.8                      | 531.9  | 531.9  | 531.9                                      |
| <b>CO</b>                      | 533.0                      | 533.1  | 533.2  | 533.2                                      |
| <b>H<sub>2</sub>O</b>          | -                          | 535.5  | 535.5  | 535.5                                      |
| <b>CO<sub>2</sub></b>          | 536.9                      | 536.9  | 537.0  | 537.0                                      |
|                                | <b>C 1s</b>                |  |  |  |
|                                | <b>2 CO<sub>2</sub></b>    | <b>2 CO<sub>2</sub> + 0.2 H<sub>2</sub>O</b> | <b>2 CO<sub>2</sub> + 0.7 H<sub>2</sub>O</b> | <b>2 CO<sub>2</sub> + 2 H<sub>2</sub>O</b> |
|                                | <b>2 CO<sub>2</sub></b>    | <b>2 CO<sub>2</sub> + 0.2 H<sub>2</sub>O</b> | <b>2 CO<sub>2</sub> + 0.7 H<sub>2</sub>O</b> | <b>2 CO<sub>2</sub> + 2 H<sub>2</sub>O</b> |
| <b>Carbide C</b>               | 283.0                      | 283.0  | 283.0  | 282.8                                      |
| <b>C-C</b>                     | 284.6                      | 284.7  | 284.8  | 284.8                                      |
| <b>C-O</b>                     | 286.2                      | 286.3  | 286.3  | 286.3                                      |
| <b>C=O</b>                     | 289.2                      | 289.0  | 289.0  | 289.0                                      |
| <b>CO<sub>2</sub></b>          | 293.3                      | 293.3  | 293.3  | 293.3                                      |

The C 1s signal (Figure 4.6) can be fitted to 5 different chemical species. The previously mentioned carbide that is always present on the surface at a binding energy of 283 eV (blue), contamination from hydrocarbon compounds coming from the impurities of the

CO<sub>2</sub> gas at 284.5 eV (green), CO adsorbed on the surface that it is also present in the O 1s signal (pink) at 286.2 eV, carbonyl on the surface with a peak at 289 eV,<sup>31</sup> and the vapour CO<sub>2</sub> at 293.3 eV (maroon). The binding of CO to the surface is reported slow,<sup>31</sup> and initially gives a spectrum very similar to that from binding CO<sub>2</sub>. This CO impurity is much easier to observe in the O 1s spectra.

The presence of the C-O and C=O species could be explained by the formation of FeCO<sub>3</sub> on the surface. In Chapter 1 it was mentioned that sweet corrosion leads to the formation of a passivation layer of FeCO<sub>3</sub>, and this experiment confirms it is present under sweet conditions.

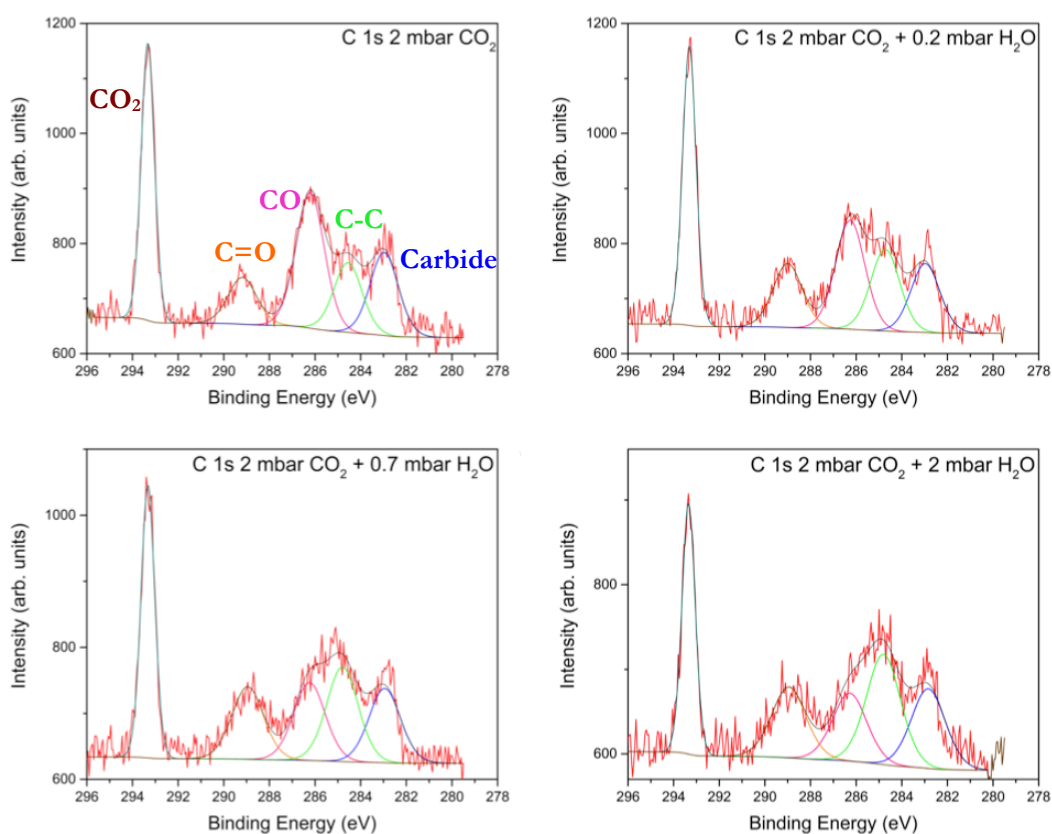


Figure 4.6. NAP XPS C 1s core level spectra recorded in the presence of 2 mbar of CO<sub>2</sub> (top left) with 0.2 (top right), 0.7 (bottom left) and 2 mbar (bottom right) of H<sub>2</sub>O on an Fe(110) surface.

The Fe 2p spectra (Figure 4.7) show a higher level of oxidation than was seen on the surface in the presence of H<sub>2</sub>O alone at high temperatures as the doublet assigned to the oxidised Fe is much more obvious than in the previous case. A possible explanation

for this is that in this case both iron oxide and iron carbonate are corrosion products that form on the surface, whereas in the presence of  $\text{H}_2\text{O}$  itself there is only formation of iron oxide.

To summarise the results from the control experiments, the Fe(110) single crystal becomes oxidised in the presence of  $\text{H}_2\text{O}$  vapour and higher temperatures promote oxidation. However the presence of  $\text{CO}_2$  on its own is corrosive enough to cause more oxidation than the  $\text{H}_2\text{O}$  at high temperatures.

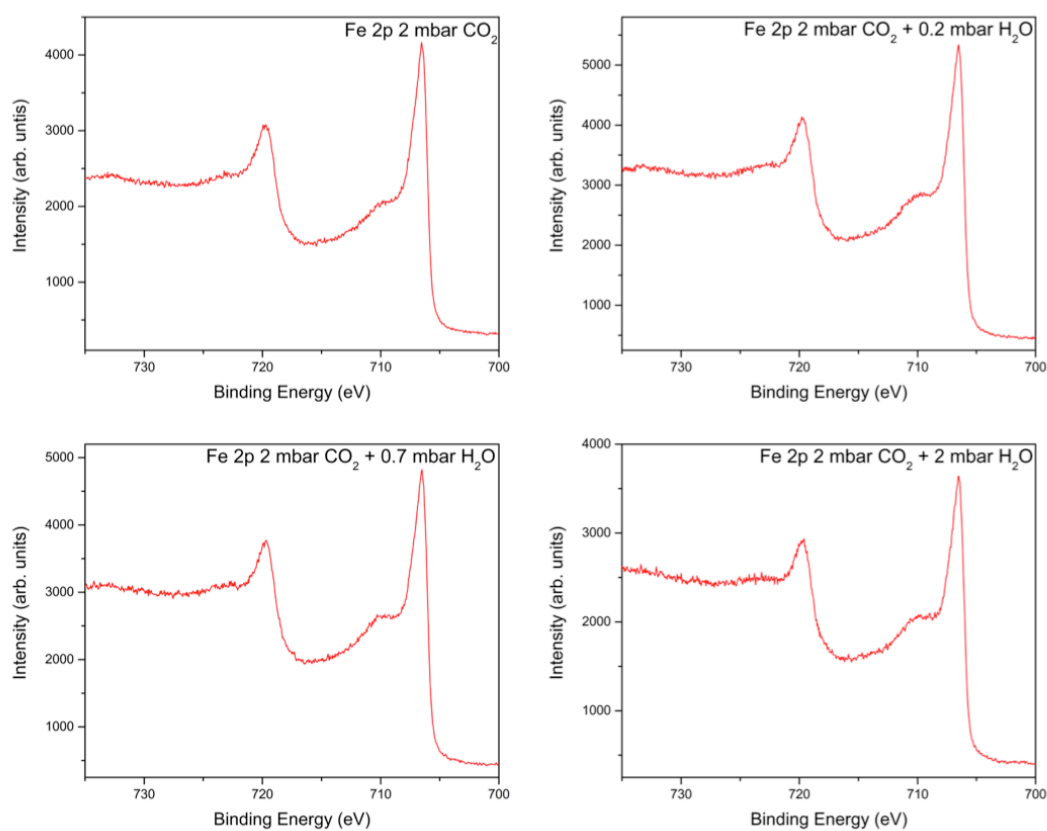


Figure 4.7. NAP XPS Fe 2p core level spectra recorded in the presence of 2 mbar of  $\text{CO}_2$  (top left) with 0.2 (top right), 0.7 (bottom left) and 2 mbar (bottom right) of  $\text{H}_2\text{O}$  on an Fe(110) surface.

### 4.3.3. Dibutyl phosphate ester on Fe(110)

#### 4.3.3.1. XPS study in UHV

The Fe(110) single crystal was cleaned by repeated 1 keV Ar<sup>+</sup> ion bombardment and annealing to 773 K. Once the carbide contamination got to a stationary state dibutyl phosphate ester (DbPO<sub>2</sub>H) was deposited onto the sample by vacuum sublimation from a Knudsen cell at room temperature in a preparation chamber and core level spectra were recorded in UHV at different temperatures. Figure 4.8 shows the wide scan and core level spectra of C 1s, O 1s and P 2p recorded at room temperature.

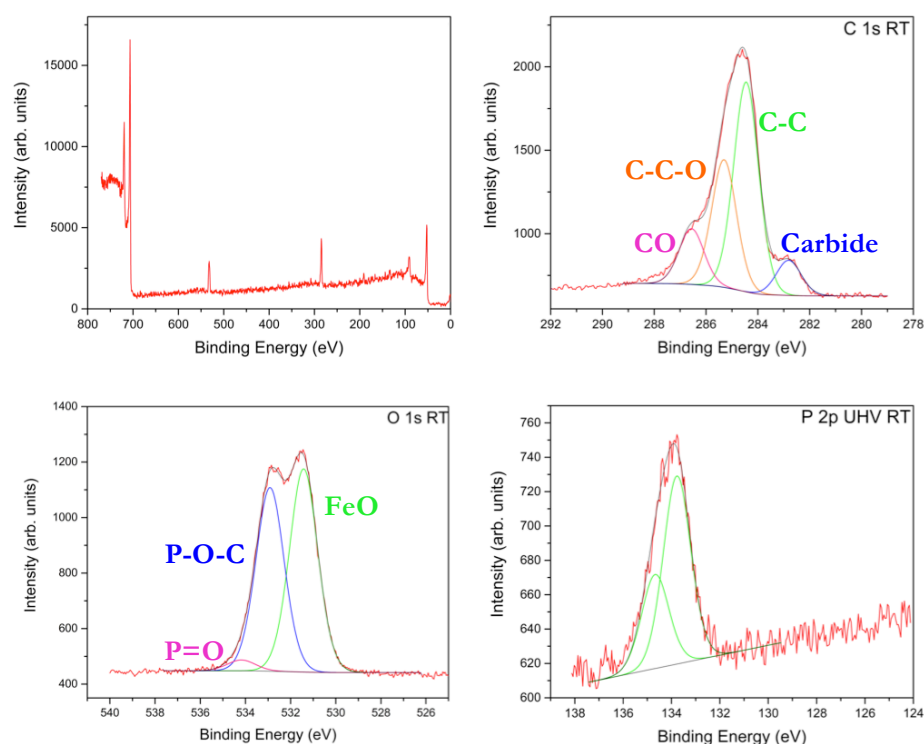


Figure 4.8. UHV XPS survey scan (top left), core level for C 1s (top right), O 1s (bottom left) and P 2p (bottom right) for deposited DbPO<sub>2</sub>H on an Fe(110) surface recorded at room temperature.

The core level 2p spectrum for P shows only one chemical species with peaks at 133.8 and 134.2 eV for the doublet, suggesting that all the compound on the surface is deprotonated.<sup>32</sup> This peak becomes less intense when raising the temperature, but does not suffer any other changes and for this reason it will not be further discussed. The C

1s signal fits to 4 chemical species, the assignments of which are in Table 4.3. The peak at 283 eV (blue) is from the carbide C contamination already mentioned for previous experiments. The most intense peak at 284.4 eV (green) is assigned to the C in the aliphatic chain and the peak at 285.3 eV (orange) is thought to be due to the C atoms on the aliphatic chain that are also bound to C atoms but closer to the O atoms. The peak found at higher binding energies (pink) is assigned to the C atoms directly bound to the O atoms on the ester.

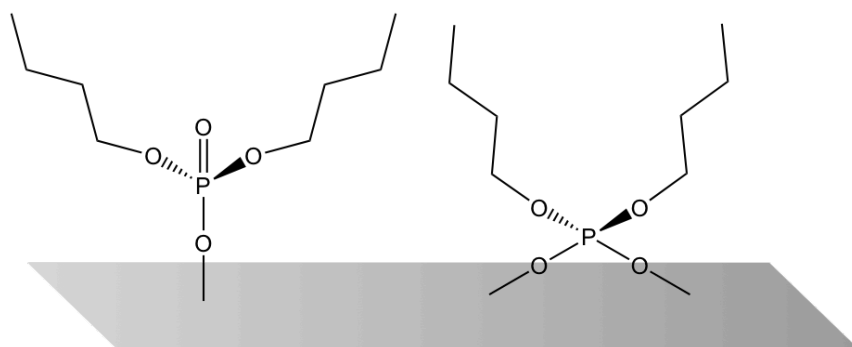


Figure 4.9. Schematic representation of the binding modes that  $\text{DbPO}_2\text{H}$  shows on the Fe surface.

The O 1s core level fits to three chemical species. The most intense signal at 531.4 eV (green) is assigned to the O atoms on the compound that are directly bound to the Fe surface, the blue peak at 533 eV is assigned to the O bound to the P and C (P-O-C) of the aliphatic chain and the least intense peak at 534 eV (pink) is assigned to an O bound to the P through a double bond that is not interacting with the surface.

The fitting of these data suggests that even though the phosphate ester is never found protonated on the surface it presents two different binding modes, monodentate and bidentate. A schematic representation of these is shown in Figure 4.9. This is thought because of the presence of the P=O peak in the O 1s spectrum that would not be present if the compound were bound through the two O atoms in a bidentate binding mode.

The Fe crystal was then heated in 50 degree steps to investigate the stability of the adsorbed molecules as function of the temperature. Figures 4.10 and 4.11 show the C 1s and O 1s spectra when raising the temperature; this is important in order to understand how the compound and the surface behave at higher temperatures. In upstream applications, for example, temperatures of around 373 K are commonly used.

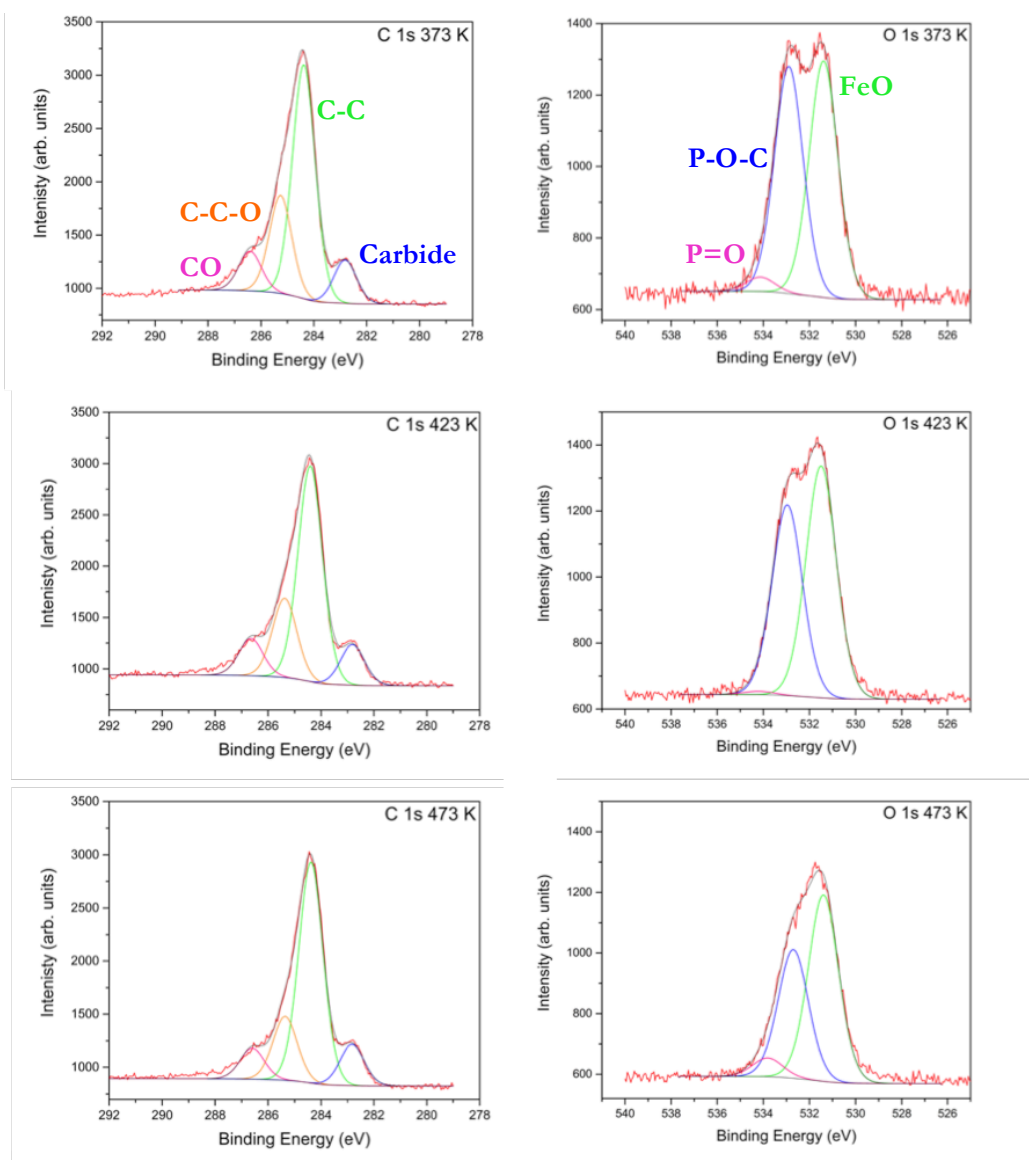


Figure 4.10. UHV XPS core level for C 1s (left) and O 1s (right) for  $\text{DbPO}_2\text{H}$  on an Fe(110) surface recorded at 373 (top), 423 (middle) and 473 K (bottom).

In the C 1s spectra there are no major changes and the compound remains stable at high temperatures. There only is a small decrease in the intensity of the peak at 285 eV

(orange in Figure 4.10). In the O 1s signal at different temperatures the peak assigned to P-O-C decreases in intensity, this could be explained by the surface becoming more oxidised and so the signal assigned to the more negative O increases. The change in the intensities of these peaks could also be as a result of the monodentate binding mode interconverting into the bidentate as this would cause a higher Fe-O-P:P-O ratio. It is not possible to confirm the nature of this change as both processes might take place at the same time.

Table 4.3. Peak assignments and their respective binding energies (eV) for the spectra of DbPO<sub>2</sub>H on Fe(110) single crystal in Figures 4.8, 4.10 and 4.11.

| <b>Binding Energy (eV)</b> |           |              |              |              |              |              |
|----------------------------|-----------|--------------|--------------|--------------|--------------|--------------|
| <b>C 1s</b>                |           |              |              |              |              |              |
|                            | <b>RT</b> | <b>373 K</b> | <b>423 K</b> | <b>473 K</b> | <b>523 K</b> | <b>573 K</b> |
| <b>Carbide C</b>           | 282.8     | 282.8        | 282.8        | 282.8        | 282.9        | 282.9        |
| <b>C-C</b>                 | 284.5     | 284.4        | 284.4        | 284.4        | 284.4        | 284.4        |
| <b>C-C-O</b>               | 285.0     | 285.3        | 285.4        | 285.4        | 285.3        | 285.4        |
| <b>C-O</b>                 | 286.6     | 286.4        | 286.6        | 286.6        | 286.5        | 286.6        |
| <b>O 1s</b>                |           |              |              |              |              |              |
|                            | <b>RT</b> | <b>373 K</b> | <b>423 K</b> | <b>473 K</b> | <b>523 K</b> | <b>573 K</b> |
| <b>Fe-O-P</b>              | 531.4     | 531.4        | 531.5        | 531.4        | 531.4        | 531.3        |
| <b>P-O</b>                 | 532.9     | 532.9        | 533.0        | 532.7        | 532.7        | 532.7        |
| <b>P=O</b>                 | 534.2     | 534.1        | 534.2        | 533.8        | 534.2        | 534.4        |

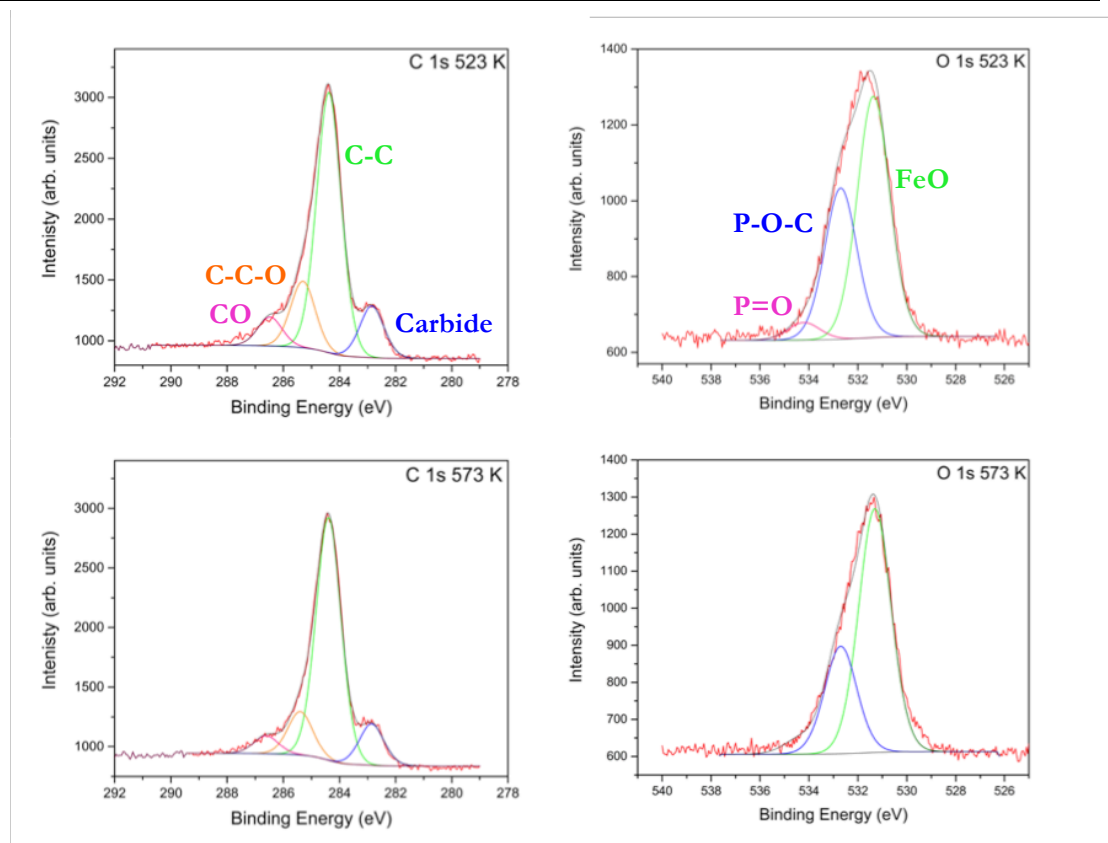


Figure 4.11. UHV XPS core level for C 1s (left) and O 1s (right) for  $\text{DbPO}_2\text{H}$  on an Fe(110) surface recorded at 523 (top) and 573 K (bottom).

### 4.3.3.2. XPS study under NAP conditions

The Fe(110) single crystal was cleaned and dibutyl phosphate ester was evaporated in UHV at room temperature. The sample was then exposed to 10 mbar vapour H<sub>2</sub>O and the core level spectra recorded, which are shown in Figure 4.12.

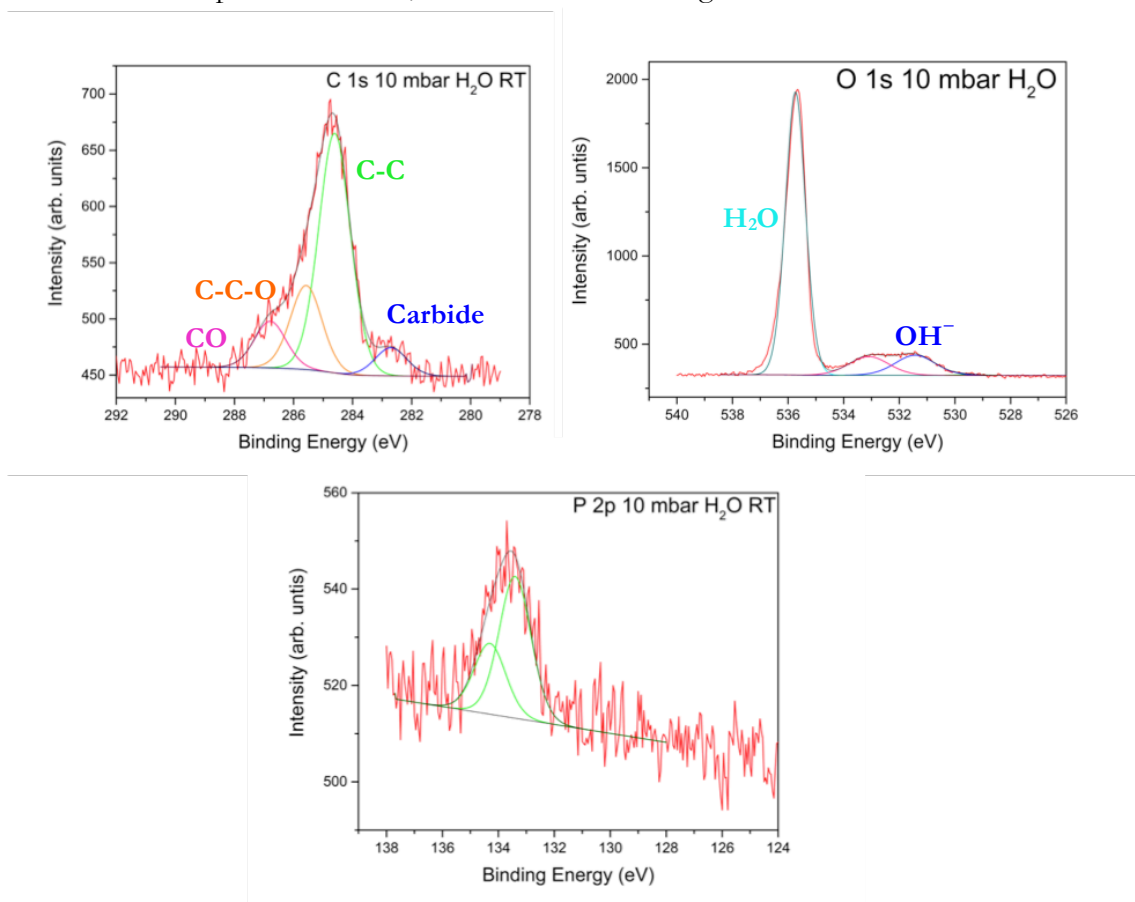


Figure 4.12. NAP XPS core level for C 1s (top left), O 1s (top right) and P 2p (bottom) for DbPO<sub>2</sub>H on an Fe(110) surface recorded in the presence of 10 mbar of H<sub>2</sub>O at room temperature.

After recording the spectra at room temperature it was decided that the pressure of H<sub>2</sub>O was too high as the signal from the compound is barely visible due to the high intensity of the H<sub>2</sub>O vapour peak so it was decided to reduce the ambient water to 8 mbar. The P 2p spectrum contains only one chemical species corresponding to the deprotonated phosphate with doublet peaks at 133.3 and 134.2 eV, suggesting that the compound is present only in its deprotonated state as was seen in UHV. As the P 2p spectrum did not change at higher temperatures and it will not be shown again.

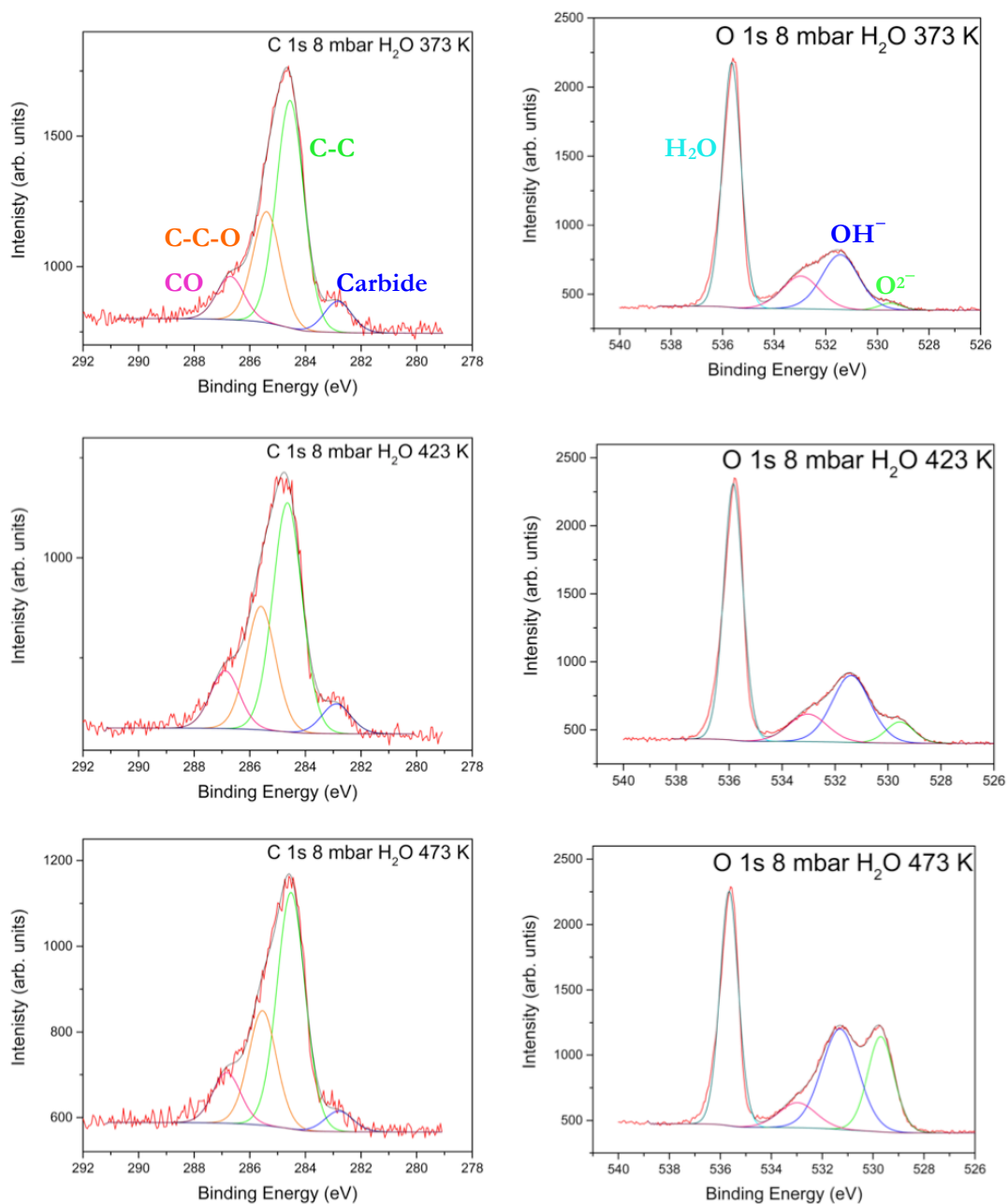


Figure 4.13. NAP XPS core level for C 1s (left) and O 1s (right) for  $\text{DbPO}_2\text{H}$  on an Fe(110) surface recorded in the presence of 8 mbar of  $\text{H}_2\text{O}$  at 373 (top), 423 (middle) and 473 K (bottom).

Figure 4.13 shows the C 1s and O 1s spectra recorded at different temperatures. The C 1s spectra look very similar as the ones recorded in UHV suggesting that the alkyl chains behave in the same way under  $\text{H}_2\text{O}$  pressure and at UHV. In this case the peak at 285.5 eV (orange) does not change its relative intensity like it did in UHV, the nature of this is not known. For this compound the fitting of the O 1s spectra has been done taking into account only 1  $\text{OH}^-$  peak so it has been allowed to have a bigger full width

at half maximum (FWHM). Table 4.4 shows the assignment of the peaks for the spectra recorded at different temperatures. The  $O^{2-}$  peak increases as the surface becomes more oxidised with temperature.

Table 4.4. Peak assignments and their respective binding energies (eV) for the spectra of  $DbPO_2H$  on Fe(110) single crystal in Figures 4.12 and 4.13.

|                                   | Binding Energy (eV) |       |       |       |       |
|-----------------------------------|---------------------|-------|-------|-------|-------|
|                                   | C 1s                |       |       |       |       |
|                                   | RT                  | 373 K | 423 K | 473 K | 523 K |
| <b>Carbide C</b>                  | 282.7               | 282.8 | 282.9 | 282.8 | 283.0 |
| <b>C-C</b>                        | 284.6               | 284.6 | 284.7 | 284.5 | 284.5 |
| <b>C-C-O</b>                      | 285.6               | 285.4 | 285.6 | 285.5 | 285.5 |
| <b>C-O</b>                        | 286.8               | 286.7 | 286.9 | 286.8 | 286.8 |
|                                   | O 1s                |       |       |       |       |
| <b>Fe-O-P/<math>O^{2-}</math></b> | 529.5               | 529.5 | 529.6 | 529.7 | 529.7 |
| <b>OH<sup>-</sup></b>             | 531.4               | 531.4 | 531.9 | 531.3 | 531.3 |
| <b>Other</b>                      | 533.1               | 533.0 | 533.0 | 535.7 | 532.8 |
| <b>H<sub>2</sub>O</b>             | 535.7               | 535.7 | 535.8 | 533.0 | 535.4 |

The surface was then cleaned and the  $DbPO_2H$  was deposited again under the same conditions.  $CO_2$  gas was injected in the NAP cell very slowly in order to maintain a constant pressure of 2 mbar. The spectra recorded are shown in Figure 4.14.

The C 1s spectrum can be fitted with 6 chemical species of the same FWHM and it is very complicated. The most intense peak at 293.8 eV (maroon) is due to the  $CO_2$  gas, the peak at 288 and 286 eV are assigned to  $C=O$  and  $CO$  adsorbed on the surface respectively,<sup>31</sup> again confirming the formation of a  $FeCO_3$  layer. The peak at 283 eV (blue) is due to carbide carbon, this is bigger than it has been shown in previous experiments as it does not only come from contamination from the Fe crystal but also from impurities from the  $CO_2$  gas cylinder. Due to the presence of impurities and so many peaks the interpretation of the C 1s spectrum becomes very complicated. The

spectra are found to barely change when adding water and for this reason they will not be shown again (peak assignments are however shown in Table 4.5).

In the P 2p spectrum there is only one chemical species with peaks at 133.4 and 134.3 eV, corresponding to the deprotonated form of the phosphate ester.

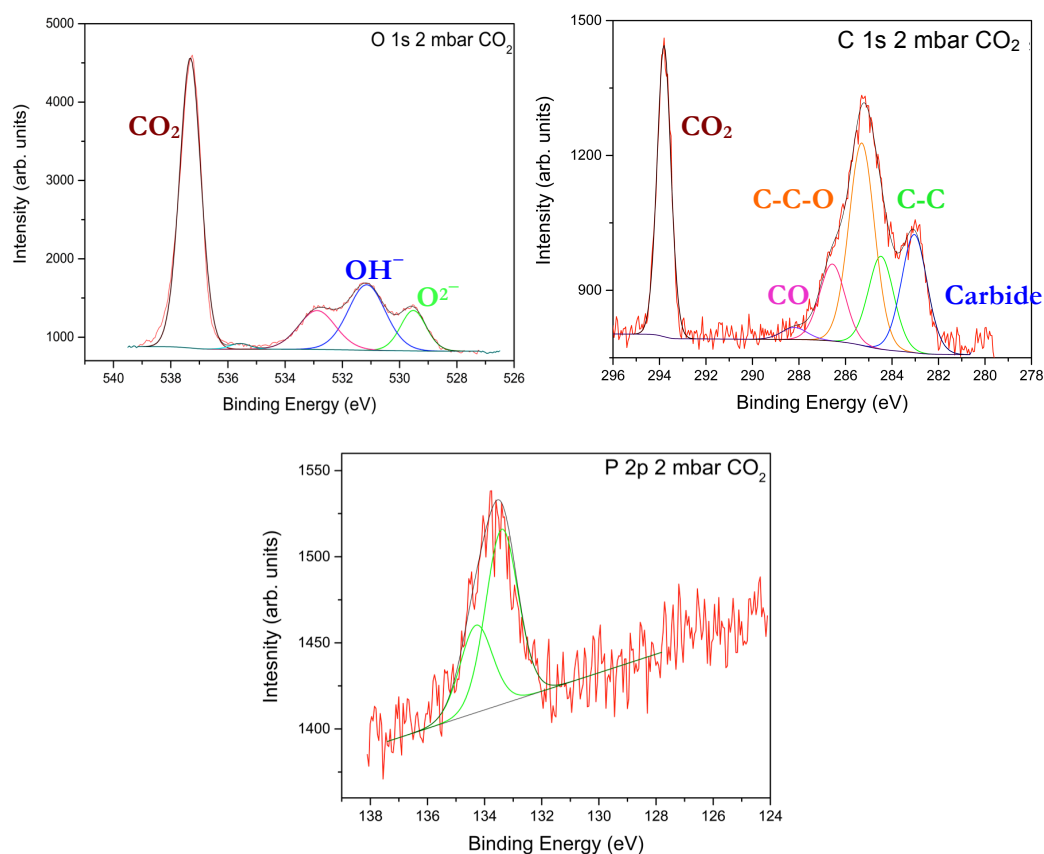


Figure 4.14. NAP XPS core level for O 1s (top left), C 1s (top right) and P 2p (bottom) for DbPO<sub>2</sub>H on an Fe(110) surface recorded in the presence of 2 mbar of CO<sub>2</sub>.

Figure 4.15 shows the O 1s spectra for DbPO<sub>2</sub>H in the presence of both CO<sub>2</sub> and H<sub>2</sub>O. Again the O 1s peak has been fitted with only one component for OH<sup>-</sup> allowing a broader FWHM. In these it can be seen that the surface does not become more oxidised when adding the water as the relative intensity of the peaks barely changes. Table 4.5 shows the assignment of the peaks for C 1s and O 1s recorded in the presence of CO<sub>2</sub> and H<sub>2</sub>O. In Figure 4.14 it can be seen that the presence of CO<sub>2</sub> does not appear to oxidise the surface as the relative intensity of the O<sup>2-</sup> peak to the H<sub>2</sub>O is much smaller than it was without the DbPO<sub>2</sub>H, suggesting that it binds to the active

sites on the surface stopping them from interacting with  $\text{CO}_2$  and forming oxide and/or carbonate. When letting the  $\text{H}_2\text{O}$  vapour in the NAP cell the surface barely oxidises suggesting that  $\text{DbPO}_2\text{H}$  may be a good corrosion inhibitor for Fe in a sweet environment.

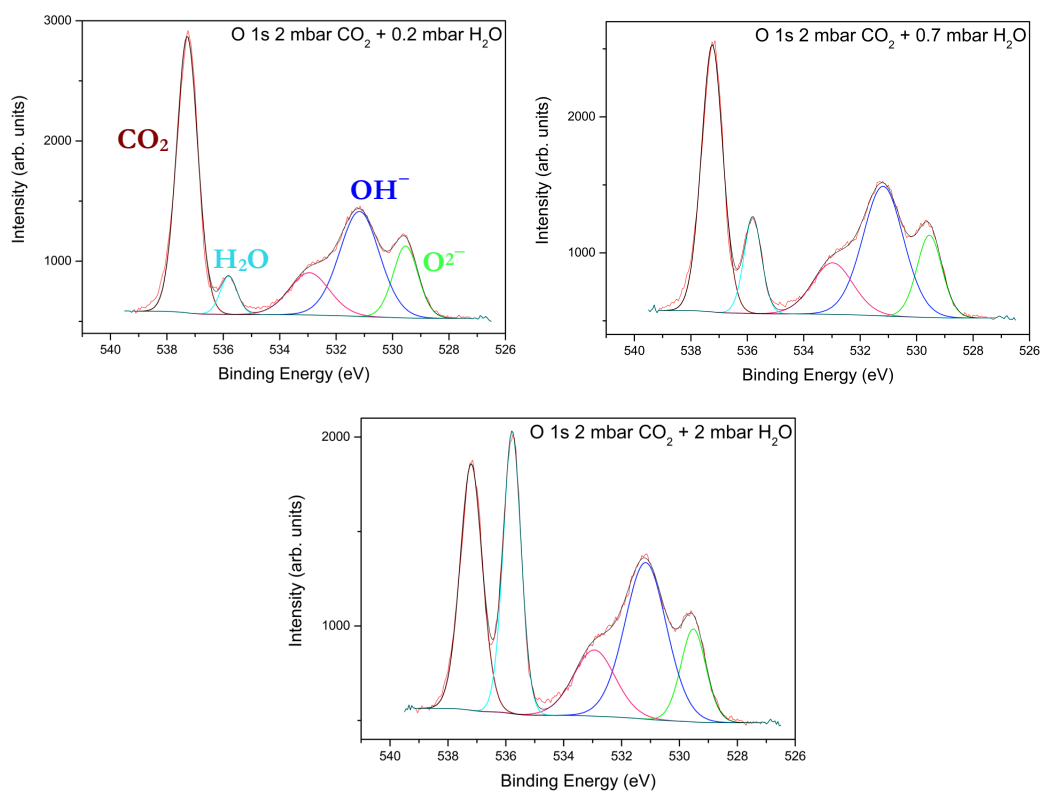


Figure 4.15. NAP XPS core level for O 1s for  $\text{DbPO}_2\text{H}$  on an Fe(110) surface recorded in the presence of 2 mbar of  $\text{CO}_2$  (top left) and with 0.7 (top right) and 2 mbar (bottom) of  $\text{H}_2\text{O}$ .

Table 4.5. Peak assignments and their respective binding energies (eV) for the spectra of DbPO<sub>2</sub>H on Fe(110) single crystal in figures 4.14 and 4.15.

|                              | Binding Energy (eV) |  |  |  |
|------------------------------|---------------------|--|--|--|
|                              | C 1s                |  |  |  |
|                              | 2 CO <sub>2</sub>   | 2 CO <sub>2</sub> + 0.2 H <sub>2</sub> O | 2 CO <sub>2</sub> + 0.7 H <sub>2</sub> O | 2 CO <sub>2</sub> + 2 H <sub>2</sub> O |
| <b>Carbide C</b>             | 283.0               | 283.0                                    | 283.1                                    | 283.0                                  |
| <b>C-C</b>                   | 284.5               | 284.6                                    | 284.8                                    | 284.7                                  |
| <b>Other</b>                 | 285.3               | 285.3                                    | 285.5                                    | 285.3                                  |
| <b>C-O</b>                   | 286.6               | 286.6                                    | 286.7                                    | 286.7                                  |
| <b>C=O</b>                   | 288.2               | 288.5                                    | 288.5                                    | 288.6                                  |
| <b>CO<sub>2</sub></b>        | 293.8               | 293.7                                    | 293.7                                    | 293.6                                  |
|                              | O 1s                |  |  |  |
| <b>Fe-O-P/O<sup>2-</sup></b> | 529.5               | 529.6                                    | 529.6                                    | 529.6                                  |
| <b>OH<sup>-</sup></b>        | 531.2               | 531.3                                    | 531.3                                    | 531.3                                  |
| <b>CO</b>                    | 532.9               | 533.0                                    | 533.1                                    | 533.1                                  |
| <b>H<sub>2</sub>O</b>        | 534.8               | 535.8                                    | 535.8                                    | 535.8                                  |
| <b>CO<sub>2</sub></b>        | 537.3               | 537.3                                    | 537.2                                    | 537.2                                  |

#### 4.3.4. PAE 136 on Fe(110) surface

Commercial corrosion inhibitor PAE 136 is a mixture of mono and diphosphate esters with different length chains and different ethoxylation levels as shown in Figure 4.16 manufactured by Lakeland Laboratories. They produce their corrosion inhibitors on a large scale and because purity is not important to get a good protection they do not carry out any purification processes. For this reason the composition of the commercial product is not well known and it contains a mixture of compounds with different chain lengths, the XPS spectra for it are expected to be complicated. Figure 4.16 shows the chemical structure of the components thought to be in the commercial corrosion inhibitor, including monoesters and diesters with different levels of ethoxylation.

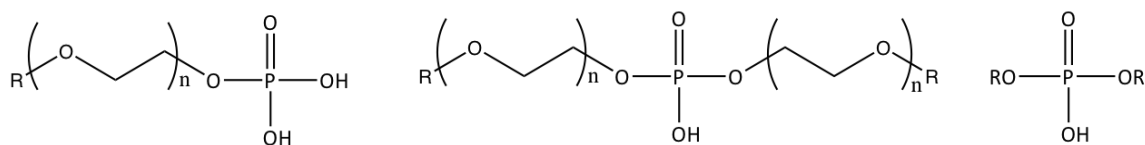


Figure 4.16. Chemical structure of the composition of the commercial corrosion inhibitor PAE 136 where  $n = 13-15$ .

#### 4.3.4.1. XPS study in UHV

A first deposition was carried out for 10 minutes by heating the PAE 136 inhibitor to 120 °C in a Knudsen cell. The spectra were collected at room temperature and at different temperatures in order to see how determine the ability of the inhibitor at higher temperatures.

Figure 4.17 shows the XPS spectra collected at room temperature. In the C 1s spectrum there are three main chemical species. The small blue peak at 282.8 eV is attributed to carbide C, the most intense peak (green) at 284.8 eV, is from the aliphatic chains and the pink peak at 286 eV is assigned to the C atoms bound to O atoms. The peak at 285 eV is assigned to the C atoms that are closer to the O atoms on the aliphatic chains, but not directly bound to them. There is a small peak at 287.5 eV (dark yellow) at a binding energy of which possibly arises from unknown minority species in the commercial corrosion inhibitor, which, as mentioned above is not purified.

The O 1s spectra can be fitted with three peaks corresponding to the same chemical species seen for  $\text{DbPO}_2\text{H}$  (see Figure 4.10 in the previous section), the green peak at 531.2 eV corresponds to the O atoms bound to the metallic surface, the peak at 532.6 eV (blue) is assigned to the O bound to the P ( $\text{P}=\text{O}$ ) and to the alkyl chains and the smallest peak in intensity at 533.7 eV is due to the O bound to the P atoms through a double bond, which are not interacting with the surface. The C 1s and O 1s assignments are specified in Table 4.6.

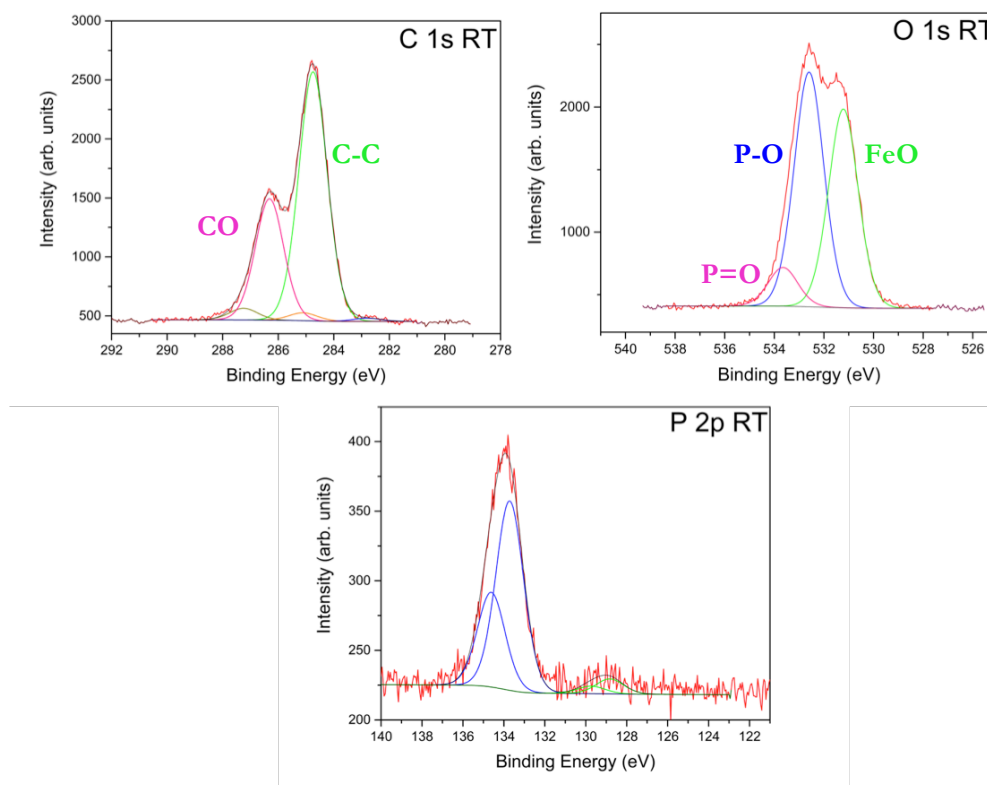


Figure 4.17. UHV XPS core level for C 1s (top left) and O 1s (top right) and P 2p (bottom) PAE 136 on an Fe(110) surface recorded at room temperature.

In the P 2p spectra there are two chemical species, the weak doublet at low binding energy (green) is barely visible and it will be explained in more detail in Section 4.4.2.2 where the NAP XPS results are presented. The P doublet with peaks at 133.7 and 134.6 eV is assigned to the deprotonated form of the phosphate meaning that there is no protonated O present on the surface. The P 2p spectra do not show any change when raising the temperature and for this reason will not be further discussed for in this section.

Table 4.6. Peak assignments and their respective binding energies (eV) for the spectra of PAE 136 on Fe(110) single crystal in Figures 4.17 and 4.18 in UHV.

|                  | <b>Binding Energy (eV)</b> |              |              |              |              |
|------------------|----------------------------|--------------|--------------|--------------|--------------|
|                  | <b>C 1s</b>                |              |              |              |              |
|                  | <b>RT</b>                  | <b>370 K</b> | <b>470 K</b> | <b>520 K</b> | <b>573 K</b> |
| <b>Carbide C</b> | 282.8                      | 282.8        | 283.0        | 283.0        | 283.1        |
| <b>C-C</b>       | 284.8                      | 284.8        | 284.6        | 284.7        | 284.7        |
| <b>C-C-O</b>     | 285.1                      | 285.5        | 285.3        | 285.4        | 185.5        |
| <b>C-O</b>       | 286.3                      | 286.5        | 286.4        | 286.5        | 286.6        |
|                  | <b>O 1s</b>                |              |              |              |              |
| <b>Fe-O-P</b>    | 531.2                      | 531.4        | 531.4        | 531.5        | 531.6        |
| <b>P-O</b>       | 532.6                      | 532.8        | 532.8        | 532.8        | 532.6        |
| <b>P=O</b>       | 533.6                      | 533.9        | 533.9        | 533.7        | 533.7        |

In Figure 4.18 all the spectra recorded in UHV and at different temperatures are shown. It can be seen that, for the C 1s spectra, the relative intensity of the C 1s peak assigned to the aliphatic chains (green) slightly increases with respect to the one assigned to the C-O bound, which decreases with respect to the unknown peak (orange).

The O 1s spectra at high temperatures show a similar behaviour to the DbPO<sub>2</sub>H data. The peak at 531.0 eV increases in intensity and the one at 532 eV decreases suggesting a different behaviour of the compound at high temperatures.

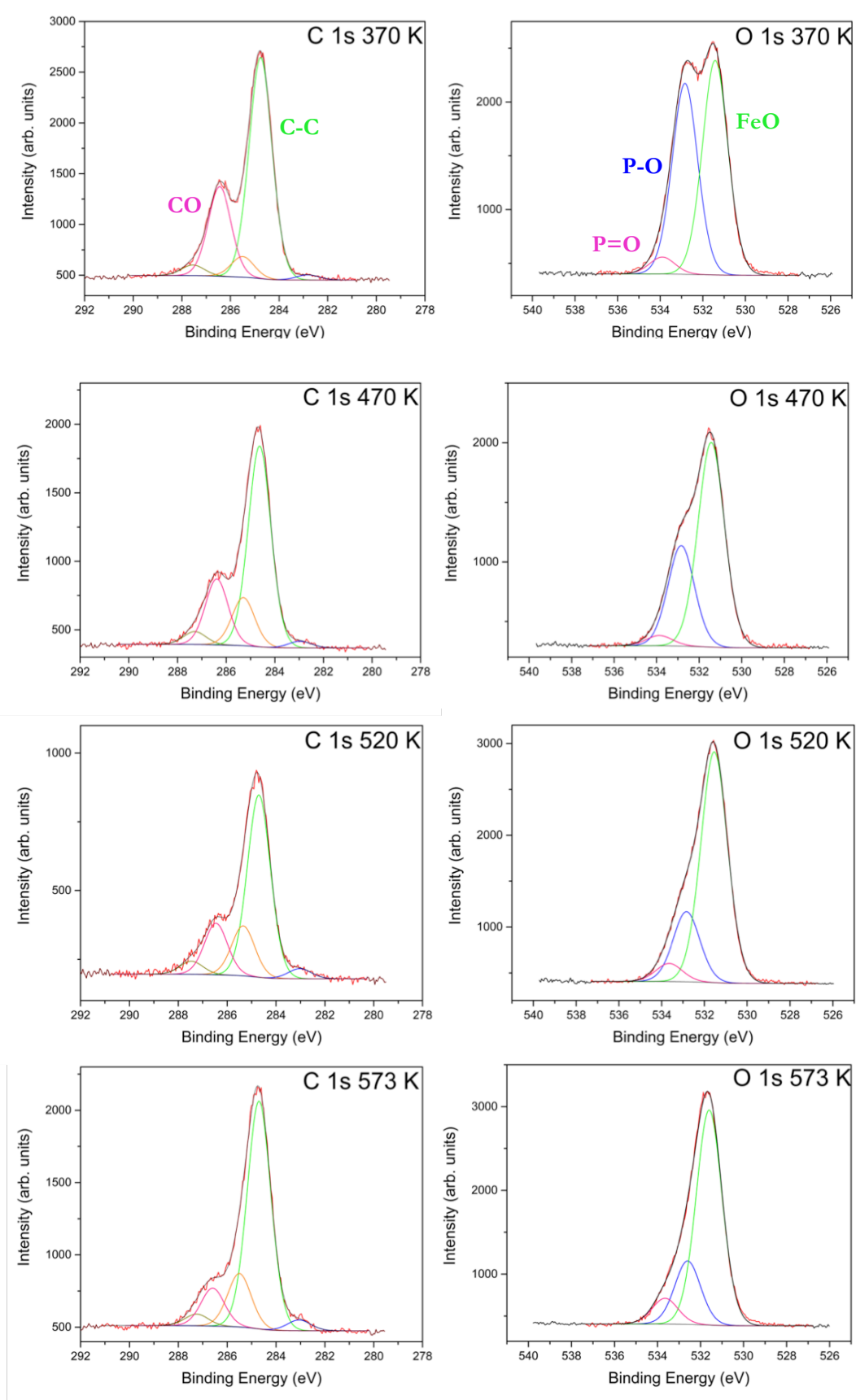


Figure 4.18. UHV XPS core level for C 1s (left) and O 1s (right) PAE 136 on an Fe(110) surface recorded at 370, 470, 520 and 573 K.

### 4.3.4.2. XPS study under NAP conditions

The Fe(110) crystal was cleaned, PAE 136 was deposited again by the same method as before and H<sub>2</sub>O was admitted into the NAP cell to a pressure of 0.3 mbar (Figure 4.19). In the O 1s spectrum there are the same three chemical species seen for the mixture of compounds in UHV plus a new peak at 535.9 eV due to the presence of H<sub>2</sub>O vapour.

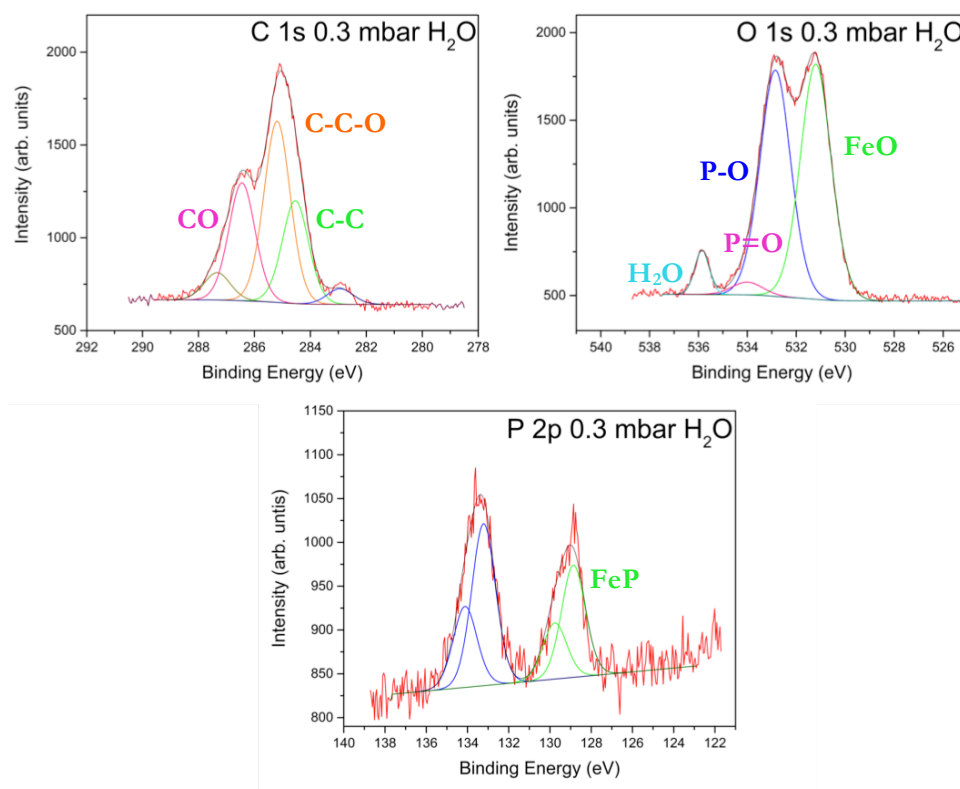


Figure 4.19. NAP XPS core level for C 1s (top left) and O 1s (top right) and P 2p (bottom) for PAE 136 on an Fe(110) surface recorded under a H<sub>2</sub>O pressure of 0.3 mbar.

In the P 2p spectrum there is a doublet with peaks at 133.2 and 134.1 eV assigned to P-O bound to the surface. There is a new doublet with peaks at 128.9 and 129.8 eV (green), the binding energy of which corresponds to iron phosphide.<sup>30,33</sup> It seems that, when in contact with the surface and water, the active compound reacts and the P is reduced whilst the surface oxidises. This metal phosphide creates a passivation layer that protects from further corrosion. This peak was also present in the UHV spectra

although with a very small relative intensity, it is not clear however why it is present when there is no H<sub>2</sub>O in the system.

The C 1s spectra do not provide much information. There are three main peaks, one at 284.5 eV (green) assigned to the C in the aliphatic chains; one at 285 eV (orange) assigned to the  $\beta$ -C to the O; and a peak at 286.5 eV (pink) assigned to the C atoms bound to the ethoxylated O atoms. The variation on the binding energies for this experiment could be due to the fact that the experiment was performed overnight. The spectra at room temperature were recorded one day and the temperature variation experiments were done the following day, with the sample left in the UHV overnight.

Table 4.7. Peak assignments and their respective binding energies (eV) for the spectra of PAE 136 on Fe(110) single crystal in Figures 4.19, 4.20 and 4.21 under H<sub>2</sub>O pressure (mbar) and at different temperatures (K).

|                              | Binding Energy (eV)      |                        |                         |                         |                             |
|------------------------------|--------------------------|------------------------|-------------------------|-------------------------|-----------------------------|
|                              | C 1s                     |                        |                         |                         |                             |
|                              | 0.3 H <sub>2</sub> O, RT | 3 H <sub>2</sub> O, RT | 3 H <sub>2</sub> O, 373 | 3 H <sub>2</sub> O, 423 | 3 H <sub>2</sub> O, 423 (2) |
| <b>Carbide C</b>             | 282.9                    | 282.9                  | 282.8                   | 282.9                   | 282.9                       |
| <b>C-C</b>                   | 284.5                    | 284.5                  | 284.5                   | 284.5                   | 284.3                       |
| <b>C-C-O</b>                 | 285.2                    | 285.2                  | 285.3                   | 285.9                   | 285.2                       |
| <b>C-O</b>                   | 286.5                    | 286.5                  | 286.6                   | 286.6                   | 286.2                       |
| <b>C=O</b>                   | 287.3                    | 287.6                  | 287.7                   | 287.7                   | 286.9                       |
|                              | O 1s                     |                        |                         |                         |                             |
| <b>Fe-O-P/O<sup>2-</sup></b> | 531.2                    | 531.2                  | 531.3                   | 531.3                   | 531.3                       |
| <b>OH<sup>-</sup></b>        | 532.9                    | 532.9                  | 532.7                   | 532.3                   | 532.1                       |
| <b>CO</b>                    | 534.0                    | 534.0                  | 533.6                   | 533.7                   | 533.3                       |
| <b>H<sub>2</sub>O</b>        | 535.9                    | 535.9                  | 535.8                   | 535.7                   | 535.7                       |

Figure 4.20 shows the spectra recorded with the sample exposed to 3 mbar of H<sub>2</sub>O vapour. It can be seen that the spectra do not change much when increasing the pressure as the relative intensities of the oxide and hydroxide peaks in the O 1s spectrum are the same compared as those recorded at 0.3 mbar.

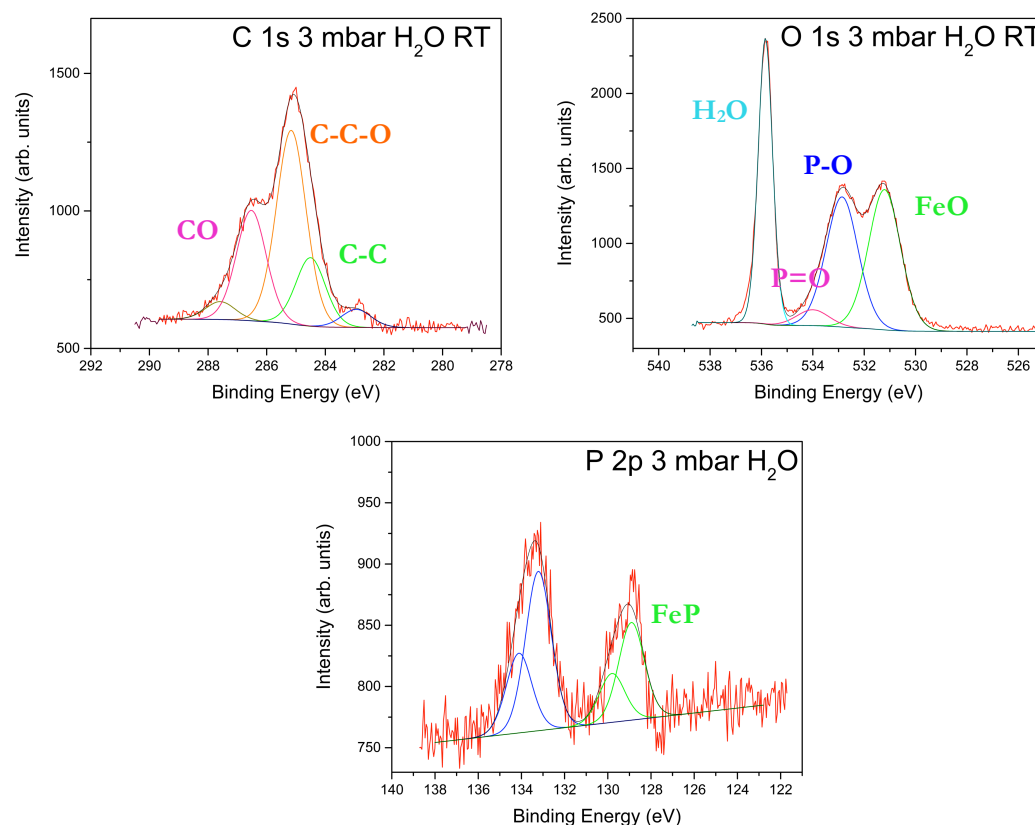


Figure 4.20. NAP XPS core level for C 1s (top left) and O 1s (top right) and P 2p (bottom) for PAE 136 on an Fe(110) surface recorded under a H<sub>2</sub>O pressure of 3 mbar.

Finally the sample was heated to 373 and 423 K and the core level spectra were recorded (Figure 4.21). As recording each set of spectra takes more than 2 hours it is important to check if there are any changes with time. For this reason the spectra were recorded at 423 K three times and the resulting data was compared. Figure 4.21 shows the O 1s spectra recorded at 423 K with a time difference of approximately 4 hours. In these spectra it can be seen that the surface becomes more oxidised as the oxide peak's relative intensity increases in the second spectrum. This suggests that the oxidation does not reach a static state and even though there is no change in H<sub>2</sub>O vapour pressure or temperature of the sample, the surface continues to oxidise.

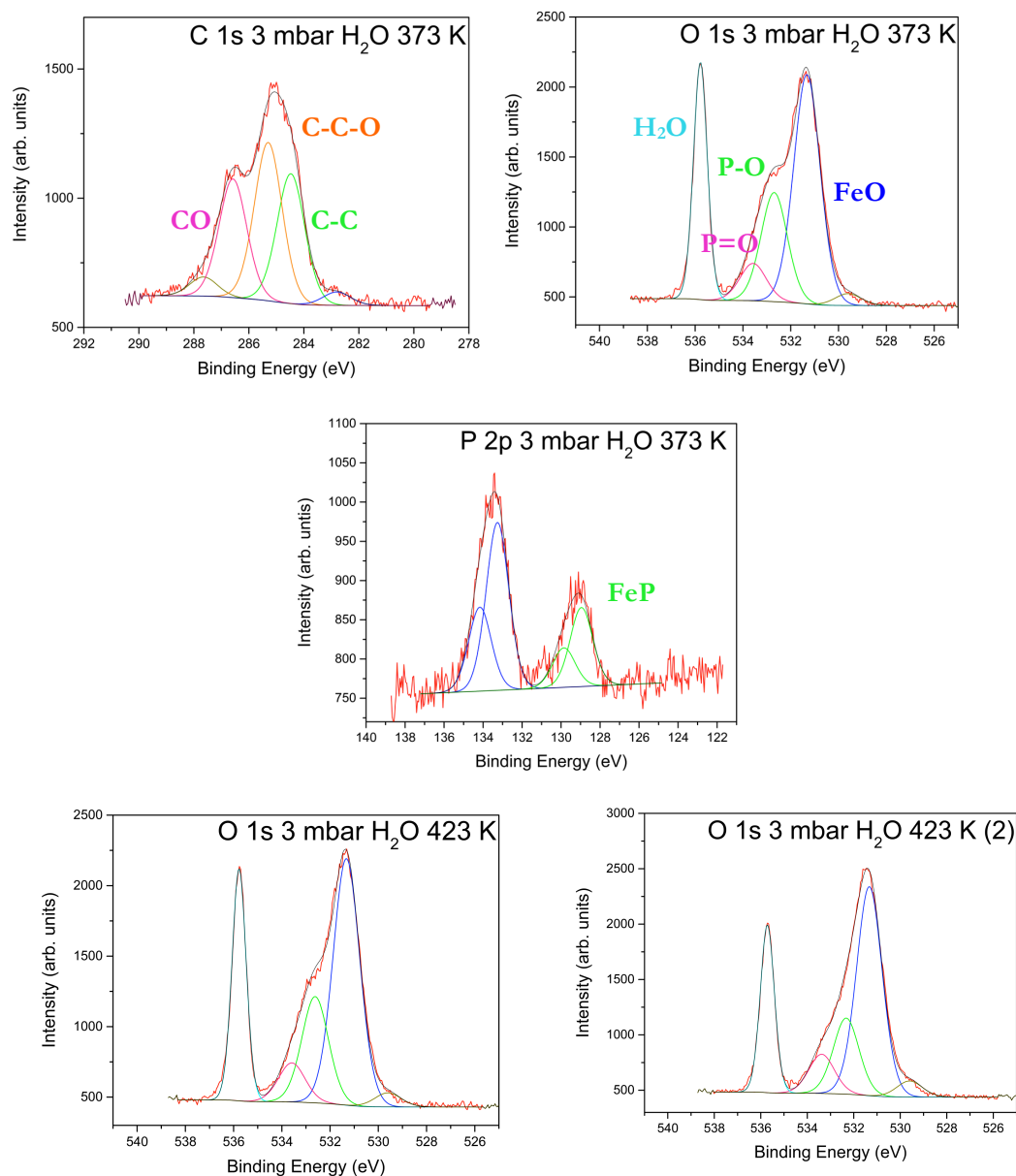


Figure 4.21. NAP XPS core level for C 1s (top left) and O 1s at 373 K (top right), P 2p (middle) and O 1s (bottom) at 423 K measured with 4 h of difference for PAE 136 on an Fe(110) surface recorded under a H<sub>2</sub>O pressure of 3 mbar.

The CO<sub>2</sub>/H<sub>2</sub>O pressure experiment was not performed on PAE 136 because when these series of experiments were done the NAP XPS instrument did not have CO<sub>2</sub> gas installed.

## 4.4. Conclusions

XPS studies at near ambient pressure (NAP) on a Fe(110) single crystal show that this ideal Fe(110) surface oxidises in the presence of H<sub>2</sub>O at high temperatures. The presence of CO<sub>2</sub> also causes oxidation in the form of FeCO<sub>3</sub>, even when no H<sub>2</sub>O is added to the NAP cell. However, this does not mean that pure CO<sub>2</sub> is the corroding agent because in a sweet environment it is the acidic HCO<sub>3</sub><sup>-</sup> that causes oxidation. The cause of the oxidation in this study might be a result of trace impurities such as CO in the CO<sub>2</sub> or the displacement of H<sub>2</sub>O or CO from the walls of the NAP cell. The combination of high CO<sub>2</sub> and H<sub>2</sub>O pressure results in oxidation of the surface but an increase in the H<sub>2</sub>O pressure does not cause a substantial increase in the intensities of the oxidation peaks.

The adsorption of dibutyl phosphate ester (DbPO<sub>2</sub>H) has been studied as an ideal model that leads to a better understanding of the data obtained from the commercial corrosion inhibitor's experiment. In UHV it is always deprotonated on the surface and exhibits a mixed bidentate and monodentate binding mode, with the bidentate mode being more thermally stable. Both in the presence of ambient pressures of H<sub>2</sub>O vapour and a combination of CO<sub>2</sub> and H<sub>2</sub>O, DbPO<sub>2</sub>H remains bonded to the surface and presents the same binding modes in each case. DbPO<sub>2</sub>H does not stop oxidation of the Fe surface in the presence of H<sub>2</sub>O at high temperatures, but reduces it in the presence of the CO<sub>2</sub>:H<sub>2</sub>O mixture, potentially making it a good corrosion inhibitor for a sweet environment at low or ambient pressures.

The results obtained for PAE 136, a commercial corrosion inhibitor, are difficult to interpret because of the mixture of compounds in the sample. However, comparison with the results obtained from DbPO<sub>2</sub>H suggests that PAE 136 binds to the surface in a similar manner to DbPO<sub>2</sub>H in UHV. At higher temperatures PAE 136 shows a different behaviour where it seems to promote oxidation of the surface, whereas DbPO<sub>2</sub>H does not. In the presence of H<sub>2</sub>O vapour PAE 136 does not stop oxidation, instead some of the P reduces whilst the Fe is oxidised. This appears to create an iron phosphide film that is thought to protect the surface from further corrosion.

It is not clear if the phosphide formation is deliberate and given by the main components to create a passivation layer on the commercial mixture or, whether it is a secondary process caused by the impurities and minority products, but it is not seen for  $\text{DbPO}_2\text{H}$ . Oxidation does not stop when the  $\text{H}_2\text{O}$  pressure and all other conditions are kept constant, the surface keeps getting more oxidised with time.

According to the obtained results, it is thought that  $\text{DbPO}_2\text{H}$  could be a better inhibitor than PAE 136 for Fe in a sweet environment at low pressures. However, this experiment has been performed in an ideal clean environment and this might be different in the presence of crude oil or for a real steel surface at high pressure and temperature.

## 4.5. References

- 1 E. J. Mittemeijer, *Fundamentals of Materials Science: The Microstructure-Property Relationship*, Springer, Berlin, 2010.
- 2 J. Häglund, G. Grimvall and T. Jarlborg, *Phys. Rev. B*, 1991, **44**, 2914–2919.
- 3 C. S. Kuivila, J. B. Butt and P. C. Stair, *Appl. Surf. Sci.*, 1988, **32**, 99–121.
- 4 J. B. Butt, *Catal. Letters*, 1990, **7**, 61–81.
- 5 T. L. Barr, *J. Vac. Sci. Technol. A Vacuum, Surfaces, Film.*, 1995, **13**, 1239–1246.
- 6 E. Papastavros, P. J. Shea and M. A. Langell, *Langmuir*, 2004, **20**, 11509–11516.
- 7 P. F. Alewood, R. B. Johns and R. M. Valerio, *Synthesis*, 1983, 30–31.
- 8 V. B. Oza and R. C. Corcoran, *J. Org. Chem.*, 1995, **60**, 3680–3684.
- 9 A. J. O’Lenick and J. K. Parkinson, *Surfactants*, 1995, **27**, 17–20.
- 10 B. Alink, S. A. Ramachandran, S. A. Campbell, B. A. Outlaw and V. A. Jovancicevic, *Corros. 99*, 1999, **37**.

- 11 S. Whitfield, *Sci. Technol. Concr. Admixtures*, 2015, 471–479.
- 12 A. Shida, H. Sugimura, M. Futsuhara and O. Takai, *Surf. Coatings Technol.*, 2003, **169-170**, 686–690.
- 13 I. Felhősi and E. Kálmán, *Corros. Sci.*, 2005, **47**, 695–708.
- 14 P. M. Karlsson, A. Baeza, A. E. C. Palmqvist and K. Holmberg, *Corros. Sci.*, 2008, **50**, 2282–2287.
- 15 R. G. Wurstner, 1965, **3215715**, United States.
- 16 J. Bretz, 1968, **3411923**, United States.
- 17 R. L. Martin and R. R. Annand, *Corrosion*, 1981, **37**, 297–301.
- 18 R. L. Martin, 1985, **4722805**, United States.
- 19 X. Gao, S. Liu, H. Lu, F. Gao and H. Ma, *Ind. Eng. Chem. Res.*, 2015, **54**, 1941–1952.
- 20 J. W. Bishop and N. J. Roselle, 1951, **2574954**, United States.
- 21 A. L. Larsen, 1974, **3836462**, United States.
- 22 B. T. Outlaw, B. A. Oude Alink, J. A. Kelley and C. S. Caywell, *4511480*, 1983, United States.
- 23 A. Naraghi and N. Grahmann, 1996, **5611992**, United States.
- 24 Casa Software Ltd., *CasaXPS Version 2.3.16 PR 1.6*.
- 25 D. Briggs, *Surface Analysis by Auger and X-ray Photoelectron Spectroscopy*, IM Publications, Chichester, 2003.
- 26 M. Textor, L. Ruiz, R. Hofer, A. Rossi, K. Feldman, G. Hähner and N. D. Spencer, *Langmuir*, 2000, **16**, 3257–3271.
- 27 A. P. Grosvenor, B. A. Kobe and N. S. McIntyre, *Surf. Sci.*, 2004, **572**, 217–227.

- 28 A. P. Grosvenor, B. A. Kobe and N. S. McIntyre, *Surf. Sci.*, 2004, **565**, 151–162.
- 29 A. P. Grosvenor, B. A. Kobe, M. C. Biesinger and N. S. McIntyre, *Surf. Interface Anal.*, 2004, **36**, 1564–1574.
- 30 A. P. Grosvenor, S. D. Wik, R. G. Cavell and A. Mar, *Inorg. Chem.*, 2005, **44**, 8988–8998.
- 31 D. J. Miller, M. C. Biesinger and N. S. McIntyre, *Surf. Interface Anal.*, 2002, **33**, 299–305.
- 32 M. Wagstaffe, A. Thomas, M. J. Jackman, M. Torres-Molina, K. L. Syres and K. Handrup, *J. Phys. Chem. C*, 2016, **120**, 1693–1700.
- 33 L. Song, S. Zhang, X. Wu and K. Wang, *Vacuum*, 2015, **112**, 12–16.



## Chapter 5. Phosphonic acids for the protection of Fe



## 5.1. Introduction

Organic phosphonic acids are surface active compounds that have been shown to act as corrosion inhibitors in water-cooling systems and are environmentally friendly as they do not contain any heavy metals or inorganic components.<sup>1</sup> Figure 5.1 shows some known phosphonic acids used as corrosion inhibitors.<sup>2</sup> It is believed that they inhibit corrosion by reacting with the surface by oxidizing it and forming sparingly soluble compounds, which then precipitate on the surface, to form a protective film that prevents corrosive agents from attacking the surface.<sup>3,4</sup> Kuznetsov used the term, ‘corrosion inhibitors of the complexing type’ because they act by complexation with metal surfaces.<sup>5</sup> In the oil and gas industry phosphate esters are used instead of organic phosphonic acids. They are added to the crude oil in order to inhibit corrosion in upstream processes (Chapter 1 and Chapter 4). However it is relevant to study both families and for this reason both phosphonic acids and phosphate esters have been studied on a Fe(110) single crystal and steel (Chapter 6) in order to understand the inhibitive mechanism and investigate similarities and differences on mode of action under different conditions.

The phosphonate group has three oxygen atoms with lone pairs of electrons that can interact with the vacant orbitals of a transition metal surface. They can potentially interact with a surface in many different ways (Figure 5.2) so it would be of interest if it could be identified whether or not certain binding modes confer greater inhibition properties, and whether this might be something that could ultimately be controlled to make improved inhibitor compounds. Vibrational spectroscopy and X-ray spectroscopy have been selected as the tools to probe the binding mode and coupled these measurements with a model compound approach. Such a systematic study has not been reported previously for this functional group.

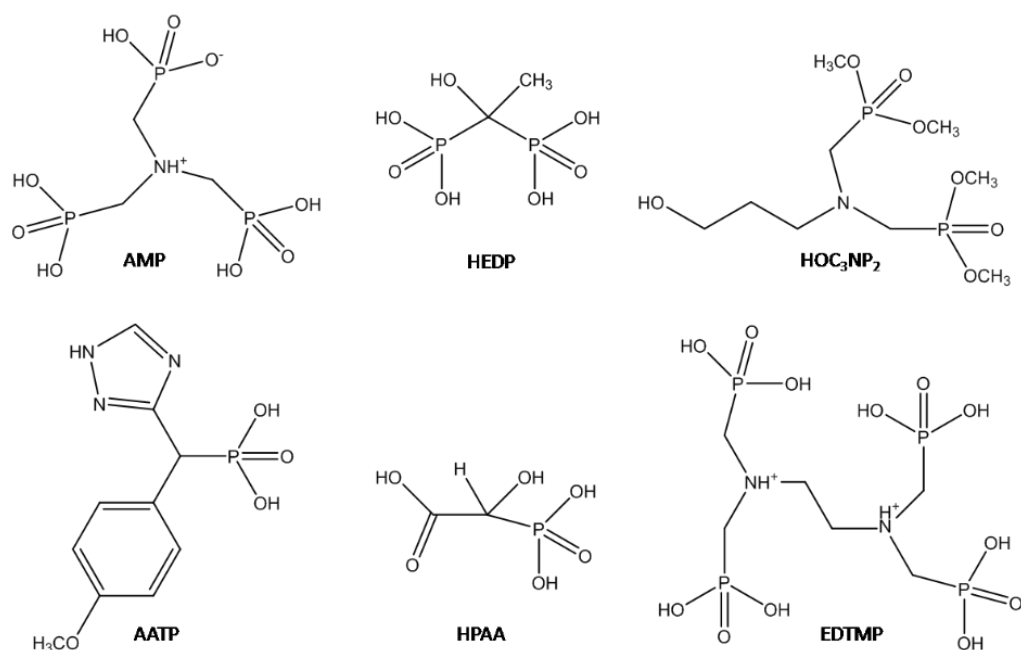


Figure 5.1. Some organic phosphonic acids and esters used as corrosion inhibitors.

Abbreviations: AMP = amino-tris(methylene-phosphonic acid), HEDP = 1-hydroxyethylidene-bisphosphonic acid, HO<sub>3</sub>NP<sub>2</sub> = N,N-tetramethyl-bis(phosphonate)-3-hydroxylpropyl-bis(methylene)amine, AATP = 3-anisalidene-amino-1,2,4-triazole phosphonate, HPAA = hydroxyphosphonoacetic acid, EDTMP = ethylenediamine-tetrakis(methylenephosphonic acid).<sup>2</sup>

X-ray Photoelectron Spectroscopy (XPS) and Near Edge X-ray absorption Fine Structure (NEXAFS) are powerful techniques that allow us to obtain information about the elemental and chemical composition, the electronic structure, the binding mode and orientation of the molecules on a surface as well as the state of the surface itself. A combination of studying the fingerprints of the model complexes and the surface measurements should lead to a good understanding on how these compounds interact with metals.

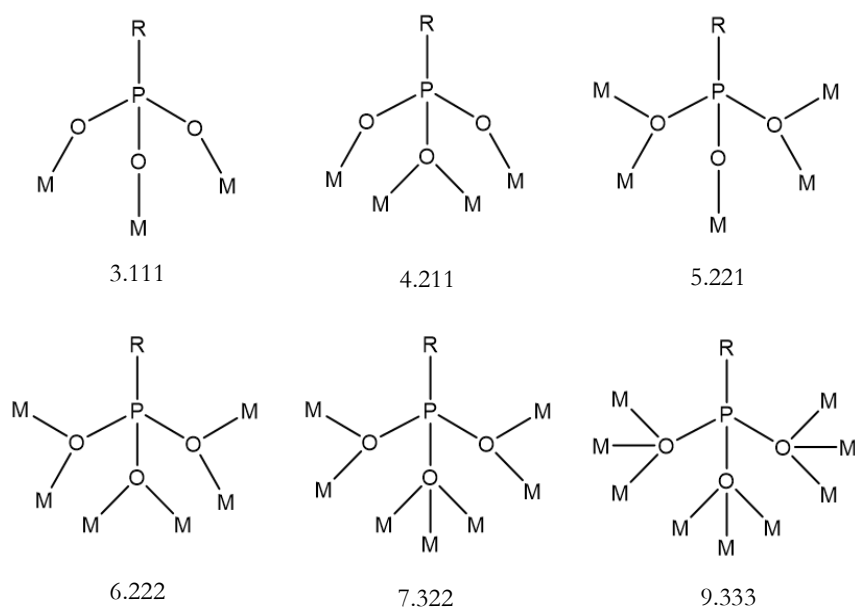


Figure 5.2. An illustration of a number of possible binding modes for doubly deprotonated phosphonate ligands labelled using Harris notation.<sup>6</sup>

The chemistry of phosphonate ligands is widely studied in coordination chemistry due to the great versatility in their binding modes and the structures they can adopt. Organic phosphonic acids have two replaceable protons and can bind up to nine metal atoms. Figure 5.2 shows some of the possible binding modes for phosphonate ligands, labeled using the Harris notation.<sup>6</sup>

The interaction of organic phosphonic acids with different oxide surfaces has recently been studied by XPS as they are good surface modifying agents and are used to improve the efficiency in organic electronic applications.<sup>7,8,9</sup> They have been shown to have higher binding energies to metal oxides than other compounds such as benzoic acids.<sup>10</sup> Perkins *et al.* found that hexylphosphonic acid interacts with a ZnO surface bonding in a tridentate mode<sup>11</sup> (see 3.111 binding mode in Figure 5.2).

The adsorption of phenylphosphonic acid ( $\text{PhPO}_3\text{H}_2$ ) has previously been studied on an amorphous alumina surface ( $\text{Al}_2\text{O}_3$ ).<sup>12</sup> In that study it was shown that the acid group reacts with the hydroxyl groups in the aluminium oxide surface to form a chemical bond through the three oxygen atoms. As part of this project it has recently been reported the deposition of phenylphosphonic acid on anatase  $\text{TiO}_2(101)$  single crystal.<sup>13</sup> The XPS data show that at low coverage the phosphonate group deprotonates when

interacting with the surface and it binds to the surface through two O atoms. When the deposition time is increased and there is more compound on the surface the compound binds both as bidentate and monodentate (Figure 5.3). Angle resolved NEXAFS measurements show that the phosphonic acid binds to the surface with the aromatic ring at 25 ° relative to the surface normal.<sup>13</sup>

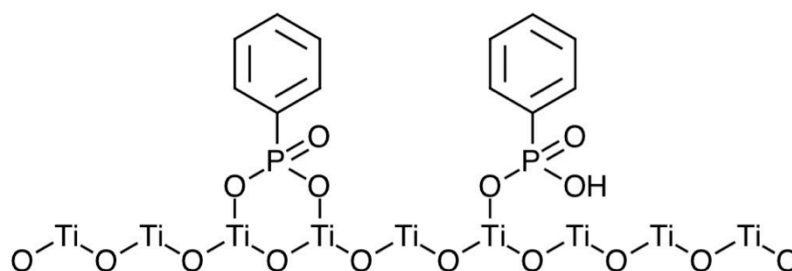


Figure 5.3. Illustration representing the suggested binding modes for phenylphosphonic acid on an anatase  $\text{TiO}_2(101)$  surface.<sup>13</sup>

Both  $\text{PhPO}_3\text{H}_2$  and benzylphosphonic acid ( $\text{BzPO}_3\text{H}_2$ ) have been studied on a gallium doped zinc oxide surface showing a tridentate binding mode<sup>14</sup> (see 3.111 binding mode in Figure 5.2).

Even though some work on phosphonates has been done on oxide surfaces nothing has been reported on pure single crystal Fe. Such a study can be helpful to understand the anticorrosive properties of phosphorus based corrosion inhibitors that are used for the protection of steel.

Here the infrared spectra of twelve compounds synthesized with  $\text{PhPO}_3\text{H}_2$  and *tert*-butylphosphonic acid ( $\text{tBuPO}_3\text{H}_2$ ) it are reported as well as the assignment of the bands involving the phosphonate group for different binding modes. The XPS spectra for  $\text{PhPO}_3\text{H}_2$ ,  $\text{tBuPO}_3\text{H}_2$  and hexadecylphosphonic acid ( $\text{HdPO}_3\text{H}_2$ ) on a single crystal Fe(110) surface in ultra high vacuum (UHV) and the behavior when increasing the temperature are also reported. Hexadecylphosphonic acid was of special interest as it has long aliphatic chains, a similar structure to the commercial corrosion inhibitor PAE136 presented in Chapter 4 and might help understanding its behavior better.

## 5.2. Model compounds

### 5.2.1. Experimental

Reagents were purchased from Aldrich and used without further purification. All solvents were from Fisher Scientific and Sigma Aldrich and were used without further purification.

Analytical data were obtained by the Microanalytical Service at the University of Manchester. Carbon, nitrogen, phosphorus and hydrogen analysis was performed using a Flash 200 elemental analyser. Metal analysis was performed by Thermo iCap 6300 Inductively Coupled Plasma Optical Emission Spectroscopy (ICP-OES).

IR spectra of neat powders were recorded using a Thermo Scientific Nicolet iS5 FTIR spectrometer equipped with an iD5 ATR. The penetration depth of the beam is directly proportional to the wavelength of the incident beam, which means that photons with higher wavenumbers penetrate the sample less than photons with lower wavenumbers. This causes attenuation on the intensity of the peaks on the left hand side of the spectra.

Raman spectra were recorded with a HORIBA T64000 Raman Spectrometer in the Photon Science Institute at the University of Manchester.

X-ray data were collected in-house on a SuperNova, Single source at offset Atlas diffractometer. Using Olex2,<sup>31</sup> the structure was solved with the Superflip<sup>32</sup> structure solution program using Charge Flipping and refined with the ShelXL<sup>33</sup> refinement package using Least Squares minimisation.

**[Fe<sub>3</sub>O(PhCO<sub>2</sub>)<sub>6</sub>(H<sub>2</sub>O)<sub>3</sub>]Cl (17):** PhCO<sub>2</sub>H (50 mmol, 6.10 g) and NaOH (48 mmol, 1.92 g) of NaOH were dissolved in H<sub>2</sub>O (40 mL) and the solution was stirred for 30 min. To the reaction mixture a solution of FeCl<sub>3</sub>·6H<sub>2</sub>O (4.32 g, 16 mmol) in H<sub>2</sub>O (40 mL) was added leading to the appearance of an orange precipitate which was filtered and washed with H<sub>2</sub>O.<sup>15,16</sup>

**[Fe<sub>3</sub>O(PhCO<sub>2</sub>)<sub>6</sub>(H<sub>2</sub>O)<sub>3</sub>]NO<sub>3</sub> (18):** PhCO<sub>2</sub>H (50 mmol, 6.10 g) and NaOH (48 mmol, 1.92 g) were dissolved in H<sub>2</sub>O (40 mL). The solution was stirred for 30 min. To the reaction mixture a solution of FeNO<sub>3</sub>·9H<sub>2</sub>O (6.46 g, 16 mmol) in H<sub>2</sub>O (40 mL) was added leading to the appearance of an orange precipitate which was filtered and washed with H<sub>2</sub>O.<sup>15,16</sup>

**[Fe<sub>3</sub>O(<sup>t</sup>BuCO<sub>2</sub>)<sub>6</sub>(H<sub>2</sub>O)<sub>3</sub>]NO<sub>3</sub> (19):** <sup>t</sup>BuCO<sub>2</sub>H (50 mmol, 5.10 g) and NaOH (48 mmol, 1.92 g) were dissolved in H<sub>2</sub>O (40 mL). The solution was stirred for 30 min. To the reaction mixture a solution of FeNO<sub>3</sub>·9H<sub>2</sub>O (6.46 g, 16 mmol) in H<sub>2</sub>O (40 mL) was added leading to the appearance of an orange precipitate, which was filtered and washed with H<sub>2</sub>O.<sup>15,16</sup>

**[Fe<sub>3</sub>O(<sup>t</sup>BuCO<sub>2</sub>)<sub>6</sub>(H<sub>2</sub>O)<sub>3</sub>](<sup>t</sup>BuCO<sub>2</sub>)·2<sup>t</sup>BuCO<sub>2</sub>H (20):** FeNO<sub>3</sub>·9H<sub>2</sub>O (20.0 g, 48 mmol) was reacted with an excess of <sup>t</sup>BuCO<sub>2</sub>H (60 g, 600 mmol) at 160 °C for 4 h until the elimination of NO<sub>2</sub> had finished. The flask was cooled to 80 °C and EtOH (180 mL) was added. The obtained solution was diluted by adding H<sub>2</sub>O (50 mL) dropwise and cooled to room temperature. The red/brown crystalline precipitate was filtered the next day and washed with toluene and hexane. The EtOH and H<sub>2</sub>O were removed by drying to give [Fe<sub>3</sub>O(<sup>t</sup>BuCO<sub>2</sub>)<sub>6</sub>(H<sub>2</sub>O)<sub>3</sub>](<sup>t</sup>BuCO<sub>2</sub>)·2<sup>t</sup>BuCO<sub>2</sub>H.<sup>17</sup>

**[Fe<sub>3</sub>O(<sup>t</sup>BuCO<sub>2</sub>)<sub>6</sub>(H<sub>2</sub>O)<sub>3</sub>]Cl (21):** <sup>t</sup>BuCO<sub>2</sub>H (50 mmol, 5.10 g) and NaOH (48 mmol, 1.92 g) of NaOH were dissolved in H<sub>2</sub>O (40 mL) and the solution was stirred for 30 min. To the reaction mixture a solution of FeCl<sub>3</sub>·6H<sub>2</sub>O (4.32 g, 16 mmol) in H<sub>2</sub>O (40 mL) was added leading to the appearance of an orange precipitate, which was filtered and washed with H<sub>2</sub>O.<sup>15,16</sup>

**[Fe<sub>7</sub>O<sub>2</sub>(PhCO<sub>2</sub>)<sub>9</sub>(PhPO<sub>3</sub>)<sub>4</sub>(py)<sub>6</sub>] (22):** A solution of **17** (0.61 g, 0.61 mmol), py (0.29 mL, 3.7 mmol) and PhPO<sub>3</sub>H<sub>2</sub> (0.19 g, 1.22 mmol) in MeCN/CH<sub>2</sub>Cl<sub>2</sub> 1:1 (10 mL) was stirred for 5 h and then filtered. Et<sub>2</sub>O was allowed to diffuse into the red filtrate giving red crystals.<sup>18</sup> Elemental analysis calculated (%) for C<sub>117.5</sub>H<sub>96</sub>Fe<sub>7</sub>N<sub>6</sub>O<sub>32</sub>ClP<sub>4</sub>: C 53.17, H 3.65, N 3.17, Fe 14.73, P 4.67; found: C 53.23, H 3.50, N 3.20, Fe 15.13, P 4.56.<sup>40</sup> ATR-FTIR ν/cm<sup>-1</sup>: 2362 (w), 1609 (m), 1568 (m), 1548 (m), 1528 (w), 1445 (w), 1402 (s), 1218 (m), 1175 (m), 1134 (m), 1090 (s), 1063 (s), 1040 (w), 1007 (m),

993 (m), 865 (w), 839 (w), 755 (s), 695 (s), 673 (m), 631 (m), 543 (s). Raman  $\nu/\text{cm}^{-1}$ : 618 (m), 652 (w), 722 (w), 844 (m), 867 (m), 1003 (s), 1012 (s), 1041 (m), 1062 (m), 1105 (w), 1136 (br, m), 1148 (br, m), 1222 (w), 1408 (br, m), 1432 (br, m).

**[Fe<sub>7</sub>O<sub>2</sub>(PhCO<sub>2</sub>)<sub>8</sub>(NO<sub>3</sub>)(PhPO<sub>3</sub>)<sub>4</sub>(py)<sub>6</sub>] (23):** The same procedure was followed as for compound **22** but replacing **17** with **18**.<sup>18</sup> Elemental analysis calculated (%) for C<sub>110</sub>H<sub>90</sub>Fe<sub>7</sub>N<sub>7</sub>O<sub>33</sub>P<sub>4</sub>: C 51.76, H 3.55, N 3.84, P 4.88; found C 52.52, H 3.15, N 3.38, P 4.56. ATR-FTIR  $\nu/\text{cm}^{-1}$ : 3056 (br, w), 1608 (m), 1568 (m), 1547 (m), 1492 (w), 1400 (br, s), 1218 (m), 1134 (m), 1088 (s), 1062 (s), 1039 (w), 1006 (m), 993 (m), 865 (w), 839 (w), 754 (w), 754 (m), 716 (s), 695 (s), 673 (m), 632 (m), 543 (m). Raman  $\nu/\text{cm}^{-1}$ : 480 (br, w), 620 (w), 635 (w), 849 (m), 1004 (s), 1013 (s), 1043 (m), 1106 (w), 1141 (br, w), 1222 (w), 1406 (m), 1432 (m).

**[Fe<sub>6</sub>O<sub>2</sub>(O<sub>2</sub>)(<sup>t</sup>BuCO<sub>2</sub>)<sub>8</sub>(PhPO<sub>3</sub>)<sub>2</sub>(H<sub>2</sub>O)<sub>2</sub>] (24):** **19** (0.26 g, 0.28 mmol) and PhPO<sub>3</sub>H<sub>2</sub> (45.1 mg, 0.28 mmol) were added to MeCN (7 mL) and 2 drops of H<sub>2</sub>O<sub>2</sub> (30% in H<sub>2</sub>O) were added. The solution was stirred for 1 h after which it turned red. Dark red crystals appeared after leaving the solution undisturbed at 4 °C.<sup>18</sup> Elemental analysis calculated (%) for C<sub>42</sub>H<sub>81</sub>Fe<sub>6</sub>NO<sub>28</sub>P<sub>4</sub>: C 33.47, H 5.42, N 0.93, P 8.22; found: C 33.98, H 5.67, N 0.97, P 8.05. ATR-FTIR  $\nu/\text{cm}^{-1}$ : 2961 (br, w), 1557 (m), 1530 (m), 1483 (m), 1423 (m), 1380 (w), 1362 (w), 1310 (br, w), 1230 (m), 1140 (w), 1110 (m), 1045 (m), 1004 (w), 990 (w), 947 (m), 903 (w), 785 (w), 750 (w), 721 (w), 693 (m), 595 (w), 536 (m). Raman  $\nu/\text{cm}^{-1}$ : 620 (w), 644 (w), 713 (m), 796 (m), 863 (br, m), 1001 (s), 1030 (m), 1105 (m), 1145 (br, m), 1228 (br, m), 1304 (br, m), 1449 (br, m).

**[Fe<sub>9</sub>O<sub>4</sub>(<sup>t</sup>BuCO<sub>2</sub>)<sub>13</sub>(PhPO<sub>3</sub>)<sub>3</sub>] (25):** A solution of **20** (2.3 g, 2.0 mmol) and PhPO<sub>3</sub>H<sub>2</sub> (0.32 g, 2.0 mmol) in MeCN (30 mL) was stirred for 24 h, leading to a dissolution of starting materials and precipitation of a brown powder. The powder was collected by filtration and washed with MeCN until the washing solution became yellow. The residual solid was dissolved in Et<sub>2</sub>O (50 mL), filtered, and the filtrate was diluted with MeCN (25 mL). Concentration of the solution by slow evaporation at ambient temperature gave large brown crystals after five days. The crystals were filtered and washed with MeCN.<sup>19</sup> Elemental analysis calculated (%) for C<sub>87</sub>H<sub>142</sub>Fe<sub>9</sub>O<sub>40</sub>P<sub>3</sub>: C 43.12,

H 5.91, N 0.0, Fe 20.74, P 3.83; found: C 42.39, H 5.69, N 0.0, Fe 21.30, P 3.70. ATR-FTIR  $\nu/\text{cm}^{-1}$ : 2960 (br, m), 2928 (m), 1552 (s), 1481 (s), 1428 (m), 1415 (m), 1375 (m), 1360 (m), 1227 (m), 1145 (m), 1124 (m), 1044 (w), 966 (s), 899 (w), 786 (m), 750 (w), 725 (w), 692 (m), 597 (m), 574 (br, s). Raman  $\nu/\text{cm}^{-1}$ : 644 (s), 722 (m), 798 (m), 841 (br, m), 876 (br, m), 939 (w), 1001 (br, m), 1105 (m), 1147 (m), 1233 (br, m), 1408 (m).

**[Co<sub>10</sub>(chp)<sub>12</sub>(PhCO<sub>2</sub>)<sub>4</sub>(PhPO<sub>3</sub>)<sub>2</sub>(H<sub>2</sub>O)] (26):** Co(BF<sub>4</sub>)·6H<sub>2</sub>O (0.68 g, 2.0 mmol), 6-chloro-2-hydroxypyridine (Hchp) (0.52 g, 4.0 mmol), PhPO<sub>3</sub>H<sub>2</sub> (0.052 g, 0.33 mmol), benzoic acid (0.24 g, 2.0 mmol) and trimethylamine (0.79 mL, 5.66 mmol) were added to MeCN (25 mL) and stirred for 6 h. The solution was then filtered and the solvent removed under vacuum to give a purple oil, recrystallization in MeCN of which gave purple crystals.<sup>20</sup> Elemental analysis calculated (%) for C<sub>100</sub>H<sub>68</sub>Cl<sub>12</sub>Co<sub>10</sub>N<sub>12</sub>O<sub>27</sub>P<sub>2</sub>: C 40.76, H 2.33, N 5.7, P 2.1, Cl 14.44; found: C 42.03, H 2.27, N 5.97, P 2.04, Cl 14.87. ATR-FTIR  $\nu/\text{cm}^{-1}$ : 3065 (br, w), 1706 (w), 1592 (s), 1557 (m), 1540 (m), 1491 (s), 1399 (s), 1336 (m), 1255 (w), 1226 (w), 1168 (m), 1139 (w), 1055 (m), 1026 (m), 1003 (m), 937 (m), 923 (m), 858 (w), 838 (w), 776 (m), 716 (s), 697 (m), 574 (m).

**[Fe<sub>9</sub>O<sub>2</sub>(OH)(<sup>t</sup>BuCO<sub>2</sub>)<sub>10</sub>(PhPO<sub>3</sub>)<sub>6</sub>(H<sub>2</sub>O)<sub>5</sub>(MeCN)] (27):** **21** (0.176 g, 0.2 mmol) and PhPO<sub>3</sub>H<sub>2</sub> (0.0316 g, 0.2 mmol) were added to MeCN (5 mL) and stirred overnight. The resulting solution was filtered and Et<sub>2</sub>O was added. Crystals were formed after leaving the solution at 4 °C for a few days.<sup>21</sup> Elemental analysis calculated (%) for C<sub>88</sub>H<sub>134</sub>N<sub>1</sub>O<sub>46</sub>P<sub>6</sub>: C 40.2, H 5.14, N 0.53, P 7.07; found: C 39.96, H 5.02, N 0.57, P 6.90. ATR-FTIR  $\nu/\text{cm}^{-1}$ : 2960 (m), 1557 (s), 1538 (s), 1482 (s), 1423 (s), 1379 (m), 1362 (m), 1228 (m), 1138 (s), 1041 (s), 1028 (w), 969 (m), 898 (w), 787 (m), 749 (w), 694 (m), 634 (m), 599 (s), 561 (s).

**[Fe<sub>4</sub>O(PhCO<sub>2</sub>)<sub>3</sub>(<sup>t</sup>BuPO<sub>3</sub>)<sub>3</sub>(py)<sub>3</sub>Cl] (28):** **17** (0.499 g, 0.5 mmol) and <sup>t</sup>BuPO<sub>3</sub>H<sub>2</sub> (0.138 g, 1 mmol) were dissolved in pyridine (25 mL) and stirred for 24 h at room temperature. The resulting solution was filtered and petroleum ether was allowed to slowly diffuse to give dark yellow crystals after a couple of days.<sup>22</sup> Elemental analysis calculated (%) for C<sub>48</sub>H<sub>57</sub>ClFe<sub>4</sub>N<sub>3</sub>O<sub>16</sub>P<sub>3</sub>: C 44.91, H 4.48, N 3.27, P 7.24, Cl 2.76; found:

C 46.03, H 4.35, N 3.17, P 7.12, Cl 2.98. ATR-FTIR  $\nu/\text{cm}^{-1}$ : 2970 (w), 1688 (br, w), 1595 (s), 1561 (s), 1478 (w), 1444 (m), 1403 (br, s), 1379 (m), 1293 (br, w), 1174 (w), 1130 (br, s), 1080 (m), 1068 (m), 1001 (s), 834 (w), 816 (9w), 756 (9w), 717 (m), 701 (m), 659 (m), 629 (m), 595 (m).

**[Fe<sub>6</sub>O<sub>2</sub>(O<sub>2</sub>)('BuCO<sub>2</sub>)<sub>8</sub>('BuPO<sub>3</sub>)<sub>2</sub>(py)<sub>2</sub>] (29):** **19** (0.27 g, 0.3 mmol), <sup>t</sup>BuPO<sub>3</sub>H<sub>2</sub> (0.041 g, 0.3 mmol) were dissolved in MeCN (7 mL) and 2 drops of H<sub>2</sub>O<sub>2</sub> and 4-5 drops of pyridine were added. The solution was stirred for 4 h and then placed in the fridge where crystals formed after 3 days.<sup>21</sup> Elemental analysis calculated (%) for C<sub>58</sub>H<sub>100</sub>Fe<sub>6</sub>N<sub>2</sub>O<sub>26</sub>P<sub>2</sub>: C 42.52, H 6.15, N 1.71, P 3.78; found: C 42.70, H 6.11, N 1.64, P 3.67. ATR-FTIR  $\nu/\text{cm}^{-1}$ : 2960 (w), 2927 (w), 2902 (w), 2866 (w), 1604 (w), 1561 (s), 1544 (s), 1482 (s), 1456 (w), 1422 (s), 1370 (m), 1361 (m), 1227 (m), 1119 (m), 1071 (w), 1029 (m), 968 (s), 898 (m), 833 (w), 787 (m), 758 (w), 696 (m), 632 (m), 597 (s), 551 (m).

**[Fe<sub>14</sub>O<sub>4</sub>(OH)<sub>8</sub>('BuCO<sub>2</sub>)<sub>14</sub>('BuPO<sub>3</sub>)<sub>6</sub>] (30):** A mixture of **20** (0.095 g, 0.1 mmol), Fe(BF<sub>4</sub>)<sub>2</sub> (0.034 g, 0.1 mmol) and <sup>t</sup>BuPO<sub>3</sub>H<sub>2</sub> (0.014 g, 0.1 mmol) in MeCN (8 mL) was stirred for 15 min to give a dark red solution, which was transferred to a Teflon-lined autoclave and heated to 100 °C for 12 h, followed by cooling to room temperature with a rate of 0.05 °C/min. Orange sheets crystals were filtered and washed with small amount of MeCN.<sup>23</sup> Elemental analysis calculated (%) for C<sub>74</sub>H<sub>188</sub>Fe<sub>14</sub>O<sub>58</sub>P<sub>6</sub>: C 29.89, H 6.37, P 6.25; found: C 30.82, H 6.24, P 6.47. ATR-FTIR  $\nu/\text{cm}^{-1}$ : 2963 (br, m), 1558 (m), 1526 (m), 1483 (s), 1424 (s), 1380 (m), 1362 (m), 1229 (m), 1112 (m), 1085 (w), 1047 (w), 998 (m), 966 (m), 930 (m), 788 (w), 608 (w), 567 (br, m). Raman  $\nu/\text{cm}^{-1}$ : 644 (w), 666 (m), 801 (s), 831 (m), 881 (br, w), 940 (br, m), 1005 (br, m), 1204 (m), 1236 (m), 1425 (m).

**[Fe<sub>6</sub>Tb<sub>2</sub>O<sub>2</sub>(H<sub>2</sub>O)<sub>2</sub>('BuCO<sub>2</sub>)<sub>12</sub>('BuCO<sub>2</sub>H)<sub>2</sub>('BuPO<sub>3</sub>)<sub>4</sub>] (31):** This compound was provided by Dr Karzan Zangana. ATR-FTIR  $\nu/\text{cm}^{-1}$ : 2960 (m), 2869 (w), 1571 (w), 1538 (s), 1482 (s), 1458 (m), 1421 (s), 1378 (m), 1361 (m), 1227 (m), 1101 (m), 1046 (s), 1019 (s), 987 (s), 894 (m), 832 (w), 808 (w), 787 (m), 659 (m), 605 (m).

**[Ni<sub>6</sub>Gd<sub>6</sub>(OH)<sub>2</sub>(MeO)<sub>2</sub>(<sup>t</sup>BuCO<sub>2</sub>)<sub>16</sub>(PhPO<sub>3</sub>)<sub>6</sub>] (32):** [Ni<sub>2</sub>(OH)<sub>2</sub>(<sup>t</sup>BuCO<sub>2</sub>)<sub>4</sub>(<sup>t</sup>BuCO<sub>2</sub>H)<sub>4</sub>] (0.1 g, 0.1 mmol), [Gd<sub>2</sub>(<sup>t</sup>BuCO<sub>2</sub>)<sub>6</sub>(<sup>t</sup>BuCO<sub>2</sub>H)<sub>6</sub>] (0.075 mmol), PhPO<sub>3</sub>H<sub>2</sub> (0.1 mmol) and trimethylamine (0.1 mL, 1 mmol) were dissolved in MeCN (8mL) and stirred at room temperature for 5 min. The resulting solution was transferred into a 10 mL Teflon-lined autoclave and heated to 150 °C for 12 h, followed by cooling to room temperature with a rate of 0.05 °C/min. Yellow crystals were obtained directly from the autoclave. Elemental analysis calculated (%) for C<sub>122</sub>H<sub>188</sub>Gd<sub>6</sub>N<sub>2</sub>Ni<sub>6</sub>O<sub>54</sub>P<sub>6</sub>: C 36.45, H 4.69, N 0.68, Ni 8.62, Gd 23.10, P 4.55; found: C 36.04, H 4.82, N 0.87, Ni 8.34, Gd 23.29, P 4.69.<sup>24</sup> ATR-FTIR  $\nu/\text{cm}^{-1}$ : 2958 (w), 1661 (w), 1604 (m), 1556 (s), 1538 (s), 1483 (s), 1460 (w), 1427 (s), 1377 (m), 1359 (m), 1230 (m), 1122 (m), 1106 (m), 1029 (m), 1003 (m), 985 (s), 897 (w), 872 (w), 787 (m), 750 (m), 721 (m), 691 (m).

Compounds [Fe<sub>6</sub>O(OH)<sub>3</sub>(MeCO<sub>2</sub>)<sub>3</sub>(PhPO<sub>3</sub>)<sub>4</sub>(py)<sub>9</sub>]<sup>18</sup> (33),  
 [Fe<sub>4</sub>OCl(PhCO<sub>2</sub>)<sub>3</sub>(PhPO<sub>3</sub>)<sub>3</sub>(py)<sub>5</sub>]<sup>18</sup> (34), [Fe<sub>7</sub>O<sub>2</sub>(MeCO<sub>2</sub>)<sub>9</sub>(PhPO<sub>3</sub>)<sub>4</sub>(py)<sub>6</sub>]<sup>18</sup> (35),  
 [Fe<sub>4</sub>OCl(MeCO<sub>2</sub>)<sub>3</sub>(C<sub>6</sub>H<sub>9</sub>PO<sub>3</sub>)<sub>3</sub>(py)<sub>5</sub>] · 2H<sub>2</sub>O<sup>25</sup> (36),  
 [Fe<sub>7</sub>O<sub>2</sub>(PhCO<sub>2</sub>)<sub>9</sub>(C<sub>6</sub>H<sub>9</sub>PO<sub>3</sub>)<sub>4</sub>(py)<sub>6</sub>]CH<sub>3</sub>CN · 3H<sub>2</sub>O<sup>25</sup> (37), [Fe<sub>4</sub>(<sup>t</sup>BuCO<sub>2</sub>)<sub>5</sub>(<sup>t</sup>BuPO<sub>3</sub>)<sub>3</sub>Br]<sup>23</sup> (38),  
 [Fe<sub>4</sub>(<sup>t</sup>BuPO<sub>3</sub>)<sub>4</sub>(HphpzH)<sub>4</sub>] · 5CH<sub>3</sub>CN · 5CH<sub>2</sub>Cl<sub>2</sub><sup>26</sup> (39),  
 [Mn<sub>3</sub>(C<sub>5</sub>H<sub>9</sub>PO<sub>3</sub>)<sub>2</sub>(phen)<sub>6</sub>](ClO<sub>4</sub>)<sub>2</sub> · 7CH<sub>3</sub>OH<sup>27</sup> (40), [Mn<sub>3</sub>(<sup>t</sup>BuPO<sub>3</sub>)<sub>2</sub>(dpzpy)<sub>3</sub>](ClO<sub>4</sub>)<sub>2</sub> · H<sub>2</sub>O<sup>27</sup>  
 (41), [Mn<sub>4</sub>(C<sub>5</sub>H<sub>9</sub>PO<sub>3</sub>)<sub>2</sub>(phen)<sub>8</sub>(H<sub>2</sub>O)<sub>2</sub>](ClO<sub>4</sub>)<sub>4</sub>]<sup>27</sup> (42), Fe[(CH<sub>3</sub>(CH<sub>2</sub>)<sub>2</sub>PO<sub>3</sub>)(H<sub>2</sub>O)]<sup>28</sup> (43),  
 [Cu<sub>4</sub>(L1)<sub>2</sub>(<sup>t</sup>BuPO<sub>3</sub>)](CH<sub>3</sub>OH)<sub>2</sub>(C<sub>6</sub>H<sub>6</sub>)<sup>29</sup> (44),  
 [Cu<sub>4</sub>(L1)<sub>2</sub>(H<sub>2</sub>O)<sub>2</sub>(NMe<sub>2</sub>CHO)(PhPO<sub>3</sub>)](H<sub>2</sub>O)<sub>2</sub><sup>29</sup> (45), [Cu<sub>4</sub>(L2)<sub>2</sub>(C<sub>5</sub>H<sub>9</sub>PO<sub>3</sub>)](CH<sub>3</sub>OH)<sub>2</sub>  
<sup>29</sup>(46), [Cu<sub>4</sub>(L2)<sub>2</sub>(c-C<sub>6</sub>H<sub>11</sub>PO<sub>3</sub>)](MeOH)<sub>4</sub>(H<sub>2</sub>O)<sub>2</sub><sup>29</sup> (47),  
 [Co<sub>16</sub>(OH)<sub>6</sub>(chp)<sub>22</sub>(C<sub>6</sub>H<sub>9</sub>PO<sub>3</sub>)<sub>2</sub>(H<sub>2</sub>O)<sub>4</sub>] · 10CH<sub>2</sub>Cl<sub>2</sub> · 2H<sub>2</sub>O<sup>30</sup> (48),  
 [Ni<sub>8</sub>(OH)<sub>4</sub>(OMe)<sub>2</sub>(<sup>t</sup>BuCO<sub>2</sub>)<sub>6</sub>(<sup>t</sup>BuCO<sub>2</sub>H)<sub>8</sub>(RPO<sub>3</sub>)<sub>2</sub>]<sup>31</sup> (49),  
 [Co<sub>12</sub>(OH)<sub>4</sub>(HCO<sub>3</sub>)<sub>6</sub>(RPO<sub>3</sub>)<sub>4</sub>(<sup>t</sup>BuCO<sub>2</sub>)<sub>6</sub>(<sup>t</sup>BuCO<sub>2</sub>H)<sub>6</sub>]<sup>31</sup> (50),  
 [Co<sub>12</sub>(OH)<sub>4</sub>(HCO<sub>3</sub>)<sub>6</sub>(RPO<sub>3</sub>)<sub>4</sub>(<sup>t</sup>BuCO<sub>2</sub>)<sub>6</sub>(<sup>t</sup>BuCO<sub>2</sub>H)<sub>6</sub>]<sup>31</sup> (51)  
 and [Ni<sub>12</sub>(OH)<sub>4</sub>(HCO<sub>3</sub>)<sub>6</sub>(RPO<sub>3</sub>)<sub>4</sub>(<sup>t</sup>BuCO<sub>2</sub>)<sub>6</sub>(<sup>t</sup>BuCO<sub>2</sub>H)<sub>6</sub>]<sup>31</sup> (52) were not synthesised, but  
 their published IR data is studied and reported here. H<sub>2</sub>phpzH = 3(5)-(2-  
 hydroxyphenyl)pyrazole, dpzpy = 2,6-bis(pyrazol-3-yl)pyridine.

## 5.2.2. Results and discussion

Compounds **22–32** were synthesized with  $\text{PhPO}_3\text{H}_2$  or  $t\text{BuPO}_3\text{H}_2$  acid. The ATR-FTIR spectra of the whole series were recorded on samples in the crystalline state. This allows the study of the IR spectra of representative compounds showing each binding mode for both phosphonate ligands, and even a mixture of binding modes in the same coordination compound, which have been previously identified by single crystal X-ray diffraction.

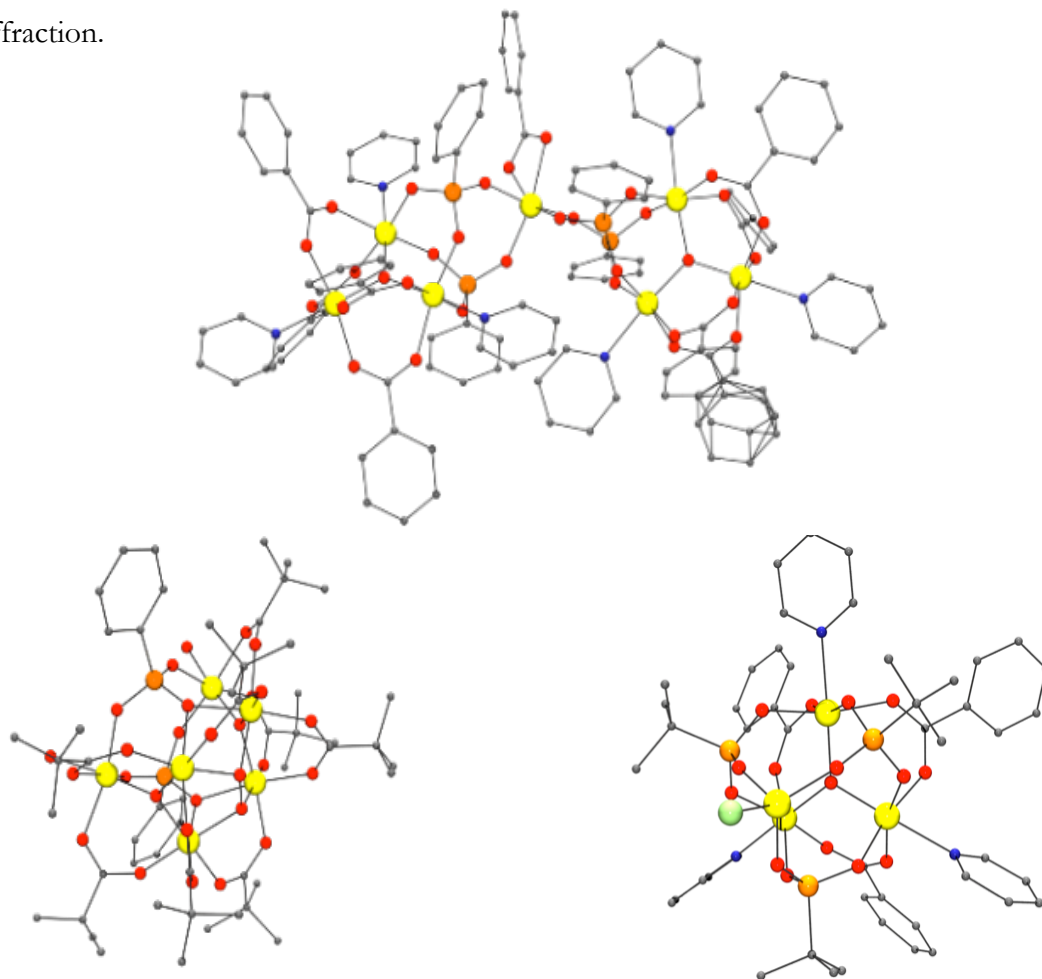


Figure 5.4. Single crystal X-ray structure for compounds **22** (top), **24** (bottom left) and **28** (bottom right). Colours: C, grey; O, red; P, orange; Cl, green; Fe, yellow. Hydrogen atoms omitted for clarity.

In compounds **22**, **23** and **28** the phosphonate ligand shows a 3.111 binding mode.<sup>18,22</sup> In compounds **24** and **29** one of the oxygen atoms on the phosphonate binds two metal atoms to give a 4.211 binding mode.<sup>18,21</sup> Compound **25** shows a 5.221 binding mode.<sup>19</sup>

Compound **26** has a 6.222 binding mode, but there are no compounds displaying this binding mode for *tert*-butylphosphonate.<sup>20</sup>

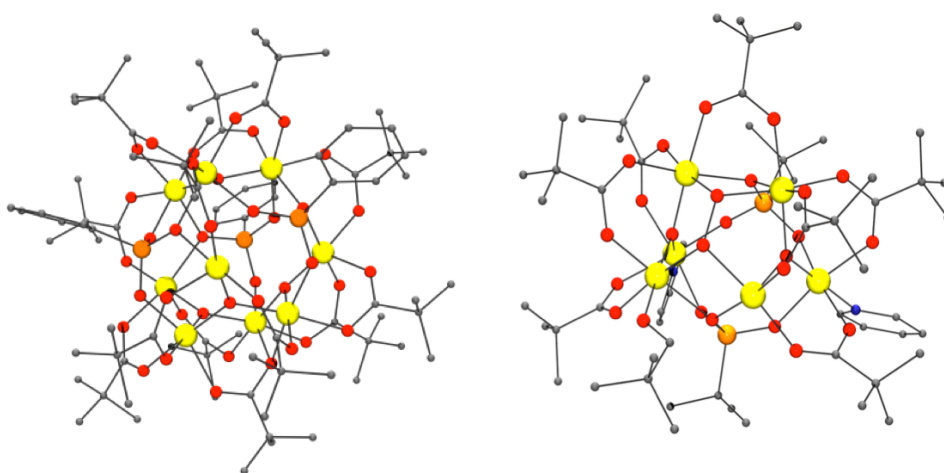


Figure 5.5. Single crystal X-ray structure for compounds **25** and **29**. Colours: C, grey; O, red; P, orange; Fe, yellow. Hydrogen atoms omitted for clarity.

In compound **27** there are two different types of phosphonates. Two of them show the binding mode 3.111 and the other four show the 4.211 binding mode.<sup>21</sup> A similar thing happens in compound **30** in which four of the phosphonates have a 4.211 binding mode while the other two have the 5.221 binding mode.<sup>23</sup>

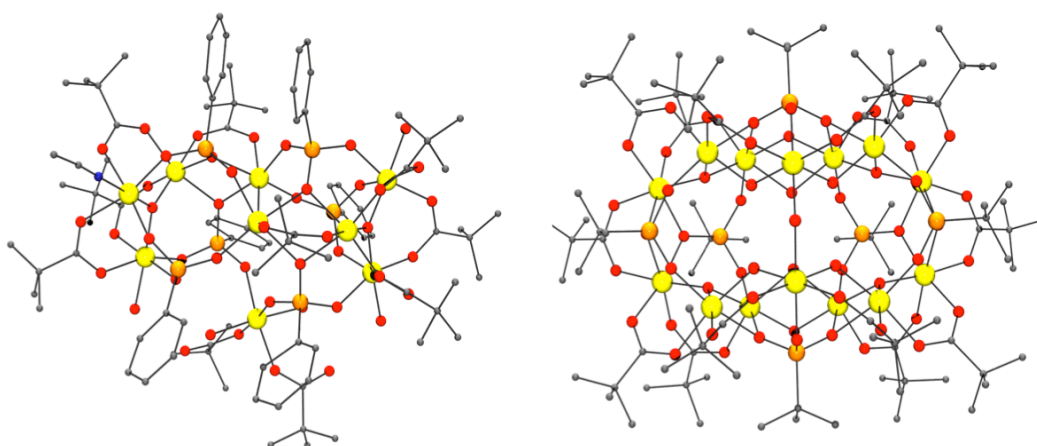


Figure 5.6. Single crystal X-ray structure for compounds **27** and **30**. Colours: C, grey; O, red; P, orange; Fe, yellow. Hydrogen atoms omitted for clarity.

Compound **31** is more complicated as it is a heterometallic compound and it shows two different binding modes. Two of the phosphonate ligands show the 3.111 binding mode and are bound to two Fe<sup>3+</sup> and to one Tb<sup>3+</sup>, while the other two phosphonates display the 4.221 binding mode in which one oxygen atom is bound to two Tb<sup>3+</sup> ions, another oxygen atom binds to both a Tb<sup>3+</sup> and an Fe<sup>3+</sup> ion, and the last one binds only to a single iron ion.

In compound **32**, four of the phosphonates show the 6.222 binding mode in which two of the oxygen atoms bind a Ni<sup>2+</sup> and a Gd<sup>3+</sup>, and the other oxygen binds two Gd<sup>3+</sup> atoms. The other two phosphonates have a 5.221 binding mode in which two of the oxygen atoms bind a Ni<sup>2+</sup> and a Gd<sup>3+</sup> and the other one binds one Gd<sup>3+</sup> atom.<sup>24</sup>

All of these compounds have in common the presence of a carboxylate ligand that exhibits an antisymmetric stretch in the IR spectrum at *ca.* 1600 cm<sup>-1</sup> and a symmetric one at *ca.* 1400 cm<sup>-1</sup> for the benzoate, and at 1550 and 1110 cm<sup>-1</sup> for the pivalate ligand. Another common motif in the spectra of all of the compounds is the presence of a band due to the methyl bending at 1480 cm<sup>-1</sup> (apart from compounds **22**, **23** and **32** which do not contain any methyl group).

For a C<sub>3v</sub> symmetry group two stretching bands are expected for the isolated, pyramidal PO<sub>3</sub> group: a symmetric one (A<sub>1</sub>) and an antisymmetric one with a double degeneracy (E).

Table 5.1. IR frequencies, binding mode and assignment of the bands of the PO<sub>3</sub> group for compounds **22-32**.

|           | Binding mode | ν <sub>as</sub> PO <sub>3</sub> (cm <sup>-1</sup> ) |      | ν <sub>s</sub> PO <sub>3</sub> (cm <sup>-1</sup> ) |
|-----------|--------------|---|------|--|
| <b>22</b> | 3.111        | 1089  | 1063 | 993  |
| <b>23</b> | 3.111        | 1088  | 1063 | 993  |
| <b>24</b> | 4.211        | 1045  |      | 991  |
| <b>25</b> | 5.221        | 1044  |      | 966  |
| <b>26</b> | 6.222        | 1055  |      | 1003   |
| <b>27</b> | 3.111/4.211  | 1041  |      | 969  |
| <b>28</b> | 3.111        | 1080  | 1068 | 1001   |
| <b>29</b> | 4.211        | 1030  |      | 969  |
| <b>30</b> | 4.211/5.221  | 1022  |      | 993  |
| <b>31</b> | 3.111/4.221  | 1047  |      | 987  |
| <b>32</b> | 5.221/6.222  | 1030  |      | 986  |

PhPO<sub>3</sub>H<sub>2</sub> has a band at 1142 cm<sup>-1</sup> due to a combination of the P=O bond stretch and the C<sub>ar</sub>-P bond stretch. The antisymmetric P-O bond stretch shows a pair of peaks at 1010 and 998 cm<sup>-1</sup>, and the symmetric stretch for the same bond appears at 923 cm<sup>-1</sup>, where a contribution is also seen from the C<sub>ar</sub>-H bond.<sup>32</sup> For <sup>t</sup>BuPO<sub>3</sub>H<sub>2</sub> the P=O stretch has a band at 1184 cm<sup>-1</sup> with the antisymmetric bands at 999 and 990 cm<sup>-1</sup> and the symmetric band with a frequency of 917 cm<sup>-1</sup>. The difference in the frequency of the bands between the acids suggests a stronger double bond and weaker single bonds for <sup>t</sup>BuPO<sub>3</sub>H<sub>2</sub>, and is supported by the crystallographic data, which show a longer P-O bond distance for *tert*-butyl (1.551(2) and 1.561(3) Å) corresponding to the phenyl derivative (1.536(2) and 1.555(2) Å). This is a clear demonstration of the utility of infrared spectroscopy as a method for interrogating structural parameters.<sup>33,34</sup>

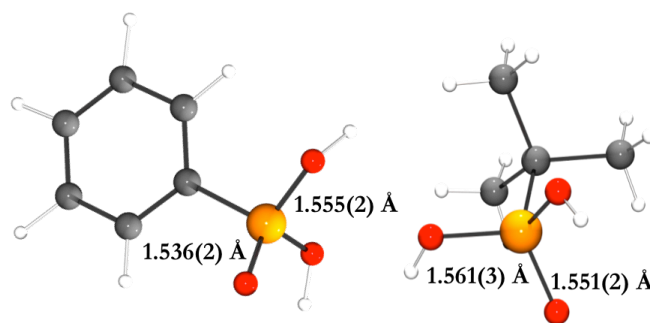


Figure 5.7. Single crystal X-ray structure of PhPO<sub>3</sub>H<sub>2</sub> (left) and <sup>t</sup>BuPO<sub>3</sub>H<sub>2</sub> (right).

Colours: C, grey; O, red; P, orange; Fe; H, white.

In the case of binding, it would be expected that the bands due to O–H bending and P=O stretching to disappear following coordination. Additionally, since the  $C_{3v}$  symmetry of the system is likely to be broken upon binding, it is also expected for the antisymmetric band to split. The frequencies of the symmetric and antisymmetric stretch for compounds **22** to **32** are shown in Table 5.1. The data show the expected splitting of the antisymmetric band for all of the compounds with the 3.111 binding mode (compounds **22**, **23** and **28**). For these the double antisymmetric band appears at *ca.* 1085 and 1065  $\text{cm}^{-1}$  and the symmetric stretch at approximately 1000  $\text{cm}^{-1}$ . For the 4.211 and 5.221 binding modes there is no obvious splitting although this band is broader than for the 3.111 binding mode. This suggests that the splitting does occur, but that the resolution of the data is not high enough to resolve the bands.

When the phosphonate binds to more than three metal ions the same electron density of the oxygen atom has to be shared between more d-orbitals, making the P–O bonds weaker. This is reflected in a shift to lower frequencies as the phosphonate binds to four, five or six metal atoms for binding modes 4.211, 5.221 and 6.222. The antisymmetric stretch for compounds with phenylphosphonate is at *ca.* 1050  $\text{cm}^{-1}$  and at lower frequencies (1025  $\text{cm}^{-1}$ ) for the *tert*-butyl derivative. The frequency depends on the metal bound to the phosphonate, the frequency of vibration decreases as the mass of the metal increases and also depends on the oxidation state (Chapter 1).

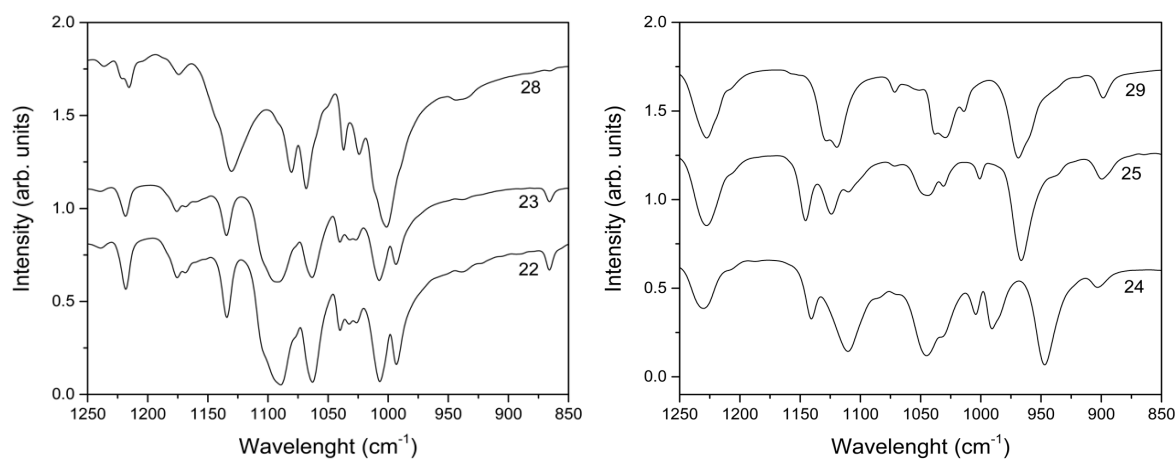


Figure 5.8. Selected region of the IR spectra for compounds **28**, **23**, **22** (left) and **29**, **25** and **24** (right).

The symmetric stretch shows some variations but does not seem to be related to the binding mode, as it does not show any measurable differences between binding modes. Compounds **27**, **30**, **31** and **32** have a mixture of binding modes. Compounds **30** and **32** have a combination of 4.211 and 5.221, and 5.221 and 6.222 binding modes, respectively, the difference between these binding modes is not appreciably large in the spectra as seen from the other compounds. Symmetric and antisymmetric bands for compound **30** are similar to the ones shown by the 5.221 mode alone. The same bands are seen for compound **32** (Figure 5.9).

However, compounds **27** and **31** both exhibit the 3.111 binding mode as well as the 4.211 and 4.221 respectively, which leads to a significant difference in the spectra. In the spectra of these compounds the antisymmetric stretch does not show splitting but looks broader suggesting a smaller splitting takes place but it results on a much broader band. The same thing happens for the 4.211 and 5.221 binding modes suggesting that 4.211 and 4.221 binding modes for compounds **27** and **31** respectively have more contribution to the spectra than the 3.111 mode.

According to this interpretation of the recorded spectra, IR spectroscopy cannot be used alone to identify the binding mode of the phosphonates although it can be a useful

tool to compare compounds synthesized with the same phosphonate but, with different binding modes.

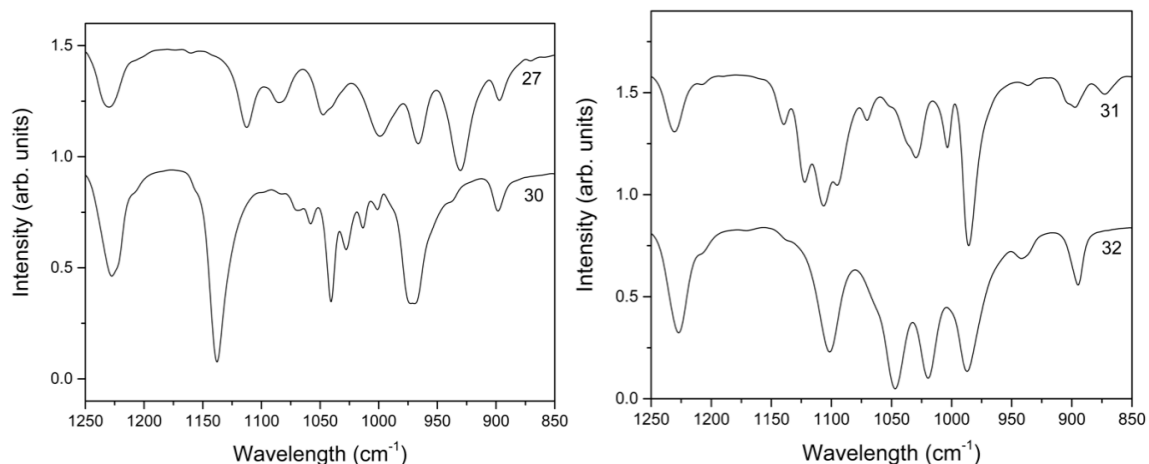


Figure 5.9. Selected region of the IR spectra for compounds **27**, **31** (left), **30** and **32** (right).

Published spectroscopic data for phosphonate compounds has been used to assign the symmetric and asymmetric bands (Table 5.2). Data for compounds with a 3.111 binding mode exhibit the same splitting of the asymmetric band that has been seen in the compounds reported in Table 5.1. The symmetric stretch is at *ca.* 990  $\text{cm}^{-1}$  and the antisymmetric stretch is a double band with one peak at *ca.* 1090 and one at *ca.* 1060  $\text{cm}^{-1}$ . There is some fluctuation in the vibration frequency for compounds **41** and **42** but all of these compounds have been synthesized with different metallic atoms, different ligands and their IR spectra have been recorded using different spectrometers. For these reasons the data have to be analysed cautiously.

Compounds with 4.211 and 5.221 binding mode show one peak for the  $\nu_{as}$  as seen for the compounds in Table 5.1. The symmetric band reported in Table 5.2 again shows some fluctuations that do not seem to depend on the binding mode.

Table 5.2. IR frequencies and assignment for compounds found in the literature.

|                         | Binding mode | $\nu_{as}\text{PO}_3$ ( $\text{cm}^{-1}$ ) |      | $\nu_s\text{PO}_3$ ( $\text{cm}^{-1}$ ) |
|-------------------------|--------------|--|------|---|
| <b>33</b> <sup>18</sup> | 3.111        | 1119                                       | 1068 | 994                                     |
| <b>34</b> <sup>18</sup> | 3.111        | 1095                                       | 1068 | 994                                     |
| <b>35</b> <sup>18</sup> | 3.111        | 1089                                       | 1067 | 994                                     |
| <b>36</b> <sup>25</sup> | 3.111        | 1087                                       | 1038 | 998                                     |
| <b>37</b> <sup>25</sup> | 3.111        | 1089                                       | 1066 | 1000                                    |
| <b>38</b> <sup>23</sup> | 3.111        | 1079                                       | —    | 991                                     |
| <b>39</b> <sup>26</sup> | 3.111        | 1059                                       | 1036 | 984                                     |
| <b>40</b> <sup>27</sup> | 3.111        | 1091                                       | —    | 986                                     |
| <b>41</b> <sup>27</sup> | 3.111        | 1091                                       | 1047 | 985                                     |
| <b>42</b> <sup>27</sup> | 3.111        | 1089                                       | 1056 | 987                                     |
| <b>43</b> <sup>28</sup> | 4.221        | 1068                                       |      | 999                                     |
| <b>44</b> <sup>29</sup> | 4.211        | —  |      | 986                                     |
| <b>45</b> <sup>29</sup> | 4.211        | 1061                                       |      | 996                                     |
| <b>46</b> <sup>29</sup> | 4.211        | 1062                                       |      | 964                                     |
| <b>47</b> <sup>29</sup> | 4.211        | 1061                                       |      | 960                                     |
| <b>48</b> <sup>30</sup> | 4.211        | 1069                                       |      | 1004                                    |
| <b>49</b> <sup>31</sup> | 5.221        | 1110                                       |      | 1000                                    |
| <b>50</b> <sup>31</sup> | 6.222        | 1096                                       | —    | 972                                     |
| <b>51</b> <sup>31</sup> | 6.222        | 1098                                       | 1029 | 990                                     |
| <b>52</b> <sup>31</sup> | 6.222        | 1090                                       | 1028 | 991                                     |

The experimental spectroscopic data for the synthesized compounds show a clear pattern whereby, for the totally symmetric binding modes (3.111 and 6.222), the antisymmetric stretch for the P-O bond splits. This either does not happen for the antisymmetric binding modes, or if it does happen it does so with a smaller separation

between the peaks making the peak look broader. Although IR spectroscopy does not allow direct identification of the binding modes for phosphonate ligands, it can differentiate between symmetric and antisymmetric binding modes. It is a useful technique to compare compounds, which have different binding modes and it can assist in the characterization of the compounds.

## 5.3. X-ray Photoelectron Spectroscopy

### 5.3.1. Phenylphosphonic acid on Fe(110)

#### 5.3.1.1. Experimental

The work presented in this Section was carried out on beamline D1011 ( $30 \leq h\nu \leq 1600$  eV), a bending magnet soft X-ray beamline, at MAX-lab in Sweden. The D1011 endstation is equipped with a Scienta SES200 200 mm mean-radius hemispherical electron energy analyser, a microchannel plate (MCP) NEXAFS detector, a low-energy electron diffraction (LEED) camera, and a residual gas analyser (RGA). The analysis chamber is separated from the sample preparation chamber by means of a gate valve. The Fe(110) crystal was held in place by a tantalum wire. A thermocouple was attached to the sample plate to monitor the temperature of the sample. The base pressure in the analysis chamber was about  $1.5 \times 10^{-10}$  mbar during the measurements. Phenylphosphonic acid ( $\text{PhPO}_3\text{H}_2$ ) was deposited onto the Fe crystal surface by vacuum sublimation from a Knudsen cell at a temperature of 383-403 K for different amounts of time depending on the desired thickness of the molecular layer. Photoemission spectra were collected at normal emission. A survey scan was recorded at 1200 eV photon energy. For the narrow, high resolution scans the photon energy was tuned such that the photoemitted electrons had a kinetic energy of *ca.* 100 eV. This ensures that the probing is roughly the same depth of surface and gives high surface sensitivity i.e. a probe depth of roughly 6 nm.<sup>35</sup> Peak fitting was carried out using CASA XPS Software.<sup>36</sup>

### 5.3.1.2. Results and discussion

The Fe(110) single crystal was cleaned by repeated 1 keV  $\text{Ar}^+$  ion bombardment and annealing to 873 K in vacuum. Figure 5.10 shows a survey scan XPS spectrum and the O 1s, N 1s, C 1s and P 2p core level spectra for the clean surface. At high surface sensitivity some C and N contamination is observed, but these are well-established contaminants in Fe single crystals and are difficult to remove completely. The low energy electron diffraction image obtained from the sputtered and annealed surface was consistent with an ordered N overlayer, which is well documented in the literature.<sup>37</sup>

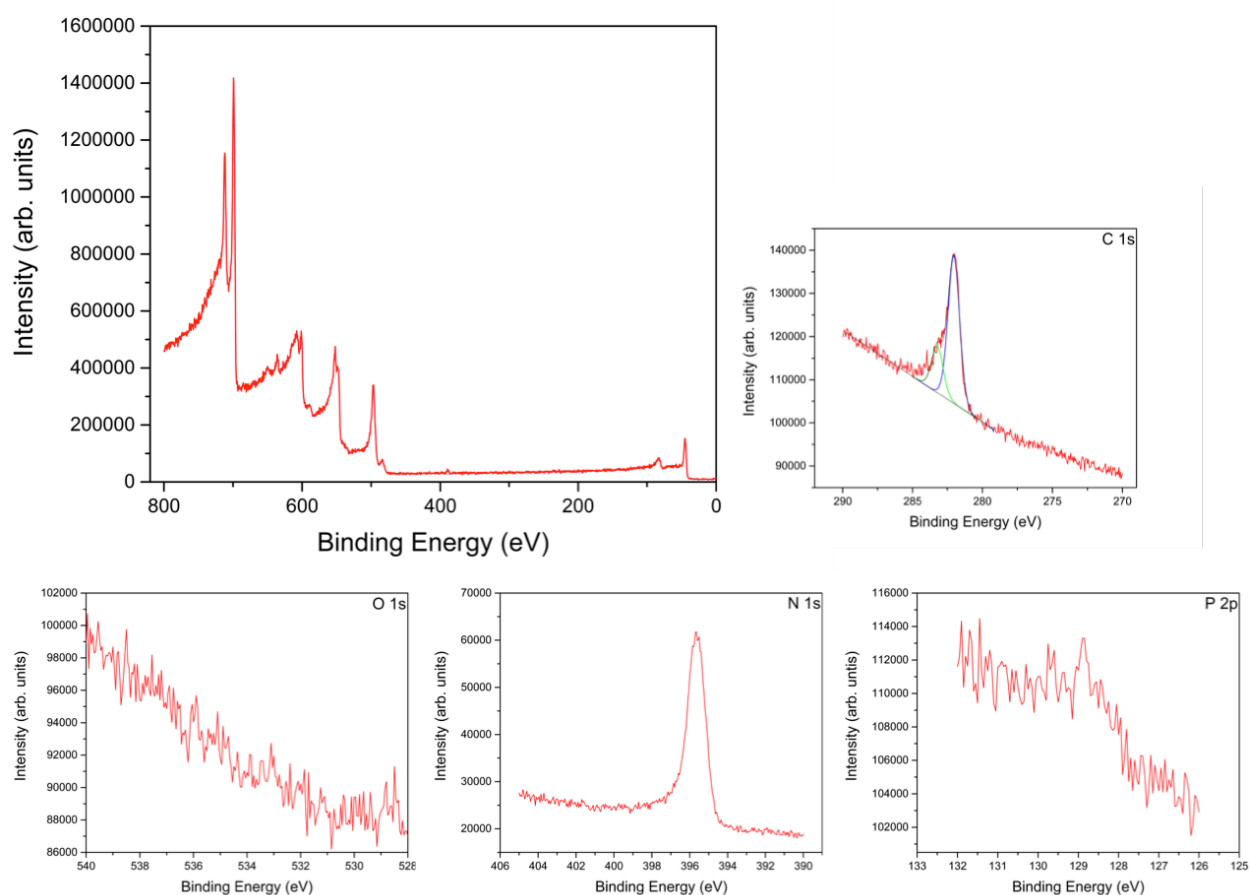


Figure 5.10. UHV XPS survey (top left), C 1s (top right), O 1s (bottom left), N 1s (bottom middle) and P 2p (bottom right) spectra recorded from the sputtered and annealed Fe(110) single crystal.

The first deposition was carried out in the preparation chamber by heating the Knudsen cell containing  $\text{PhPO}_3\text{H}_2$  powder (Sigma Aldrich 99%) to a temperature of 398-403 °C for 10 minutes at a pressure of  $1 \times 10^{-5}$  mbar in the preparation chamber. The sample was roughly 20 cm from the Knudsen cell. The pressure in the evaporation chamber was  $4 \times 10^{-7}$  mbar. The XPS spectra obtained following this deposition are shown in Figure 5.11. The O 1s peak that can be fitted with three components is also present. The most intense peak at a binding energy of 528.5 eV (green) arises from the deprotonated O atoms bound to the surface (P-O-Fe) whilst the central peak at 529.2 eV arises from the P=O group. The least intense peak at higher binding energy (pink) is due to the free acid form suggesting that there is some residual compound in the acid form that is not interacting with the surface.<sup>38</sup>

Table 5.3. Peak assignments for O 1s and P 2p peaks and their respective binding energies (eV) for the recorded spectra of  $\text{PhPO}_3\text{H}_2$  on an Fe(110) surface.

|                                      | Binding Energy (eV) |             |       |
|--------------------------------------|---------------------|-------------|-------|
|                                      | O 1s                |             |       |
|                                      | Thin layer          | Thick layer | 423 K |
| <b>P-O-Fe</b>                        | 528.6               | 528.5       | 528.5 |
| <b>P=O</b>                           | 529.4               | 529.5       | 529.6 |
| <b>P-OH</b>                          | 530.6               | 530.5       | 530.6 |
|                                      | P 2p                |             |       |
| <b>Tridentate P 2p<sub>3/2</sub></b> | 132.4               | 132.5       | 132.5 |
| <b>Tridentate P 2p<sub>1/2</sub></b> | 133.3               | 133.4       | 133.4 |
| <b>Bidentate P 2p<sub>3/2</sub></b>  | 133.0               | 133.0       | 133.0 |
| <b>Bidentate P 2p<sub>1/2</sub></b>  | 133.9               | 133.9       | 133.9 |
| <b>Free acid P 2p<sub>3/2</sub></b>  | -                   | 133.6       | -     |
| <b>Free acid P 2p<sub>1/2</sub></b>  | -                   | 134.5       | -     |

The P 2p core orbital peak is quite broad and has a clear shoulder on the high binding energy side of the spectrum. Since the separation between the main peak and the

shoulder, and their relative intensities are not consistent with the 2p spin orbit splitting of P,<sup>39,40</sup> two sets of spin orbit doublets must be used for the fitting, suggesting P is in two different chemical environments. The P  $2p_{3/2}$  and  $2p_{1/2}$  doublets are constrained with an energy difference of 0.9 eV<sup>41</sup> and a 2:1 ratio for the areas. The doublet with peaks at 132.4 and 133.3 eV (blue) is assigned to the compound bound to the surface through the three O atoms in a tridentate binding mode; the doublet with peaks at 133.0 and 133.9 eV (green) is assigned to partially protonated compound, suggesting that there is also some molecule displaying a bidentate mode on the surface.

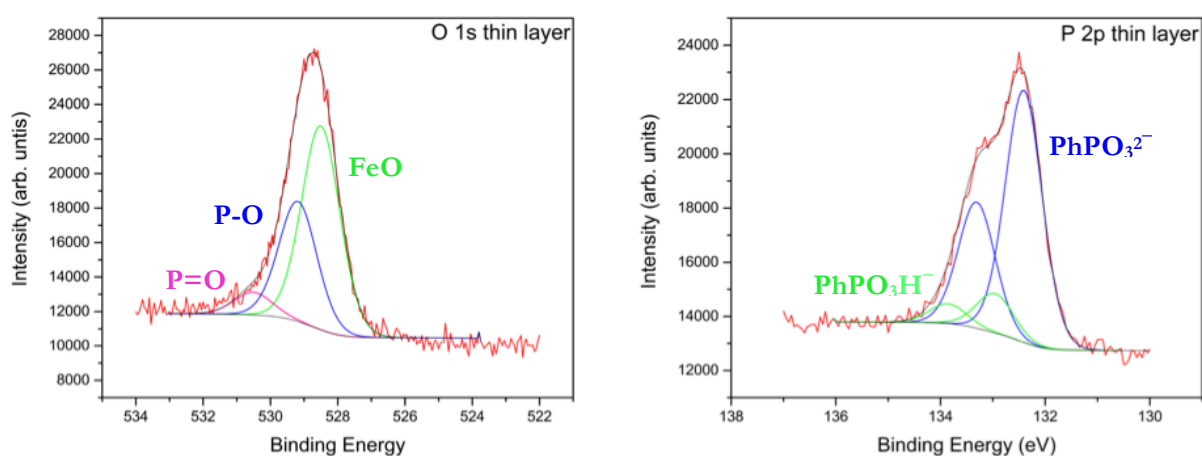


Figure 5.11. UHV XPS core level O 1s (left) and P 2p (right) spectra recorded after a first deposition of  $\text{PhPO}_3\text{H}_2$  on an Fe(110) surface.

A second deposition was then carried out for 20 minutes in order to obtain a thicker layer of  $\text{PhPO}_3\text{H}_2$ . The P peak can be fitted by adding a set of doublets assigned to the presence of the non bonded acid form (pink). This supports the assignment of the O 1s derived features because the signal due to the unbounded acid increases in intensity when a multilayer of the phosphonic acid is deposited.

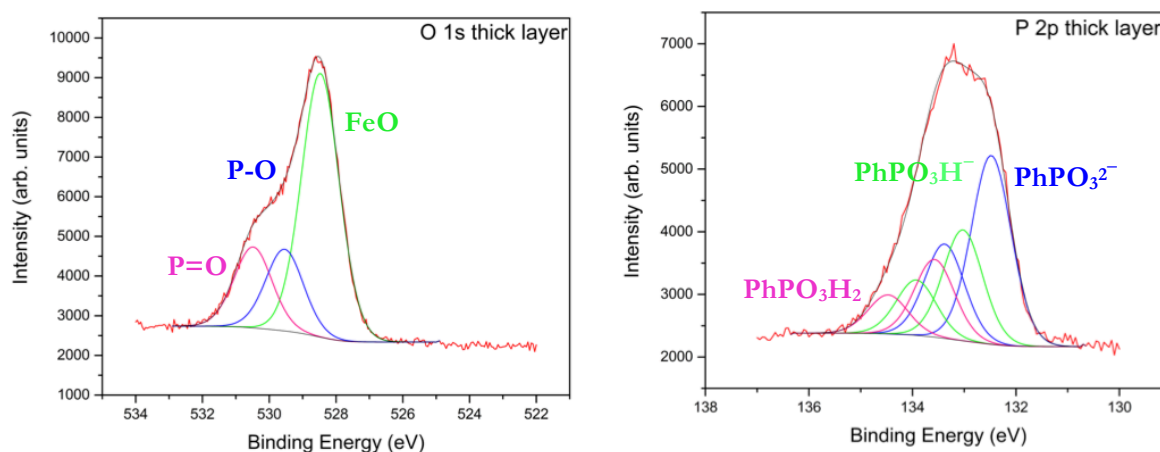


Figure 5.12. UHV XPS core level for O 1s (left) and P 2p (right) spectra recorded after a second deposition of  $\text{PhPO}_3\text{H}_2$  on an Fe(110) surface.

The sample was then heated in order to see how the system responded to a change with temperature. After 20 minutes of heating at 323-333 K, 35 minutes at 368-378 K and finally at 393 K for 10 minutes there was no change in the spectra. A change was seen after raising the sample temperature to *ca.* 423 K and kept for 10 minutes. The narrow range spectra for the O 1s and P 2p core level following this heating cycle are shown in Figure 5.13. The O 1s spectrum is now dominated by the peak at binding energy of 528.5 eV assigned to the deprotonated O atoms bound to the surface (P-O-Fe). This suggests that the majority of the phosphonate is now bonded in a tridentate geometry. Some small fraction of the molecule is found to be bonded in a bidentate mode via the deprotonated P-OH which is consistent with the presence of the peak at 529.6 eV (blue) assigned to the P=O, and it is in agreement with similar work studying the adsorption of  $\text{PhPO}_3\text{H}_2$  on  $\text{TiO}_2(101)$ .<sup>13</sup> At this stage it is thought that every possible binding site of the surface is occupied, and the compounds is forming a monolayer (ML).

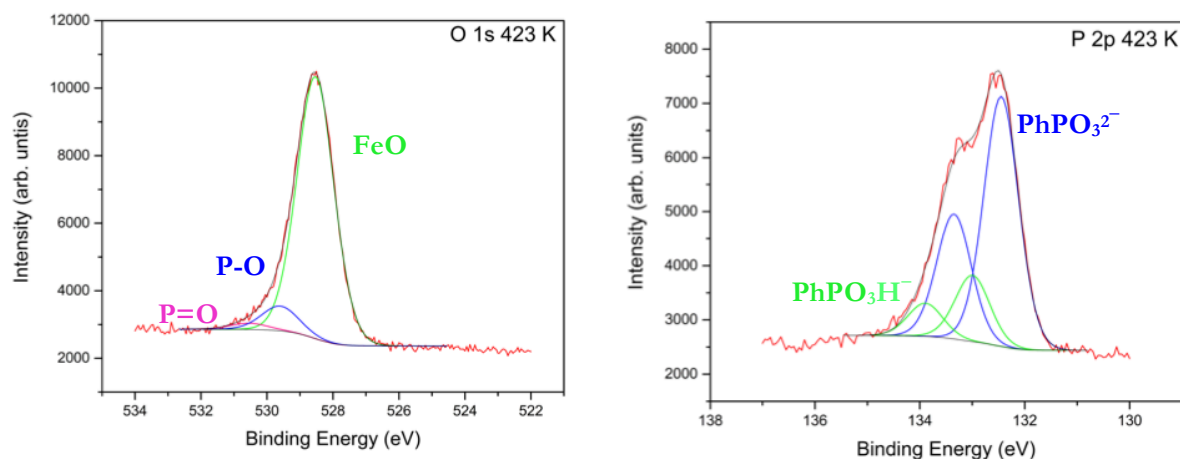


Figure 5.13. UHV XPS O 1s (left) and P 2p (right) core level spectra of  $\text{PhPO}_3\text{H}_2$  on an Fe(110) surface recorded after heating the sample to 423 K.

There was no further change in the shape of the spectra after heating the sample at 473 K for 30 minutes suggesting the compound remains strongly bound to the surface even at high temperatures. However, after heating between of 673-773 K for 20 minutes, the compound was completely removed although there were some remnants of O on the surface.

By integrating to find the total area of the P 2p and Fe 3p peaks, the thickness of the film for the compound in each set of experiments can be estimated. The P 2p:Fe 3p ratio – Table 5.4 – suggests that there is a coverage of 0.22 ML for the thin layer and of 1.18 ML for when the thick layer experiment is mentioned. It is not possible to provide an absolute number as the sample position is changed in between experiments and so the measurements are not comparable.

Table 5.4. Absolute areas for the P 2p and Fe 3p peaks corresponding to the experiments of  $\text{PhPO}_3\text{H}_2$  on a Fe(110) surface.

|                    | P 2p area | Fe 3p area | P 2p:Fe 3p |
|--------------------|-----------|------------|------------|
| <b>Thin layer</b>  | 14526.10  | 113497.80  | 0.13       |
| <b>Thick layer</b> | 8944.00   | 12773.90   | 0.70       |
| <b>Monolayer</b>   | 7434.60   | 12588.60   | 0.59       |

In addition to the photoemission spectroscopy, which gives information on the mode of adsorption, Near Edge X-ray absorption Fine Structure (NEXAFS) measurements were also performed when a monolayer of the phosphonate was bound to the Fe(110) surface – following a heating to 423 K. NEXAFS allows the adsorption geometry of the molecule to be probed, specifically the angles of the phenyl ring relative to the surface normal and the azimuthal plane.

Analysis of the intensities of the peak labelled A in the NEXAFS spectra presented in Figure 5.14 allows the tilt angle to be deduced and degree of ordering of the molecules along a particular crystalline direction. This to some extent gives an idea of the packing density that can be achieved by the molecule. Peak A arises from transitions from the C 1s core level to unoccupied  $\pi^*$  orbitals of the phenyl ring. As previously reported by Wagstaffe *et al.*, who assigned the peaks both experimentally and theoretically, this is a transition from C 1s (C-P) as opposed to C 1s (C-C).<sup>13</sup>

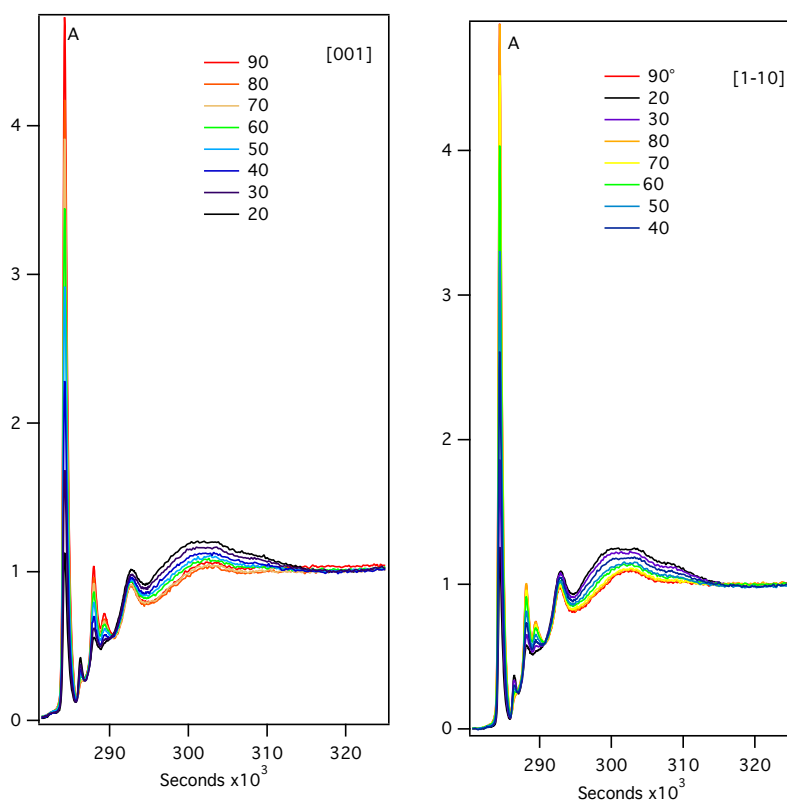


Figure 5.14. NEXAFS spectra recorded of  $\text{PhPO}_3\text{H}_2$  on an Fe(110) surface along the [001] (left) and [1-10] (right) crystal directions.

The  $\pi^*$  orbitals lie perpendicular to the plane of the aromatic ring. The interaction of the plane polarised synchrotron radiation with the excited electrons affects the intensity of these peaks in a manner that when the  $\mathbf{E}$  of the synchrotron radiation beam is in the same direction as the  $\pi^*$  orbitals the intensity of peak A is at its maximum. As the sample is rotated and the angle between the electric vector of the light and the  $\pi^*$  orbitals is increased, the intensity of the peak A is reduced. At the same time the rather broad peaks at around 300-350 eV arising from transitions from C 1s to  $\sigma^*$ , which lie in the plane of the ring, become more intense. Analysis of the intensity of the peak A as a function of incidence angle allows the tilt of the plane of the ring to be determined. A fit to these intensities along two different crystal directions using the Stöhr equations<sup>42</sup> (Chapter 1) is shown in Figure 5.15.

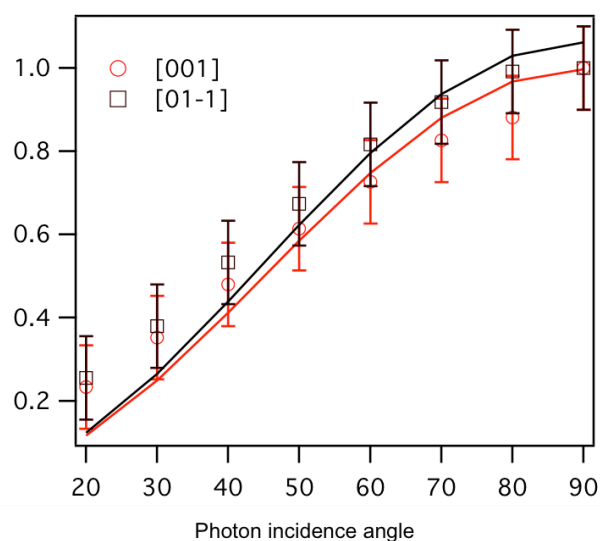


Figure 5.15. Plot of intensity of C 1 $\sigma$  to  $\pi^*$  transitions versus incident angle of photons fitted with Stöhr equations for the [001] (red) and [1-10] (black) crystal directions.

According to the fitting, the intensity of the A peak the molecules bound to the surface with the aromatic ring perpendicular to the surface. Figure 5.16 shows a schematic representation on how the molecules interact with the Fe surface.

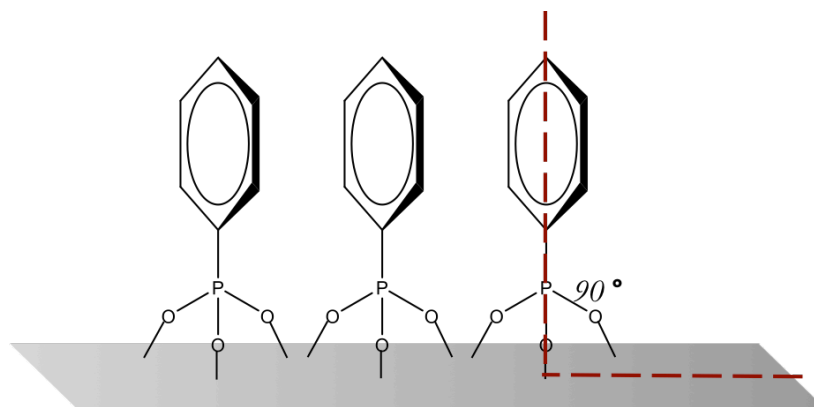


Figure 5.16. Schematic representation of the suggested interaction of PhPO<sub>3</sub>H<sub>2</sub> with the given Fe(110) surface when forming a monolayer at 423 K.

The NEXAFS spectra were also recorded after the second deposition, when there was a thick layer of compound on the surface and the acidic form was present. This though did not show any change in the intensity for the transition from the C 1s core level to unoccupied  $\pi^*$  orbitals suggesting that the aromatic rings were not ordered on the surface. Figure 5.17 shows a schematic representation of a suggested interaction of PhPO<sub>3</sub>H<sub>2</sub> in this case.

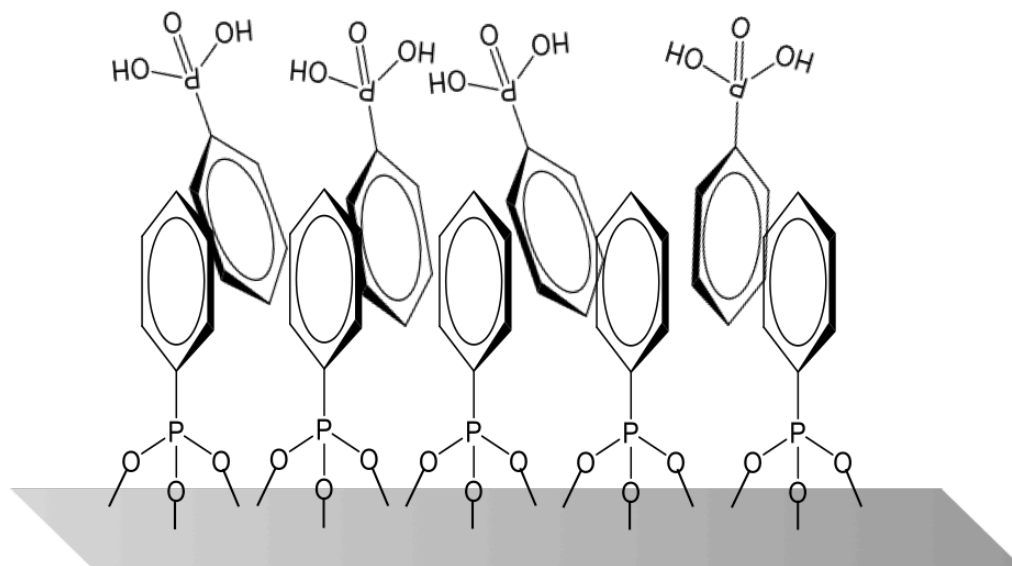


Figure 5.17. Schematic representation of the suggested interaction of PhPO<sub>3</sub>H<sub>2</sub> with the given Fe(110) surface when there is a thick layer.

## 5.3.2. Benzylphosphonic acid on Fe(110)

### 5.3.2.1. Experimental

The work presented in this section was carried out in the Photon Science Institute in Manchester in a near ambient pressure (NAP) XPS instrument equipped with a SPECS Focus 500 monochromated Al K $\alpha$  source (photon energy 1486.6 eV), which is focussed to a spot size of 300  $\mu\text{m}$ . The analyser is a SPECS 150 mm Phoibos 150 NAP analyser. The analysis chamber is separated from the sample preparation chamber by means of a gate valve. The Fe(110) crystal was held in place by a tantalum wire. A thermocouple was attached to the sample plate allowing the temperature of the sample to be monitored. The pressure in the analysis chamber was about  $1.5 \times 10^{-10}$  mbar during the measurements. Benzylphosphonic acid ( $\text{BzPO}_3\text{H}_2$ ) was evaporated onto the Fe crystal surface by vacuum sublimation at a temperature of 403-413 K for different amounts of time depending on the desired thickness of the molecular layer. Photoemission spectra were collected at normal emission (NE) and grazing emission (GE). This ensures that roughly the same depth of surface is probed and gives high surface sensitivity i.e. a probe depth of roughly 6 nm.<sup>35</sup>

### 5.3.2.2. Results and discussion

The Fe(110) single crystal was cleaned by repeated 1 keV  $\text{Ar}^+$  ion bombardment and annealing to 873 K. Figure 5.18 shows a wide scan and a narrow scan for the C 1s core level of the clean surface. After 18 cycles of sputter and anneal the N and O contamination was successfully removed, the C contamination reached a stationary stage, but it could not be completely removed. In the narrow scan the C signal is composed of two components: C present in hydrocarbon compounds from atmospheric contamination, surface component at 284.5 eV (green) and the carbide C, bulk contamination at 283.1 eV (blue). This was confirmed by recording the spectra at normal and grazing angles.

The first deposition of  $\text{BzPO}_3\text{H}_2$  was carried out for 3 minutes at 408 K in the UHV load lock at a pressure of  $1.12 \times 10^{-6}$  mbar. Figure 5.19 shows the XPS spectra recorded after deposition. The C 1s core level can be fitted with 30% Gaussian 70% Lorentzian peaks. The peak at 283.1 eV belongs to the bulk contamination carbide C (blue). The intense peak at 285.5 eV (green) is assigned to the C in the aromatic ring, the presence of which is confirmed by the satellite signal at a binding energy of 291.2 eV corresponding to a  $\pi-\pi^*$  shake up process in the phenyl group (Figure 5.19). The peak at 285.5 eV (pink) is assigned to the  $\text{Csp}^3$  between the aromatic ring and the P.

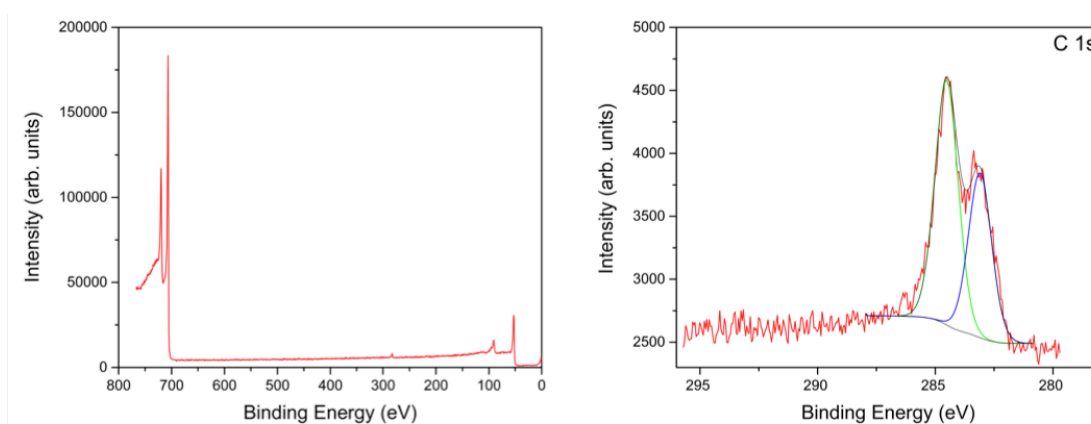


Figure 5.18. UHV XPS survey (left) and C 1s (right) spectra recorded from the sputtered and annealed Fe(110) single crystal.

The P 2p spectrum is consistent with the 2p spin orbit splitting of P with two sets of spin orbit doublets, suggesting P is in two different chemical environments. The P  $2p_{3/2}$  and  $2p_{1/2}$  doublets are constrained with an energy separation of  $0.9 \text{ eV}^{41}$  ref and a 2:1 ratio for the areas.

Table 5.5. Peak assignments for O 1s and P 2p spectra and their respective binding energies (eV) for the spectra of BzPO<sub>3</sub>H<sub>2</sub> in Figures 5.19, 5.20, 5.21 and 5.22, NE = normal emission and GE = grazing emission.

|                                      | Binding Energy (eV) |          |          |          |          |          |
|--------------------------------------|---------------------|----------|----------|----------|----------|----------|
|                                      | O 1s                |          |          |          |          |          |
|                                      | NE 300 K            | NE 350 K | NE 400 K | NE 550 K | GE 400 K | GE 550 K |
| <b>P-O-Fe</b>                        | 531.2               | 531.2    | 531.2    | 531.2    | 531.3    | 531.2    |
| <b>P=O</b>                           | 532.4               | 532.3    | 532.4    | 532.4    | 532.4    | 532.4    |
| <b>P-OH</b>                          | 533.2               | 533.2    | 533.3    | 533.3    | -        | -        |
|                                      | P 2p                |          |          |          |          |          |
| <b>Tridentate P 2p<sub>3/2</sub></b> | 132.6               | 132.6    | 132.7    | -        | 132.7    | -        |
| <b>Tridentate P 2p<sub>1/2</sub></b> | 133.5               | 133.5    | 133.6    | -        | 133.6    | -        |
| <b>Bidentate P 2p<sub>3/2</sub></b>  | 133.3               | 133.3    | 133.3    | 133.4    | 133.3    | 133.2    |
| <b>Bidentate P 2p<sub>1/2</sub></b>  | 134.2               | 134.1    | 134.2    | 134.3    | 134.2    | 134.1    |

A comparison with the data from PhPO<sub>3</sub>H<sub>2</sub> suggests that both the acid (green) and the phosphonate (blue) species are present. In the phosphonate species the three O atoms are deprotonated and interacting with the surface, these are assigned to the peak at 531.1 eV in the O 1s spectrum. The peaks at 532.3 (blue) and 533.2 eV (pink) correspond to the acid species, the former arising from the P=O and the latter from the protonated P-OH. This suggests that the compound binds to the surface and forms a monolayer of doubly deprotonated phosphonate bound through all three O atoms; and a second layer of non-interacting acid forms on top of it.

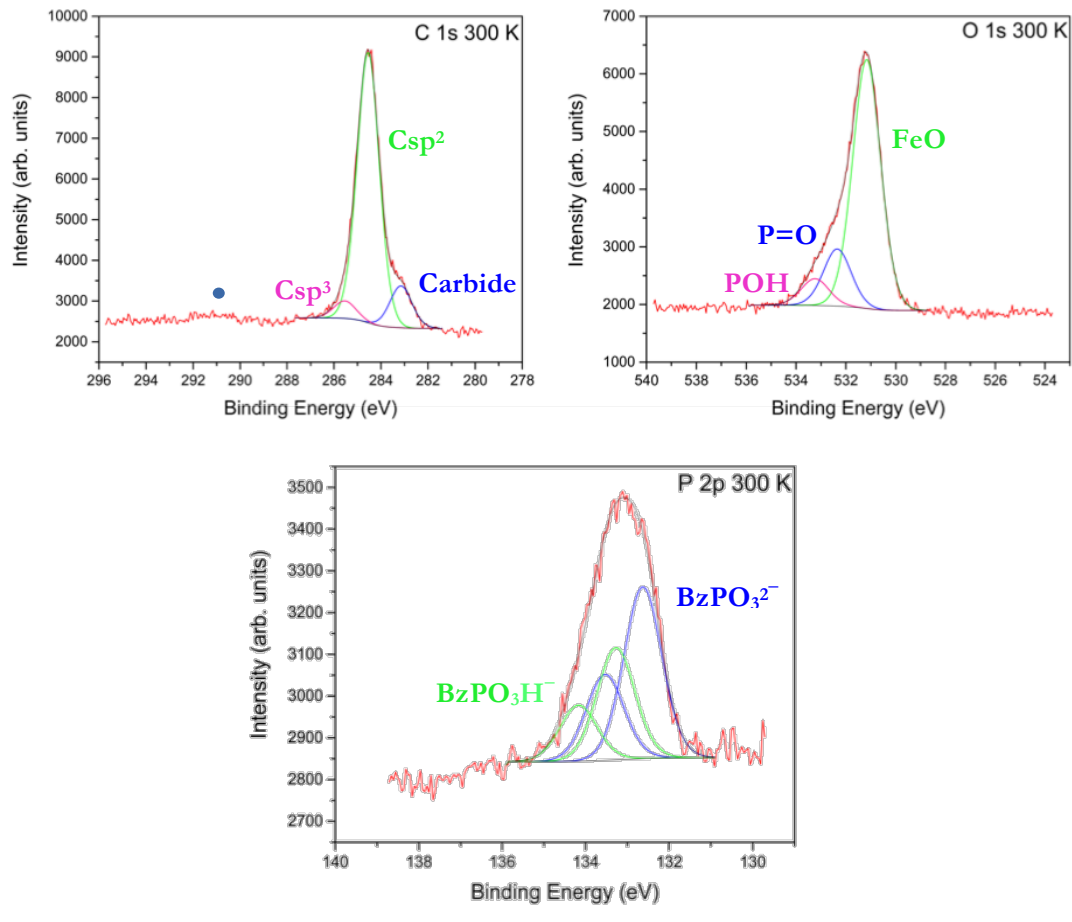


Figure 5.19. UHV XPS core level spectra for C 1s (top left), O 1s (top right) and P 2p (bottom) recorded after a 3 minute deposition of  $\text{BzPO}_3\text{H}_2$  on an Fe(110) surface, the  $\pi-\pi^*$  shake up process marked with a dot on the C 1s spectrum.

In order to investigate the stability of the adsorbed molecule a temperature dependent study was carried out. The sample was heated in 50 degree steps and core level XPS spectra recorded. Figure 5.20 shows the recorded spectra at 350 K, where it can be seen that all signals belonging to the acid species have decreased in intensity suggesting that the second layer is not strongly interacting with the surface i.e. it is physisorbed and can be removed from the surface by heating it.

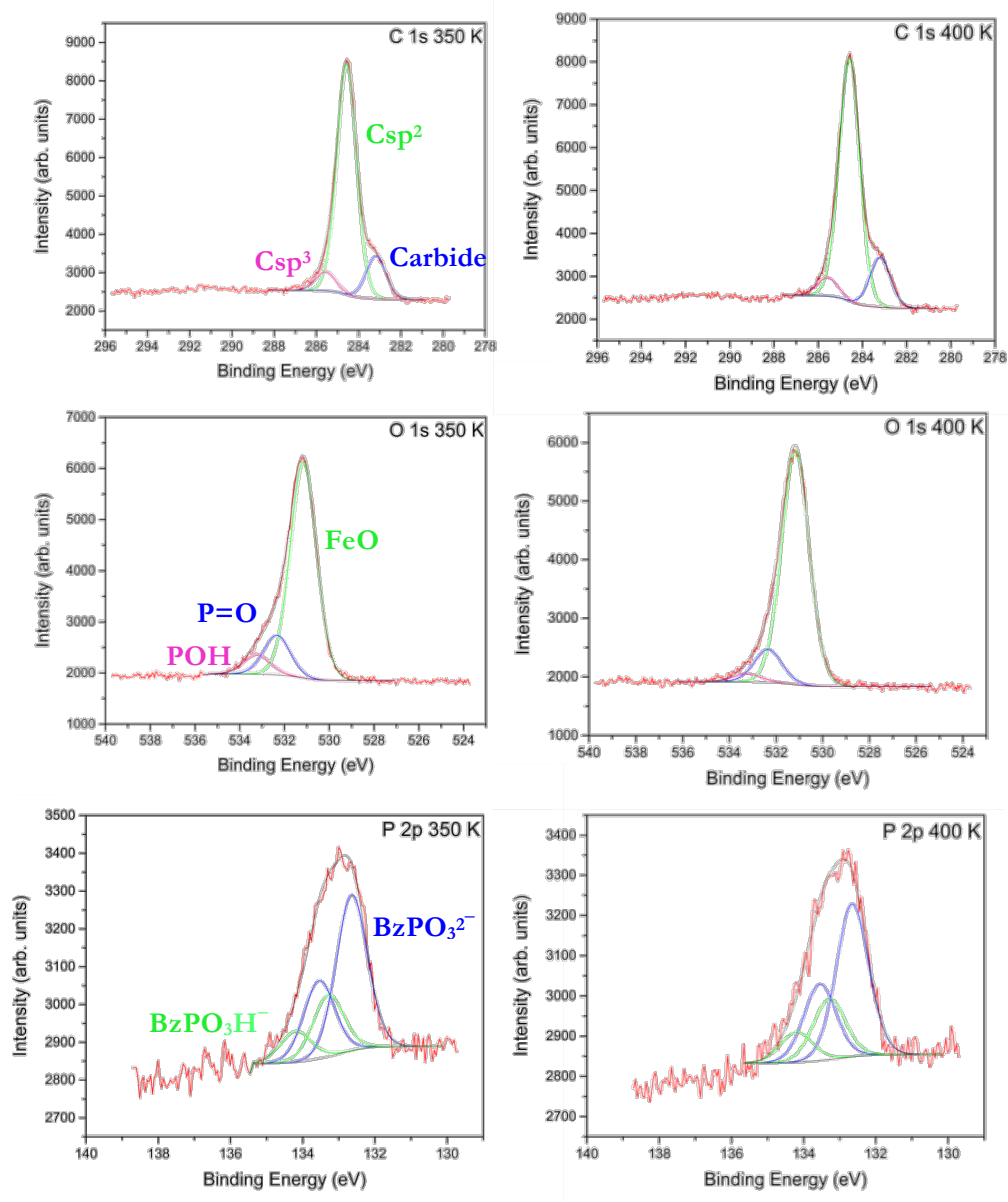


Figure 5.20. UHV XPS core level of  $\text{BzPO}_3\text{H}_2$  spectra recorded for C 1s (top), O 1s (middle) and P 2p (bottom) at 350 (left) and 400 K (right).

Figure 5.20 also shows the spectra recorded at 400 K where it can be seen that the peak due to the P-OH in the O spectrum is almost completely removed and the peak due to P=O is reduced in intensity. No other big changes are seen. The spectrum was not changing much at this point and so the temperature was raised to 550 K.

After heating the sample at 550 K the P signal significantly decreased. One possible interpretation is that the molecule decomposes and there are only fragments of it on the surface. This also explains the appearance of a peak at 529.8 eV in the O 1s spectrum,

which could be assigned to an iron oxide peak because the binding energy is consistent with  $\gamma$ - $\text{Fe}_2\text{O}_3$  (529.9 eV).<sup>43</sup>

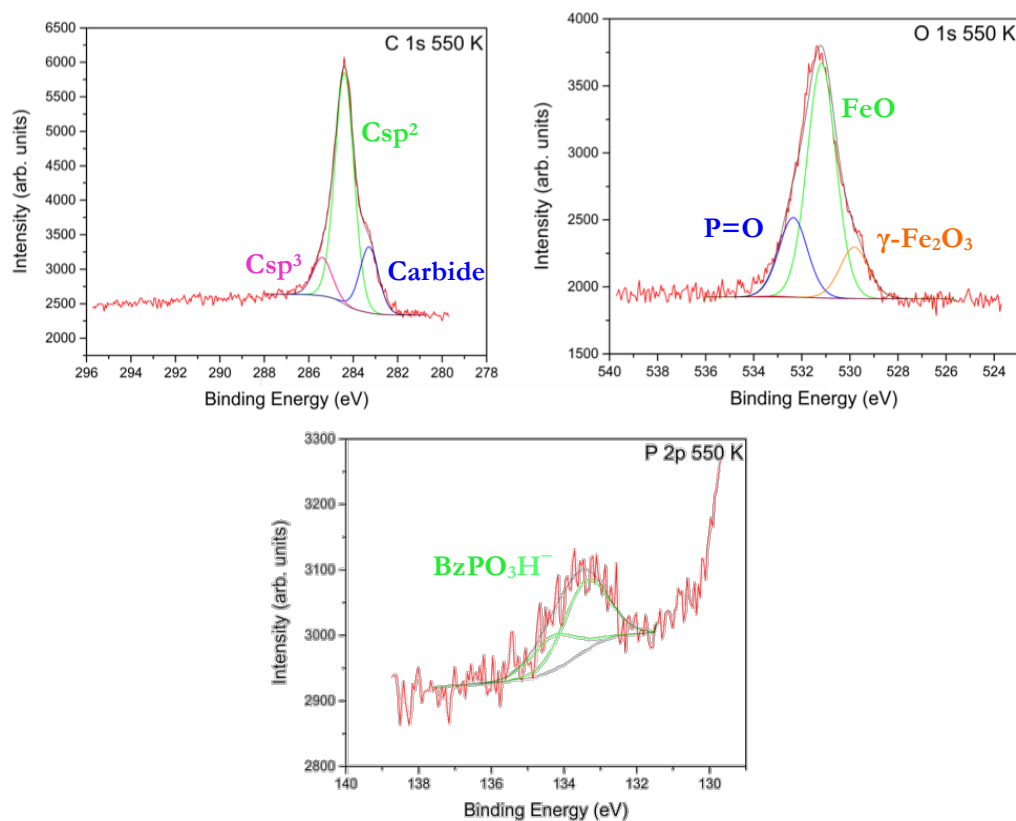


Figure 5.21. UHV XPS core level spectra of BzPO<sub>3</sub>H<sub>2</sub> on an Fe(110) surface for C 1s (top left), O 1s (top right) and P 2p (bottom) recorded at 550 K.

Changing the sample from normal emission (NE) to grazing emission (GE), 70 °, increases the distance the electrons have to travel through the sample also increasing the surface sensitivity and reducing the bulk contribution to the signal. For this reason changes in the relative intensities of the peaks at NE and GE can give more information about the chemistry of the surface.

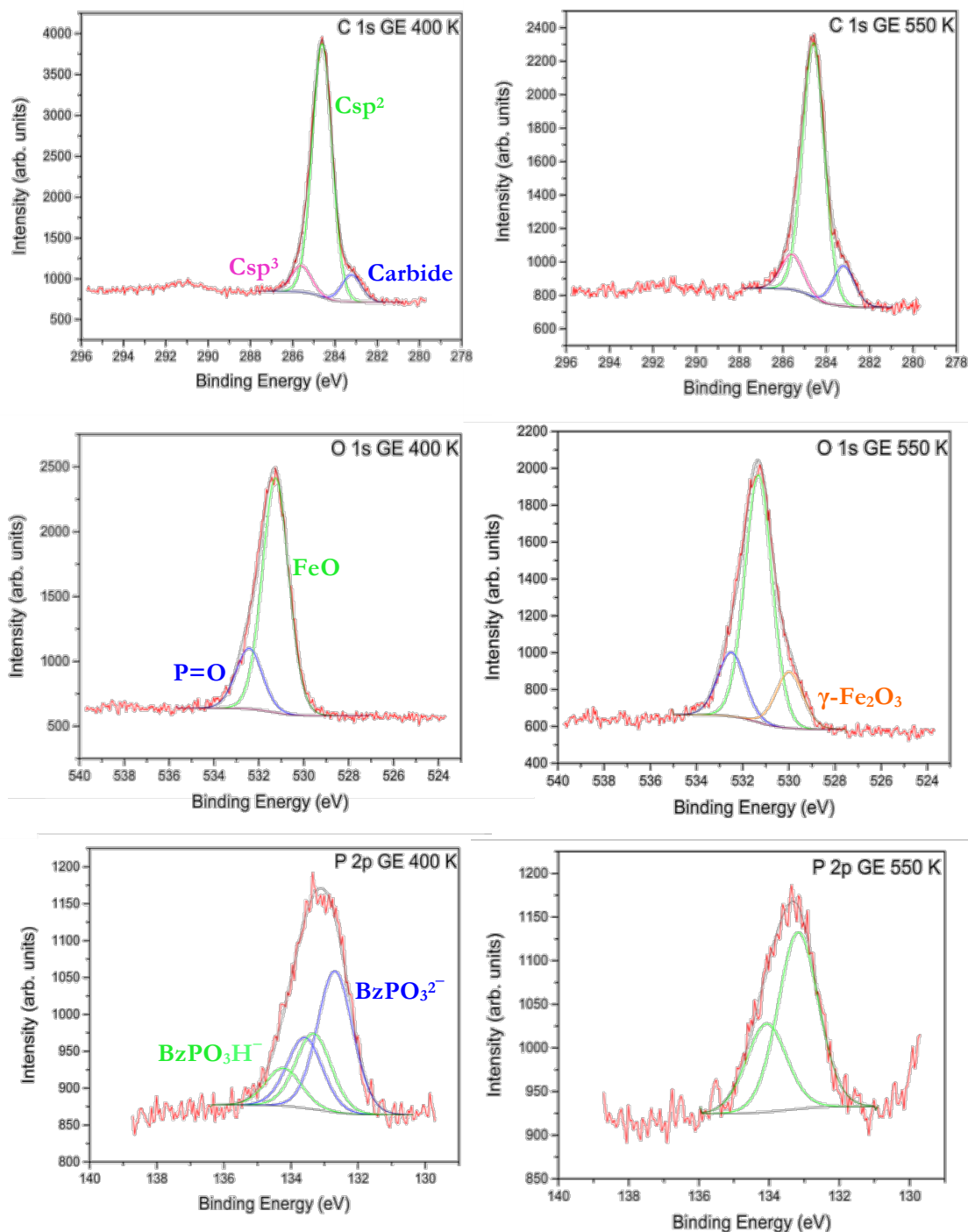


Figure 5.22. UHV XPS core level spectra of BzPO<sub>3</sub>H<sub>2</sub> on an Fe(110) surface recorded at GE for C 1s (top), O 1s (middle) and P 2p (bottom); at 400 and 550 K.

The data were recorded at GE at a temperature of 400 K (Figure 5.22). When comparing these data with those recorded at NE it can be seen that in the P 2p spectrum the signal belonging to the acid species has increased in intensity. The same

thing happens with the  $\text{OH}^-$  signal in the O 1s peak suggesting the acidic species is on a more superficial layer. This supports what has been said before that the excess of compound is not bound to the Fe surface but forms a physisorbed layer on top of the bound phosphonate.

The spectra were also recorded at GE at 550 K (Figure 5.22). These spectra do not show much difference when compared to the spectra recorded at normal emission. It is noted that the oxide peak assigned to  $\gamma\text{-Fe}_2\text{O}_3$  at 529.8 eV is reduced in intensity relative to the molecular peaks suggesting it is buried beneath the molecular fragments. This would support the formation of iron oxide species.

### 5.3.3. Hexadecylphosphonic acid on Fe(110)

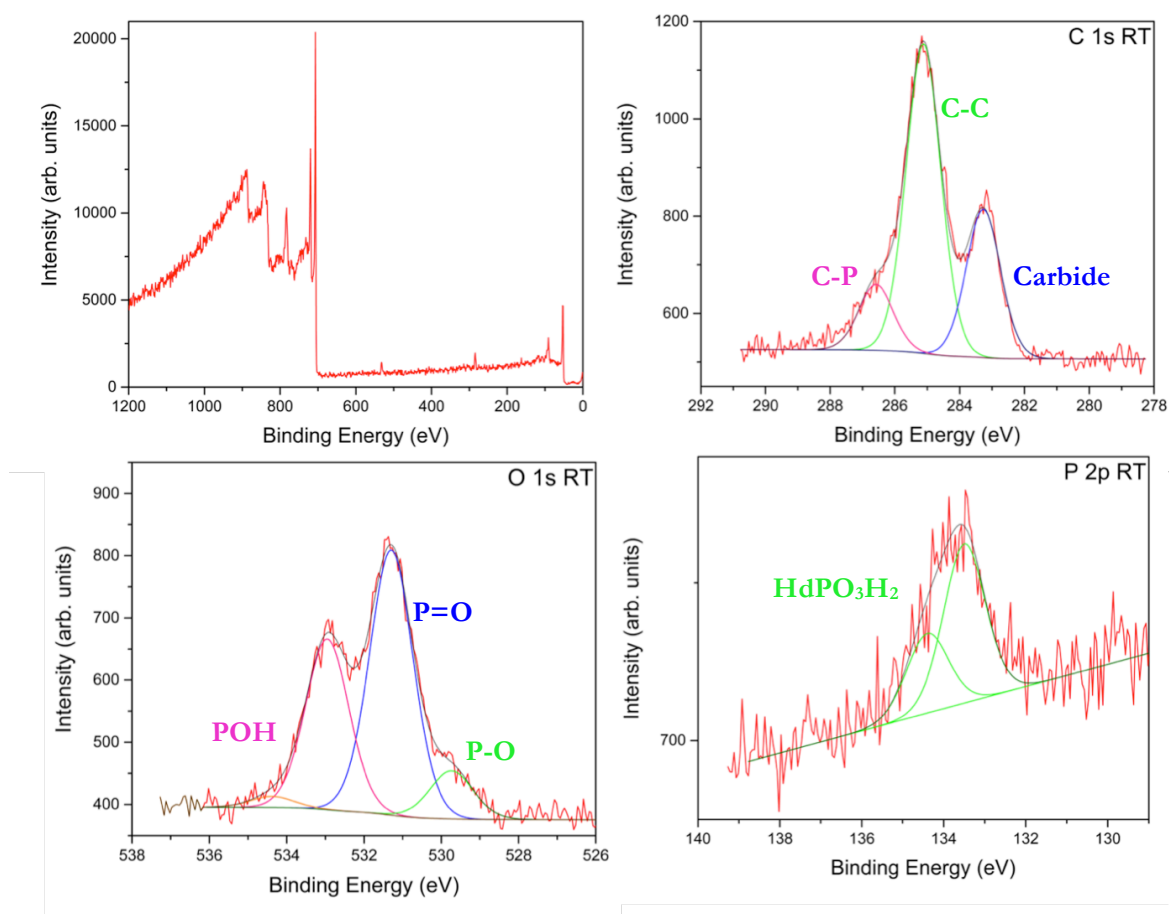
#### 5.3.3.1. Experimental

This work was carried out in the Photon Science Institute in Manchester in a near ambient pressure (NAP) XPS instrument equipped with a SPECS Focus 500 monochromated Al  $\text{K}\alpha$  source (photon energy 1486.6 eV), which is focussed to a spot size of 300  $\mu\text{m}$ . The analyser is a SPECS 150 mm Phoibos 150 NAP analyser. The analysis chamber is separated from the sample preparation chamber by means of a gate valve. The Fe(110) crystal was held in place by a tantalum wire. A thermocouple was attached to the sample plate allowing the temperature of the sample to be monitored. The pressure in the analysis chamber was about  $1.5 \times 10^{-10}$  mbar during the measurements. Hexadecylphosphonic acid ( $\text{HdPO}_3\text{H}_2$ ) was evaporated onto the Fe crystal surface by vacuum sublimation without the need to apply heat for different amounts of time depending on the desired thickness of the molecular layer. Photoemission spectra were collected at normal emission. This ensures that roughly the same depth of surface to be probed and gives high surface sensitivity i.e. a probe depth of roughly 6 nm.<sup>35</sup>

### 5.3.3.2. Results and discussion

#### 5.3.3.2.1. XPS study in UHV

The Fe(110) single crystal was cleaned by repeated 1 keV  $\text{Ar}^+$  ion bombardment and annealing to 873 K. A first deposition of  $\text{HdPO}_3\text{H}_2$  was carried out at UHV once the carbide C contamination (blue peak in the C 1s spectrum in Figure 5.23) of the Fe(110) single crystal achieved a stationary state.



5.23. UHV XPS core level spectra of  $\text{HdPO}_3\text{H}_2$  on an Fe(110) surface recorded at room temperature wide scan (top left), C 1s (top right), O 1s (bottom left) and P 2p (bottom right).

Figure 5.23 shows the spectra following deposition. The C 1s spectrum can be fitted with three peaks assigned to carbide, (blue), the C bound to the P at *ca.* 286 eV (pink)

and the most intense signal at *ca.* 285 eV due to the CH<sub>2</sub> and CH<sub>3</sub> on the alkyl chain (green).

The O 1s peak can also be fitted with three peaks. Based on the assignment of the other spectra the peak at *ca.* 529.7 eV is due to the P-O bound to the surface (green), the one at 531.2 eV to the P=O (blue) and the one at 532.9 eV to the protonated O (pink). The interpretation of these fittings and intensity of the signals suggests that the phosphonic acid is bound to the surface through only one O atom, with a monodentate binding mode. This is confirmed by the P 2p peak where there is only one chemical species due to the acid. The origin of the small feature at highest binding energy in the O 1s signal (orange) has not been assigned, because of the low quality of the data it is not clear if this is a real peak as the data could also be fitted adequately without its presence.

Table 5.6. Peak assignments and their respective binding energies (eV) for the spectra of HdPO<sub>3</sub>H<sub>2</sub> in Figures 5.23 and 5.24.

|                  | Binding Energy (eV) |       |       |       |       |
|------------------|---------------------|-------|-------|-------|-------|
|                  | C1s                 |       |       |       |       |
|                  | RT                  | 373 K | 423 K | 473 K | 523 K |
| <b>Carbide C</b> | 283.3               | 283.1 | 283.3 | 283.1 | 283.1 |
| <b>C-C</b>       | 285.1               | 284.9 | 285.0 | 284.7 | 283.4 |
| <b>C-P</b>       | 286.6               | 286.3 | 286.5 | 286.2 | 286.1 |
|                  | O 1s                |       |       |       |       |
|                  | RT                  | 373 K | 423 K | 473 K | 523 K |
|                  | <b>P-O-Fe</b>       | 529.7 | 529.8 | 529.8 | 529.8 |
| <b>P=O</b>       | 531.3               | 531.1 | 531.3 | 531.2 | 531.2 |
| <b>P-OH</b>      | 533.0               | 532.8 | 532.9 | 532.7 | 532.8 |

The surface was then heated in 50 degree steps to check how the system reacts to temperature. Table 5.6 shows the assignment of C 1s and O 1s for all the temperature steps showing only fluctuations that are within the accepted range of variations. Figure

5.24 shows the spectra, the P 2p peak is not shown, as it also does not change while increasing the temperature. The lack of change in all spectra with temperature indicates that  $\text{HdPO}_3\text{H}_2$  does not seem to be affected when raising the temperature up until 473 K suggesting that the interaction is thermodynamically very stable and that the compound is strongly bound to the Fe(110) surface.

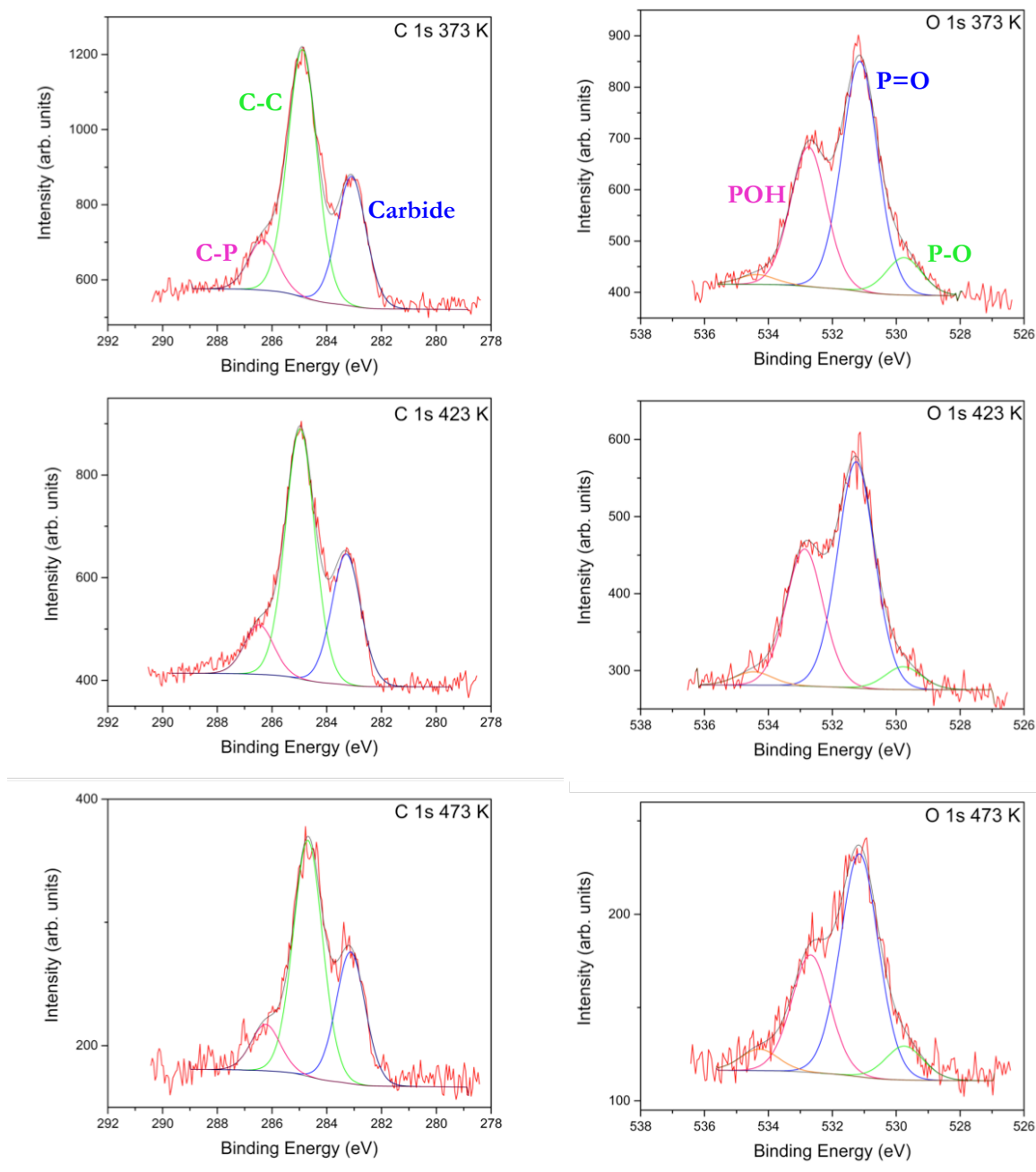


Figure 5.24 UHV XPS core level spectra of  $\text{HdPO}_3\text{H}_2$  on an Fe(110) surface recorded at 373 (top), 423 (middle) and 473 K (bottom).

### 5.3.3.2.2. XPS study under NAP conditions

For control experiments on how the surface behaves in the presence of  $\text{H}_2\text{O}$  and  $\text{CO}_2$  refer to Chapter 4. The Fe(110) single crystal was cleaned using the same method explained above and the deposition was carried out in the same way to get a similar amount of compound on the surface. An  $\text{H}_2\text{O}$  vapour of 2.5 mbar pressure was then injected into the NAP cell and the spectra shown in Figure 5.25 recorded. Because the data were acquired in low vacuum there was some loss in the intensity of the signal, making the P 2p peak too low in intensity, noisy and too broad to fit and for this reason it is not shown. The C 1s signal is identical to the spectrum acquired in UHV, showing the three chemical environments assigned above: carbide C, C directly bound to the P atom and the C in the alkyl chain. In Table 5.7 shows that the binding energy for the peaks agrees with the previous results.

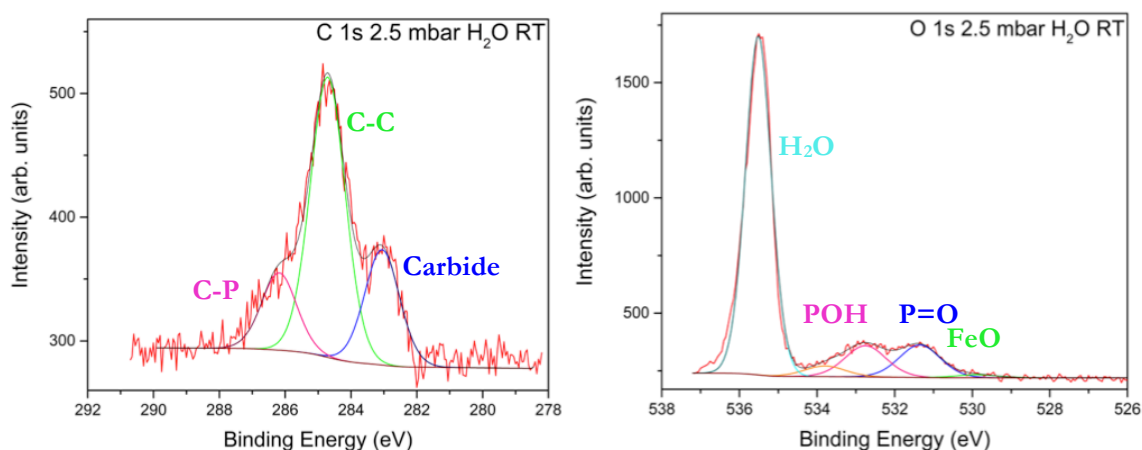


Figure 5.25. NAP XPS C 1s (right) and O 1s (left) core level spectra of  $\text{HdPO}_3\text{H}_2$  on an Fe(110) surface in the presence of 2.5 mbar of  $\text{H}_2\text{O}$  recorded at room temperature.

The O 1s signal exhibits a new feature at a binding energy of *ca.* 535 eV due to the  $\text{H}_2\text{O}$  vapour in the NAP cell. The O 1s core level shows the same three chemical species for the compound as seen in UHV experiments.

Table 5.7. Peak assignments and their respective binding energies (eV) for the spectra of  $\text{HdPO}_3\text{H}_2$  in the presence of 2.5 mbar of  $\text{H}_2\text{O}$  shown in Figures 5.25 and 5.26.

|                       | Binding Energy (eV) |       |       |
|-----------------------|---------------------|-------|-------|
|                       | C1s                 |       |       |
|                       | RT                  | 373 K | 423 K |
| <b>Carbide C</b>      | 283.1               | 283.1 | 283.2 |
| <b>C-C</b>            | 284.7               | 284.6 | 284.4 |
| <b>C-P</b>            | 286.2               | 286.2 | 286.2 |
|                       | O 1s                |       |       |
|                       | RT                  | 373 K | 473 K |
|                       | RT                  | 373 K | 473 K |
| <b>P-O-Fe</b>         | 529.9               | 529.8 | 529.7 |
| <b>P=O</b>            | 531.4               | 531.3 | 531.2 |
| <b>P-OH</b>           | 532.8               | 532.7 | 532.4 |
| <b>H<sub>2</sub>O</b> | 535.5               | 535.4 | 535.1 |

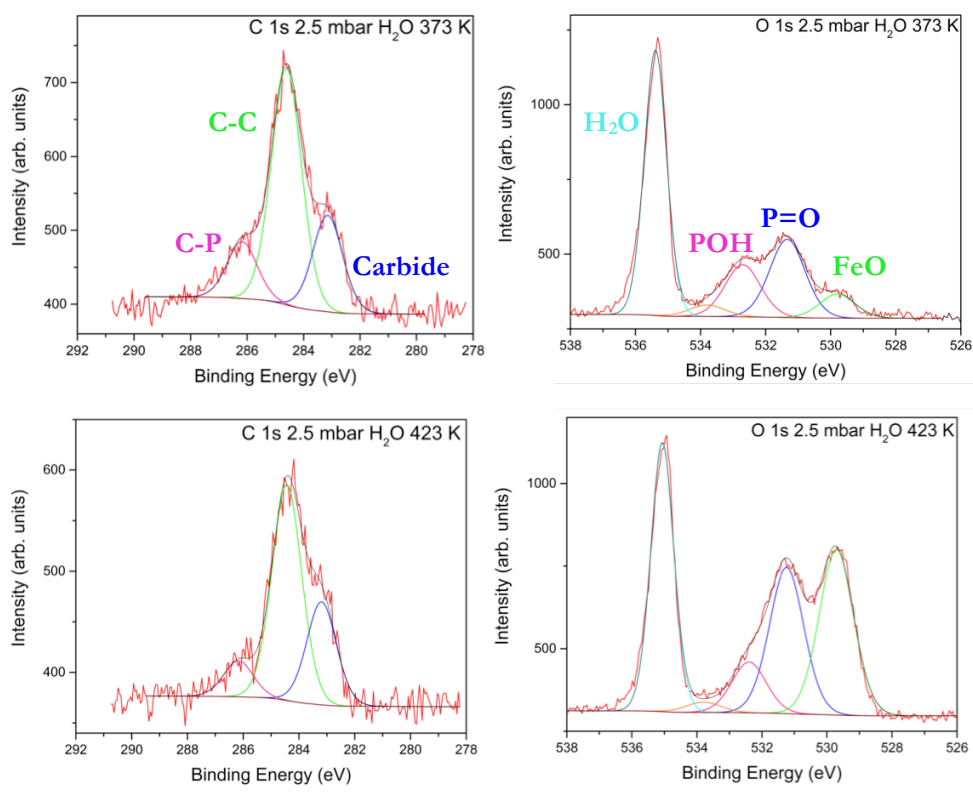


Figure 5.26. NAP XPS core level spectra of  $\text{HdPO}_3\text{H}_2$  on an Fe(110) surface in the presence of 2.5 mbar of  $\text{H}_2\text{O}$  recorded at 373 (top) and 423 K (bottom).

Heating the sample to 373 K does not have much effect on the C 1s signal. However in the O 1s spectrum there is evidence of oxidation in the growth of the O<sup>2-</sup> peak (green) at a binding energy of *ca.* 529.8 eV and the OH<sup>-</sup> (blue). At 423 K there is some loss of intensity for the peaks assigned to the molecule in the C 1s signal in comparison with the one assigned to the carbide C suggesting the compound is starting to be removed from the surface. In the O 1s signal it can be seen how the surface is now highly oxidised suggesting the compound binds to the surface, but does not stop the surface from interacting with the H<sub>2</sub>O.

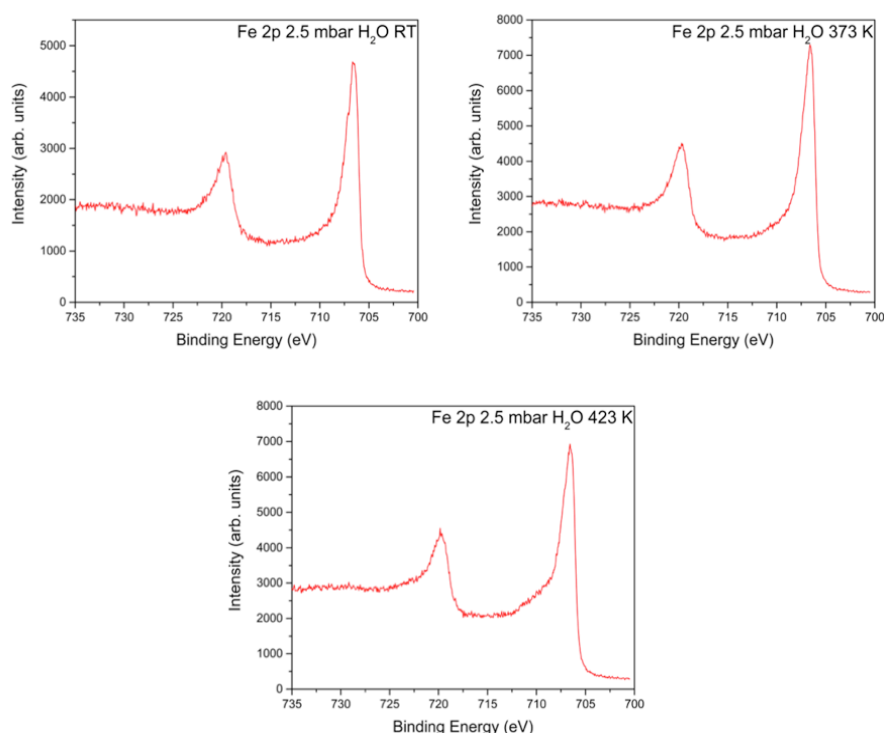


Figure 5.27. NAP XPS Fe 2p core level spectra of HdPO<sub>3</sub>H<sub>2</sub> on an Fe(110) surface in the presence of 2.5 mbar of H<sub>2</sub>O recorded at room temperature (top left), 373 (top right) and 423 K (bottom).

Analysis of the Fe 2p spectrum (Figure 5.27) shows how the oxidation becomes evident at 423 K when the doublet due to the oxidised Fe starts to show two small shoulders on the high binding energy side of the Fe 2p<sub>3/2</sub>.

The Fe(110) crystal was cleaned again and more HdPO<sub>3</sub>H<sub>2</sub> was deposited on the surface. Figure 5.28 shows the core level spectra recorded in the presence of 2 mbar of

CO<sub>2</sub>. From the relative intensity of the peaks compared to the data presented in the previous section it is obvious that there is less compound on the surface. The P 2p spectrum appears very weak and broad and because fitting cannot be successfully done it is not shown. The C 1s signal shows a peak due to gas phase CO<sub>2</sub> at *ca.* 293.3 eV as well as the three peaks already identified for the compound in UHV conditions. The ratio of the molecular C species to the carbide signal suggests that there is less compound on the surface than in the two cases described above. The O 1s core level spectrum also exhibits a peak due to gas phase CO<sub>2</sub> at *ca.* 536.9 eV as well as the three peaks arising from the compound. Table 5.8 shows the assignment and binding energies of the peaks, showing a good agreement with the spectra recorded in UHV and in the presence of H<sub>2</sub>O.

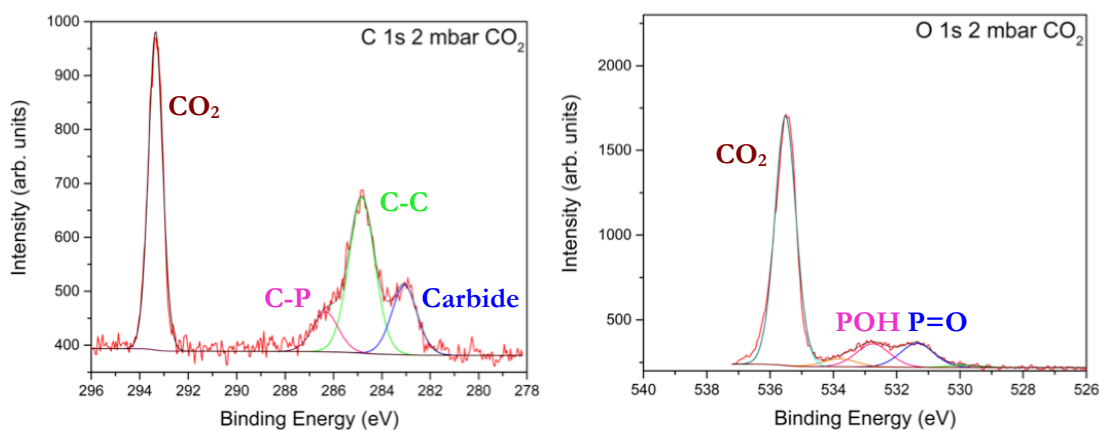


Figure 5.28. NAP XPS C 1s (left) and O 1s (right) core level spectra of HdPO<sub>3</sub>H<sub>2</sub> on an Fe(110) surface recorded in the presence of 2 mbar of CO<sub>2</sub>.

Water vapour was then added to the NAP cell in order to mimic the sweet corrosion that is found in the extraction of oil. This was done in different ratios of H<sub>2</sub>O:CO<sub>2</sub> 1:10, 1:2 and 1:1. Figure 5.29 shows these spectra. In the O 1s core level it can be seen how the intensity of the H<sub>2</sub>O peak increases when the pressure is increased, the peaks previously assigned to the compound (pink, blue and green) do not change when H<sub>2</sub>O is added, suggesting that HdPO<sub>3</sub>H<sub>2</sub> stops oxidation, at room temperature in a CO<sub>2</sub>/H<sub>2</sub>O mixed vapour.

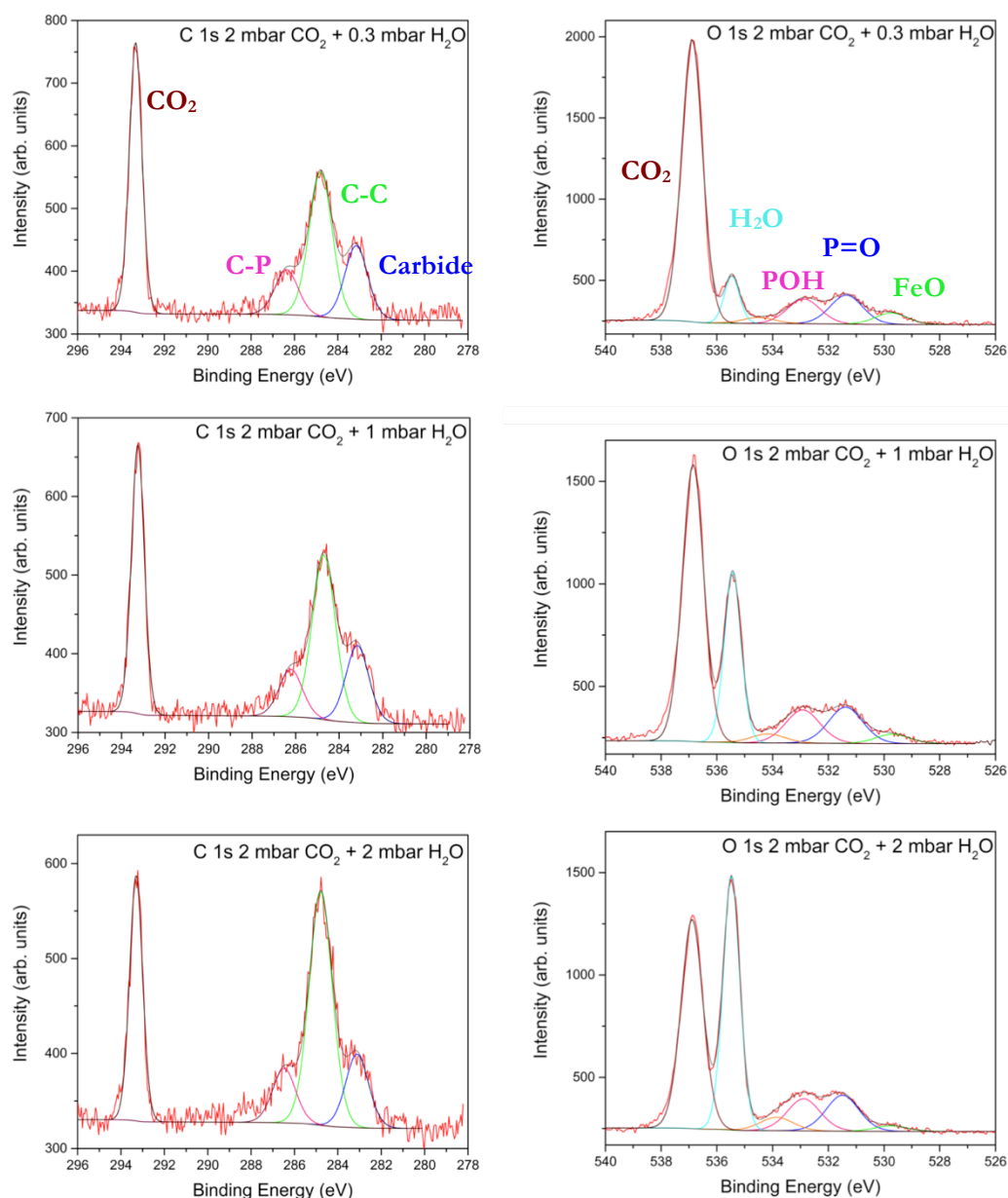


Figure 5.29. NAP XPS core level spectra of  $\text{HdPO}_3\text{H}_2$  on an Fe(110) surface recorded in the presence of 2 mbar of  $\text{CO}_2$  with 0.3 (top), 1 (middle) and 2 mbar of  $\text{H}_2\text{O}$  (bottom).

In the C 1s core level spectrum the peak assigned to the aliphatic C on the compound increases in intensity when the  $\text{H}_2\text{O}$  pressure is increased whilst the relative intensities of the C bound to the P and the carbide C remain constant.  $\text{HdPO}_3\text{H}_2$  is highly hydrophobic. It is possible that in contact with water the alkyl chain straightens up. This has the effect of increasing the depth of the hydrophobic aliphatic C position of the

molecule. Since the C-P and carbide are located at the surface the signal due to these species is reduced.

This behaviour has been seen in polymeric brushes, which swell in aqueous solution and other solvents. There has been a lot of studies recently that show when at a pH below their pKa the brushes become protonated due to absorption of the solvent creating electrostatic repulsion between the groups and causing the swelling, whilst at more basic pHs they contract, Figure 30 shows a schematic representation of this process<sup>44-46</sup> for  $\text{HdPO}_3\text{H}_2$ .

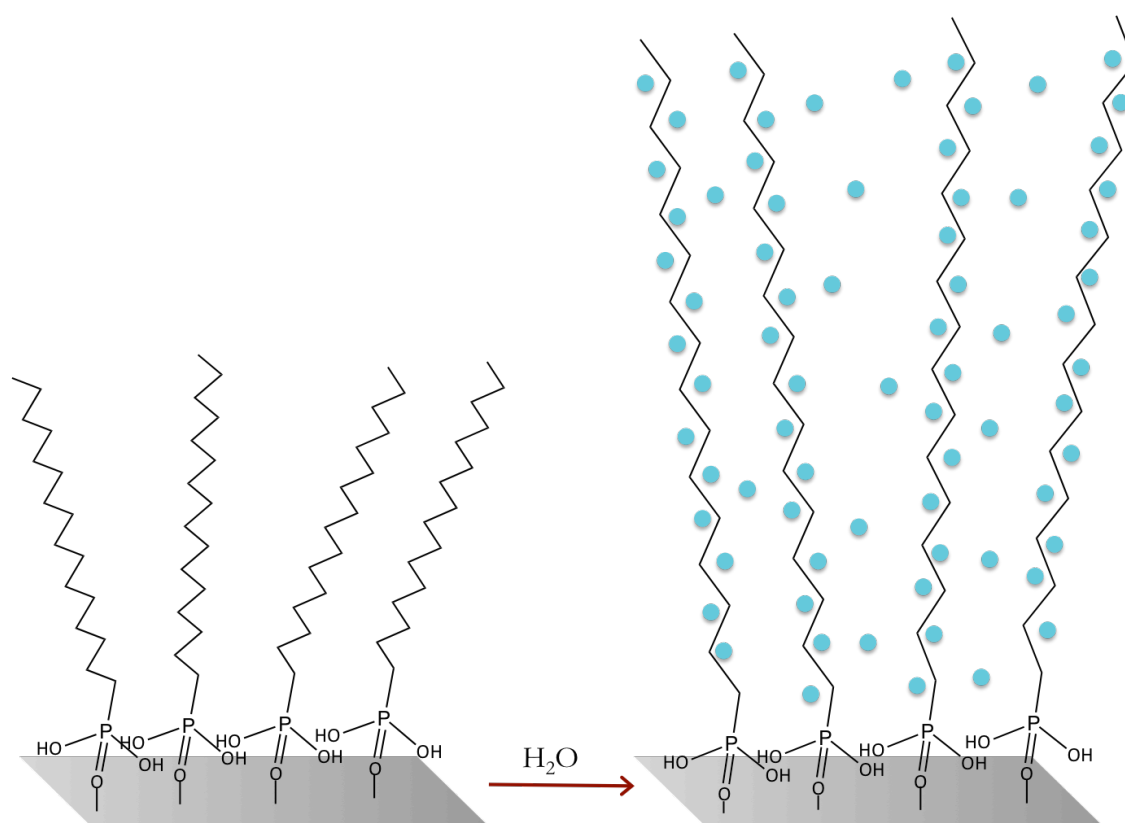


Figure 5.30. Schematic representation of the swelling process  $\text{HdPO}_3\text{H}_2$  suffers following the addition of  $\text{H}_2\text{O}$ .

It could be debated that  $\text{HdPO}_3\text{H}_2$  is not in a liquid environment during experiment as the  $\text{H}_2\text{O}$  present is in a vapour state due to the low pressure. However it has been reported that polymer brushes also present swelling in solvent vapours.<sup>47-49</sup> This is one of the reasons why corrosion inhibitors for the oil extraction have long aliphatic chains, because, on top of making the compounds partially soluble in the oil crude, they also

make the surface hydrophobic under acidic conditions promoting protection against the corrosive agents.

Table 5.8. Peak assignments and their respective binding energies (eV) for the spectra of  $\text{HdPO}_3\text{H}_2$  in the presence of 2 mbar of  $\text{CO}_2$  and different ratios of  $\text{H}_2\text{O}$  (in mbar) in Figures 5.29 and 5.31.

|  | Binding Energy (eV) |  |  |  |
|--|---------------------|--|--|--|
|  | C 1s                |  |  |  |
|  | 2 $\text{CO}_2$     | 2 $\text{CO}_2$ + 0.3 $\text{H}_2\text{O}$ | 2 $\text{CO}_2$ + 1 $\text{H}_2\text{O}$ | 2 $\text{CO}_2$ + 2 $\text{H}_2\text{O}$ |
| <b>Carbide C</b>                       | 283.1               | 283.2                                      | 283.2                                    | 283.1                                    |
| <b>C-C</b>                             | 284.8               | 284.8                                      | 284.7                                    | 284.8                                    |
| <b>C-P</b>                             | 286.3               | 286.4                                      | 286.2                                    | 286.5                                    |
| <b><math>\text{CO}_2</math></b>        | 293.3               | 293.3                                      | 293.3                                    | 293.3                                    |
|  | O 1s                |  |  |  |
|  | 2 $\text{CO}_2$     | 2 $\text{CO}_2$ + 0.3 $\text{H}_2\text{O}$ | 2 $\text{CO}_2$ + 1 $\text{H}_2\text{O}$ | 2 $\text{CO}_2$ + 2 $\text{H}_2\text{O}$ |
|  | <b>P-O-Fe</b>       | 529.7                                      | 529.7                                    | 529.7                                    |
| <b>P=O</b>                             | 531.3               | 531.4                                      | 531.4                                    | 531.5                                    |
| <b>P-OH</b>                            | 532.7               | 532.9                                      | 532.9                                    | 532.9                                    |
| <b><math>\text{H}_2\text{O}</math></b> | 535.5               | 535.5                                      | 535.4                                    | 535.5                                    |
| <b><math>\text{CO}_2</math></b>        | 537.0               | 536.9                                      | 536.9                                    | 536.9                                    |

The Fe 2p spectra are shown in Figure 5.31, indicating that the surface becomes slowly oxidised. However, by comparison to the control experiments in Chapter 4 it can be seen that the oxidation caused by  $\text{CO}_2$  in the presence of  $\text{HdPO}_3\text{H}_2$  is reduced, suggesting that the compound binds to the surface and stops it from interacting with  $\text{CO}_2$  and shows the no oxidation  $\text{CO}_2/\text{H}_2\text{O}$  vapour. In the C 1s spectra there is a very small peak arising at *ca.* 289 eV that has been previously assigned to the formation of  $\text{FeCO}_3$  under the same conditions. This feature however is so small that confirms that there is  $\text{HdPO}_3\text{H}_2$  stops the formation of the passivation  $\text{FeCO}_3$  layer.

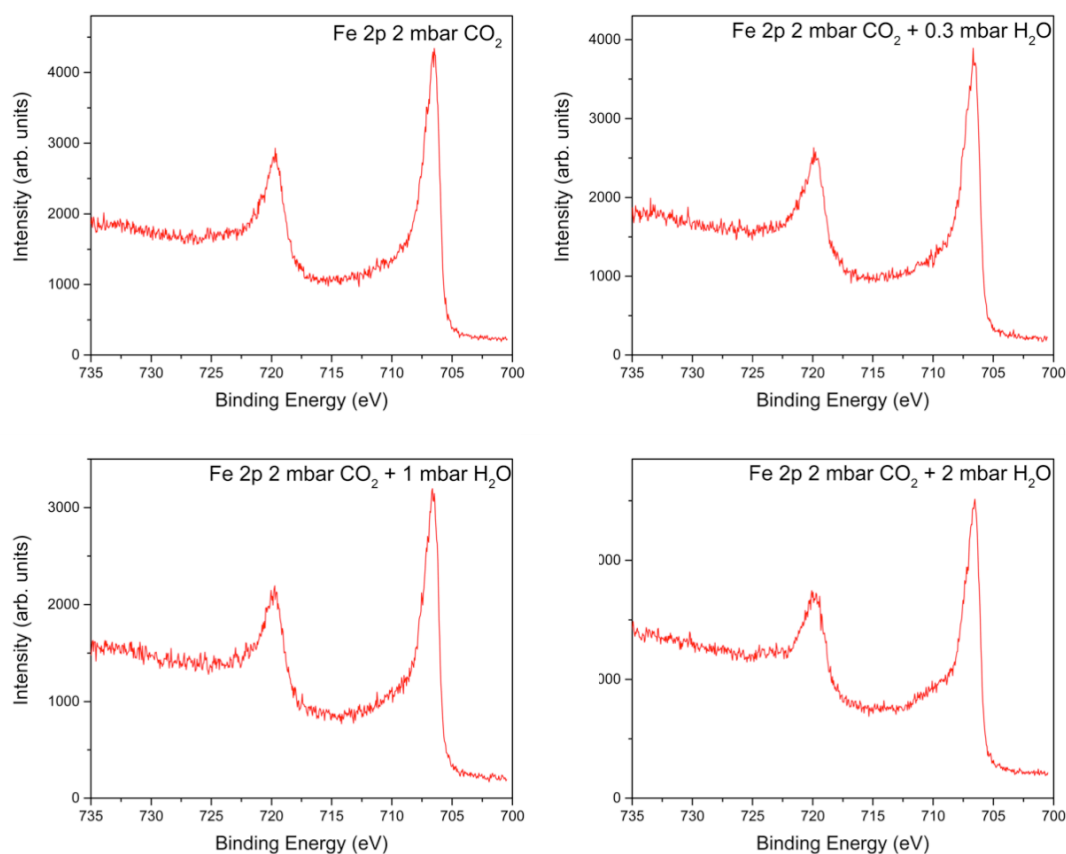


Figure 5.31. NAP XPS Fe 2p core level spectra of  $\text{HdPO}_3\text{H}_2$  on an Fe(110) surface recorded in the presence of 2 mbar of  $\text{CO}_2$  (top left) with 0.3 (top left), 1 (bottom left) and 2 mbar of  $\text{H}_2\text{O}$  (bottom right).

## 5.4. Conclusions

The experimental spectroscopic data for the synthesized compounds show a clear pattern whereby, for the binding mode 3.111 the antisymmetric stretch for the P-O bond splits. This either does not happen for the other binding modes, or if it does happen it does so with a smaller separation between the peaks making the peak look broader. Although IR spectroscopy does not allow identification of the binding modes for phosphonate ligands, it can differentiate between symmetric and antisymmetric binding vibrational modes. It is a useful technique to compare compounds, which have different binding modes and it can assess in the characterization of the compounds.

Even though the experimental data found in the literature supports the discussion above, it is not clear why the splitting of the band occurs and so it should be taken as a helpful tool in assessing the characterization but not as a way to determine the binding mode itself.

Phenylphosphonic acid ( $\text{PhPO}_3\text{H}_2$ ) and benzylphosphonic acid ( $\text{BzPO}_3\text{H}_2$ ) bind to the Fe(110) surface through the 3 deprotonated O atoms. Neither of them self saturates on the surface as a second layer of the acid is deposited on top of the phosphonate when the surface is exposed to the compounds for times as long as hours.

Both compounds remain bound to the surface at around 400 K, which suggests a strong interaction.  $\text{BzPO}_3\text{H}_2$  decomposes on the surface at 550 K and  $\text{PhPO}_3\text{H}_2$  decomposes in the range of 500-673 K. A more detailed study with smaller temperature steps is needed in order to determine the exact temperature at which the compound decomposes. This though is not as important as seeing how the compounds behave at lower temperatures such as would be used in the oil and gas industry and for this reason those decomposition studies have not been done.

Hexadecylphosphonic acid ( $\text{HdPO}_3\text{H}_2$ ) shows a different behaviour as it does not undergo deprotonation following reaction with the Fe(110) surface, and it binds only through one O atom. It remains bound to the surface at 473 K suggesting that the interaction is strong and thermodynamically very stable. This interaction is not as strong in the presence of  $\text{H}_2\text{O}$  as some of the compound is removed from the surface at 423 K. The weaker interaction under these conditions might be an explanation of why the compound does not stop oxidation as some of the active binding sites of the surface are free and react with the  $\text{H}_2\text{O}$  causing the surface to oxidise.  $\text{HdPO}_3\text{H}_2$  reduces oxidation in the presence of  $\text{CO}_2$  suggesting that is strongly bound to the Fe surface and stops the active binding sites from reacting with the  $\text{CO}_2$ . This could be due to the formation of a very thin layer of  $\text{FeCO}_3$  on the surface that promotes the interaction between the compound and the surface. The presence of  $\text{H}_2\text{O}$  may cause the long aliphatic chains on the compound to swell making the surface hydrophobic promoting corrosion protection, showing a similar behaviour to that seen for polymeric brushes.

## 5.5. References

- 1 G. Gunasekaran, R. Natarajan, V. S. Muralidharan, N. Palaniswamy and B. V. A. Rao, *Anti-Corrosion Methods Mater.*, 1997, **44**, 248–259.
- 2 M. Papadaki and K. D. Demadis, *Comments Inorg. Chem.*, 2009, **30**, 89–118.
- 3 K. D. Demadis, C. Mantzaridis and P. Lykoudis, *Ind. Eng. Chem. Res.*, 2006, **45**, 7795–7800.
- 4 M. Papadaki and K. D. Demadis, *Comments Inorg. Chem.*, 2009, **30**, 89–118.
- 5 Y. I. Kuznetsov, *Prot. Met.*, 1991, **26**, 736.
- 6 R. A. Coxall, S. G. Harris, D. K. Henderson, S. Parsons, P. A. Tasker and R. E. P. Winpenny, *J. Chem. Soc. Dalton Trans.*, 2000, 2349–2356.
- 7 P. J. Hotchkiss, M. Malicki, A. J. Giordano, N. R. Armstrong and S. R. Marder, *J. Mater. Chem.*, 2011, **21**, 3107–3112.
- 8 B. Zhang, T. Kong, W. Xu, R. Su, Y. Gao and G. Cheng, *Langmuir*, 2010, **26**, 4514–4522.
- 9 Y. Paukku, A. Michalkova and J. Leszczynski, *J. Phys. Chem. C*, 2009, **113**, 1474–1485.
- 10 R. Lushtinetz, J. Frenzel, T. Milek and G. Seifert, *J. Phys. Chem. C*, 2009, **113**, 5730–5740.
- 11 C. L. Perkins, *J. Phys. Chem. C*, 2009, **113**, 18276–18286.
- 12 N. Tsud and M. Yoshitake, *Surf. Sci.*, 2007, **601**, 3060–3066.
- 13 M. Wagstaffe, A. Thomas, M. J. Jackman, M. Torres-Molina, K. L. Syres and K. Handrup, *J. Phys. Chem. C*, 2016, **120**, 1693–1700.
- 14 H. Li, E. L. Ratcliff, A. K. Sigdel, A. J. Giordano, S. R. Marder, J. J. Berry and J. L. Brédas, *Adv. Funct. Mater.*, 2014, **24**, 3593–3603.

- 15 M. K. Johnson, D. B. Powell and R. D. Cannon, *Spectrochim. Acta Part A Mol. Spectrosc.*, 1981, **37**, 995–1006.
- 16 B. A. B. Blake and L. R. Fraser, *Dalton Trans.*, 1975, 193–197.
- 17 A. S. Batsanow, Y. T. Struchkoc and G. A. Timko, *Koord. Khim.*, 1988, **14**, 266.
- 18 E. I. Tolis, M. Helliwell, S. K. Langley, J. Raftery and R. E. P. Winpenny, *Angew. Chemie - Int. Ed.*, 2003, **42**, 3804–3808.
- 19 E. I. Tolis, L. P. Engelhardt, P. V. Mason, G. Rajaraman, K. Kindo, M. Luban, A. Matsuo, H. Nojiri, J. Raftery, C. Schröder, G. A. Timco, F. Tuna, W. Wernsdorfer and R. E. P. Winpenny, *Chem. - A Eur. J.*, 2006, **12**, 8961–8968.
- 20 S. K. Langley, M. Helliwell, S. J. Teat and R. E. P. Winpenny, *Dalt. Trans.*, 2012, **41**, 12807.
- 21 S. Khanra, S. Konar, A. Clearfield, M. Helliwell, E. J. L. McInnes, E. Tolis, F. Tuna and R. E. P. Winpenny, *Inorg. Chem.*, 2009, **48**, 5338–5349.
- 22 R. Murugavel, N. Gogoi and R. Clérac, *Inorg. Chem.*, 2009, **48**, 646–651.
- 23 Y. Zheng and R. E. P. Winpenny, *Sci. China Chem.*, 2012, **55**, 910–913.
- 24 E. M. Pineda, F. Tuna, Y.-Z. Zheng, R. E. P. Winpenny and E. J. L. McInnes, *Inorg. Chem.*, 2013, **52**, 13702–7.
- 25 H. C. Yao, Y. Z. Li, L. M. Zheng and X. Q. Xin, *Inorganica Chim. Acta*, 2005, **358**, 2523–2529.
- 26 J. Goura, P. Bag, V. Mereacre, A. K. Powell and V. Chandrasekhar, *Inorg. Chem.*, 2014, **53**, 8147–8154.
- 27 V. Chandrasekhar, J. Goura and E. C. Sañudo, *Inorg. Chem.*, 2012, **51**, 8479–8487.
- 28 C. Bellitto, E. M. Bauer, P. Léone, A. Meerschaut, C. Guillot-Deudon and G. Righini, *J. Solid State Chem.*, 2006, **179**, 579–589.

- 29 V. Chandrasekhar, T. Senapati, A. Dey and E. C. Sañudo, *Inorg. Chem.*, 2011, **50**, 1420–1428.
- 30 Y.-S. Ma, Y. Song, X.-Y. Tang and R.-X. Yuan, *Dalton Trans.*, 2010, **39**, 6262–6265.
- 31 J. A. Sheikh, A. Adhikary, H. S. Jena, S. Biswas and S. Konar, *Inorg. Chem.*, 2014, **53**, 1606–1613.
- 32 U. Dietze, *J. Prakt. Chemie.*, 1974, **316**, 485–490.
- 33 M. Mehring, M. Schürmann and R. Ludwig, *Chem. A Eur. J.*, 2003, **9**, 837–849.
- 34 T. J. R. Weakley, *Acta Crystallogr. Sect. B Struct. Crystallogr. Cryst. Chem.*, 1976, **32**, 2889–2890.
- 35 M. P. Seah, *Surf. Interface Anal.*, 2012, **44**, 497–503.
- 36 Casa Software Ltd., *CasaXPS Version 2.3.16 PR 1.6*.
- 37 G. Brodén, G. Gafner and H. P. Bonzel, *Appl. Phys.*, 1977, **13**, 333–342.
- 38 A. G. Thomas, M. J. Jackman, M. Wagstaffe, H. Radtke, K. Syres, J. Adell, A. Lévy and N. Martsinovich, *Langmuir*, 2014, **30**, 12306–12314.
- 39 C. D. Wagner, A. V. Naumkin, A. Kraut-Vass, J. W. Allison, C. J. Powell and J. R. J. Rumble, *NIST Stand. Ref. Database 20, Version 3.4*, 2003.
- 40 J. F. Moulder, W. F. Stickle, P. E. Sobol and K. D. Bomben, *Handbook of X-ray Photoelectron Spectroscopy*, Perkin-Elm., 1992.
- 41 M. Textor, L. Ruiz, R. Hofer, A. Rossi, K. Feldman, G. Hähner and N. D. Spencer, *Langmuir*, 2000, **16**, 3257–3271.
- 42 J. Stöhr, *NEXAFS Spectroscopy*, Springer Science & Business Media, Berlin, Illustrate., 2003.
- 43 A. P. Grosvenor, B. A. Kobe, M. C. Biesinger and N. S. McIntyre, *Surf. Interface*

- Anal.*, 2004, **36**, 1564–1574.
- 44 B. T. Cheesman, E. G. Smith, T. J. Murdoch, C. Guibert, G. B. Webber, S. Edmondson and E. J. Wanless, *Phys. Chem. Chem. Phys.*, 2013, **15**, 14502–10.
- 45 J. D. Willott, T. J. Murdoch, B. A. Humphreys, S. Edmondson, G. B. Webber and E. J. Wanless, *Langmuir*, 2014, **30**, 1827–1836.
- 46 J. D. Willott, T. J. Murdoch, B. A. Humphreys, S. Edmondson, E. J. Wanless and G. B. Webber, *Langmuir*, 2015, **31**, 3707–17.
- 47 M. Wagman, S. Medalion and Y. Rabin, *Macromolecules*, 2012, **45**, 9517–9521.
- 48 C. J. Galvin, M. D. Dimitriou, S. K. Satija and J. Genzer, *J. Am. Chem. Soc.*, 2014, **136**, 12737–12745.
- 49 C. J. Galvin and J. Genzer, *Macromolecules*, 2016, **49**, 4316–4329.



# Chapter 6. Protecting steel from corrosion



## 6.1. Introduction

Steel is the most commonly used material in the oil and gas industry. It is an alloy of Fe with between 0.001 % to 1.5 % of C. It has a wide range of properties, which depend on C content, heat treatment, cooling rate and addition of other alloying elements such as Mn, Cr, Ni or Al amongst others.

Metallic Fe and steel have different structures; the different allotropes of Fe have been described in Chapter 4. Martensite is a saturated solution of C in Fe that is formed by rapid cooling. C substitution in ferrite is very low and has a maximum solubility of *ca.* 0.02 % at 723 °C and 0.005 % at 0 °C. Austenite, which has a fcc system (Chapter 4), has a high C solubility. When the cooling is fast C diffusion is restricted leading to lattice distorting in order to accommodate the high C content and forming a body centred tetragonal system (bct). However, this causes stress so the resulting material is hard and brittle – the higher C content, the harder the material – and less ductile. Cementite also known as iron carbide<sup>1</sup> is a hard, brittle intermetallic Fe and C compound with an orthorhombic crystal structure in which there are 12 Fe atoms and 4 C atoms in the unit cell.<sup>2</sup> Combining cementite with ferrite in a laminar structure forms perlite, a common structure for steel. This material combines the hardness and strength of cementite with the ductility of ferrite.

In the oil extraction process, acids are injected into the rocks in order to dissolve them and promote the extraction of the crude oil, this is known as the ‘well acidizing procedure’.<sup>3</sup> Hydrochloric, hydrofluoric and acetic acids are all used, sometimes individually but sometimes as a mixture of these and others. Mud acid (6% HCl : 1% HF) is commonly used for this purpose.<sup>3-5</sup> HCl is quite widely used because when it reacts with a metallic surface, metal chlorides form, which are soluble in the aqueous phase, and therefore do not lead to the formation of scales.<sup>6</sup>

Clearly the acidic environment can have corrosive effects on the steel work in the vicinity, be that pipework or drilling rigs. The aim of this final chapter is to study the surface chemical changes on a mild steel substrate exposed to HCl with and without

inhibitors. This is achieved by monitoring the degree of oxidation or reaction at the steel surface. These control laboratory experiments will provide information on static processes involving the corrosion inhibitors, i.e., how do the inhibitors simply adsorb to the steel surface and provide a protective barrier. The studies also investigate whether these phosphorus based corrosion inhibitors adsorb to the native oxide film on the steel, or the metal exposed following exposure to HCl as suggested by Lindsay *et al.*<sup>7</sup> Figure 6.1 represents how the immersion of the steel on 1 M HCl removes the oxide surface and forms an iron chloride layer.

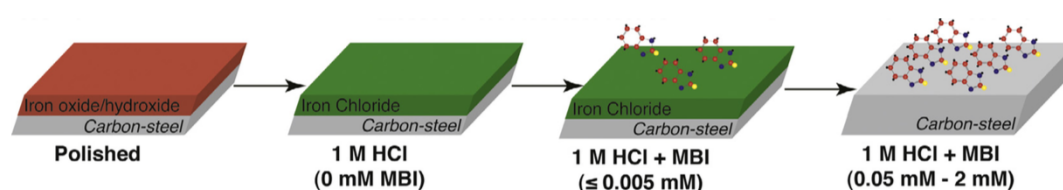


Figure 6.1. Cartoon illustrating steel termination as a function of environment.<sup>7</sup>

The XPS data reported in the previous chapters under highly idealised conditions allow interpretation of the data obtained here. Conversely the real system studied here helps to validate the model, vacuum measurements reported in previous chapters. The main aim of this chapter is to investigate whether both phosphonic acids and phosphate esters display a different behaviour under different and more realistic conditions

## 6.2. Experimental

The work presented in this section was carried out using an in-house Kratos Axis Ultra DLD XPS instrument equipped with a monochromated Al K $\alpha$  source (photon energy 1486.6 eV), and hemispherical analyser with a delay line detector that enables fast acquisition of a narrow binding energy region. This is used for sample position optimisation. An electromagnet in the analysis chamber below the sample position is used to increase the yield of photoelectrons reaching the analyser. A charge neutraliser is used to compensate for any differential charging or any poor connections between

the sample and sample plate. Survey spectra over a wide binding energy range were acquired with a pass energy of *ca.* 160 eV while high-resolution narrow scans of the important atomic core levels were acquired using a pass energy of *ca.* 40 eV. The base pressure in the analysis chamber was about  $1.5 \times 10^{-8}$  mbar during the measurements.

1 M HCl was prepared by mixing 83.5 mL of HCl 37% in 1 L of deionised water. The corrosion inhibitor solutions were prepared by dissolving the required amount of each compound in the 1 M HCl to give a 0.01 mM concentration, with the exception of PAE 136 since the molecular mass is not known, 1 mL was added to the solution.

The steel used is AISI 1010 carbon steel, with 0.080-0.13 % of C. Other elements present in this alloy are Mn (0.30-0.60 %), S ( $\leq 0.050$  %) and P ( $\leq 0.040$  %).

The steel plates (1 cm x 1 cm) were suspended in the solutions, covered with parafilm (see Figure 6.2) and left undisturbed for 20 h. They were then transferred to a nitrogen filled glovebox attached to the load lock of the XPS instrument, removed from the solution, rinsed with deionised water and dried with N<sub>2</sub> gas to minimise contact with air. The experiment was performed this way in order to model, as closely as possible, the corrosive conditions of the extraction of oil that is O<sub>2</sub> free. It has also been shown that even momentary exposure to air leads to significant changes in the degree of oxidation.<sup>8</sup>

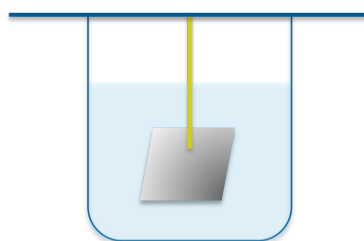


Figure 6.2. Schematic representation of the steel plates submerged in the acidic solutions and sealed with parafilm.

### 6.3. Results and discussion

Figure 6.3 shows a photograph of the steel plates in the glovebox before being introduced in the UHV system. Plate 1 is the control sample exposed only to 1 M HCl to determine how the steel oxidises under acidic solution. Plates 2 to 5 are the plates that had been submerged in aqueous HCl in the presence of different corrosion inhibitors. It can be seen that samples 2 and 3 show some signs of corrosion whilst 4 and 5 present a smoother surface suggesting that PAE 136 and  $\text{DbPO}_2\text{H}$  (plates 4 and 5) provide a better protection to the metal than  $\text{PhPO}_3\text{H}_2$ ,  $\text{BzPO}_3\text{H}_2$  (plates 2 and 3). The results obtained from these will be discussed below. Unfortunately no XPS data was obtained for the  $\text{PhPO}_3\text{H}_2$  sample and therefore it is not going to be discussed further.

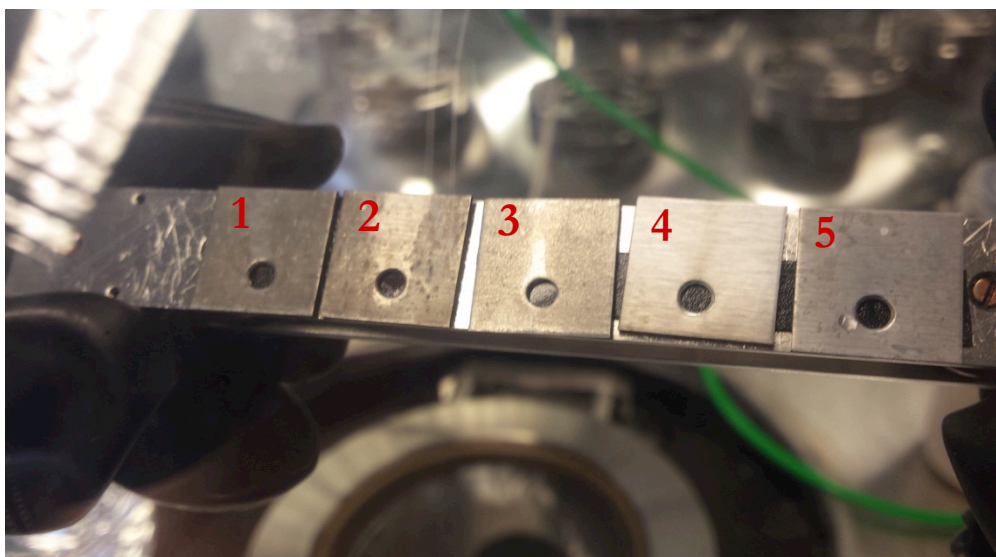


Figure 6.3. Photograph of the steel plates before introducing them in the UHV system of the XPS instrument. Plate 1 control experiment. Plates 2-5 are labelled according to the inhibitor used: 2  $\text{PhPO}_3\text{H}_2$ , 3  $\text{BzPO}_3\text{H}_2$ , 4 PAE 136 and 5  $\text{DbPO}_2\text{H}$ .

Figure 6.4 shows an XPS survey scan of the steel plate submerged in 1 M HCl without any corrosion inhibitor. In the spectrum peaks corresponding to Fe 2p, O 1s, C 1s, Cl 2p and Si 2s and 2p are clearly visible, Si is a common contaminant to samples prepared in glassware.

In this section the core level spectra for Fe 2p, O 1s, C 1s and Cl 2p are going to be presented for each compound to determine the compound phases. A more detailed examination of the P 2p core level spectra is going to be presented later in order to compare the binding mode of all the compounds to the surface.

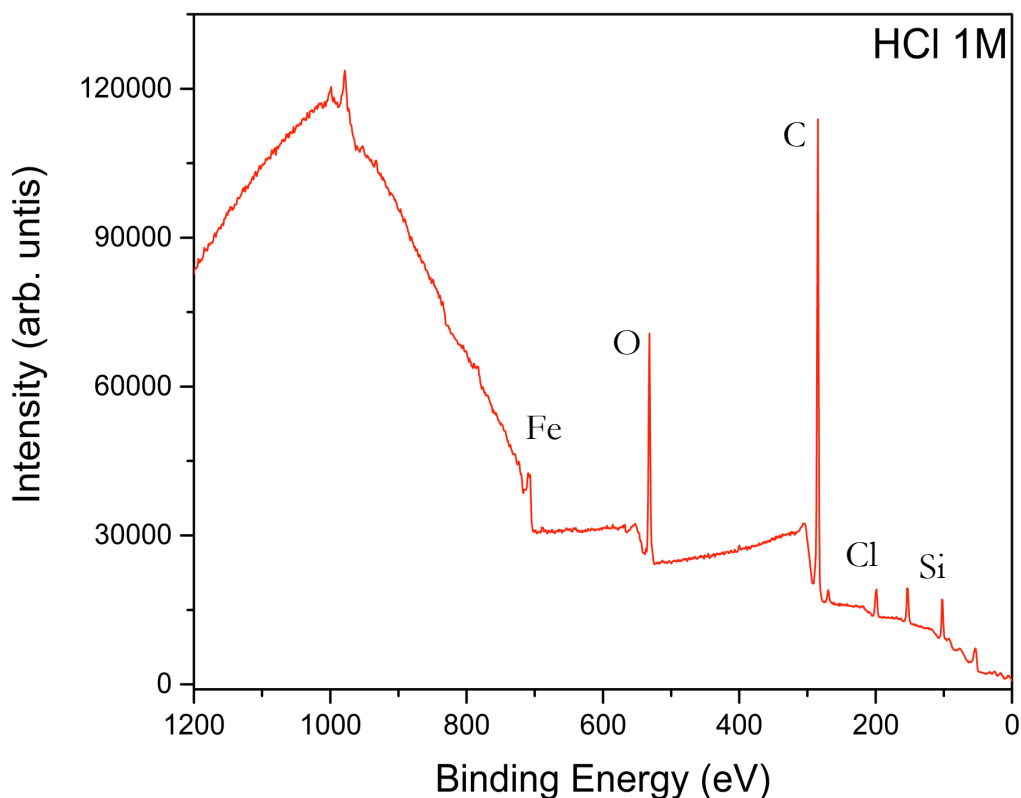


Figure 6.4. UHV XPS survey scan of a steel plate submerged for 20 h in 1 M HCl.

Figure 6.5 shows high resolution Fe 2p, O 1s, C 1s and Cl 2p core level XPS spectra. The main peak in the O 1s spectrum is assigned to adsorbed hydroxide from the solution at 531.9 eV (blue), the peak at 530.5 eV is assigned residual Fe oxide (pink),<sup>7,9,10</sup> the peak at 533.5 eV (green) is assigned to O in adventitious hydrocarbon<sup>7</sup> and the one at 528.2 eV (dark yellow) it is believed to arise from the oxide of another metal. A small peak at 537.2 eV is due to physisorbed water on the surface.<sup>11,12</sup>

In the C 1s spectrum there is a strong peak at 284.6 eV (blue), assigned to the atmospheric hydrocarbon contamination, the peak at 283.0 eV (pink) is assigned to the carbide within the steel. The peaks at 286.5 eV (green) and 288.5 eV (orange) are

thought to be due to C-OH and C=O respectively also from atmospheric contamination.<sup>10</sup>

The Fe 2p signal shows clear evidence of oxidation although the Fe<sup>0</sup> peak at 706.6 eV is still appreciable. The shape of Fe 2p<sub>3/2</sub> peak and the energy difference between the main oxidised peak and the satellite are a fingerprint of different Fe compounds.<sup>13</sup> In this case there is an energy difference of 5.5 eV suggesting that this is not due to Fe<sub>2</sub>O<sub>3</sub> or FeOOH, because for these the energy difference is of 8.5 eV.<sup>13</sup> However, the presence of Fe<sub>2</sub>O<sub>3</sub> and FeOOH cannot be ruled out completely, since the satellite would partly lie beneath the Fe 2p<sub>1/2</sub> feature from the metal located at a binding energy of 720 eV. This would be consistent with the small amount of O<sup>2-</sup> observed in the O 1s spectra.

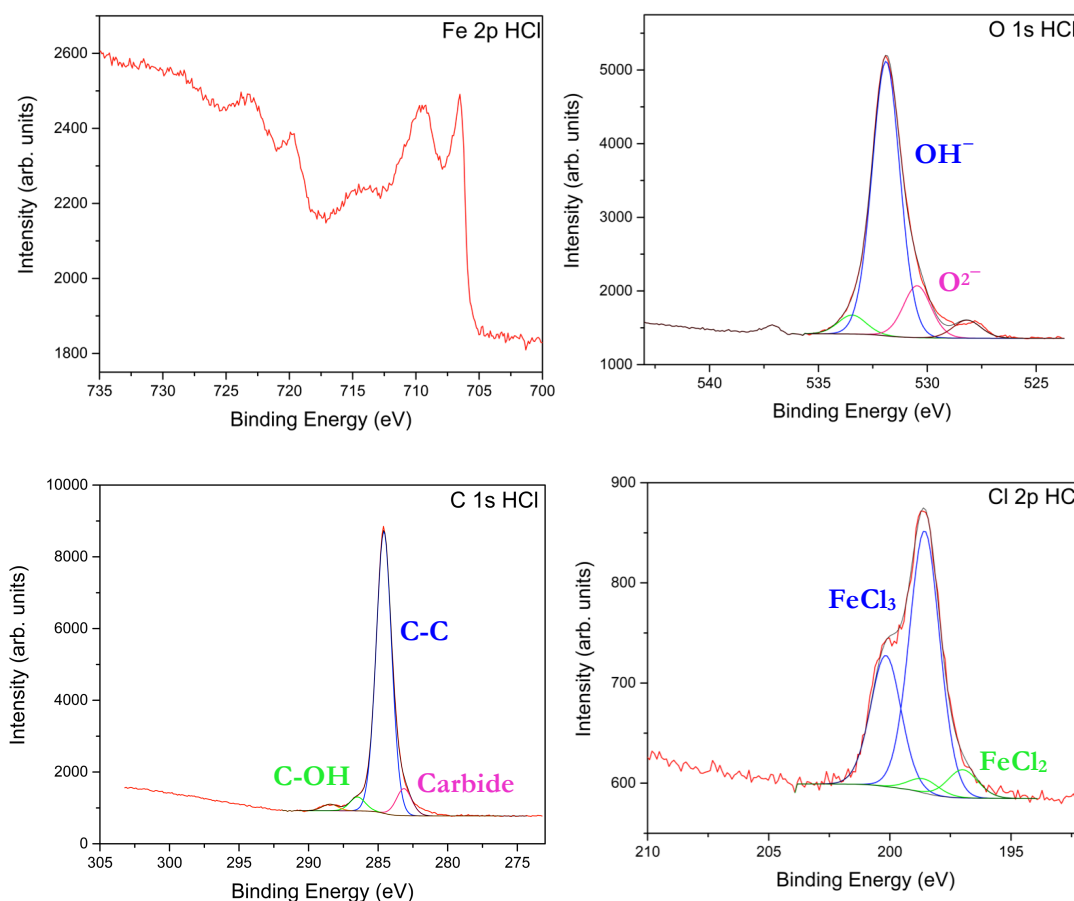


Figure 6.5. UHV XPS spectra recorded for Fe 2p, O 1s, C 1s and Cl 2p for a steel plate submerged in 1 M HCl for 20 h.

The dominant species present on the surface are  $\text{FeCl}_3$ ,  $\text{FeCl}_2$  and  $\text{FeO}$ , which have an energy difference that is comparable with the data. In order to identify which species is formed on the surface it is necessary to fit the  $\text{Fe } 2p_{3/2}$  peak constraining the fitting parameters to the Gupta and Sen multiplet peak tabulated parameters.<sup>13</sup>

Figure 6.6 shows the fitted  $\text{Fe } 2p_{3/2}$  spectra for the different species. In these it can be seen that the best fitting is obtained when using the GS parameters for  $\text{FeCl}_3$ , suggesting that this is the oxidised species that forms on the steel surface. It is possible that there is a small amount of that  $\text{FeO}$  despite this giving the worse fitting out of the three. However, the fitting for  $\text{FeCl}_3$  is not perfect which could be due to the presence of both  $\text{FeCl}_3$  and  $\text{FeCl}_2$  on the surface.<sup>13</sup>

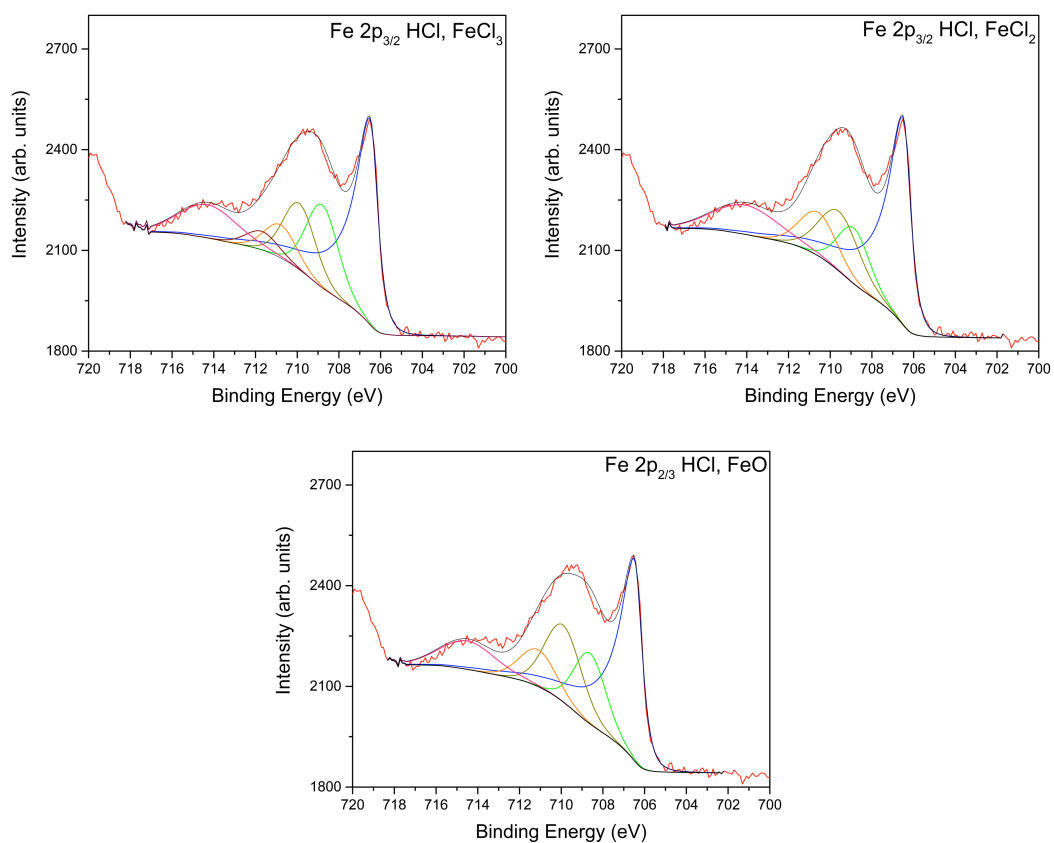


Figure 6.6. UHV XPS spectra recorded for  $\text{Fe } 2p_{3/2}$  for a steel plate submerged in 1 M HCl for 20 h fitted for  $\text{FeCl}_3$  (top left),  $\text{FeCl}_2$  (top right) and  $\text{FeO}$  (bottom).

The Cl 2p spectrum shows 2 chemical species one with doublet peaks at 200.2 and 198.6 eV (blue) assigned to the presence of FeCl<sub>3</sub> on the surface, and another with doublet peaks at 198.6 and 197.0 eV (green) assigned to presence of FeCl<sub>2</sub> on the surface. This would appear to support the presence of both chloride species.

The same experiment was performed with acidic solution of BzPO<sub>3</sub>H<sub>2</sub>, PAE 136 and DbPO<sub>2</sub>H, which have been studied on pure Fe(110) (Chapters 4 and 5). Figure 6.7 shows the core level spectra recorded for a steel plate submerged for 20 h in an 1 M HCl solution containing BzPO<sub>3</sub>H<sub>2</sub>. In Chapter 5 it was reported that when deposited from the vacuum phase this phosphonic acid becomes totally deprotonated and it binds to an Fe(110) surface through the 3 O atoms and a small quantity remained partially protonated and bound to the surface with a bidentate binding mode. The Fe 2p data obtained for the steel surface following immersion in HCl/BzPO<sub>3</sub>H<sub>2</sub> suggests that the surface becomes highly oxidised by the acid.

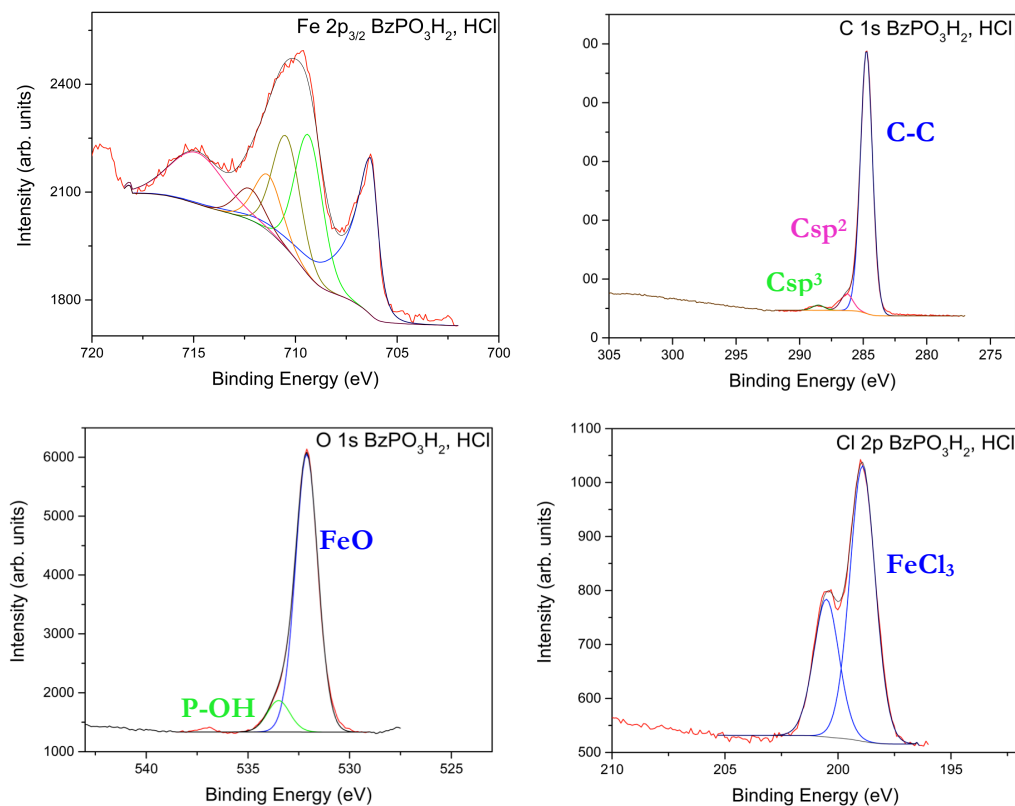


Figure 6.7. UHV XPS spectra recorded for Fe 2p<sub>3/2</sub>, O 1s, C 1s and Cl 2p for a steel plate submerged in 1 M HCl and BzPO<sub>3</sub>H<sub>2</sub> for 20 h.

The fits to the Fe  $2p_{3/2}$  spectrum using the GS parameters for  $\text{FeCl}_3$ <sup>14</sup> follow the data very well suggesting that in this case there is a layer of  $\text{FeCl}_3$  on the surface.<sup>13</sup> Metallic Fe is also observed. This is confirmed by the Cl 2p spectrum that shows only one component with doublet peaks at 200.5 and 198.9 eV, which is assigned to  $\text{FeCl}_3$  at the surface. In this case there is no experimental evidence of the presence of  $\text{FeCl}_2$ .

The C 1s spectrum shows a main peak at 284.8 eV (blue) assigned to the hydrocarbon contamination, and two very weak peaks at 286.3 (pink) and 288.5 eV (green) assigned to the C atoms of the aromatic ring and the aliphatic C, respectively.

In the O 1s spectrum the peak at 532.1 eV (blue) is assigned to the O atoms of the phosphonate bound to the surface and possibly adsorbed hydroxide from the solution.<sup>7</sup> There is another peak at 533.5 eV (green) that could be assigned to protonated P-O-H that is not bound to the surface suggesting the compound also shows a monodentate or bidentate binding mode as it did on a Fe(110) single crystal surface in UHV conditions (Chapter 5). However this peak is also consistent with O in adsorbed hydrocarbon contamination. Therefore the binding mode in solution cannot be unambiguously determined.

From the photograph taken of the samples before measuring them it can already be seen that both PAE 136 and  $\text{DbPO}_2\text{H}$  appear to provide better protection against corrosion of the steel plates than does  $\text{BzPO}_3\text{H}_2$ .

Figure 6.8 shows the XPS spectra for a steel plate treated with and acidic solution of the commercial corrosion inhibitor PAE 136. In the Fe 2p spectrum the metallic Fe peak dominates. There is less evidence of oxidation with PAE 136 than with  $\text{BzPO}_3\text{H}_2$ , confirming what was initially thought from the aspect of the steel plates. Again the best fitting is obtained constraining the multiplet splitting parameters to the ones for  $\text{FeCl}_3$ .

The O 1s peak is a symmetric spectrum to which 4 peaks can be fitted. The main one convolutes into two peaks of almost equal intensity with binding energies of 533.2 (green) and 532.0 eV, (blue) assigned to P-OH in the corrosion inhibitor and C-OH from contamination.<sup>7</sup> There are also two smaller peaks at 537.2 (dark yellow) and 527.8

eV (pink). The first one is assigned to water trapped in the viscous PAE 136 inhibitor that remains on the surface, and/or physisorbed water on the surface. The one at a lower binding energy is assigned to the P-O-C bonds.

The C 1s spectrum presents 3 chemical species. The main peak at 285 eV (blue) is assigned to the hydrocarbon contamination from the atmosphere and C-C bonds in the aliphatic chain of the compound, the peak at 286.7 eV (pink) is assigned to C-O-P and the peak at 288.5 eV (green) to C-O and C=O both in the compound. The Cl 2p spectrum can be fitted with only the doublet that has a binding energy similar to that for  $\text{FeCl}_3$ ,<sup>13</sup> confirming the presence of this species seen in the Fe 2p spectrum.

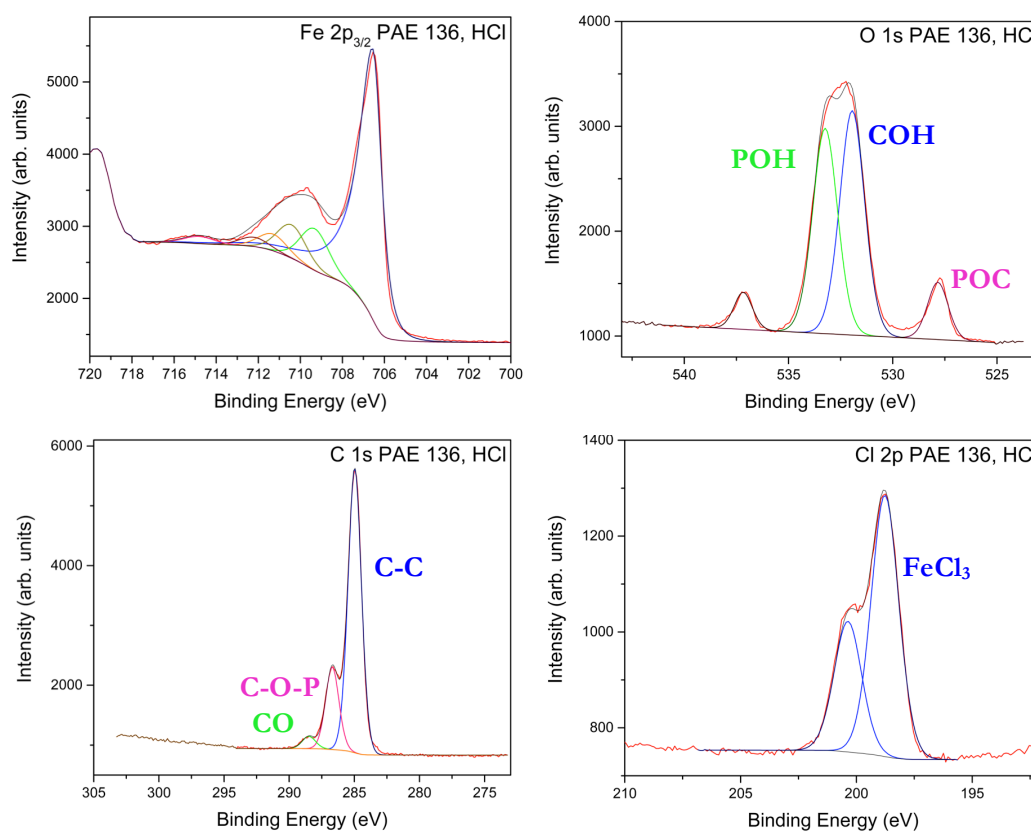


Figure 6.8. UHV XPS spectra recorded for Fe  $2p_{3/2}$ , O 1s, C 1s and Cl 2p for a steel plate submerged in 1 M HCl and PAE 136 for 20 h.

Figure 6.9 shows the core level spectra for a steel plate treated with an acidic solution of  $\text{DbPO}_2\text{H}$ . In the Fe  $2p_{3/2}$  peak the metallic  $\text{Fe}^0$  form dominates and there is barely any

sign of oxidation. There is a shoulder suggesting that there is some oxidation but nothing comparable with the previous cases. The fitting of the multiplet structure Fe  $2p_{3/2}$  spectrum has been done using the same constraints that had been used for the other compounds corresponding to  $FeCl_3$ .<sup>13</sup> Although an assignment is speculative with such a weak feature, it is supported by Cl 2p spectra in Figure 6.9 these data confirm that, as seen in Chapter 4,  $DbPO_2H$  provides a better protection to the metallic surface in acidic conditions than PAE 136 and  $BzPO_3H_2$  over 20 hours.

There are 4 different chemical species can be fitted in the C 1s spectrum. The peak at 283.2 eV (pink) has been assigned to the carbide within the steel and the one at 284.6 eV (blue) to the atmospheric hydrocarbon contamination. The peak at 286.8 eV (orange) has been assigned to COH contamination, although it is barely present. Finally the peak at 281.6 eV (green) is thought to be the C present in the molecule.

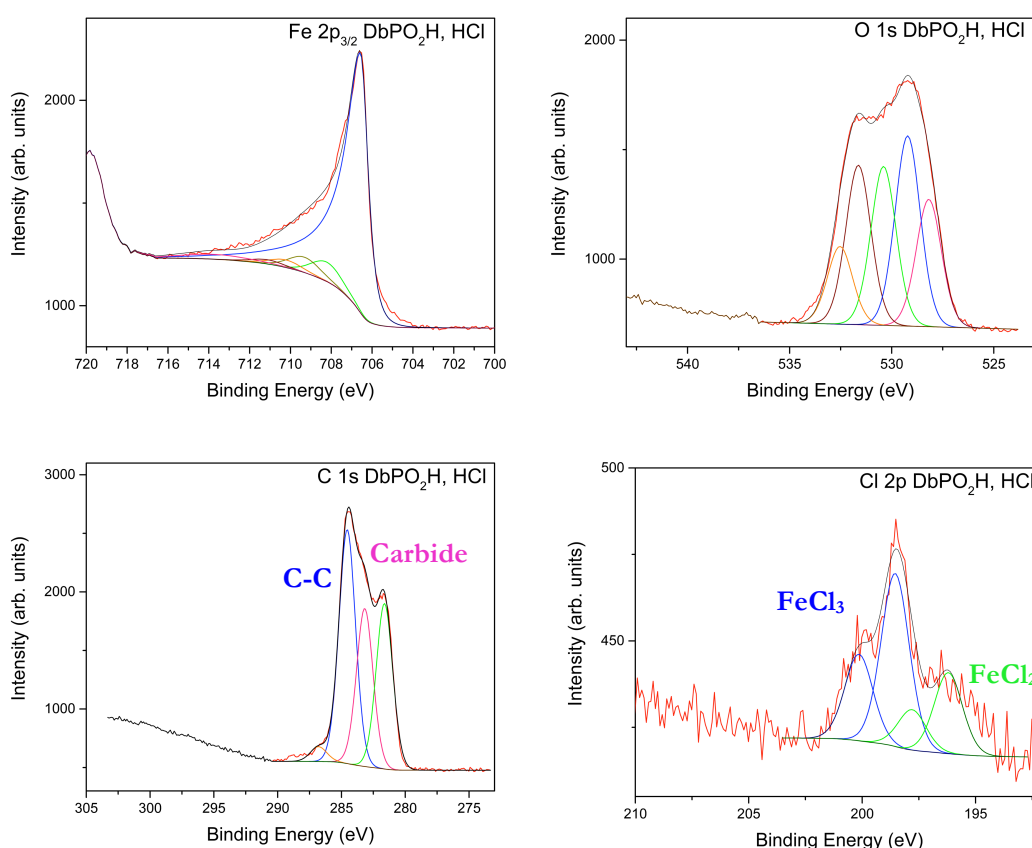


Figure 6.9. UHV XPS spectra recorded for Fe  $2p_{3/2}$ , O 1s, C 1s and Cl 2p for a steel plate submerged in 1 M HCl and  $DbPO_2H$  for 20 h.

The O 1s spectrum fits with 5 chemical species; to facilitate the understanding of this fitting the assignment for the O 1s spectra for all the samples are shown in table 6.1. The peak at 532.5 eV (orange) has been assigned to protonated O in the molecule and to the O present in the hydrocarbon contamination. The peak at 531.6 eV (maroon) has contributions of the O on the molecule bound to the steel plate, the adsorbed OH from the solution<sup>7</sup> and the P=O bond<sup>15</sup> present when the molecule is bound with a monodentate binding mode. There is a peak at 530.4 eV (green) which binding energy is consistent to iron oxide, however there is no evidence of oxidation in the Fe 2p spectrum and so the nature of this peak is not clear. The O bound to the steel plate arises at 528.8 eV (pink), which is consistent with the other compounds, and the peak at 529.2 eV (blue) is of unknown nature.

The fact that for this compound the peaks assigned to the inhibitor molecule are equal in intensity to the ones coming from the oxidation of the surface indicates that the surface barely becomes oxidised.

Table 6.1. Peak assignments and their respective binding energies (eV) for the O 1s core level spectra for samples 1, 3, 4 and 5.

|                                      | <b>Binding Energy (eV)</b> |                   |   |                       |
|--------------------------------------|----------------------------|-------------------|---|-----------------------|
| <b>HCl</b>                           | 528.8<br>unknown           | 530.5<br>Fe oxide | 531.9<br>ads OH                                   | 533.5<br>C-OH         |
| <b>BzPO<sub>3</sub>H<sub>2</sub></b> | -                          | -                 | 532.1<br>ads OH<br>P-O-steel                      | 533.5<br>C-OH<br>P-OH |
| <b>PAE 136</b>                       | 529.2<br>P-O-C             | -                 | 532.0<br>ads OH<br>P-O-steel                      | 533.2<br>C-OH<br>P-OH |
| <b>DbPO<sub>3</sub>H<sub>2</sub></b> | 528.2<br>P-O-C             | 530.6<br>unknown  | 529.2<br>ads OH<br>P-O-steel<br>P=O <sup>15</sup> | 533.5<br>C-OH<br>P-OH |

In the Cl 2p spectrum there are clearly 2 chemical species with doublet peaks at 200.1 and 198.5 eV (blue doublet) and 197.8 and 196.2 eV (green doublet). The doublet at

lower binding energy is assigned to the  $\text{FeCl}_2$  present on the surface. The doublet at higher binding energies has been assigned whereas the previously reported compounds to the presence of  $\text{FeCl}_3$ , although the presence of this compound is not supported in the Fe 2p spectrum. The spectrum is very noisy and this is due to the low intensity of the signal. In this case there is not much chloride on the surface because there is no formation of  $\text{FeCl}_3$  or  $\text{FeCl}_2$ .

Table 6.2. Peak assignments and their respective binding energies (eV) for the Fe  $2p_{3/2}$ , C 1s, and Cl 2p core level spectra for samples 1, 3, 4 and 5.

|  | Binding Energy (eV) |                                  |         |                     |
|--|---------------------|----------------------------------|---------|---------------------|
|  | HCl                 | BzPO <sub>3</sub> H <sub>2</sub> | PAE 136 | DbPO <sub>2</sub> H |
| <b>Fe<sup>0</sup> 2p<sub>3/2</sub></b>   | 706.5               | 706.3                            | 706.4   | 706.5               |
| <b>Fe<sup>x+</sup> 2p<sub>3/2</sub></b>  | 709.5               | 710.2                            | 710.0   | -                   |
| <b>Satellite</b>                         | 714.3               | 714.8                            | 714.8   | -                   |
| <b>C steel</b>                           | 284.6               | 284.8                            | 285.0   | 284.6               |
| <b>FeCl<sub>3</sub> 2p<sub>1/2</sub></b> | 200.2               | 200.5                            | 200.4   | 200.1               |
| <b>FeCl<sub>3</sub> 2p<sub>3/2</sub></b> | 198.6               | 198.9                            | 198.8   | 198.5               |
| <b>FeCl<sub>2</sub> 2p<sub>1/2</sub></b> | 198.6               | -                                | -       | 197.8               |
| <b>FeCl<sub>2</sub> 2p<sub>3/2</sub></b> | 197.0               | -                                | -       | 196.2               |

Figure 6.10 shows the P 2p spectra for the control experiment, BzPO<sub>3</sub>H<sub>2</sub>, PAE 136 and DbPO<sub>2</sub>H treated steel as they have not been discussed yet. The control experiment shows no P confirming that the steel does not have any phosphorus. For steel treated with acidic solution of BzPO<sub>3</sub>H<sub>2</sub> the signal is so weak and noisy that it has not been fitted. However it shows one chemical species for P *ca.* 134 eV assigned to the P bound to O in the molecule. This might suggest that under solution conditions the binding of the molecule is minimal. This is why a large amount of  $\text{FeCl}_3/\text{FeCl}_2$  formation is seen.

For steel treated with acidic solution of PAE 136 there are clearly two chemical species. One with doublet peaks at 133.9 and 134.8 eV and another one at 129.3 and 130.2 eV, assigned to P-O and iron phosphide. These binding energies are consistent with the experiments performed on PAE 136 on single crystal Fe(110) in the presence of H<sub>2</sub>O vapour. This confirms that the commercial corrosion inhibitor has a similar behaviour on an ideal surface and under controlled conditions in a more realistic system.

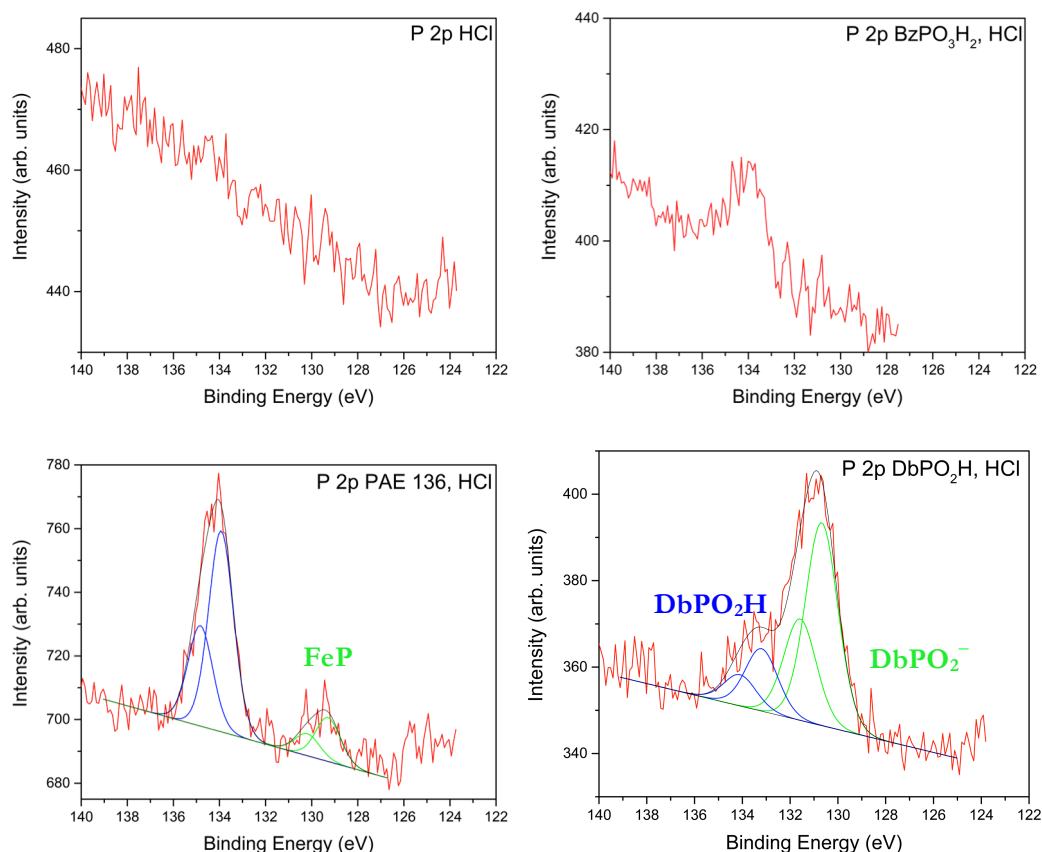


Figure 6.10. UHV XPS spectra recorded for P 2p for a steel plate submerged in 1 M HCl (top left), BzPO<sub>3</sub>H<sub>2</sub> (top right), PAE 136 (bottom left) and DbPO<sub>2</sub>H (bottom right) for 20 h.

The P 2p core level spectrum for a steel plate treated with acidic solution of DbPO<sub>2</sub>H shows two chemical species as well, one doublet with peaks at 133.2 and 135.0 eV (green) and another one with peaks at 130.7 and 131.6 eV (blue). The first peak's binding energy is consistent with the binding energy for the protonated phosphate ester and the most intense one at lower binding energy is assigned to the deprotonated

phosphate. This is a different behaviour than was reported in Chapter 4 for the experiments recorded for  $\text{DbPO}_2\text{H}$  on a single crystal  $\text{Fe}(110)$  surface in UHV, in the presence of  $\text{H}_2\text{O}$  and in the presence of a mixture of  $\text{CO}_2$  and  $\text{H}_2\text{O}$ . It is thought that the different behaviour is a product of the acidic medium that does not promote deprotonation of all the compound absorbed on the surface. This would mean a difference in the binding modes for the different surfaces. Figure 6.11 shows a schematic representation of the possible binding modes for  $\text{DbPO}_2\text{H}$  on a steel surface. Binding modes **a** and **b** are the ones seen for the  $\text{Fe}(110)$  surface, where  $\text{DbPO}_2\text{H}$  was deposited under vacuum conditions. Binding mode **c** is more consistent with the data from the acidic medium. However it is not clear if in this case the compound shows a mixture of **a** and **c**, **b** and **c** or if the three binding modes are present on the surface.

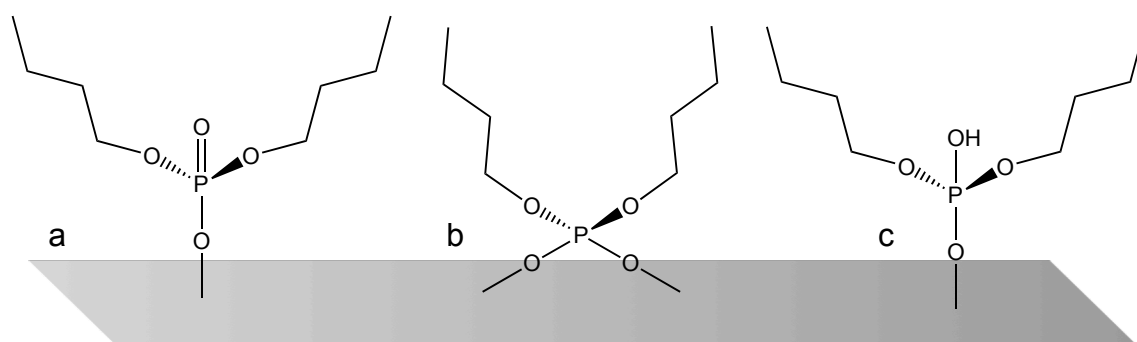


Figure 6.11. Schematic representation of the possible binding modes for  $\text{DbPO}_2\text{H}$  on a steel surface in an acidic media.

A steel surface has a layer of oxide that has been formed by contact with air.<sup>7</sup> The data obtained for  $\text{DbPO}_2\text{H}$  confirms the hypothesis suggested by Lindsay *et al.* in which the  $\text{HCl}$  removes the initial layer of oxide and the corrosion inhibitor binds to the non-oxidised surface.

## 6.4. Conclusions

The oxidation of steel plates has been studied in similar conditions to the ones found in the oilfield sweet environment, acidic and  $O_2$  free. These experiments were necessary in order to compare the results presented in the previous chapters that had been performed on a single crystal Fe(110) surface and laboratory controlled ideal systems. Analysis of the behaviour of a steel plate in acidic conditions in the absence of a corrosion inhibitor shows the formation of  $FeCl_3$ ,  $FeCl_2$  and  $FeO$ .

The presence of  $BzPO_3H_2$  in the solution promotes corrosion of the metallic surface leading to the formation of  $FeCl_3$  and  $FeCl_2$ . There is no evidence of a change on the compound's binding modes between the steel and Fe(110) surfaces as there is evidence of both bidentate and tridentate binding modes.

PAE 136 presents a very similar behaviour to that on the Fe(110) surface. There was some oxidation of the steel surface caused by the reduction of the phosphorus containing compounds leading to the formation of a metallic phosphide layer. This passivation layer is present both on steel and on single crystal Fe(110). The O 1s core level spectra show some differences suggesting that the compound might bind differently to the surface. However, because this a mixture of different compounds it is not known if the different behaviour comes from the active compound or the minority products present on the mixture. However, a different behaviour does not compromise the performance of the corrosion inhibitor.

$DbPO_2H$  shows the most difference between the interaction with steel and the interaction with single crystal Fe(110) surface out of all the compounds under study.  $DbPO_2H$  presented bidentate and monodentate binding modes and was always deprotonated on the surface of the single crystal. However on the steel surface and in an acidic medium the compound is found mainly protonated and bound to the metallic surface with a monodentate binding mode. It is not clear though if the deprotonated phosphate ester is bound to the surface through one or two O atoms. However it was seen that a bidentate mode was more stable on the single crystal Fe(110) surface.

DbPO<sub>2</sub>H, which was thought to be a better corrosion inhibitor than PAE 136 on a Fe surface (Chapter 4), also gives a better protection to the steel surface. The fact that the anticorrosive behaviour is present for an ideal Fe(110) surface and for a real steel surfaces and, in UHV, low pressures of H<sub>2</sub>O and CO<sub>2</sub> and acidic aqueous solution confirms that DbPO<sub>2</sub>H is a good corrosion inhibitor. However, PAE 136 might mix better with the crude oil as it is more hydrophobic and for this reason this experiment should be performed in a mixed organic/aqueous acidic medium in order to test the effect.

## 6.5. References

- 1 J. Häglund, G. Grimvall and T. Jarlborg, *Phys. Rev. B*, 1991, **44**, 2914–2919.
- 2 W. F. Smith and J. Hashemi, *Foundations of Materials Science and Engineering*, McGraw-Hill, 4th Editio., 2006.
- 3 J. Jackson and M. Finšgar, *Corros. Sci.*, 2014, **86**, 17–41.
- 4 D. Brondel, R. Edwards, A. Hayman, D. Hill and S. Mehta, *Oilf. Rev.*, 1994, 6, 4–18.
- 5 D. G. Hill and H. Romijn, *Corrosion*, 2000, 00342.
- 6 D. Jayaperumal, *Mater. Chem. Phys.*, 2010, **119**, 478–484.
- 7 P. Morales-Gil, M. S. Walczak, R. A. Cottis, J. M. Romero and R. Lindsay, *Corros. Sci.*, 2014, **85**, 109–114.
- 8 X. Li, *Intern. MEng Rep.*, 2016, The University of Manchester.
- 9 T. Hryniewicz and K. Rokosz, *Surf. Coatings Technol.*, 2010, **204**, 2583–2592.
- 10 V. P. Shinde and P. P. Patil, *Electrochim. Acta*, 2012, **78**, 483–494.
- 11 D. Klyachko, P. Rowntree and L. Sanche, *Surf. Sci.*, 1996, **346**, L49–L54.

- 12 M. Schindler, F. C. Hawthorne, M. S. Freund and P. C. Burns, *Geochim. Cosmochim. Acta*, 2009, **73**, 2471–2487.
- 13 A. P. Grosvenor, B. A. Kobe, M. C. Biesinger and N. S. McIntyre, *Surf. Interface Anal.*, 2004, **36**, 1564–1574.
- 14 R. P. Gupta and S. K. Sen, *Phys. Rev. B*, 1975, **12**, 15–19.
- 15 M. Wagstaffe, A. Thomas, M. J. Jackman, M. Torres-Molina, K. L. Syres and K. Handrup, *J. Phys. Chem. C*, 2016, **120**, 1693–1700.

# Chapter 7. Conclusions and further work



## 7.1. Conclusions

Corrosion inhibitors have been known and used for a very long time and yet, how they perform is still a question without a straightforward answer. Something one should be aware of is that corrosion cannot be prevented, but can be controlled. It is also important to know that a given corrosion inhibitor might inhibit corrosion for a given surface and specific conditions, but it might not behave the same in a different environment. For this reason all corrosion inhibitors have to be tested in the media in which they are going to be used.

Here different corrosion inhibitors have been studied using several approaches and methodologies to assess similarities and differences for various kinds of corrosion inhibitors.

For nitrogen based corrosion inhibitors a fundamental approach has been applied here in order to understand the binding of these to metallic cations in molecular compounds. Spectroscopic study of the vibrational modes assisted by solid state theoretical calculations of the vibrational modes for the corrosion inhibitor have led to a good understanding of the binding modes. Surface measurements are also needed in order to get closer to knowing the binding and mechanism of these to a metallic surface. It is not enough to do a meticulous fundamental study, it is also necessary to study systems as close as possible to the real ones in order to get more meaningful results.

Surface measurements have been carried out for 2-mercaptobenzimidazole, MBIH<sub>2</sub>, proving that the model compounds approach combined with theoretical calculations help in the interpretation and assignment of the surface sensitive data acquired. The first experiments were done on an Au surface because it is very inert. However Au and steel are such different materials that the binding could be completely different for each and it is for this reason that an experiment on steel, a more realistic system, was needed. The preliminary data obtained on steel suggested that, as expected, the binding is different.

A spectroscopic study of metallic compounds with phosphonate ligands has been done in order to design a method capable of identifying the binding modes without the need to resolve a structure from single crystal X-ray diffraction. However, the complexity of the compounds and the great variety of binding modes has proven that the spectroscopic data are not enough to identify a structure, but can assist in suggesting possible modes of binding.

Vibrational spectroscopy of metallic complexes has been proven to be a good method to assist in the characterisation of the binding mode of the ligand for both nitrogen and phosphorus containing compounds. However it has not been possible to devise a method that allows direct identification of a binding mode.

Figures 7.1 and 7.2 show a schematic representation of the proposed modes for some of the corrosion inhibitors under study in this thesis based on the reinterpretation of the experimental results. It is known that a picture is worth a thousand words and Figures 7.1 and 7.2 are the best way to summarise this thesis.

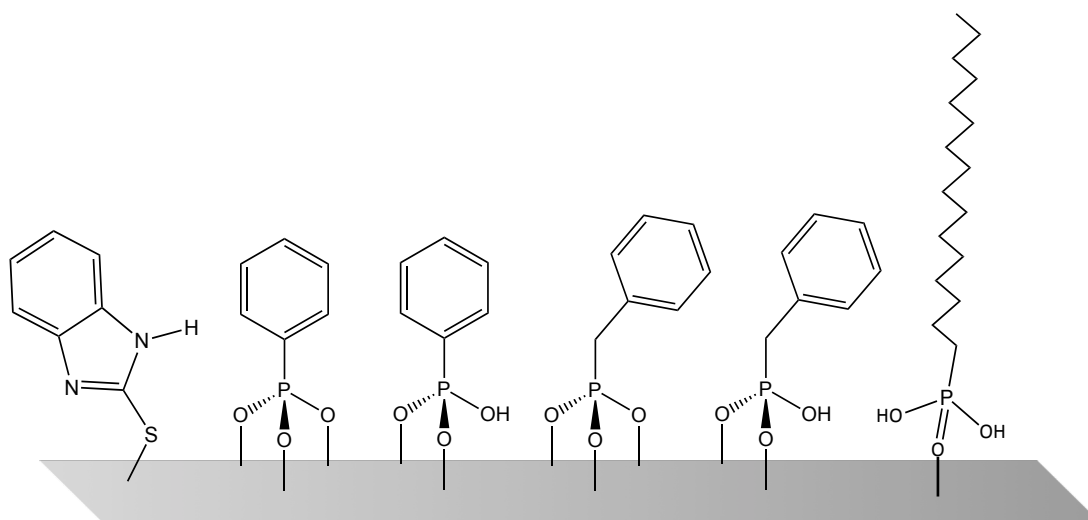


Figure 7.1. Schematic representation of the proposed binding modes for MBIH<sub>2</sub>, PhPO<sub>3</sub>H<sub>2</sub>, BzPO<sub>3</sub>H<sub>2</sub> and HdPO<sub>3</sub>H<sub>2</sub> on a single crystal Fe(110) surface.

Similar compounds sometimes behave differently under the same conditions, for example the aromatic phosphonic acids bind to a single crystal Fe(110) surface with a tridentate mode and hexadecylphosphonic acid, HdPO<sub>3</sub>H<sub>2</sub> remains protonated and

binds with a monodentate binding mode on the same surface and under the same conditions. This is a perfect example of how a change in the substituents on a compound, even if the anchor group remains the same, might change completely the interaction, which might lead to a completely different anticorrosive behaviour.

Dibutyl phosphate ester,  $\text{DbPO}_2\text{H}$ , is a good example of how the same compound might have a completely different interaction with a different surface and/or under different conditions.  $\text{DbPO}_2\text{H}$  has proved to be a good corrosion inhibitor for both an ideal  $\text{Fe}(110)$  single crystal and steel. Comparison with the data obtained for PAE 136, a commercial corrosion inhibitor, suggests that  $\text{DbPO}_2\text{H}$  is a better corrosion inhibitor than the one used by BP. However, PAE 136 might mix better with the crude oil as it is more hydrophobic and for this reason this experiment should be performed in a mixed organic/aqueous acidic medium in order to test the effect. In this case though, the change in the binding to the surface does not compromise the anticorrosive properties of the compound.

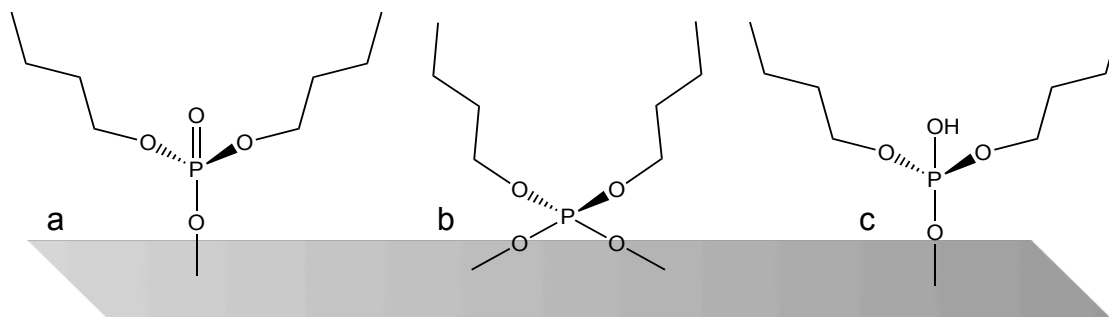


Figure 7.2. Schematic representation of the proposed binding modes for  $\text{DbPO}_2\text{H}$  on a single crystal  $\text{Fe}(110)$  surface (a and b) and on a steel surface (a, b and c).

All these results confirm that every corrosion inhibitor needs to be tested in the particular conditions in which it is going to be used, as it is not possible to predict if their behaviour it is going to be the same for completely different environment and systems.

## 7.2. Further work

A crucial remaining experiment is to study both  $\text{DbPO}_2\text{H}$  and PAE 136, a commercial corrosion inhibitor, on a steel surface and in mixed organic/aqueous acidic media. This experiment is needed to confirm if  $\text{DbPO}_2\text{H}$  is also a better corrosion inhibitor in a 'sweet' environment. The reason why this experiment was not carried out is because the steel samples were measured at the very end of the project when there was no time left to do any more experiments, because the time slots for the XPS instrument are allocated quarterly. The conditions of  $\text{CO}_2$  and  $\text{H}_2\text{O}:\text{CO}_2$  on PAE 136 have not been studied because the corrosion inhibitor was measured before  $\text{CO}_2$  was installed in the NAP XPS instrument. However PAE 136 would be investigated under these conditions to determine whether the suppression of carbonate formation is involved in the mechanisms of corrosion inhibition by this method.

There was a plan to study enough phosphonic acids and phosphate esters with both aromatic and aliphatic groups in order to see if the substituents affect the binding and anticorrosive properties. However phosphonic acids with aromatic rings and phosphate esters with alkyl chains were prioritised. For this reason it would be of interest to study phosphonic acids with different length alkyl chains and phosphate esters with aromatic groups in order to see if the substituents have a systematic effect on how the active compounds bind to the surface. Figure 7.3 shows some examples of compounds that would be used to further understand the inhibition mechanism. Looking at the nature of the chain length, or size of the functional groups would allow the effect of steric hindrance to be investigated. This coupled with measurement of the surface coverage, would aid in deconvoluting steric effect from simple chemical interaction of the phosphonate/phosphate groups directly blocking the surface. In addition, it would be useful to extend the temperature measurements to more realistic conditions, i.e. those used upstream, in order to assess factors, which might affect the effectiveness of the inhibitors in the field.

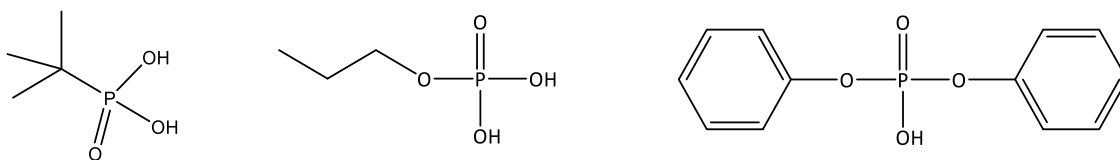


Figure 7.3. Chemical structure of compounds that would be of interest to study: *tert*-butylphosphonic acid ( $t\text{BuPO}_3\text{H}_2$ , left), *n*-butyl phosphate ester ( $n(\text{BuO})\text{PO}_3\text{H}_2$ , centre), diphenyl phosphate ester ( $\text{DpPO}_2\text{H}$ , right).

Phosphate esters have proved to have a stronger interaction with the metallic surface and to be better corrosion inhibitors for the extraction of oil than phosphonic acids. Because compounds with longer aliphatic chains mix better with the crude oil it would be of interest to study phosphate esters with chain lengths between  $\text{DbPO}_2\text{H}$  (4 C) and PAE 136 (13-15 C) in order to optimise the chain length and investigate the effect of branching.

Finally it would be useful to extend the measurements using vibrational sum frequency spectroscopy (VSFS), used in Chapter 2. This would include measurements of known inhibitors on steel surfaces as well as model compounds reported in this thesis and mentioned above.



# Appendices



## Appendix 1: structural data for [Fe(IMH)<sub>4</sub>Cl<sub>2</sub>]Cl (1)

Table 8.1. Structural parameters for compound 1.

|                                    |  |
|------------------------------------|--|
| Formula                            | C <sub>12</sub> H <sub>16</sub> FeN <sub>8</sub> Cl <sub>3</sub> |
| Formula weight /gmol <sup>-1</sup> | 434.51   |
| Temperature / K                    | 150  |
| Radiation type                     | Mo <i>K</i> α  |
| λ / Å                              | 0.7107   |
| Crystal system                     | Orthorhombic   |
| Space group                        | <i>Pnm</i> 2 <sub>1</sub>  |
| <i>a</i> / Å                       | 8.5138(8)  |
| <i>b</i> / Å                       | 20.602(2)  |
| <i>c</i> / Å                       | 13.2068(14)  |
| α / °                              | 90   |
| β / °                              | 90   |
| γ / °                              | 90   |
| Volume / Å <sup>3</sup>            | 2316.5(4)  |
| Z                                  | 8  |
| Density / gcm <sup>-3</sup>        | 1.469  |
| F(000)                             | 1011.4544  |
| Reflections collected              | 3955   |
| Completeness                       | 99%  |
| R <sub>int</sub>                   | 0.033  |
| Final R indices (all data)         | R1 = 0.067, wR2 = 0.210  |



Table 8.2. List of selected atomic distances for compound **1**.

| Atom | Atom | Distance (Å) | Atom | Atom | Distance (Å) |
|------|------|--------------|------|------|--------------|
| Fe1  | Cl2  | 2.355(5)     | N1   | C2   | 1.38(2)      |
| Fe1  | Cl1  | 2.354(5)     | N4   | C5   | 1.41(3)      |
| Fe1  | N6   | 2.162(13)    | N4   | C3   | 1.38(2)      |
| Fe1  | N16  | 2.105(14)    | N9   | C8   | 1.36(2)      |
| Fe1  | N1   | 2.151(14)    | C18  | C17  | 1.42(3)      |
| Fe1  | N11  | 2.113(11)    | C13  | C12  | 1.40(2)      |
| O6A  | O5A  | 1.455(18)    | C2C  | C3C  | 1.17(4)      |
| N3A  | N4A  | 1.457(17)    | C2C  | C5C  | 1.71(5)      |
| N6   | C10  | 1.32(2)      | C2C  | N1C  | 1.21(3)      |
| N6   | C7   | 1.36(2)      | C7   | C8   | 1.34(2)      |
| N19  | C18  | 1.31(2)      | N11  | C12  | 1.389(19)    |
| N19  | C20  | 1.34(2)      | N11  | C15  | 1.35(2)      |
| N4B  | C3B  | 1.82(4)      | N4C  | C3C  | 1.91(4)      |
| N4B  | C5B  | 1.18(4)      | N4C  | C5C  | 1.48(4)      |
| N16  | C17  | 1.39(2)      | C2B  | C3B  | 1.31(4)      |
| N16  | C20  | 1.36(2)      | C2B  | C5B  | 1.71(4)      |
| N14  | C13  | 1.42(2)      | C2B  | N1B  | 1.28(3)      |
| N14  | C15  | 1.337(18)    | C3   | C2   | 1.32(3)      |
| C10  | N9   | 1.386(18)    | C5B  | N1B  | 1.35(3)      |
| N1   | C5   | 1.28(2)      | C5C  | N1C  | 1.41(4)      |

Table 8.3. List of selected atomic angles for compound 1.

| Atom | Atom | Atom | Angle (°) | Atom | Atom | Atom | Angle (°) |
|------|------|------|-----------|------|------|------|-----------|
| Cl1  | Fe1  | Cl2  | 179.3(3)  | N19  | C18  | C17  | 110.0(17) |
| N6   | Fe1  | Cl2  | 88.3(4)   | C12  | C13  | N14  | 107.3(14) |
| N6   | Fe1  | Cl1  | 91.6(4)   | C3C  | C2C  | C5C  | 100(3)    |
| N16  | Fe1  | Cl2  | 89.1(4)   | C3C  | C2C  | N1C  | 155(4)    |
| N16  | Fe1  | Cl1  | 91.6(4)   | N1C  | C2C  | C5C  | 55(2)     |
| N16  | Fe1  | N6   | 91.1(5)   | C8   | C7   | N6   | 108.8(14) |
| N16  | Fe1  | N1   | 179.0(6)  | C12  | N11  | Fe1  | 126.5(11) |
| N16  | Fe1  | N11  | 89.6(5)   | C15  | N11  | Fe1  | 128.7(10) |
| N1   | Fe1  | Cl2  | 90.0(4)   | C15  | N11  | C12  | 104.8(13) |
| N1   | Fe1  | Cl1  | 89.3(4)   | N16  | C17  | C18  | 106.6(16) |
| N1   | Fe1  | N6   | 89.2(5)   | C5C  | N4C  | C3C  | 81(2)     |
| N11  | Fe1  | Cl2  | 90.9(3)   | C2C  | C3C  | N4C  | 90(3)     |
| N11  | Fe1  | Cl1  | 89.2(3)   | C7   | C8   | N9   | 106.4(14) |
| N11  | Fe1  | N6   | 178.9(6)  | N11  | C12  | C13  | 108.5(16) |
| N11  | Fe1  | N1   | 90.1(5)   | C3B  | C2B  | C5B  | 91(3)     |
| C10  | N6   | Fe1  | 124.9(11) | N1B  | C2B  | C3B  | 142(4)    |
| C10  | N6   | C7   | 109.5(14) | N1B  | C2B  | C5B  | 51.5(16)  |
| C7   | N6   | Fe1  | 125.6(11) | C2B  | C3B  | N4B  | 85(3)     |
| C18  | N19  | C20  | 105.7(18) | C2   | C3   | N4   | 106.0(16) |
| C5B  | N4B  | C3B  | 90(3)     | N14  | C15  | N11  | 115.0(14) |
| C17  | N16  | Fe1  | 130.3(13) | N4B  | C5B  | C2B  | 94(3)     |
| C20  | N16  | Fe1  | 126.1(12) | N4B  | C5B  | N1B  | 142(3)    |
| C20  | N16  | C17  | 103.5(15) | N1B  | C5B  | C2B  | 47.8(15)  |
| C15  | N14  | C13  | 104.5(14) | N4C  | C5C  | C2C  | 89(3)     |
| N6   | C10  | N9   | 106.1(15) | N1C  | C5C  | C2C  | 44.3(16)  |
| C5   | N1   | Fe1  | 123.0(13) | N1C  | C5C  | N4C  | 133(3)    |
| C5   | N1   | C2   | 108.5(15) | C3   | C2   | N1   | 110.2(15) |
| C2   | N1   | Fe1  | 128.5(11) | N19  | C20  | N16  | 114.1(17) |
| C3   | N4   | C5   | 107.1(17) | C2B  | N1B  | C5B  | 81(2)     |
| C8   | N9   | C10  | 109.2(13) | C2C  | N1C  | C5C  | 81(2)     |
| N1   | C5   | N4   | 108.2(19) |      |      |      |           |

**Appendix 2: structural data for**  
**[Fe<sub>3</sub>O(HCO<sub>2</sub>)<sub>6</sub>(BIH)<sub>3</sub>]Cl · 2(C<sub>2</sub>H<sub>3</sub>N) (2)**

Table 8.4. Structural parameters for compound **2**.

|                                     |  |
|-------------------------------------|--|
| Formula                             | C <sub>27</sub> H <sub>24</sub> Fe <sub>3</sub> N <sub>6</sub> O <sub>13</sub> Cl · 2(C <sub>2</sub> H <sub>3</sub> N) |
| Formula weight / gmol <sup>-1</sup> | 925.63   |
| Temperature / K                     | 150  |
| Radiation type                      | Mo K $\alpha$  |
| $\lambda$ / Å                       | 0.7107   |
| Crystal system                      | Monoclinic   |
| Space group                         | P2 <sub>1</sub> /n   |
| <i>a</i> / Å                        | 8.6570(6)  |
| <i>b</i> / Å                        | 26.9371(19)  |
| <i>c</i> / Å                        | 17.1471(12)  |
| $\alpha$ / °                        | 90   |
| $\beta$ / °                         | 104.494(7)   |
| $\gamma$ / °                        | 90   |
| Volume / Å <sup>3</sup>             | 3871.3(5)  |
| Z                                   | 4  |
| Density / gcm <sup>-3</sup>         | 1.588  |
| F(000)                              | 1884   |
| Reflections collected               | 7846   |
| Completeness                        | 99%  |
| R <sub>int</sub>                    | 0.164  |
| Final R indices (all data)          | R1 = 0.0835, wR2 = 0.2213  |

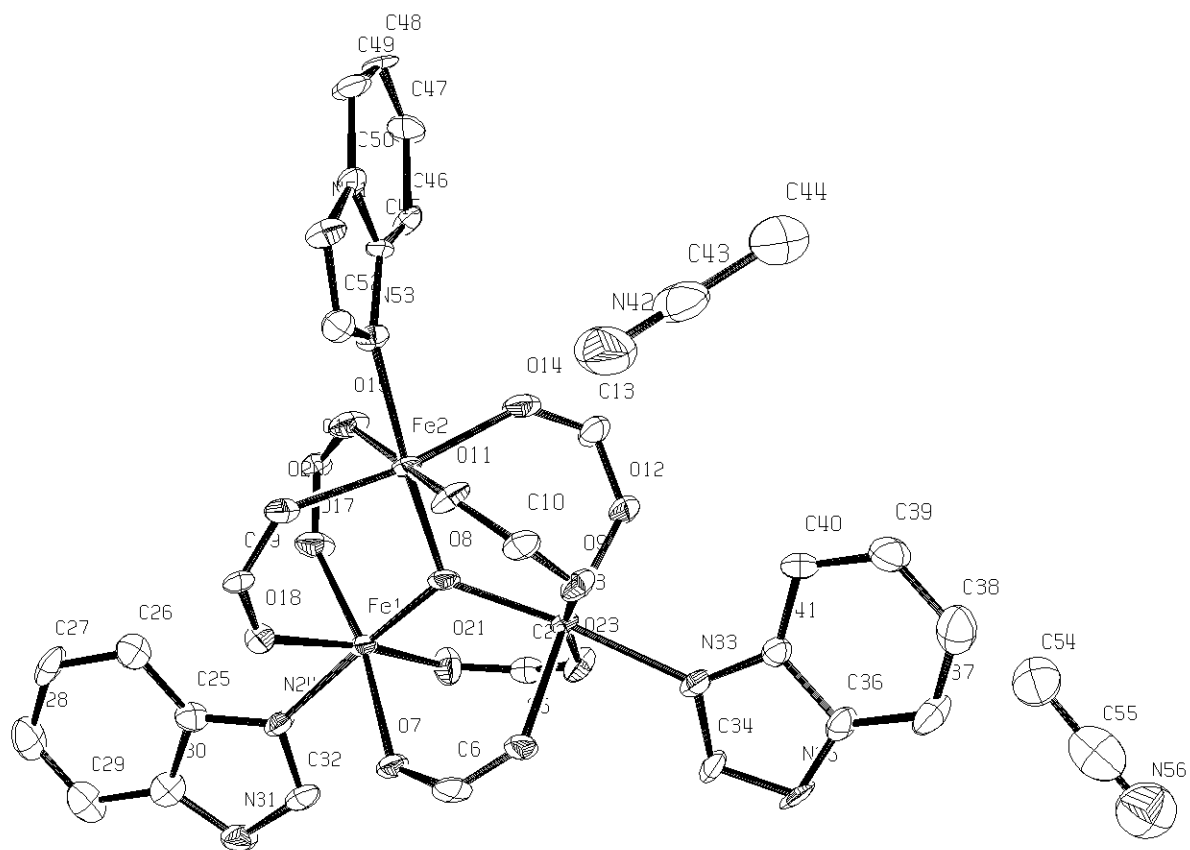


Figure 8.2. X-ray structure for compound 2.

Table 8.5. List of selected atomic distances for compound **2**.

| Atom | Atom | Distance (Å) | Atom | Atom | Distance (Å) |
|------|------|--------------|------|------|--------------|
| Fe1  | O7   | 2.046(4)     | N35  | C36  | 1.385(8)     |
| Fe1  | O8   | 1.895(4)     | N35  | C34  | 1.342(7)     |
| Fe1  | O17  | 2.018(5)     | C26  | C25  | 1.388(9)     |
| Fe1  | O18  | 2.016(4)     | C26  | C27  | 1.415(8)     |
| Fe1  | O21  | 2.011(4)     | N42  | C43  | 1.129(9)     |
| Fe1  | N24  | 2.131(5)     | C36  | C37  | 1.381(9)     |
| Fe2  | O8   | 1.921(4)     | C36  | C41  | 1.404(8)     |
| Fe2  | O11  | 2.032(4)     | N53  | C45  | 1.397(7)     |
| Fe2  | O14  | 2.001(4)     | N53  | C52  | 1.320(7)     |
| Fe2  | O15  | 2.013(4)     | N33  | C34  | 1.299(8)     |
| Fe2  | O20  | 2.035(4)     | N33  | C41  | 1.402(7)     |
| Fe2  | N53  | 2.113(5)     | C25  | C30  | 1.397(8)     |
| Fe3  | O8   | 1.929(4)     | C39  | C40  | 1.372(9)     |
| Fe3  | O9   | 1.999(4)     | C39  | C38  | 1.422(11)    |
| Fe3  | O23  | 2.025(4)     | N51  | C52  | 1.338(8)     |
| Fe3  | O12  | 2.012(4)     | N51  | C50  | 1.381(7)     |
| Fe3  | O5   | 2.038(4)     | N31  | C32  | 1.348(8)     |
| Fe3  | N33  | 2.154(5)     | N31  | C30  | 1.376(8)     |
| O7   | C6   | 1.250(7)     | C40  | C41  | 1.393(8)     |
| O11  | C10  | 1.253(7)     | C45  | C46  | 1.388(8)     |
| O14  | C13  | 1.251(7)     | C45  | C50  | 1.397(8)     |
| O17  | C16  | 1.250(7)     | C37  | C38  | 1.365(10)    |
| O15  | C16  | 1.238(7)     | C29  | C28  | 1.378(11)    |
| O20  | C19  | 1.244(7)     | C29  | C30  | 1.391(9)     |
| O9   | C10  | 1.256(7)     | C46  | C47  | 1.393(9)     |
| O23  | C22  | 1.240(7)     | C50  | C49  | 1.377(8)     |
| O18  | C19  | 1.249(7)     | C28  | C27  | 1.370(10)    |
| O12  | C13  | 1.269(7)     | C48  | C47  | 1.381(9)     |
| O21  | C22  | 1.253(7)     | C48  | C49  | 1.368(9)     |
| O5   | C6   | 1.236(7)     | C55  | C54  | 1.453(15)    |
| N24  | C25  | 1.397(8)     | C55  | N56  | 1.134(13)    |
| N24  | C32  | 1.325(7)     | C43  | C44  | 1.461(11)    |

Table 8.6. List of selected atomic angles for compound **2**.

| Atom | Atom | Atom | Angle (°)  | Atom | Atom | Atom | Angle (°)  |
|------|------|------|------------|------|------|------|------------|
| O17  | Fe1  | O7   | 168.14(16) | O8   | Fe3  | N33  | 174.98(18) |
| O17  | Fe1  | N24  | 86.29(18)  | O9   | Fe3  | O23  | 167.82(17) |
| O18  | Fe1  | O7   | 86.34(17)  | O9   | Fe3  | O12  | 90.75(18)  |
| O18  | Fe1  | O17  | 90.12(18)  | O9   | Fe3  | O5   | 87.54(17)  |
| O18  | Fe1  | N24  | 85.28(17)  | O9   | Fe3  | N33  | 84.09(18)  |
| O21  | Fe1  | O7   | 91.65(19)  | O23  | Fe3  | O5   | 93.33(18)  |
| O21  | Fe1  | O17  | 89.94(19)  | O23  | Fe3  | N33  | 83.99(18)  |
| O21  | Fe1  | O18  | 170.31(17) | O12  | Fe3  | O23  | 86.63(18)  |
| O21  | Fe1  | N24  | 85.05(17)  | O12  | Fe3  | O5   | 171.64(17) |
| O8   | Fe2  | O11  | 93.93(17)  | O12  | Fe3  | N33  | 89.26(18)  |
| O8   | Fe2  | O14  | 93.02(16)  | O5   | Fe3  | N33  | 82.42(18)  |
| O8   | Fe2  | O15  | 95.07(17)  | C6   | O7   | Fe1  | 131.3(4)   |
| O8   | Fe2  | O20  | 96.05(16)  | Fe1  | O8   | Fe2  | 119.9(2)   |
| O8   | Fe2  | N53  | 176.10(17) | Fe1  | O8   | Fe3  | 120.9(2)   |
| O11  | Fe2  | O20  | 83.63(18)  | Fe2  | O8   | Fe3  | 119.21(19) |
| O11  | Fe2  | N53  | 83.04(17)  | C10  | O11  | Fe2  | 129.6(4)   |
| O14  | Fe2  | O11  | 94.34(18)  | C13  | O14  | Fe2  | 135.7(4)   |
| O14  | Fe2  | O15  | 90.87(18)  | C16  | O17  | Fe1  | 130.4(4)   |
| O14  | Fe2  | O20  | 170.82(18) | C16  | O15  | Fe2  | 131.6(4)   |
| O14  | Fe2  | N53  | 84.78(18)  | C19  | O20  | Fe2  | 130.8(4)   |
| O15  | Fe2  | O11  | 169.35(17) | C10  | O9   | Fe3  | 132.3(4)   |
| O15  | Fe2  | O20  | 89.76(18)  | C22  | O23  | Fe3  | 131.1(4)   |
| O15  | Fe2  | N53  | 88.19(17)  | C19  | O18  | Fe1  | 132.2(4)   |
| O20  | Fe2  | N53  | 86.09(17)  | C13  | O12  | Fe3  | 127.1(4)   |
| O8   | Fe3  | O9   | 96.54(16)  | C22  | O21  | Fe1  | 130.6(4)   |
| O8   | Fe3  | O23  | 95.56(16)  | C6   | O5   | Fe3  | 130.9(4)   |
| O8   | Fe3  | O12  | 95.70(16)  | C25  | N24  | Fe1  | 131.9(4)   |
| O8   | Fe3  | O5   | 92.62(16)  | C32  | N24  | Fe1  | 122.6(4)   |

### Appendix 3: structural data for [Cu(MBIH<sub>2</sub>)(dppp)Cl] (3)

Table 8.7. Structural parameters for compound 3.

|                                     |  |
|-------------------------------------|--|
| Formula                             | 2(C <sub>34</sub> H <sub>32</sub> ClCuN <sub>2</sub> P <sub>2</sub> S) |
| Formula weight / gmol <sup>-1</sup> | 1323.21  |
| Temperature / K                     | 150  |
| Radiation type                      | Mo <i>K</i> α  |
| λ / Å                               | 0.7107   |
| Crystal system                      | Monoclinic   |
| Space group                         | <i>C</i> 2/ <i>c</i>   |
| <i>a</i> / Å                        | 25.9458(15)  |
| <i>b</i> / Å                        | 9.1661(5)  |
| <i>c</i> / Å                        | 30.0718(19)  |
| α / °                               | 90   |
| β / °                               | 111.500(7)   |
| γ / °                               | 90   |
| Volume / Å <sup>3</sup>             | 6654.1   |
| Z                                   | 4  |
| Density / gcm <sup>-3</sup>         | 1.321  |
| F(000)                              | 2736   |
| Reflections collected               | 7698   |
| Completeness                        | 99%  |
| R <sub>int</sub>                    | 0.051  |
| Final R indices (all data)          | R1 = 0.0527, wR2 = 0.1226  |

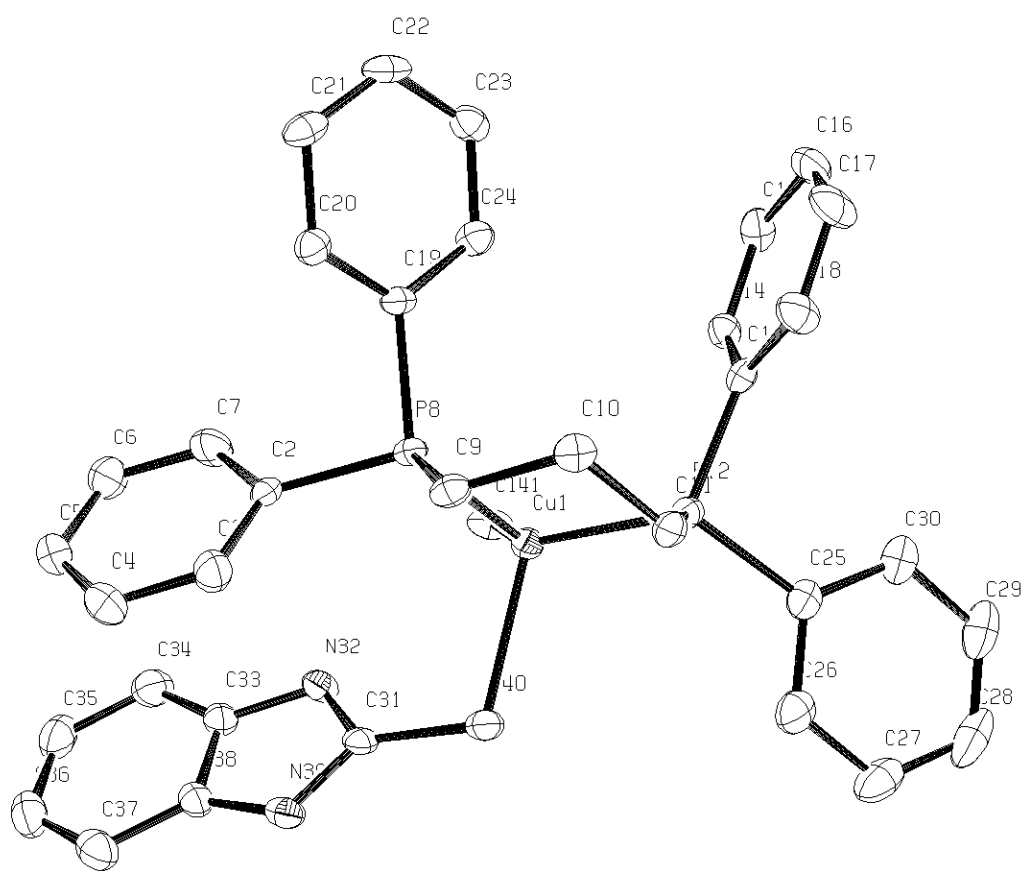


Figure 8.3. X-ray structure for compound 3.

Table 8.8. List of selected atomic distances for compound **3**.

| Atom | Atom | Distance (Å) | Atom | Atom | Distance (Å) |
|------|------|--------------|------|------|--------------|
| Cu1  | P8   | 2.2768(8)    | N32  | C31  | 1.344(4)     |
| Cu1  | P12  | 2.2364(9)    | C33  | C38  | 1.396(4)     |
| Cu1  | S40  | 2.3895(8)    | C33  | C34  | 1.387(4)     |
| Cu1  | Cl41 | 2.3297(8)    | C23  | C24  | 1.399(4)     |
| P8   | C19  | 1.835(3)     | C38  | C37  | 1.384(4)     |
| P8   | C2   | 1.830(3)     | C20  | C21  | 1.389(4)     |
| P8   | C9   | 1.836(3)     | C25  | C30  | 1.407(4)     |
| P12  | C13  | 1.823(3)     | C25  | C26  | 1.391(4)     |
| P12  | C11  | 1.836(3)     | C2   | C3   | 1.378(4)     |
| P12  | C25  | 1.824(3)     | C2   | C7   | 1.400(4)     |
| S40  | C31  | 1.692(3)     | C3   | C4   | 1.382(4)     |
| C13  | C14  | 1.387(4)     | C16  | C17  | 1.388(4)     |
| C13  | C18  | 1.393(4)     | C18  | C17  | 1.384(4)     |
| N39  | C38  | 1.388(4)     | C30  | C29  | 1.387(5)     |
| N39  | C31  | 1.348(4)     | C26  | C27  | 1.381(5)     |
| C19  | C20  | 1.383(4)     | C34  | C35  | 1.390(5)     |
| C19  | C24  | 1.389(4)     | C6   | C7   | 1.384(4)     |
| C22  | C23  | 1.376(4)     | C6   | C5   | 1.377(4)     |
| C22  | C21  | 1.390(4)     | C4   | C5   | 1.380(5)     |
| C10  | C11  | 1.538(4)     | C37  | C36  | 1.381(5)     |
| C10  | C9   | 1.551(4)     | C29  | C28  | 1.356(5)     |
| C15  | C14  | 1.383(4)     | C35  | C36  | 1.392(5)     |
| C15  | C16  | 1.384(4)     | C28  | C27  | 1.390(5)     |
| N32  | C33  | 1.387(4)     |      |      |              |

Table 8.6. List of selected atomic angles for compound **3**.

| Atom | Atom | Atom | Angle (°)  | Atom | Atom | Atom | Angle (°) |
|------|------|------|------------|------|------|------|-----------|
| P8   | Cu1  | S40  | 99.55(3)   | C37  | C38  | N39  | 132.1(3)  |
| P8   | Cu1  | Cl41 | 113.84(3)  | C37  | C38  | C33  | 121.4(3)  |
| P12  | Cu1  | P8   | 101.02(3)  | C15  | C14  | C13  | 121.2(3)  |
| P12  | Cu1  | S40  | 103.70(3)  | C10  | C11  | P12  | 115.5(2)  |
| P12  | Cu1  | Cl41 | 127.21(3)  | C19  | C20  | C21  | 121.3(3)  |
| Cl41 | Cu1  | S40  | 107.85(3)  | C30  | C25  | P12  | 123.0(3)  |
| C19  | P8   | Cu1  | 125.97(10) | C26  | C25  | P12  | 119.0(2)  |
| C2   | P8   | Cu1  | 116.01(10) | C26  | C25  | C30  | 117.9(3)  |
| C2   | P8   | C19  | 101.12(13) | C3   | C2   | P8   | 123.6(2)  |
| C2   | P8   | C9   | 104.78(13) | C3   | C2   | C7   | 118.6(3)  |
| C9   | P8   | Cu1  | 104.21(10) | C7   | C2   | P8   | 117.5(2)  |
| C9   | P8   | C19  | 102.34(13) | C10  | C9   | P8   | 113.0(2)  |
| C13  | P12  | Cu1  | 116.07(10) | C2   | C3   | C4   | 120.7(3)  |
| C13  | P12  | C11  | 104.85(14) | C20  | C21  | C22  | 119.3(3)  |
| C13  | P12  | C25  | 103.28(14) | C19  | C24  | C23  | 120.4(3)  |
| C11  | P12  | Cu1  | 106.49(10) | C15  | C16  | C17  | 119.6(3)  |
| C25  | P12  | Cu1  | 122.00(10) | C17  | C18  | C13  | 120.5(3)  |
| C25  | P12  | C11  | 102.15(14) | N39  | C31  | S40  | 126.2(2)  |
| C31  | S40  | Cu1  | 104.06(11) | N32  | C31  | S40  | 126.9(2)  |
| C14  | C13  | P12  | 117.7(2)   | N32  | C31  | N39  | 106.9(3)  |
| C14  | C13  | C18  | 118.6(3)   | C29  | C30  | C25  | 119.9(3)  |
| C18  | C13  | P12  | 123.6(2)   | C27  | C26  | C25  | 121.0(3)  |
| C31  | N39  | C38  | 110.2(3)   | C33  | C34  | C35  | 116.4(3)  |
| C20  | C19  | P8   | 121.7(2)   | C5   | C6   | C7   | 119.6(3)  |
| C20  | C19  | C24  | 118.9(3)   | C18  | C17  | C16  | 120.2(3)  |
| C24  | C19  | P8   | 119.4(2)   | C5   | C4   | C3   | 120.1(3)  |
| C23  | C22  | C21  | 120.3(3)   | C6   | C7   | C2   | 120.7(3)  |
| C11  | C10  | C9   | 115.8(2)   | C36  | C37  | C38  | 116.9(3)  |
| C14  | C15  | C16  | 119.8(3)   | C28  | C29  | C30  | 121.6(3)  |
| C31  | N32  | C33  | 110.9(3)   | C6   | C5   | C4   | 120.2(3)  |
| N32  | C33  | C38  | 105.6(3)   | C34  | C35  | C36  | 121.7(3)  |
| C34  | C33  | N32  | 132.6(3)   | C37  | C36  | C35  | 121.8(3)  |
| C34  | C33  | C38  | 121.8(3)   | C29  | C28  | C27  | 119.1(4)  |
| C22  | C23  | C24  | 119.9(3)   | C26  | C27  | C28  | 120.4(4)  |
| N39  | C38  | C33  | 106.4(3)   |      |      |      |           |

Appendix 4: IR and Raman spectra for MeBTAH and  $[\text{Fe}_{14}\text{O}_6(\text{MeBTA})_6(\text{MeO})_{18}\text{Cl}_6]$

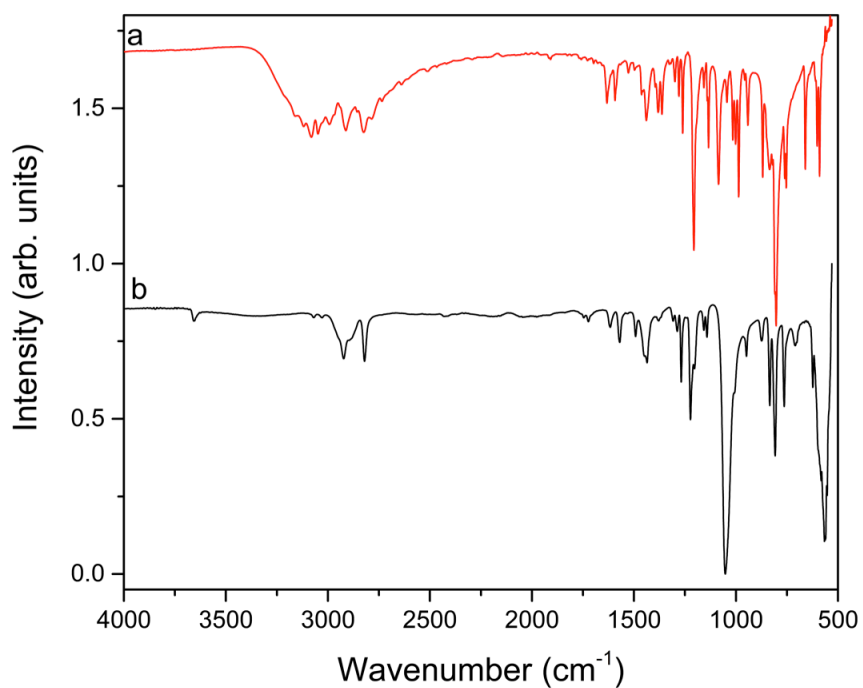


Figure 8.4. IR spectra for MeBTAH (a) and  $[\text{Fe}_{14}\text{O}_6(\text{MeBTA})_6(\text{MeO})_{18}\text{Cl}_6]$  (b).

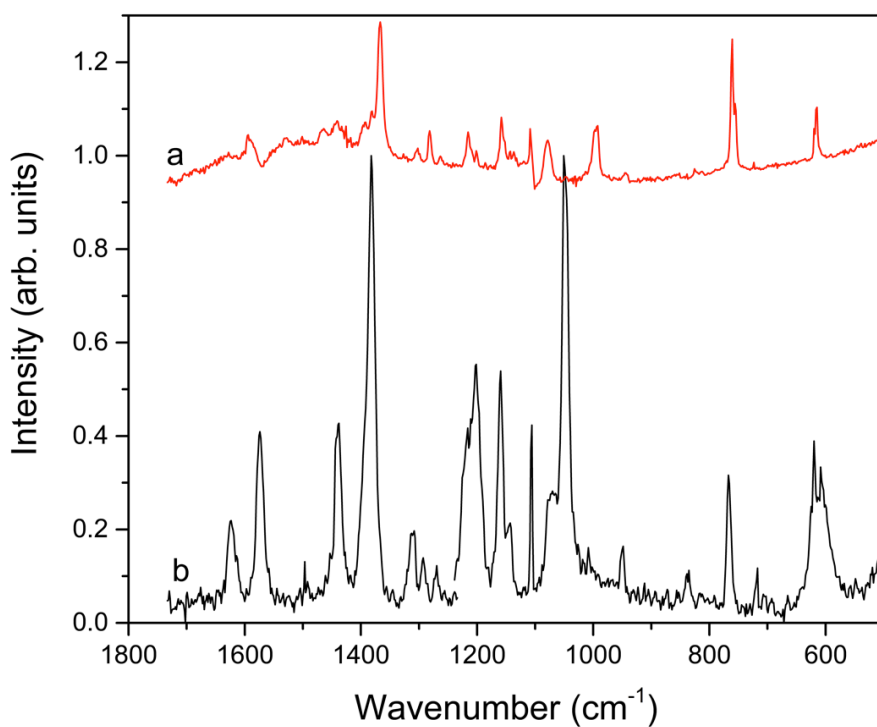


Figure 8.5. Raman spectra for MeBTAH (a) and  $[\text{Fe}_{14}\text{O}_6(\text{MeBTA})_6(\text{MeO})_{18}\text{Cl}_6]$  (b).

Appendix 5: IR and Raman spectra for Me<sub>2</sub>BTAH and [Fe<sub>14</sub>O<sub>6</sub>(Me<sub>2</sub>BTA)<sub>6</sub>(MeO)<sub>18</sub>Cl<sub>6</sub>]

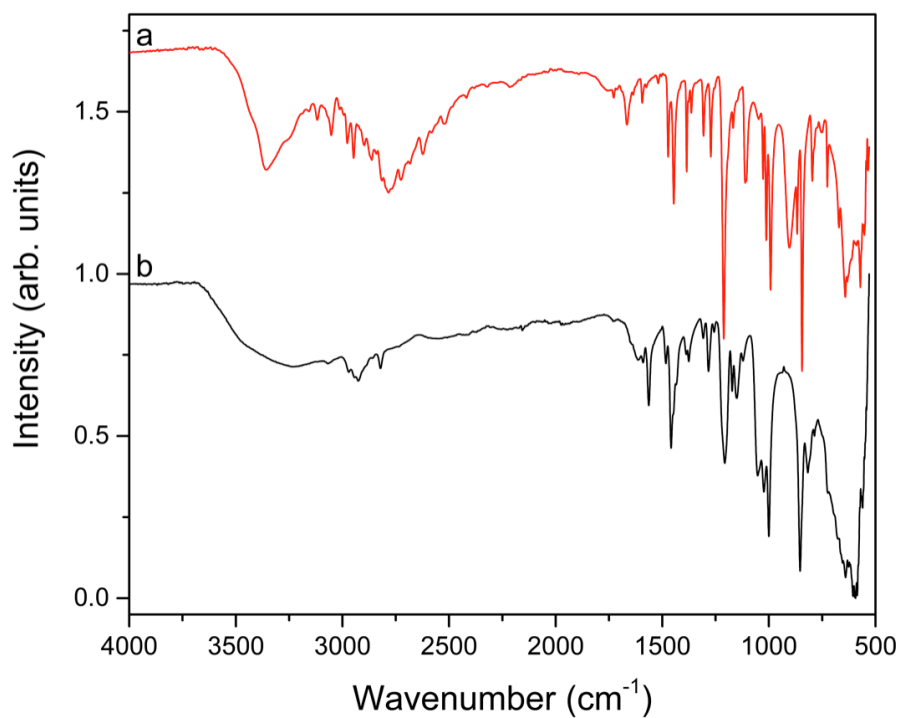


Figure 8.6. IR spectra for Me<sub>2</sub>BTAH (a) and [Fe<sub>14</sub>O<sub>6</sub>(Me<sub>2</sub>BTA)<sub>6</sub>(MeO)<sub>18</sub>Cl<sub>6</sub>] (b).

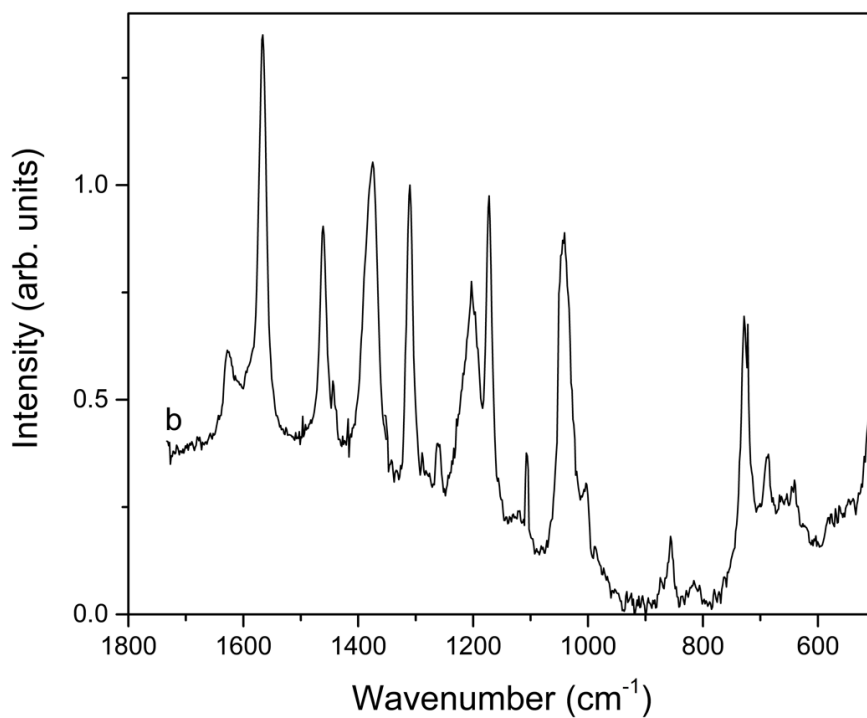


Figure 8.7. Raman spectra for [Fe<sub>14</sub>O<sub>6</sub>(Me<sub>2</sub>BTA)<sub>6</sub>(MeO)<sub>18</sub>Cl<sub>6</sub>] (b).

Appendix 6: IR and Raman spectra for ClBTAH and  $[\text{Fe}_{14}\text{O}_6(\text{ClBTA})_6(\text{MeO})_{18}\text{Cl}_6]$

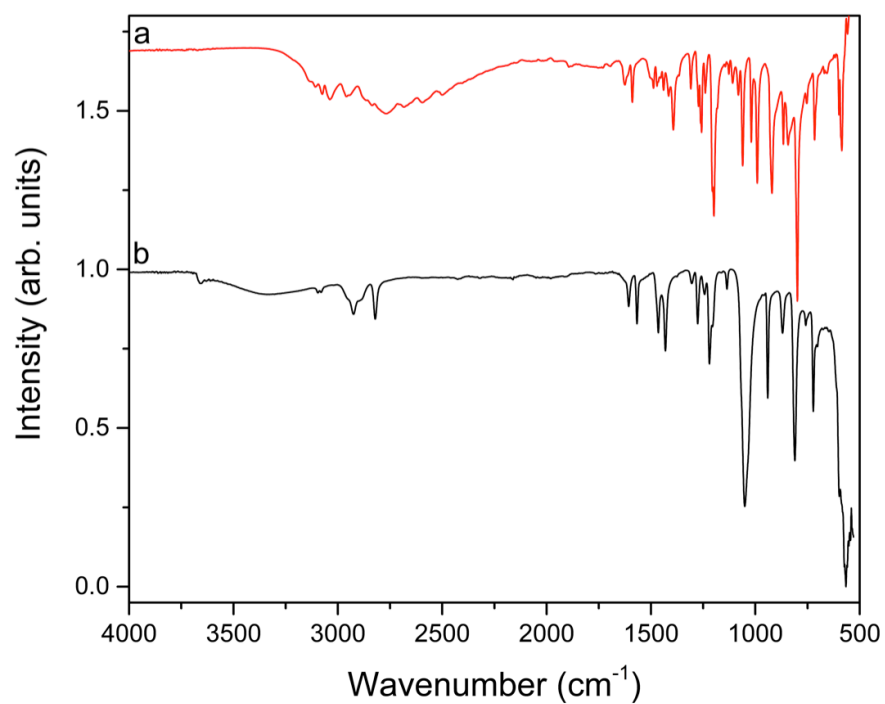


Figure 8.8. IR spectra for ClBTAH (a) and  $[\text{Fe}_{14}\text{O}_6(\text{ClBTA})_6(\text{MeO})_{18}\text{Cl}_6]$  (b).

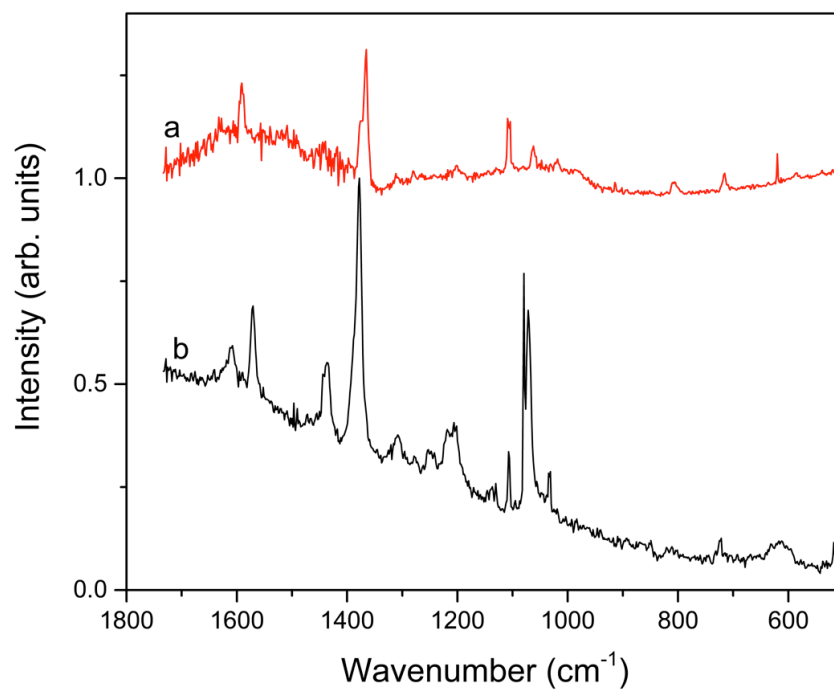


Figure 8.9. Raman spectra for ClBTAH (a) and  $[\text{Fe}_{14}\text{O}_6(\text{ClBTA})_6(\text{MeO})_{18}\text{Cl}_6]$  (b).

Appendix 7: IR spectra for TZAH and

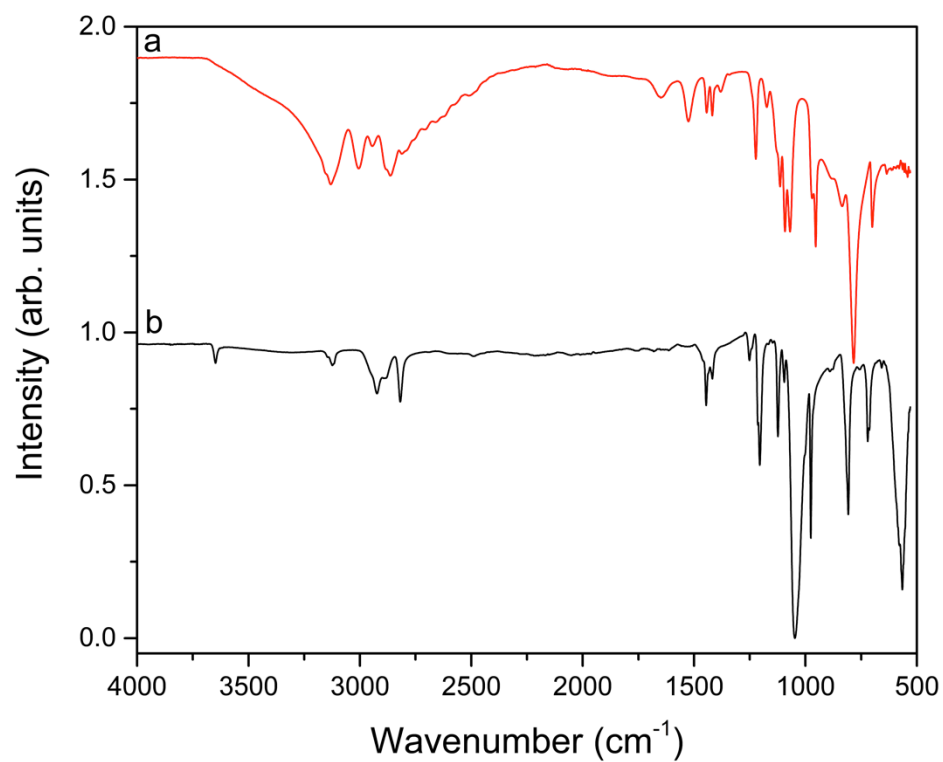


Figure 8.10. IR spectra for TZA (a) and  $[\text{Fe}_{14}\text{O}_6(\text{TZA})_6(\text{MeO})_{18}\text{Cl}_6]$  (b).

## Appendix 8: DFTP calculations

### Input files

#### Param file – general input file

```
task:phonon+efield
continuation: default
#reuse:default
xc_functional:pbe
opt_strategy:speed
num_dump_cycles:0
cut_off_energy:600.0 eV
fix_occupancy: false
metals_method:dm
write_cell_structure:true
NUM_BACKUP_ITER : 1
calculate_raman:false
phonon_fine_method: interpolate
elec_energy_tol: 1e-10
phonon_energy_tol: 1e-5
geom_force_tol: 1.5e-2
elec_force_tol: 1.5e-2
geom_max_iter:1000
```

#### Cell file – structure input file

```
#
# CELL written by cell_write: Keith Refson, Oct 2006
#
%BLOCK lattice_cart
ANG
        6.05865109014324      0.0000000000000000      0.770476292546315
```

```
0.0000000000000000    8.61763514892753    0.0000000000000000
1.01473724492288    0.0000000000000000    10.0095724297939
```

```
%ENDBLOCK lattice_cart
```

```
%BLOCK cell_constraints
```

```
0 0 0
```

```
0 0 0
```

```
%ENDBLOCK cell_constraints
```

```
%BLOCK positions_frac
```

```
H      0.304952079383703    0.989968713007029    0.094623607035176
H      0.695047920616296    0.489968713007029    0.905376392964825
H      0.304952079383703    0.510031286992971    0.094623607035176
H      0.920189037616691    0.042951458251979    0.318229097239866
H      0.079810962383309    0.542951458251979    0.681770902760134
H      0.358994704722793    0.106872191628619    0.508860686516496
H      0.641005295277208    0.893127808371380    0.491139313483504
H      0.358994704722793    0.393127808371381    0.508860686516496
H      0.641005295277208    0.606872191628620    0.491139313483504
H      0.920189037616691    0.457048541748021    0.318229097239866
H      0.079810962383309    0.957048541748021    0.681770902760134
H      0.695047920616296    0.010031286992971    0.905376392964825
C      0.636767194167086    0.2500000000000000    0.945442558989156
C      0.363232805832914    0.7500000000000000    0.054557441010844
C      0.923519483797948    0.168034401456629    0.776901369977555
C      0.076480516202053    0.668034401456629    0.223098630022445
C      0.923519483797948    0.331965598543371    0.776901369977555
C      0.076480516202053    0.831965598543371    0.223098630022445
C      0.079993900093861    0.083429266355733    0.681905336171981
C      0.920006099906139    0.583429266355732    0.318094663828020
```

|   |                   |                   |                   |
|---|-------------------|-------------------|-------------------|
| C | 0.920006099906139 | 0.916570733644268 | 0.318094663828020 |
| C | 0.079993900093861 | 0.416570733644268 | 0.681905336171981 |
| C | 0.235688937928517 | 0.168423226435487 | 0.586086576814084 |
| C | 0.764311062071483 | 0.831576773564512 | 0.413913423185916 |
| C | 0.764311062071483 | 0.668423226435488 | 0.413913423185916 |
| C | 0.235688937928517 | 0.331576773564513 | 0.586086576814084 |
| N | 0.746847031029952 | 0.123058641216138 | 0.882018667472348 |
| N | 0.253152968970047 | 0.876941358783862 | 0.117981332527652 |
| N | 0.746847031029952 | 0.376941358783862 | 0.882018667472348 |
| N | 0.253152968970047 | 0.623058641216138 | 0.117981332527652 |
| S | 0.407650138614513 | 0.250000000000000 | 0.077095249889285 |
| S | 0.592349861385487 | 0.750000000000000 | 0.922904750110716 |

%ENDBLOCK positions\_frac

FIX\_COM : true

%BLOCK species\_pot

|   |                              |
|---|------------------------------|
| H | /opt/pspots/h-optgga2.recpot |
| C | /opt/pspots/c-optgga2.recpot |
| N | /opt/pspots/n-optgga1.recpot |
| S | /opt/pspots/s-optgga1.recpot |

%ENDBLOCK species\_pot

%BLOCK symmetry\_ops

# Symm. op. 1 E

|                   |                   |                   |
|-------------------|-------------------|-------------------|
| 1.000000000000000 | 0.000000000000000 | 0.000000000000000 |
| 0.000000000000000 | 1.000000000000000 | 0.000000000000000 |
| 0.000000000000000 | 0.000000000000000 | 1.000000000000000 |
| 0.000000000000000 | 0.000000000000000 | 0.000000000000000 |

# Symm. op. 2 2\_1

```

-1.0000000000000000    0.0000000000000000    0.0000000000000000
0.0000000000000000    1.0000000000000000    0.0000000000000000
0.0000000000000000    0.0000000000000000    -1.0000000000000000
0.0000000000000000   -0.5000000000000000    0.0000000000000000

# Symm. op. 3      I
-1.0000000000000000    0.0000000000000000    0.0000000000000000
0.0000000000000000   -1.0000000000000000    0.0000000000000000
0.0000000000000000    0.0000000000000000   -1.0000000000000000
0.0000000000000000    0.0000000000000000    0.0000000000000000

# Symm. op. 4      m
1.0000000000000000    0.0000000000000000    0.0000000000000000
0.0000000000000000   -1.0000000000000000    0.0000000000000000
0.0000000000000000    0.0000000000000000    1.0000000000000000
0.0000000000000000    0.5000000000000000    0.0000000000000000

%ENDBLOCK symmetry_ops

kpoint_mp_grid :  4  2  3

phonon_kpoint_mp_grid :  3  2  2

PHONON_KPOINT_MP_OFFSET : 0.00000000 0.25000000 0.25000000

```

## Output files

CASTEP file – report on the calculation, Phonon file – phonon data and Bands file – Eigenvalues are available in electronic format due to their length.

## Appendix 9: Publication from this thesis

# An Experimental Investigation of the Adsorption of a Phosphonic Acid on the Anatase TiO<sub>2</sub>(101) Surface

Michael Wagstaffe,<sup>†</sup> Andrew G. Thomas,<sup>\*,‡</sup> Mark J. Jackman,<sup>†</sup> Maria Torres-Molina,<sup>§</sup> Karen L. Syres,<sup>||</sup> and Karsten Handrup<sup>⊥</sup>

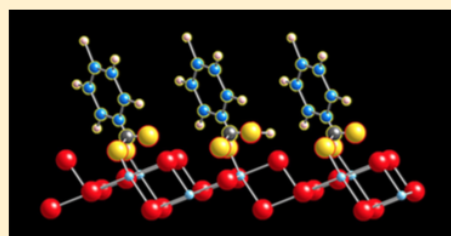
<sup>†</sup>School of Physics and Astronomy, <sup>‡</sup>School of Materials and Photon Science Institute, and <sup>§</sup>School of Chemistry, The University of Manchester, Oxford Road, Manchester M13 9PL, U.K.

<sup>||</sup>Jeremiah Horrocks Institute, The University of Central Lancashire, Fylde Road, Preston PR1 2HE, U.K.

<sup>⊥</sup>MaxLab, Ole Rømers Väg, Lund, Sweden

### Supporting Information

**ABSTRACT:** A combination of synchrotron radiation photoelectron spectroscopy and near-edge X-ray absorption fine structure (NEXAFS) spectroscopy has been used to study the adsorption of phenylphosphonic acid (PPA) on anatase TiO<sub>2</sub>(101) single crystal at coverages of 0.15 monolayer (ML) and 0.85 ML. The photoelectron spectroscopy data suggest that at 0.15 ML coverage PPA adsorbs in a bidentate geometry following deprotonation of both phosphonate hydroxyl groups, leaving the P=O group unbound. At 0.85 ML there is a shift to a mixed bidentate/monodentate binding mode. The carbon K-edge NEXAFS spectra were recorded at two azimuths. Our calculations show that for PPA on anatase TiO<sub>2</sub>(101) the phenyl ring is oriented  $65 \pm 4^\circ$  away from the surface plane with an azimuthal twist of  $57 \pm 11^\circ$  away from the [101] azimuth.



## ■ INTRODUCTION

TiO<sub>2</sub> has applications in a wide range of fields, including photovoltaics<sup>1–5</sup> and catalysis.<sup>6,7</sup> In addition, it is also thought to contribute to the high biocompatibility of Ti used in biomedical implants.<sup>8–10</sup> It is extremely abundant, has cheap manufacturing costs, and is both nontoxic and highly resistant to corrosion.<sup>11</sup> In solar applications the wide band gap of TiO<sub>2</sub> means that it is unable to efficiently utilize solar radiation, and as a result the surface functionalization and doping of TiO<sub>2</sub> have become highly researched areas. The adsorption of various organic dyes, particularly those containing aromatic ligands, on TiO<sub>2</sub> have been investigated in an attempt to shift the adsorption onset.<sup>12–16</sup> Functional groups on the dye molecule anchor the dye to the surface of a substrate and direct the charge transfer between the light harvesting molecule and the conduction band of the semiconductor.<sup>15</sup> As well as dyes, quantum dots have been suggested as light harvesting entities. In these quantum-dot-sensitized systems, in order to facilitate charge transfer between the excited quantum dot and the n-type material, linker molecules capable of bonding to both the n-type material and quantum dot are required.<sup>17</sup> One may expect that aromatic molecules may promote fast electron transfer due to the resonance structures offered by aromatics which can stabilize electrons or holes in the molecules.<sup>18</sup>

Some of the most efficient dye-sensitized solar cells (DSSCs) utilize dyes containing the carboxylic acid functional group. Despite the excellent electronic coupling between the dye and the semiconductor that this group provides, long-term stability

has been seen to be an issue.<sup>19,20</sup> This has led to investigations into alternate functional groups that can be used to anchor dyes to the semiconductor surface, one of the most promising being phosphonic acid, shown in phenylphosphonic acid in Figure 1.<sup>21–31</sup> Studies indicate that this binds more strongly to metal

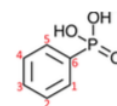


**Figure 1.** Molecular structure of phenylphosphonic acid. The numbering of the C atoms is used in assignment of the photoemission features discussed in the Results section.

oxide surfaces and as a result will have improved long-term stability.<sup>24</sup> Experimentally, the interaction between the phosphonic acid functional group and TiO<sub>2</sub> is difficult to assess, and thus experiments often lead to conflicting/indefinite conclusions.<sup>32</sup> Various techniques have been utilized in an attempt to determine the bonding mechanism, including high field <sup>17</sup>O MAS NMR (magic angle spinning nuclear magnetic resonance)<sup>30</sup> and FTIR (Fourier transform infrared) spectroscopy.<sup>26</sup> While it is generally accepted that the phosphonic acid functional group binds to the TiO<sub>2</sub> surface via Ti–O–P bonds,

**Received:** November 17, 2015

**Revised:** January 2, 2016

**Published:** January 5, 2016

a variety of different bonding mechanisms have been postulated, including monodentate, bidentate, and tridentate. Luschnitz et al.<sup>32</sup> conducted an extensive investigation into the various adsorption complexes of phosphonic acid on the anatase  $\text{TiO}_2(101)$  surface using quantum chemical periodic hybrid *ab initio* Hartree–Fock density functional theory calculations. Their work suggested that the most stable adsorption configuration on the anatase  $\text{TiO}_2(101)$  surface is that of a bidentate structure. In their optimized structure, which has an adsorption energy of 277 kJ/mol, the adsorbed phosphonic acid is fully dissociated and the P=O bond is not involved in the surface bonding. Their work also showed that there were several alternative bidentate configurations which had similar adsorption energies but different geometries. This was reinforced by Francesco Ambrosio et al.,<sup>33</sup> who studied electron injection times for phosphonated dyes bonded in various configurations, adding that this configuration also generally led to faster injection times. While DFT studies completed by O'Rourke and Bowler<sup>34</sup> agreed in the sense that the most stable adsorption mode for phosphonic acid is the bidentate bridging mode, it was a different bidentate configuration to that put forward by Luschnitz et al., bonding through the phosphonyl and a single OH group. Additionally they noted a comparably stable monodentate configuration, where the phosphonic acid binds solely through its phosphonyl group. It is likely the close relative stabilities of these various adsorption modes that has stopped a general consensus being reached.

Here, in an attempt to clarify the interaction of a phosphonic acid with the titania surface, we use X-ray photoelectron spectroscopy (XPS) and near-edge X-ray absorption fine structure (NEXAFS) spectroscopy to study phenylphosphonic acid adsorption on single crystal anatase  $\text{TiO}_2(101)$ . XPS and NEXAFS have been successfully employed to study the interaction of carboxylic acids with  $\text{TiO}_2$  surfaces.<sup>12,35</sup> The anatase  $\text{TiO}_2(101)$  surface is chosen since it is likely to be the dominant surface exposed in nanoparticle  $\text{TiO}_2$ , which is the form generally used in DSSCs based on  $\text{TiO}_2$ .<sup>12,14,32,36</sup>

## EXPERIMENTAL SECTION

The work was carried out on the bending magnet soft X-ray beamline, D1011 (photon energy range 30 eV <  $h\nu$  < 1600 eV), at MAX-lab, Sweden. The analysis chamber is equipped with a SCIENTA SES200 hemispherical electron energy analyzer, for photoemission experiments, and a multichannel partial yield detector, for use in NEXAFS experiments.

The anatase  $\text{TiO}_2$  single crystal (5 mm × 5 mm, Pikem Ltd.) was mounted on a Mo sample plate using tantalum wire and cleaned by repeated 1 keV  $\text{Ar}^+$  ion bombardment and annealing up to temperatures of 700 °C until a sharp  $1 \times 1$  LEED pattern, as shown in Figure 2, was obtained, and X-ray photoelectron spectra showed the surface to be free of contamination (see Supporting Information Figure S.1). All photoemission spectra are recorded at normal emission at room temperature. All binding energies (BE) are referenced to a Fermi edge recorded from the sample plate (with an associated error of  $\pm 0.1$  eV).

NEXAFS spectra were recorded over the C K-edge with incident photon angles,  $\theta$ , as shown in Figure 2b, ranging between 20° and 90°, in increments of 10°. Data were recorded with the surface component of the electric vector of the incident radiation at two orthogonal angles as marked in Figure 2.<sup>37</sup> The partial yield detector was tuned to retard electrons with a kinetic energy of less than 200 eV. The sample

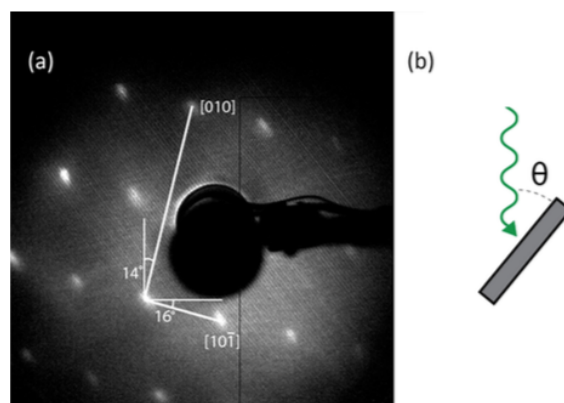


**Figure 2.** (a)  $1 \times 1$  LEED pattern obtained for anatase  $\text{TiO}_2(101)$  surface. The arrows show how the azimuthal angle is defined in the NEXAFS experiments described below. (b) Definition of the polar angle in the NEXAFS experiments.

manipulator on the end station does not allow *in situ* azimuthal rotation. In order to measure the second azimuth, the sample had to be removed from the vacuum system, remounted, and the surface reprepared and redosed, which may lead to slight differences in substrate signal between azimuths.

Phenylphosphonic acid (PPA) (99.95%, Sigma-Aldrich) was deposited on the anatase surface via evaporation into the vacuum chamber. The PPA powder was inserted into a glass crucible, and the temperature was slowly increased to around 130 °C over a period of around an hour in order to remove any impurities and adsorbed gases. The crucible temperature was then reduced and held at around 80 °C when not in use. In order to “dose” the  $\text{TiO}_2$  crystal, the evaporator was heated to around 120 °C at a pressure of  $5 \times 10^{-8}$  mbar with the anatase crystal at room temperature and facing the evaporator.

To calculate NEXAFS spectra of the gas-phase PPA molecule, we used GaussView and Gaussian 03<sup>38</sup> to produce energy-minimized geometry-optimized structures in order to obtain the atomic coordinates. These calculations were carried out using DFT B3LYP theory and the 6-31G(d,p) basis set. The coordinates obtained from Gaussian were then used to carry out further DFT calculations using the StoBe-deMon code.<sup>39</sup> StoBe was used to calculate the excited-state X-ray absorption spectra for each C atom in the molecule individually. The summation of the individual energy-calibrated spectra gives the theoretical angle-integrated NEXAFS spectrum for the molecule.

## RESULTS AND DISCUSSION

**X-ray Photoelectron Spectroscopy.** Core-level photoelectron spectra are shown in Figure 3 for Ti 2p, O 1s, C 1s, and P 2p. Fitting of core level spectra was carried out in CasaXPS, utilizing Gaussian:Lorentzian curves (0.7:0.3) atop a Shirley background.

The Ti 2p spectra prior to adsorption shows the main oxide peak due to  $\text{Ti}^{4+}$  at a binding energy of 458.7 eV, with a small shoulder at a lower binding energy of 457.1 eV, indicating the presence of around 4% of  $\text{Ti}^{3+}$  in the near surface region.<sup>36</sup> Following adsorption of the phenylphosphonic acid no changes are observed in the Ti 2p spectrum. The C 1s peak is composed of two components, at energies 284.8 and 286.1 eV. These peaks are assigned to electron emission from carbon atoms

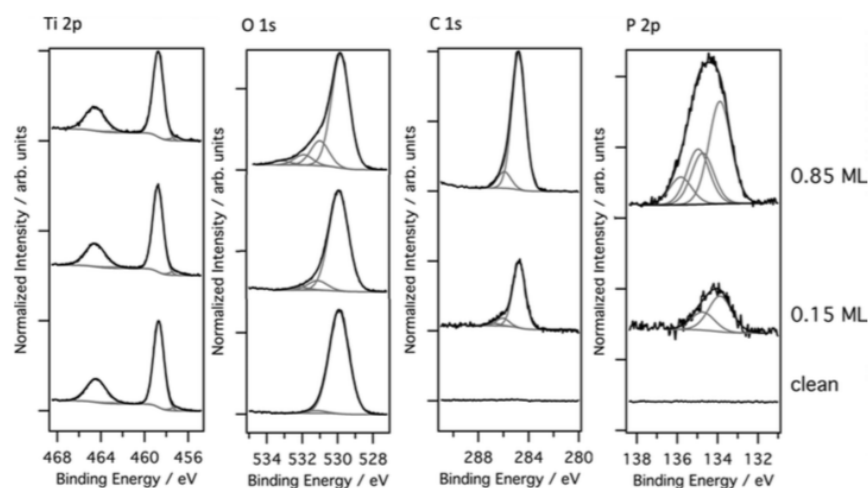


**Figure 3.** Ti 2p (photon energy 570 eV), O 1s (photon energy 650 eV), C 1s (photon energy 385 eV), and P 2p (photon energy 220 eV) XPS core-level spectra showing, from bottom to top, the clean anatase TiO<sub>2</sub>(101) surface, the anatase TiO<sub>2</sub>(101) single crystal following the adsorption of ca. 0.15 monolayer (ML) of PPA, and the anatase TiO<sub>2</sub>(101) single crystal following the adsorption of ca. 0.85 ML of PPA.

labeled 1–5 and that labeled 6 (the chemically shifted C atom bonded to P) as shown in Figure 1. From Figure 1 one would expect the ratio of the two fitted peaks to have a ratio of 5:1. The experimentally observed ratio of 5:0.6, for both coverages shown here, is in relatively good agreement with the expected ratio. The slight discrepancy in the ratio could be due to a difference in attenuation length, or photoelectron diffraction effects, which may affect the relative intensity of emission from C atoms located closer to the surface.<sup>40</sup> It is also possible that it is due to small amounts of carbon contamination. Although it was not performed in this experiment, angle-resolved XPS measurements could be used to determine whether this is a real experimental effect. In order to determine the coverage of the PPA for the two exposures we compared the ratio of the total C 1s signal and the Ti 2p<sub>3/2</sub> signal following adsorption to that of catechol, which also contains a single phenyl ring, but is known to saturate at monolayer coverage.<sup>41–43</sup> This gives us a nominal coverage of around 0.15 monolayer (ML) for the lower exposure and 0.85 ML for the higher exposure. By analogy with carboxylic acid adsorption we assume that two Ti 5c atoms are involved in the bonding of a single molecule to the surface, and so a monolayer is defined as 3 molecules/nm<sup>2</sup> (see Supporting Information, section S.2, for the calculation). The binding energies and relative peak areas for all of the features observed in the XPS spectra are shown in Table 1.

The O 1s spectra shown in Figure 3 are all dominated by the substrate oxide peak at a binding energy of 529.9 eV.<sup>36,44,45</sup> The binding energy of the oxide related O 1s peak does not change following adsorption of the PPA molecule. A small peak at binding energy 531.1 eV is also required in the fitting. The precise nature of this peak is the subject of some debate, it may arise from hydroxyls adsorbed from the residual vacuum, but it has also been suggested that it is intrinsic to the O 1s peak of the anatase TiO<sub>2</sub>(101) surface.<sup>36</sup> It can be seen that following exposure of the anatase TiO<sub>2</sub>(101) surface to PPA additional O-related features appear at the high binding energy side of the oxides O 1s peak, at similar energies to those seen following carboxylic acid<sup>12</sup> and catechol<sup>41</sup> adsorption on this surface.

**Table 1.** Peak Assignments, Their Respective Binding Energies, and the Relative Abundances as a Percentage of Total Peak Area That Are Fitted to the Core Spectra of PPA Adsorbed on Anatase for 0.15 and 0.85 ML Coverages<sup>a</sup>

| species              | assignment                        | 0.15 ML |      | 0.85 ML |      |
|----------------------|-----------------------------------|---------|------|---------|------|
|                      |                                   | BE (eV) | %    | BE (eV) | %    |
| Ti 2p <sub>3/2</sub> | Ti <sup>3+</sup>                  | 457.2   | 4.5  | 457.1   | 3.7  |
|                      | Ti <sup>4+</sup>                  | 458.8   | 95.5 | 458.7   | 96.3 |
| O 1s                 | TiO <sub>2</sub>                  | 529.9   | 88.9 | 529.9   | 74.2 |
|                      | TiOH/P–O <sup>−</sup>             | 531.1   | 8.5  | 531.1   | 16.3 |
|                      | P=O                               | 532.1   | 2.6  | 532.0   | 6.8  |
|                      | P–OH                              |         | 0    | 533.3   | 2.7  |
| C 1s                 | C (1–5)                           | 284.8   | 89.4 | 284.8   | 89.3 |
|                      | C (6)                             | 286.1   | 10.6 | 286.0   | 10.7 |
| P 2p <sub>3/2</sub>  | PO <sub>3</sub> <sup>2−</sup>     | 133.9   | 100  | 133.9   | 64.9 |
|                      | PO <sub>2</sub> (OH) <sup>−</sup> |         | 0    | 135     | 35.1 |

<sup>a</sup>Binding energies are quoted to ±0.1 eV.

Figure 4 shows a magnified view of the region in the O 1s spectra where the adsorbate related features lie. For the surface following adsorption of ca. 15% of a monolayer two peaks are fitted at binding energies of 531.1 eV, peak c, and 532.1 eV, peak b. These peaks are both assigned to O in the adsorbed PPA complex. Previous work on the pure PPA molecule in powder form, i.e., the intact acid, has shown the O 1s to be made up of two components arising from P=O and P–OH with a peak separation of 1.4 eV,<sup>43,46</sup> which is substantially larger than that seen here. From this it can be inferred that the molecule is bonding to the anatase TiO<sub>2</sub>(101) surface via the phosphonic acid group, since if there was no interaction between the phosphonate group and the anatase TiO<sub>2</sub>(101) surface, one would expect the O 1s spectrum to resemble that of the molecule in the powder state. Furthermore, the presence of two additional features in the O 1s spectrum following adsorption suggests the O atoms in the phosphonate group are not in equivalent chemical states; i.e., bonding does not occur through all three of the phosphonate O atoms. The binding energy of the peak fitted with the red line, peak b, is consistent

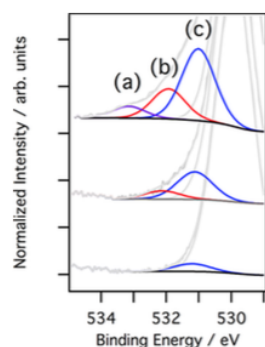


**Figure 4.** O 1s spectra, focusing on the peaks introduced after dosing PPA to the high binding energy side of the oxide peak. The blue curve (c) is assigned to Ti–O–P bonds following dissociation of the OH groups and the red curve (b) to the unbound phosphoryl P=O. At the 0.85 ML coverage a third peak is evident, marked by a purple line (a), which arises from undissociated P–OH.

with the binding energy of O 1s in P=O. The binding energy of peak c at 531.1 eV, however, is much lower than would be expected for that for the intact P–OH group,<sup>44,46,47</sup> suggesting that the OH groups are deprotonated. Thus, we propose that the molecule bonds to surface Ti atoms via the two deprotonated OH groups with the P=O not directly bonded to the surface.

Looking at the ratio of the areas of the two peaks, we obtain a value of 2:0.6 for P–O–Ti:P=O, which is in relatively good agreement with the expected value of 2:1, particularly when one considers that, as mentioned above, there is some intrinsic component of the oxide O 1s in the region of the P–O–Ti related feature. Theoretical studies of PPA adsorption on this surface generally find the bidentate mode to be the lowest energy mode. This is because of the distance between the neighboring rows of surface Ti atoms, which would introduce strain into the molecular adsorbate in order to obtain the tridentate mode.<sup>32</sup> Theory suggests the unbound phosphoryl group actually interacts with surface hydroxyls formed during adsorption of the acid via H-bonding.<sup>48</sup> The uppermost curve in Figure 4 shows the appearance of a third feature, peak a, in the O 1s spectrum at a binding energy of 533.3 eV, as the PPA coverage is increased to 85% of a ML. The binding energy of this peak corresponds to that of P–OH in the unbound molecule.<sup>47</sup> An increase in the intensity of the peaks assigned to P=O and P–O–Ti is also observed. There are two possible explanations for the appearance of this third peak. First, at this higher exposure a second layer has begun to form on top of the first layer. This results in a first layer consisting of P–O–Ti and P=O with the intact acid in the second layer. It is also plausible that as the coverage increases there is a change in bonding mode, where the reduced availability of surface Ti atoms as the coverage increases results in some molecules adsorbing in a monodentate fashion.

The P 2p spectra help us determine the most likely reason for the observed change in the O 1s spectra at higher coverage. For the 0.15 ML coverage, two peaks are fitted at 133.9 and 134.8 eV, which account for the spin–orbit splitting of the P 2p level, with the expected separation of 0.9 eV<sup>49</sup> and the intensity relationship. At 0.85 ML coverage, a second P 2p doublet is required to fit the data with P 2p<sub>3/2</sub> and 2p<sub>1/2</sub> split peaks at binding energies of 135.0 and 135.9 eV, respectively. This

suggests two chemical states of P at the higher coverage, consistent with the change in the O 1s spectrum at higher coverage. The ratio between the areas of the P 2p<sub>3/2</sub> peaks (low BE:higher BE) is 2:1, suggesting the bidentate adsorption mode observed in the 0.15 ML coverage is still dominant at higher coverage. From this we can make an assumption about the binding mode of the minority species by looking at the peak areas of the O 1s peaks labeled (a) and (c) in Figure 4. Since we can see from the P 2p spectra that the ratio of bidentate to the unknown binding mode is 2:1, we can infer that for multilayer formation we would also expect the ratio of the two O 1s peaks to be roughly 2:1 (c:a). This is because for every two bidentate adsorbed molecules we would have four P–O–Ti end groups (peak c in Figure 4) and one unbonded molecule with two P–OH groups (peak a in Figure 4). Alternatively, we can consider a mixed bidentate–monodentate mode, with two bidentate adsorbed molecules (four P–O–Ti groups) and one monodentate (one P–O–Ti and one P–OH group); this would give a peak area ratio of 5:1 (c:a).

These calculations assume that the dissociated H atoms do not go on to produce adsorbed surface hydroxyls. As mentioned above, the oxygen 1s signal for adsorbed surface hydroxyls lies at the same energy as peak c. If we assume every dissociated H atom leads to an adsorbed surface hydroxyl, one would expect the ratio of c:a to be 10:1 for the mixed bidentate–monodentate system or 4:1 for multilayer formation. The measured ratio of 6:1 lies in the range associated with the mixed bidentate–monodentate adsorption mode. It seems that as the coverage increases there is a shift toward a mixed adsorption mode. This is further supported by the fact the carbon spectra suggests we have submonolayer coverage (0.85 ML) and the observed photon energy shift in the P 2p spectra between the monodentate and bidentate adsorbed phosphonate groups. It has been shown that for phosphoric acid-terminated molecules that for each proton that is removed upon adsorption there is a shift of  $\approx 1$  eV to lower binding energy.<sup>49</sup> Therefore, the BE separation here between the two doublets would suggest a change in coordination of the phosphonate group from P(O)<sub>3</sub><sup>2-</sup> to P(O)<sub>2</sub>(OH)<sup>-</sup>. Theoretical work has suggested that the bidentate adsorption would dominate, but the energy difference between mono- and bidentate adsorption is small.<sup>32,33</sup> It seems, at room temperature at least, the surface sustains a mixed bonding geometry similar to catechol adsorption on rutile TiO<sub>2</sub>(110).<sup>50</sup>

It is not possible from these data to determine whether there is a switch to the monodentate mode as the coverage increases, i.e., the bidentate adsorbed molecule “picks up” a proton from a surface hydroxyl, or whether it is merely a statistical effect such that increasing the coverage reduces the number of bidentate states available. Future work would aim to determine whether at much higher coverage the bidentate or monodentate mode would dominate. With regard to the bidentate adsorbed PPA molecules, the data are unable to distinguish between bidentate bridging or bidentate chelating adsorption geometries. Theory, however, suggests that the bidentate bridging mode is more energetically favorable.<sup>34,48</sup> An illustration representing the proposed bonding mechanism, with respect to the surface Ti, is shown in Figure 5.

**NEXAFS.** In order to probe the unoccupied molecular states and bonding geometry of the adsorbed PPA, NEXAFS measurements were carried out on 0.15 and 0.85 ML coverages of PPA on anatase TiO<sub>2</sub>(101). The spectra were recorded with the surface component of the electric vector of the incident

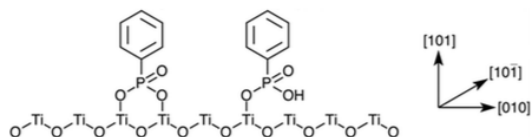


Figure 5. Illustration representing the proposed bonding mechanism of PPA on anatase  $\text{TiO}_2(101)$  as concluded from the XPS data.

light incident at  $16^\circ$  from the  $[10\bar{1}]$  azimuth and  $14^\circ$  to the  $[010]$  azimuth. The spectra are normalized by setting the edge jump from the background at 280 to 310 eV photon energy to unity. The experimental spectrum recorded from the 0.85 ML coverage with the synchrotron beam at normal incidence and the angle-integrated StoBe-calculated NEXAFS spectrum for an isolated PPA molecule are shown in Figure 6a. The calculated

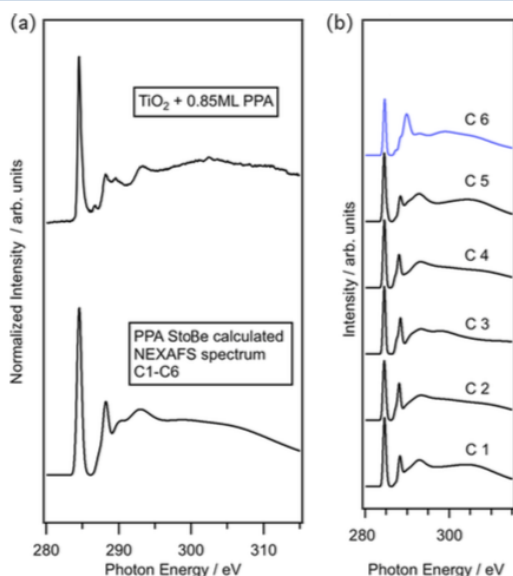


Figure 6. (a) NEXAFS spectra recorded from 0.85 ML of PPA adsorbed on an anatase  $\text{TiO}_2(101)$  single crystal compared to the StoBe-calculated NEXAFS spectrum for the free PPA molecule. (b) The individual contributions from the carbon atoms are shown. These are labeled C1–C6 with respect to the carbon atoms shown in Figure 1, with the phosphonated carbon highlighted in blue.

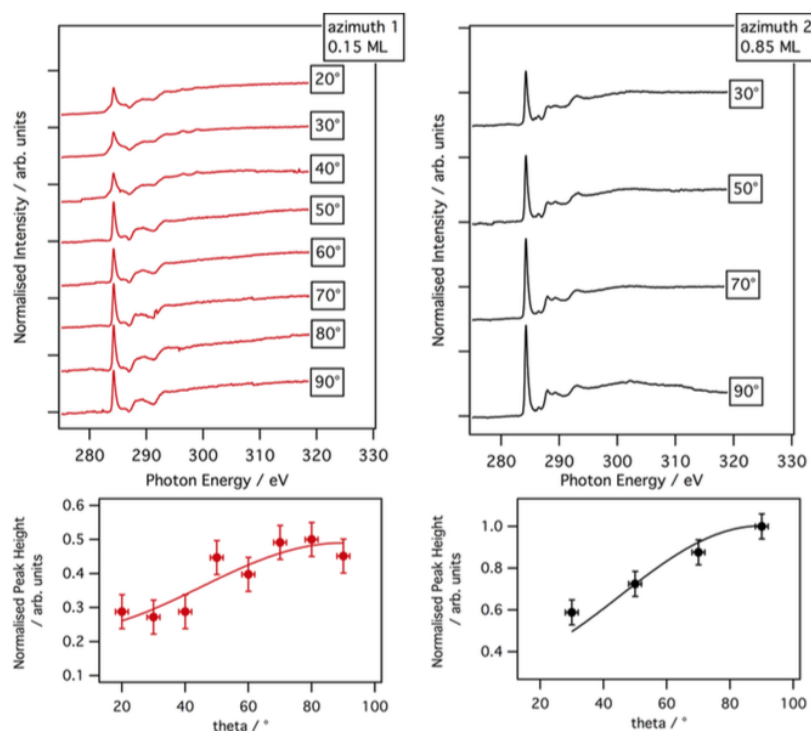
NEXAFS spectra at the C K-edge for the individual carbon atoms, as labeled in Figure 1, are shown in Figure 6b. Each spectrum is energy calibrated and convoluted with a Gaussian distribution to give a similar peak width to the experimental data. The calculated spectra, specific to each atom, can be used to determine the origin of the peaks seen in the experimental spectra. The calculated total NEXAFS spectrum in Figure 6a is aligned on the photon energy scale by aligning the main  $\pi^*$  resonance to that of the experimental spectrum.

A sharp shape resonance can be seen in both the experimental and StoBe-calculated spectra at 284.5 eV, attributed to  $\text{C } 1s_{\text{C-C}} \rightarrow \text{ring } \pi^*$  transitions. Upon careful inspection, this peak is seen to be asymmetric to higher photon energies (see Supporting Information Figure S.3 for an expanded view of the spectra). This asymmetry is mainly due to the chemical shift induced in carbon atom C6 and is

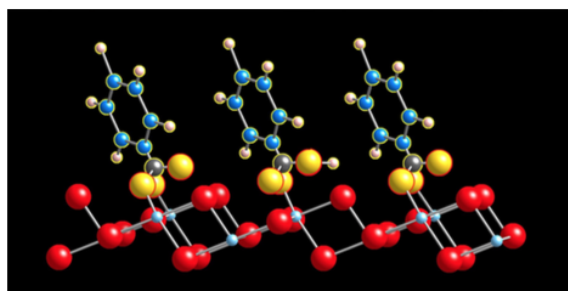
therefore attributed to  $\text{C } 1s_{\text{C-P}} \rightarrow \text{ring } \pi^*$  transitions. However, in addition to this the calculated spectra for C1 and C5 show some asymmetry. We assume this is related to excitation into  $\pi_2^*$  states, i.e.,  $\text{C } 1s_{\text{C-C}} \rightarrow \text{ring } \pi_2^*$  transitions. Note a small feature is present at 286.5 eV in all experimental data but not present in the StoBe-calculated spectra, we therefore assume that this is substrate related. A clear peak can be seen at 288.2 eV, which has been assigned to a mixture of Rydberg transitions and transitions to features of the C–H  $\sigma^*$  bonds.<sup>51–53</sup> The small bump at higher photon energy, at 289.7 and 290.0 eV in the experimental and StoBe-calculated spectra, respectively, can only be seen in the C6 spectra and is therefore attributed to transitions  $\text{C } 1s_{\text{C-P}} \rightarrow \sigma^*$  transitions. The reason for the difference in energy of the experimental and calculated spectra in this region is unclear. It is possible that the difference occurs as a result of the adsorption on the  $\text{TiO}_2$  surface, since the calculated spectrum is for the isolated molecule. However, it may also occur as a result of C contamination of the beamline optics leading to a loss of incident photon flux at these energies. This results in dip at around 290 eV, seen in all experimental spectra. Broader peaks at energies above 290 eV have been assigned to  $\text{C } 1s_{\text{C-C}} \rightarrow \text{ring } \sigma^*$  transitions.

Figure 7 shows the angle-resolved carbon K-edge NEXAFS spectra of PPA adsorbed on anatase  $\text{TiO}_2(101)$  for incident radiation angles of  $20^\circ$ – $90^\circ$  to the surface, in increments of  $10^\circ$ . Fitting to a plot of peak intensity versus incidence angle using the equations of Stöhr, for a surface of 2-fold or higher symmetry,<sup>54</sup> gives a tilt angle for the plane of the phenyl ring of  $65 \pm 5^\circ$  relative to the surface and twisted roughly  $57 \pm 8^\circ$  from the  $[10\bar{1}]$  azimuth. The tilt angle of  $25^\circ$  from the surface normal is similar to that seen for other nonsubstituted aromatic molecules adsorbed in a bidentate fashion on this surface.<sup>12,41,55</sup> Although the molecule is tilted relative to the macroscopic surface, the angle roughly correlates with the molecule in a geometry which is normal to the sawtooth structure of the anatase  $\text{TiO}_2$  surface as shown in Figure 8. Analysis of the XPS spectra shows that at higher coverages PPA shifts to a mixed bidentate/monodentate binding mode, but the NEXAFS data are unable to distinguish between the two binding modes. It is possible that both modes will lead to the molecule exhibiting similar tilt angles since previous DFT calculations have suggested that the tilt angle variation between coverages is small.<sup>52</sup> However, if there are differences in the tilt angle, then the angles obtained from NEXAFS will be an average of the tilt and twist angles the two modes.

**Summary.** The adsorption of phenylphosphonic acid on the anatase  $\text{TiO}_2(101)$  surface, under ultrahigh-vacuum conditions, has been studied using photoelectron and NEXAFS spectroscopy. The data suggest that at low coverage the molecule adsorbs in a bidentate geometry following deprotonation of both phosphonate hydroxyl groups. As the coverage is increased, a mixed bidentate/monodentate binding mode develops. From the data presented here it is not possible to determine whether this mixed mode results from bidentate adsorbed molecules switching to monodentate or as the surface becomes more crowded that only monodentate adsorption can occur. Angle-resolved NEXAFS measurements suggest the molecule is oriented with the plane of the ring roughly  $25^\circ$  relative to the surface normal, i.e., perpendicular to the sawtooth planes of the  $(101)$  surface. The upright geometry combined with the mixed monodentate/bidentate bridging adsorption mode suggests that molecules terminated with a phenylphosphonic acid group show potential for linking



**Figure 7.** Top: carbon K-edge NEXAFS spectra of PPA adsorbed on the anatase  $\text{TiO}_2(101)$  surface. The spectra labeled azimuth 1 are recorded with the surface component of the electric vector of the incident light incident at  $16^\circ$  from the  $[101]$  azimuth. The data in the plot labeled azimuth 2 are recorded with the E-vector  $14^\circ$  to the  $[010]$  azimuth. Bottom: plot of the  $\pi^*$  peak intensity plotted as a function of angle of photon incidence relative to the surface. The Stöhr equations have been fitted to the data points.<sup>54</sup>



**Figure 8.** Schematic figure of the bonding modes of phenylphosphonic acid on the anatase  $\text{TiO}_2(101)$  surface. This figure depicts both the bidentate (left and right) and monodentate (middle) bonding modes. The oxygen atoms in the PPA molecule are colored gold in order to distinguish them from the substrate oxygen atoms, colored red.

quantum dots or biomolecules to titania surfaces. The experimental data show that although it has been suggested that phosphonic acids form a stronger bond than carboxylic acids, this increased stability does not involve a tridentate bonding mode, in agreement with theoretical predictions.

## ■ ASSOCIATED CONTENT

### 5 Supporting Information

The Supporting Information is available free of charge on the ACS Publications website at DOI: 10.1021/acs.jpcc.5b11258.

Survey scan of a clean anatase  $\text{TiO}_2(101)$  surface (S.1); calculation showing how the coverage of PPA on anatase

$\text{TiO}_2(101)$  was determined and the quantitative definition of a monolayer (S.2); expanded NEXAFS spectra highlighting the asymmetry of the main  $\pi^*$  peak (S.3) (PDF)

## ■ AUTHOR INFORMATION

### Corresponding Author

\*E-mail [andrew.g.thomas@manchester.ac.uk](mailto:andrew.g.thomas@manchester.ac.uk); Ph +44 161 306 8764 (A.G.T.).

### Notes

The authors declare no competing financial interest.

## ■ ACKNOWLEDGMENTS

M.W. acknowledges a Doctoral training award studentship from EPSRC and a University of Manchester President's Scholarship; M.J.J. holds a studentship funded by the EPSRC Doctoral Training Centre NowNano (grant EP/G03737X/1). M.T.M. is funded by BP ICAM. The authors thank the EPSRC UK for funding via travel grant EP/M026817/1 and MAXLab and the Swedish Research Council for the beamtime award.

## ■ REFERENCES

- O'Regan, B.; Grätzel, M. A low-cost, high-efficiency solar cell based on dye-sensitized colloidal  $\text{TiO}_2$  films. *Nature* **1991**, *353*, 737–740.
- Ko, K. H.; Lee, Y. C.; Jung, Y. J. Enhanced efficiency of dye-sensitized  $\text{TiO}_2$  solar cells (DSSC) by doping of metal ions. *J. Colloid Interface Sci.* **2005**, *283*, 482–487.

- (3) Zhang, Q.; Cao, G. Nanostructured photoelectrodes for dye-sensitized solar cells. *Nano Today* **2011**, *6*, 91–109.
- (4) Reddy, P. Y.; Giribabu, L.; Lyness, C.; Snaith, H. J.; Vijaykumar, C.; Chandrasekharam, M.; Lakshmikantam, M.; Yum, J.-H.; Kalyanasundaram, K.; Grätzel, M.; et al. Efficient sensitization of nanocrystalline TiO<sub>2</sub> films by a near-IR-absorbing unsymmetrical zinc phthalocyanine. *Angew. Chem., Int. Ed.* **2007**, *46*, 373–376.
- (5) Crossland, E. J. W.; Noel, N.; Sivaram, V.; Leijtens, T.; Alexander-Webber, J. A.; Snaith, H. J. Mesoporous TiO<sub>2</sub> single crystals delivering enhanced mobility and optoelectronic device performance. *Nature* **2013**, *495*, 215–219.
- (6) Fujishima, A.; Honda, K. Electrochemical photolysis of water at a semiconductor electrode. *Nature* **1972**, *238*, 37–38.
- (7) Henderson, M. A. A surface science perspective on TiO<sub>2</sub> photocatalysis. *Surf. Sci. Rep.* **2011**, *66*, 185–297.
- (8) Murphy, M.; Walczak, M.; Hussain, H.; Acres, M.; Muryn, C.; Thomas, A.; Silikas, N.; Lindsay, R. An ex situ study of the adsorption of calcium phosphate from solution onto TiO<sub>2</sub>(110) and Al<sub>2</sub>O<sub>3</sub>(0001). *Surf. Sci.* **2015**, DOI: 10.1016/j.susc.2015.08.040.
- (9) Fei Yin, Z.; Wu, L.; Gui Yang, H.; Hua, S. Y. Recent progress in biomedical applications of titanium dioxide. *Phys. Chem. Chem. Phys.* **2013**, *15*, 4844–4858.
- (10) Tsuchiya, H.; Macak, J. M.; Müller, L.; Kunze, J.; Müller, F.; Greil, P.; Virtanen, S.; Schmuki, P. Hydroxyapatite growth on anodic TiO<sub>2</sub> nanotubes. *J. Biomed. Mater. Res., Part A* **2006**, *77A*, 534–541.
- (11) Yu, J. C. Effects of F-doping on the photocatalytic activity and microstructures of nanocrystalline TiO<sub>2</sub> powders. *Chem. Mater.* **2002**, *14*, 3808–3816.
- (12) Thomas, A. G.; Jackman, M. J.; Wagstaffe, M.; Radtke, H.; Syres, K.; Adell, J.; Lévy, A.; Martsinovich, N. Adsorption studies of p-aminobenzoic acid on the anatase TiO<sub>2</sub>(101) surface. *Langmuir* **2014**, *30*, 12306–12314.
- (13) Hug, H.; Bader, M.; Mair, P.; Glatzel, T. Biophotovoltaics: natural pigments in dye-sensitized solar cells. *Appl. Energy* **2014**, *115*, 216–225.
- (14) Mayor, L. C.; Ben Taylor, J.; Magnano, G.; Rienzo, A.; Satterley, C. J.; O'Shea, J. N.; Schnadt, J. Photoemission, resonant photoemission, and X-ray absorption of a Ru(II) complex adsorbed on rutile TiO<sub>2</sub>(110) prepared by in situ electrospray deposition. *J. Chem. Phys.* **2008**, *129*, 114701.
- (15) Britton, A. J.; Weston, M.; O'Shea, J. N. Charge transfer from an aromatic adsorbate to a semiconductor TiO<sub>2</sub> surface probed on the femtosecond time scale with resonant inelastic X-ray scattering. *Phys. Rev. Lett.* **2012**, *109*, 017401.
- (16) Katono, M.; Bessho, T.; Meng, S.; Humphry-Baker, R.; Rothenberger, G.; Zakeeruddin, S. M.; Kaxiras, E.; Grätzel, M. D-π-A dye system containing cyano-benzoic acid as anchoring group for dye-sensitized solar cells. *Langmuir* **2011**, *27*, 14248–14252.
- (17) Margraf, J. T.; Ruland, A.; Sgobba, V.; Guldi, D. M.; Clark, T. Quantum-dot-sensitized solar cells: understanding linker molecules through theory and experiment. *Langmuir* **2013**, *29*, 2434–2438.
- (18) Mora-Seró, L.; Giménez, S.; Moehl, T.; Fabregat-Santiago, F.; Lana-Villareal, T.; Gómez, R.; Bisquert, J. Factors determining the photovoltaic performance of a CdSe quantum dot sensitized solar cell: the role of the linker molecule and of the counter electrode. *Nanotechnology* **2008**, *19*, 424007.
- (19) Schnadt, J.; Brühwiler, P. A.; Patthey, L.; O'Shea, J. N.; Södergren, S.; Odellius, M.; Ahuja, R.; Karis, O.; Bäessler, M.; Persson, P.; et al. Experimental evidence for sub-3-fs charge transfer from an aromatic adsorbate to a semiconductor. *Nature* **2002**, *418*, 620–623.
- (20) Hagfeldt, A.; Graetzel, M. Light-induced redox reactions in nanocrystalline systems. *Chem. Rev.* **1995**, *95*, 49–68.
- (21) Zabri, H.; Gillaizeau, I.; Bignozzi, C. A.; Caramori, S.; Charlot, M.-F.; Cano-Boquera, J.; Odobel, F. Synthesis and comprehensive characterizations of new cis-RuL<sub>2</sub>(2)X(2) (X = Cl, CN, and NCS) sensitizers for nanocrystalline TiO<sub>2</sub> solar cell using bis-phosphonated bipyridine ligands (L). *Inorg. Chem.* **2003**, *42*, 6655–6666.
- (22) Gillaizeau-Gauthier, I.; Odobel, F.; Alebbi, M.; Argazzi, R.; Costa, E.; Bignozzi, C. A.; Qu, P.; Meyer, G. J. Phosphonate-based bipyridine dyes for stable photovoltaic devices. *Inorg. Chem.* **2001**, *40*, 6073–6079.
- (23) Zakeeruddin, S. M.; Nazeeruddin, M. K.; Pechy, P.; Rotzinger, F. P.; Humphry-Baker, R.; Kalyanasundaram, K.; Grätzel, M.; Shklover, V.; Haibach, T. Molecular engineering of photosensitizers for nanocrystalline solar cells: a synthesis and characterization of Ru dyes based on phosphonated terpyridines. *Inorg. Chem.* **1997**, *36*, 5937–5946.
- (24) Ganbold, E. O.; Lee, Y.; Lee, K.; Kwon, O.; Joo, S. W. Interfacial behavior of benzoic acid and phenylphosphonic acid on nanocrystalline TiO<sub>2</sub> surfaces. *Chem. - Asian J.* **2010**, *5*, 852–858.
- (25) Gao, W.; Dickinson, L.; Grozinger, C.; Morin, F. G.; Reven, L. Self-assembled monolayers of alkylphosphonic acids on metal oxides. *Langmuir* **1996**, *12*, 6429–6435.
- (26) Guerrero, G.; Mutin, P. H.; Vioux, A. Anchoring of phosphonate and phosphinate coupling molecules on titania Particles. *Chem. Mater.* **2001**, *13*, 4367–4373.
- (27) Pawsey, S.; Yach, K.; Reven, L. Self-assembly of carboxyalkyl-phosphonic acids on metal oxide powders. *Langmuir* **2002**, *18*, 5205–5212.
- (28) Lafont, U.; Simonin, L.; Gaberscek, M.; Kelder, E. Carbon coating via an alkyl phosphonic acid grafting route: Application on TiO<sub>2</sub>. *J. Power Sources* **2007**, *174*, 1104–1108.
- (29) Paramonov, P. B.; Paniagua, S. A.; Hotchkiss, P. J.; Jones, S. C.; Armstrong, N. R.; Marder, S. R.; Brédas, J.-L. Theoretical characterization of the indium tin oxide surface and of its binding sites for adsorption of phosphonic acid monolayers. *Chem. Mater.* **2008**, *20*, 5131–5133.
- (30) Brodard-Severac, F.; Guerrero, G.; Maquet, J.; Florian, P.; Gervais, C.; Mutin, P. H. High-field 17 O MAS NMR investigation of phosphonic acid monolayers on titania. *Chem. Mater.* **2008**, *20*, 5191–5196.
- (31) Galoppini, E. Linkers for anchoring sensitizers to semiconductor nanoparticles. *Coord. Chem. Rev.* **2004**, *248*, 1283–1297.
- (32) Lushtinetz, R.; Frenzel, J.; Milek, T.; Seifert, G. Adsorption of phosphonic acid at the TiO<sub>2</sub> anatase (101) and rutile (110) surfaces. *J. Phys. Chem. C* **2009**, *113*, 5730–5740.
- (33) Ambrosio, F.; Martsinovich, N.; Troisi, A. Effect of the anchoring group on electron injection: theoretical study of phosphonated dyes for dye-sensitized solar cells. *J. Phys. Chem. C* **2012**, *116*, 2622–2629.
- (34) O'Rourke, C.; Bowler, D. R. DSSC anchoring groups: a surface dependent decision. *J. Phys.: Condens. Matter* **2014**, *26*, 195302.
- (35) Patthey, L.; Rensmo, H.; Persson, P.; Westermark, K.; Vayssieres, L.; Stashans, A.; Petersson, Å.; Brühwiler, P. A.; Siegbahn, H.; Lunell, S.; et al. Adsorption of bi-isonicotinic acid on rutile TiO<sub>2</sub>(110). *J. Chem. Phys.* **1999**, *110*, 5913–5918.
- (36) Jackman, M. J.; Thomas, A. G.; Muryn, C. Photoelectron spectroscopy study of stoichiometric and reduced anatase TiO<sub>2</sub> (101) surfaces: the effect of subsurface defects on water adsorption at near-ambient pressures. *J. Phys. Chem. C* **2015**, *119*, 13682–13690.
- (37) Choudhury, T.; Saied, S. O.; Sullivan, J. L.; Abbot, A. M. Reduction of oxides of iron, cobalt, titanium and niobium by low-energy ion bombardment. *J. Phys. D: Appl. Phys.* **1989**, *22*, 1185–1195.
- (38) Frisch, M. J.; Trucks, G. W.; Schlegel, H. B.; Scuseria, G. E.; Robb, M. A.; Cheeseman, J. R.; Montgomery, J. A.; Vreven, T.; Kudin, K. N.; Burant, J. C.; et al. *Gaussian 03, Revision C.02*; Gaussian, Inc.: Wallingford, CT, 2004.
- (39) Hermann, K.; Pettersson, L. StoBe-deMon software. Stockholm - Berlin, version 2.2 of deMon, 2006.
- (40) Bishop, H. E. The effects of photoelectron diffraction on quantitative X-ray photoelectron spectroscopy. *Surf. Interface Anal.* **1991**, *17*, 197–202.
- (41) Syres, K. L.; Thomas, A. G.; Flavell, W. R.; Spencer, B. F.; Bondino, F.; Malvestuto, M.; Preobrajenski, A.; Grätzel, M. Adsorbate-induced modification of surface electronic structure: pyrocatechol adsorption on the anatase TiO<sub>2</sub> (101) and rutile TiO<sub>2</sub> (110) surfaces. *J. Phys. Chem. C* **2012**, *116*, 23515–23525.

- (42) Li, S.-C.; Wang, J.-g.; Jacobson, P.; Gong, X.-Q.; Selloni, A.; Diebold, U. Correlation between bonding geometry and band gap states at organic-inorganic interfaces: catechol on rutile TiO<sub>2</sub> (110). *J. Am. Chem. Soc.* **2009**, *131*, 980–984.
- (43) Li, S.-C.; Losovyj, Y.; Diebold, U. Adsorption-site-dependent electronic structure of catechol on the anatase TiO<sub>2</sub> (101) surface. *Langmuir* **2011**, *27*, 8600–8604.
- (44) Zorn, G.; Adadi, R.; Brener, R.; Yakovlev, V. A.; Gotman, I.; Gutmanas, E. Y.; Sukenik, C. N. Tailoring the surface of NiTi alloy using PIRAC nitriding followed by anodization and phosphonate monolayer deposition. *Chem. Mater.* **2008**, *20*, 5368–5374.
- (45) Walle, L. E.; Borg, A.; Johansson, E. M. J.; Plogmaker, S.; Rensmo, H.; Uvdal, P.; Sandell, A. Mixed dissociative and molecular water adsorption on anatase TiO<sub>2</sub> (101). *J. Phys. Chem. C* **2011**, *115*, 9545–9550.
- (46) Tsud, N.; Yoshitake, M. Vacuum vapour deposition of phenylphosphonic acid on amorphous alumina. *Surf. Sci.* **2007**, *601*, 3060–3066.
- (47) Adden, N.; Gamble, L. J.; Castner, D. G.; Hoffmann, A.; Gross, G.; Menzel, H. Phosphonic acid monolayers for binding of bioactive molecules to titanium surfaces. *Langmuir* **2006**, *22*, 8197–8204.
- (48) Nilsing, M.; Lunell, S.; Persson, P.; Ojamäe, L. Phosphonic acid adsorption at the TiO<sub>2</sub> anatase (101) surface investigated by periodic hybrid HF-DFT computations. *Surf. Sci.* **2005**, *582*, 49–60.
- (49) Textor, M.; Ruiz, L.; Hofer, R.; Rossi, A.; Feldman, K.; Hähner, G.; Spencer, N. D. Structural chemistry of self-assembled monolayers of octadecylphosphoric acid on tantalum oxide surfaces. *Langmuir* **2000**, *16*, 3257–3271.
- (50) Li, S.-C.; Chu, L.-N.; Gong, X.-Q.; Diebold, U. Hydrogen bonding controls the dynamics of catechol adsorbed on a TiO<sub>2</sub>(110) surface. *Science* **2010**, *328*, 882–884.
- (51) Hähner, G. Near edge X-ray absorption fine structure spectroscopy as a tool to probe electronic and structural properties of thin organic films and liquids. *Chem. Soc. Rev.* **2006**, *35*, 1244–1255.
- (52) Gliboff, M.; Sang, L.; Knesting, K. M.; Schalnath, M. C.; Mudalige, A.; Ratcliff, E. L.; Li, H.; Sigdel, A. K.; Giordano, A. J.; Berry, J. J.; et al. Orientation of phenylphosphonic acid self-assembled monolayers on a transparent conductive oxide: a combined NEXAFS, PM-IRRAS, and DFT study. *Langmuir* **2013**, *29*, 2166–2174.
- (53) Harding, K.; Kalirai, S.; Hayes, R.; Ju, V.; Cooper, G.; Hitchcock, A.; Thompson, M. Inner-shell excitation spectroscopy of peroxides. *Chem. Phys.* **2015**, *461*, 117–124.
- (54) Stöhr, J. *NEXAFS Spectroscopy*; Springer-Verlag: Berlin, 2003.
- (55) Thomas, A.; Flavell, W.; Chatwin, C.; Rayner, S.; Tsoutsou, D.; Kumarasinghe, A.; Brete, D.; Johal, T.; Patel, S.; Purton, J. Adsorption of bi-isonicotinic acid on anatase TiO<sub>2</sub>(101) and (001) studied by photoemission and NEXAFS spectroscopy. *Surf. Sci.* **2005**, *592*, 159–168.

